DEMONSTRATION OF IMPROVED SENSITIVITY OF ECHO ATOM INTERFEROMETERS TO GRAVITATIONAL ACCELERATION

CARSON K. MOK

A DISSERTATION SUBMITTED TO THE FACULTY OF GRADUATE STUDIES
IN PARTIAL FULFILMENT OF THE REQUIREMENTS
FOR THE DEGREE OF

DOCTOR OF PHILOSOPHY

GRADUATE PROGRAM IN PHYSICS AND ASTRONOMY
YORK UNIVERSITY
TORONTO, ONTARIO
JUNE 2013

DEMONSTRATION OF IMPROVED SENSITIVITY OF ECHO ATOM INTERFEROMETERS TO GRAVITATIONAL ACCELERATION

by **Carson K. Mok**

a dissertation submitted to the Faculty of Graduate Studies of York University in partial fulfilment of the requirements for the degree of

DOCTOR OF PHILOSOPHY

Abstract

We have developed two configurations of an echo interferometer that rely on standing wave excitation of a laser-cooled sample of rubidium atoms. Both configurations are sensitive to acceleration along the axis of excitation. For a two-pulse configuration, the signal from the interferometer is modulated at the recoil frequency and exhibits a sinusoidal frequency chirp as a function of pulse spacing. In comparison, for a three-pulse stimulated echo configuration, the signal is observed without recoil modulation and exhibits a modulation at a single frequency as a function of pulse spacing. The three-pulse configuration is less sensitive to effects of vibrations and magnetic field curvature, leading to a longer experimental timescale. For both configurations of the interferometer, we show that a measurement of acceleration with a statistical precision of 0.5% can be realized by analyzing the shape of the echo envelope, which has a temporal duration of a few microseconds. Using the two-pulse interferometer, we obtain measurements of acceleration that are statistically precise to 6 parts per million on a 25 ms timescale. In comparison, using the three-pulse interferometer, we obtain measurements of acceleration that are statistically precise to 75 parts per billion on a timescale of 70 ms. The inhomogeneous field of a magnetized vacuum

chamber limited the experimental timescale and resulted in prominent systematic effects. Extended timescales and improved signal-to-noise ratio observed in recent echo experiments using a non-magnetic vacuum chamber suggest that echo techniques are suitable for a high precision measurement of gravitational acceleration g. We discuss methods for reducing systematic effects and improving the signal-to-noise ratio. Simulations suggest that an optimized experiment with improved vibration isolation that utilizes atoms selected in the magnetic sublevel $m_F = 0$ state can result in measurements of g precise to 0.5 parts per billion with a timescale of 300 ms.

To my elders: Grandmom, Grandpa, Mom and Dad.

Acknowledgements

First and foremost, I would like to thank my supervisor Dr. Kumarakrishnan for providing me the opportunity to work in his research lab. During my second year of my undergraduate career at York University, I was offered a position in his group and have been there ever since. Conversations at the white board lasting hours about mathematics, and interpretations of physics were a memorable part of the experience. I would like to thank my supervisory committee of Eric Hessels and Cody Storry for their constructive input over the years. I thank you all for supervising me.

I have been fortunate enough to have shared experiences with many different graduate students. Matthew Weel and Scott Beattie were the people that took me under their wing at the start. Iain Chan and Adam Carew were always available in the laboratory as a sounding board for ideas and were always willing to assist in the experiment. Robert Berthiaume provided very helpful suggestions regarding the reconstruction of the apparatus. Much kudos to Brynle Barrett who has shaped much of this work with his theoretical expertise and willingness to help.

Many undergraduates have crossed my path during my time as a graduate student; each one has contributed in their own way to this body of work. My first summer

in the laboratory with David Gosset, Neil Jones, Kasia Sowka was a formative learning experience. Working with Fadi Yachoua, Vlad Popovichi and Soshana Winter helped with the basic underlying technical and mathematical concepts. Kyle Reiter had a dogged determination to finish any work I assigned him. Carol Guimares, Lianne Manzer, Hermina Beica, Eric Davidson, Raanan Marants were always willing to provide suggestions regarding the sensitive alignment of equipment. Electrical engineering from Antoine Sarrachini and Anthony Salerno was gladly accepted. Nima Afkami-Jeddi consistently provided interesting insight on the performance of home-built lasers.

This work benefited immensely from the initial theoretical efforts of Itay Yavin and David Gosset. Itay was effectively a non-resident post-doc during the entire project.

This thesis would not have been completed with support from all the staff at York university. Machine shop expertise from Ator Sarsikoff and Frank Canzona brought me a new appreciation of making something with my own hands. Their lessons of getting things right the first time, or else you'll start again from the beginning will always resonate with me. Glass blower Dirk Verdoold and the electronics gurus, thank you for answering my cries for your services always in a timely manner. Anne, your late night conversations will not be forgotten. Daniel was particularly helpful regarding shipping and chemical waste disposal. Without administrative assistants Lauren O'Brien and Marlene Caplan, I would never have the proper paperwork, keys,

access cards, contracts, website addresses, passwords, phone contact information, and everything else that I needed to get around the university.

My thanks to the National Science and Engineering Council (NSERC), the province of Ontario, and York University for their generous financial support through scholarships.

An extended loan of crucial laser components from Tycho Sleator at New York University at a critical juncture allowed the completion of the experiment. The liberal loan of a high-bandwidth scope from Wendy Taylor allowed large data sets to be acquired in reduced time.

And last, but not least, my darling wife Amanda Pulker. My life would never be complete without you on the journey.

Table of Contents

List of Tables

List of Figures

Preface

There are two legends in the world of physics that I would like to share with you:

Galileo Galilei held, in his left hand an apple, in his right hand, a rock. Standing at the top of the Leaning Tower of Pisa, he let them fall at the same time. The crowd gathered below watched the two objects fall. Both fell at the same time, and struck the ground at the same time.

Isaac Newton was sitting outside, leaning up against a tree, pondering the mysteries of the universe. All of a sudden, an apple fell on his head. The story says that at that very moment, the law of Universal Gravitation was born – a law that has been with us for the last 300 years, a law that has been tested across the solar system, the galaxy, the universe, and to this day, the tiniest microscopic lengths.

But what if these two giants didn't use an apple, but a magneto-optical trap?

0.1 Fundamental Physical Constants

Definition	Symbol	Value
Speed of light	c	2.977 924 58 $\times 10^{8}$ m/s (exact)
Permeability of Vacuum	μ_0	$4\pi \times 10^{-7}$ N/A^2 (exact)
Permittivity of Vacuum	ϵ_0	$(\mu_0 c^2)^{-1}$ (exact)
Reduced Planck's constant	$\hbar$	1.054 571 726(29) $\times 10^{-34}$ J s
Bohr Magneton	μ_b	9.274 008 99(37) $\times 10^{-24}$ J/T
Boltzmann's Constant	k_B	1.380 650 3(24)$\times 10^{-23}$ J/K
Standard acceleration of gravity	g	9.806 65 m/s^2
Universal gravitational constant	G	6.673 84(80) $\times 10^{-11}$ m^3/kg s^2

Table 1: Fundamental Physical Constants used. Values are from CODATA. [3]

0.2 ^{85}Rb $5^2S_{1/2}F = 3 \rightarrow 5^2P_{3/2}F' = 4$ Transition Values

Symbol	Definition	Value
λ	Transition wavelength (vacuum)	780.241 368 271 (27) nm
ω_0	Transition angular frequency	$2\pi\cdot$ 384.230 406 373(14) rad/s
ν_0	Transition frequency	384.230 406 373(14) THz
$k = 2\pi/\lambda$	Wavevector of laser light	$2\pi\cdot$ 12.816 546 784 96 (45) m^{-1}
M	Mass	1.409 993 199(70)$\times 10^{-25}$ kg
τ	Excited State Lifetime	26.234 88 (77) ns
$\Gamma = 1/\tau$	Decay Rate	$2\pi\cdot$ 6.066 6 (18) rad/s
$\Gamma_N = 1/2\pi\tau$	Natural Linewidth	6.066 6 (18) MHz
v_r	Recoil Velocity of ^{85}Rb	6.023 0 mm/s
α_p	$\alpha_p(5^2P_{1/2}) - \alpha_p(5^2S_{1/2})$	
	D_2 scalar polarizability	$h \cdot 0.1340(8)$ Hz/(V/cm)^2
I_{sat}	Saturation Intensity for	
	$m_F = 3 \rightarrow m_{F'} = 4, \sigma^{\pm}$ polarization	2 $\times$ 1.669 32(35) mW/cm^2
μ_{21}	$D_2(5^2S_{1/2} \rightarrow 5^2P_{3/2})$	
	Transition Dipole Matrix Element	3.584 25(74)$\times 10^{-29}$C·m

Table 2: ^{85}Rb $5^2S_{1/2}F = 3 \rightarrow 5^2P_{3/2}F' = 4$ Transition Values [1].

0.3 ^{87}Rb $5^2S_{1/2}F = 2 \rightarrow 5^2P_{3/2}F' = 3$ Transition Values

Symbol	Definition	Value
λ	Transition wavelength (vacuum)	780.241 209 868 (13) nm
ω_0	Transition angular frequency	$2\pi\cdot$ 384.230 484 468 5(62) rad/s
ν_0	Transition frequency	384.230 484 468 5(62) THz
$k = 2\pi/\lambda$	Wavevector of laser light	$2\pi\cdot$ 12.816 549 389 93 (21) m^{-1}
M	Mass	1.443 160 648(72)$\times 10^{-25}$ kg
τ	Excited State Lifetime	26.234 8 (77) ns
$\Gamma = 1/\tau$	Decay Rate	$2\pi\cdot$ 6.066 6 (18) MHz
$\Gamma_N = 1/2\pi\tau$	Natural Linewidth	6.066 6 (18) MHz
v_r	Recoil Velocity of ^{87}Rb	5.884 5 mm/s
α_p	$\alpha_p(5^2P_{1/2}) - \alpha_p(5^2S_{1/2})$	
	D_2 scalar polarizability	$h\cdot$ 0.1340(8) Hz/(V/cm)^2
I_{sat}	Saturation Intensity for	
	$m_F = 3 \rightarrow m_{F'} = 4, \sigma^{\pm}$ polarization	2 $\times$ 1.669 33(35) mW/cm^2
μ_{21}	$D_2(5^2S_{1/2} \rightarrow 5^2P_{3/2})$	
	Transition Dipole Matrix Element	3.584 25(74)$\times 10^{-29}$C·m

Table 3: ^{87}Rb $5^2S_{1/2}F = 2 \rightarrow 5^2P_{3/2}F' = 3$ Transition Values [2].

Symbols and Abbreviations

0.4 Symbols

Symbol	Definition
t	Time
T	Time separation between interferometry pulses in Raman Interferometer
F, m_F	Hyperfine quantum number, Hyperfine magnetic sub-sevel quantum number
q	Difference of wavevectors in AI beam
k	The wavevector of the laser light
ϕ_{AI}	Interferometer phase
α	Frequency chirp rate
M	Atomic mass
λ	Wavelength of the laser light
$T_1, T_2, T_3...$	Time of the first, second, third interferometry pulses
T_{21}	Time separation between first and second interferometry pulses
ω_q	Recoil frequency
u	Most probable speed in a sample of atoms
$\mathcal{T}$	Temperature of the sample
τ_{coh}	Coherence time of sample due to velocity

Table 4: List of Symbols in Chapter 1.

Symbol	Definition
Δ	One photon detuning
T_{echo}	Echo time
Δt	Time relative to echo time
T_{32}	Time separation between second and third interferometry pulses
τ_1, τ_2, τ_3	Duration of the first, second, third interferometry pulses

Table 5: List of Symbols in Chapter 2.

Symbol	Definition
ω_0, ω_L	Angular frequency of rubidium transition, laser frequency
$\|g\rangle, \|e\rangle$	Ground state, Excited state wavefunction
$\hat{\mathbf{p}}$	Momentum operator
i	$\sqrt{-1}$
$V(\mathbf{r})$	3D Standing wave light field potential
Γ	Effective radiative decay rate of excited state
μ	Electric dipole moment
A_0	Electric field amplitude of standing wave
Ω	One photon Rabi frequency
U	1D Standing wave light field potential
z	Spatial co-ordinate
$\vartheta_1, \vartheta_2, \vartheta_3$	Pulse area of first, second third pulse
J_n	Bessel function of order n
ψ	Wavefunction of atom
k_0, p_0	Initial wavevector and momentum of atom
v_{recoil}	Recoil velocity
λ_{dB}	de Broglie wavelength of atom
m', n'	Summation indices
X, Y	General operators

Table 6: List of Symbols in Chapter 2, continued.

Symbol	Definition
$\phi_g^{(2)}$	Gravity phase in the two-pulse AI
$E_0^{(2)}$	Total two-pulse AI backscattered electric field amplitude
$E_g^{(2)}$	Total two-pulse AI backscattered electric field
$E_0^{(2)}(\Delta t)$	Terms of $E_0^{(2)}$ dependent on Δt
$E_g^{(2)}(\Delta t)$	Terms of $E_g^{(2)}$ dependent on Δt
$\phi_{\mathrm{D}}^{(2)}$	Doppler phase of the two-pulse AI
$\omega_{\mathrm{D}}^{(2)}$	Frequency of the Doppler phase of the two-pulse AI
$E_0^{(2)}(T_{21})$	Terms of $E_0^{(2)}$ dependent on T_{21}
$E_g^{(2)}(T_{21})$	Terms of $E_g^{(2)}$ dependent on T_{21}
τ_{decay}	Signal decay time constant
$\phi_{\mathrm{AI}}^{(2)}$	AI phase of the two-pulse AI
$\omega_{\mathrm{AI}}^{(2)}$	Frequency of the AI phase of the two-pulse AI
$\phi_g^{(3)}$	Gravity phase in the three-pulse AI
$E_0^{(3)}$	Total three-pulse AI backscattered electric field amplitude
$E_g^{(3)}$	Total three-pulse AI backscattered electric field
$E_0^{(3)}(\Delta t)$	Terms of $E_0^{(3)}$ dependent on Δt
$E_g^{(3)}(\Delta t)$	Terms of $E_g^{(3)}$ dependent on Δt
$\phi_{\mathrm{D}}^{(3)}$	Doppler phase of the three-pulse AI
$\omega_{\mathrm{D}}^{(3)}$	Frequency of the Doppler phase of the three-pulse AI
$E_0^{(3)}(T_{21}, T_{32})$	Terms of $E_0^{(3)}$ dependent on T_{21}, T_{32}
$E_g^{(3)}(T_{21}, T_{32})$	Terms of $E_g^{(3)}$ dependent on T_{21}, T_{32}
$\phi_{\mathrm{AI}}^{(3)}$	AI phase of the three-pulse AI
$\omega_{\mathrm{AI}}^{(3)}$	Frequency of the AI phase of the three-pulse AI

Table 7: List of Symbols in Chapter 2, continued.

Symbol	Definition
$\mathcal{S}$	Classical action
$\mathcal{L}$	Classical Lagrangian
$\mathcal{L}_A, \mathcal{L}_B, \mathcal{L}_C, \mathcal{L}_O,$	Classical Lagrangian along paths A, B, C, O
$\mathcal{S}_A, \mathcal{S}_B, \mathcal{S}_C, \mathcal{S}_O,$	Classical action along paths A, B, C, O
ϕ_{path}	Classical phase difference due to difference in paths
$\phi_{\text{interaction}}$	Classical phase shift due to interaction with the light field
$z_1^U, z_2^U, z_3^U, z_4^U$	Co-ordinate of vertices of recoil diagram
Δz	Classical displacement of an object
ω_i	Incident light frequency
ω_R	Reflected light frequency

Table 8: List of Symbols in Chapter 2, continued.

Symbol	Definition
n	Number density
η	Index of refraction
Ω'	Generalized Rabi frequency
δ	AC Stark level shift
T_{velocity}	Three-pulse AI period

Table 9: List of Symbols in other Chapters

0.5 Abbreviations

Abbreviation	Definition
SQUID	Superconducting quantum interference device
ppb	Parts per billion
MOT	Magneto-Optical trap
AI	Atom Interferometer
ppm	Parts per million
BEC	Bose-Einstein condensate
GPS	Global Positioning Service
RF	Radio Frequency
AC	Alternating Current
SW	Standing Wave
RO	Read-Out
Ti:Sapphire	Titanium doped sapphire
TA	Tapered Amplifier
ECDL	External Cavity Diode Laser
CD	Compact Disc
AOM	Acousto-Optic Modulator

Table 10: List of Abbreviations.

Abbreviation	Definition
PD	Photodiode
AR	Anti-reflection
CF	Con-Flat vacuum flange
CCD	Charge Coupled Device
PMT	Photomultipler Tube
TTL	Transistor-Transistor Logic
IGBT	Insulated Gate, Bipolar Transistor
VCO	Voltage Controlled Oscillator
TV	Television
LO	Local Oscillator
DC	Direct Current
IP	In-phase
QUAD	In-quadrature

Table 11: List of Abbreviations, continued.

1 Introduction

1.1 Overview of Gravimetry

Precise measurements of the local gravitational acceleration g are important both for scientific and technological applications. Although gravity is the oldest known fundamental interaction, the strength of this interaction, defined by the universal gravitational constant G, is among the least precisely known fundamental constants [3–6]. Therefore, precision measurements of gravity continue to be an active field of study for answering questions related to the variation of the force on different length scales [7–9] and for tests of general relativity [10–14].

The technological impact of gravity measurements has enormous practical applications. Local gravity measurements that are sensitive to the spatial variation of g on the surface of earth form the basis of wide area (air/land/sea surveys) density mapping for resource prospecting associated with oil and mineral assaying. Gravitational measurements are often used in remote sensing for seismic exploration and monitoring of environmentally sensitive areas. Mapping gravity along boreholes provides the density profile along the vertical of the earth's crust providing further localization of

density variations. The temporal variation of g is of interest for the correction of tidal charts. Historically, these charts have been compiled through careful local observations averaged over many decades. With gravimetric measurements, it is possible to develop highly accurate methods of predicting these variations.

The most precise absolute gravimeter based on superconducting quantum interference devices (SQUIDs) is precise to one part in 10^{13} [15,16]. These devices monitor the current required to levitate a conductive sphere. As gravity changes, the current required to maintain the position of the sphere changes. Since the sphere is part of a conductance bridge circuit, the current gives a direct measurement of g.

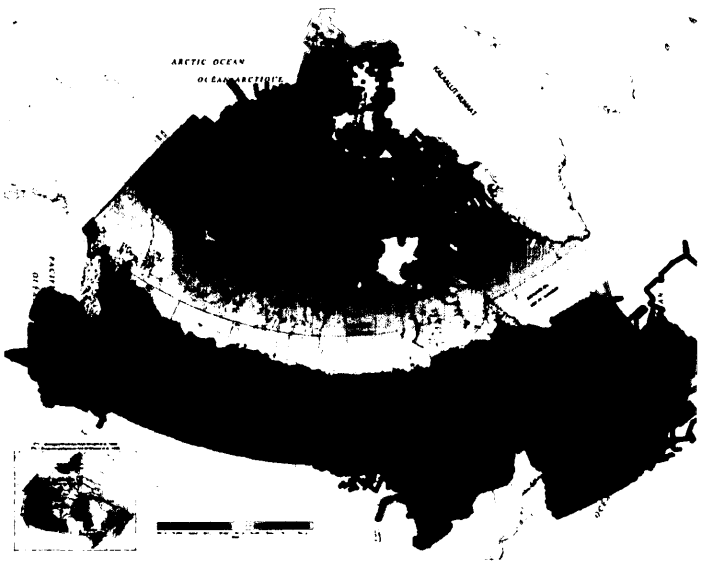

Figure 1.1: Map of measured value of gravity across Canada by cantilever sensors. The change in gravity is due to latitude and local density variations in geography. The value of g shown in blue increases as the colour code changes to from 9.8016 m/s^2 to pink 9.8304 m/s^2. Map courtesy of Government of Canada [17].

In contrast to the SQUID sensor, the most common industrial gravimeters are portable and have been designed for both relative and absolute measurements. Rela-

tive sensors are based on detecting a change in capacitance when one plate of a parallel plate capacitor, which is part of a cantilever arm, is deflected in gravity. These sensors can typically detect changes as low as 10 part per billion (ppb), but they are prone to drifts. Figure 1.1 shows a large area gravity map obtained by cantilever sensors showing a variation in g at the 0.3% level across Canada.

The most precise, portable, absolute gravimeter is based on an optical Mach-Zehnder interferometer [18], as shown in figure 1.2a. It relies on an interferometric measurement of the acceleration of a falling corner cube retro-reflector [19], as shown in figure 1.2b. This type of interferometer achieves an absolute accuracy of 1 ppb which is more than adequate to observe tidal variations, shown in figure 1.2c [20], at the level of 100 ppb. This instrument counts the number of fringes as a function of time, effectively measuring the displacement of a falling object in an inertial reference frame.

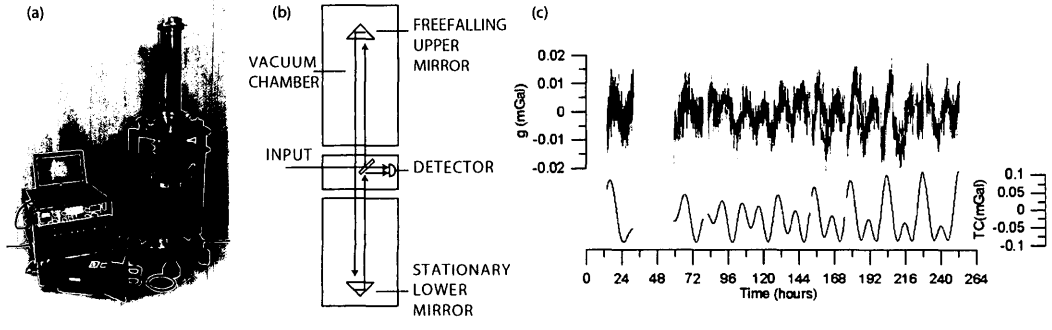

Figure 1.2: (a) Falling corner cube interferometer and control electronics. Image from Microg-LaCoste. (b) Schematic of falling corner cube detector in (a). (c) Adapted from reference [20]. Bottom trace: Expected tidal correction at Orléans, France from 9 to 19 May 2000. Top trace: residuals between the measured value of gravity and the expected tidal correction; 1 Gal = 1 cm/s^2.

1.2 Laser-Cooled Atoms and Atom Interferometry

The development of laser-cooling techniques [21] and the realization of magneto-optical traps (MOTs) [22, 23] allowed localized samples containing $\approx 10^9$ cold atoms to be routinely cooled to temperatures of a few micro-Kelvin. Under these conditions, the Doppler spectral width of the sample can be smaller than the natural linewidth of the laser-cooling transition. Additionally, the ≈ 50 nm de Broglie wavelength of an atom in a MOT becomes comparable to the ≈ 100 nm length scales of optical potentials that can be created with spatially periodic intensities associated with standing wave light fields. As a result, it became possible to develop the field of atom interferometry for precise measurements of inertial effects [24]. This field was also influenced by the study of Kapitza-Dirac scattering of atoms involving the efficient diffraction of atoms in an atomic beam using optical standing wave fields [25].

The most widely developed atom interferometer (AI) that uses cold atoms is the Raman AI developed at Stanford University [24]. This AI has produced the most precise atom-based measurement of inertial forces [26–28] and is the technique of choice for developing portable cold atom sensors [29]. The best absolute measurement of g using the Raman AI achieved a precision of 3 ppb in 1 minute [26]. Other techniques such as sensors relying on Bloch oscillations [30] have attained a statistical precision of 100 ppb for measurements of g.

1.2.1 Dissertation Overview

Despite the development of various methods based on these schemes, it is interesting to consider the possibility of achieving high precision measurements of g using a technique that offers reduced experimental complexity since such a technique will make it easier to calibrate industrial sensors. In this dissertation, we have developed two configurations of an echo-type AI [31–36] and explored appropriate analysis techniques for measuring the absolute value of acceleration. Despite the constraints of working with a magnetized apparatus that could only be partially shielded from the effect of vibrations, we report the ability to measure accelerations along the vertical with a statistical precision of 75 ppb by dropping cold atom clouds through a distance of 2.4 cm [36, 37]. Following recent demonstrations of long timescale measurements of atomic recoil [38], magnetic gradients [35] and atomic g-factor ratios [39] in which the atoms were dropped up to 30 cm in a non-magnetic apparatus, we predict that state-of-the-art measurements of g will become possible with the cold atom interferometers developed in this dissertation. Such an experiment will require a suitably stabilized, non-magnetic apparatus.

The rest of this introductory chapter is organized as follows. We first review the key developments in the area of laser-cooling and trapping. This is followed by an introduction to atom interferometric measurements of g using Raman atom interferometers and Bloch oscillations. We then present the main features of the time-domain, echo-type interferometer that was developed in this dissertation for

precise measurements of g.

1.2.2 Magneto-Optical Trapping

Efforts to trap neutral atoms using the radiation pressure force and the optical dipole force began in the early 1970s. The major proposals related to the radiation pressure force included the work in references [40–44]. This theoretical foundation led to experiments in which dielectric spheres and biological specimens were trapped by Ashkin and co-workers [45–48] using the optical dipole force.

Initial experiments in laser-cooling of neutral atoms focused on slowing an atomic beam either by shifting the laser frequency to compensate for the Doppler shift due to the absorption of photons [49] or by using a constant frequency laser and Zeeman slower[1] to shift spectral lines to maintain the resonance condition [50, 51].

The proposal with the most impact on the development of an optical molasses[2] [52] involved exploitation of the differential Doppler shift between two counter propagating laser beams in the atom's reference frame [53], as described in figure 1.3a. A typical optical molasses consisted of a relatively dilute cloud of atoms with a number density of $10^8/\text{cm}^3$ and a sample size of the order of the laser beam diameter. The idea for the laser configuration used in this experiment was first proposed by Dalibard in reference [54] and initial experiments [21] showed that the temperature of the atoms

[1] A Zeeman slower is a suitably long solenoid with a tapered magnetic field that provides a spatially varying Zeeman shift.

[2] An optical molasses refers to a dilute gas in which there is a net damping force due to the laser cooling mechanism.

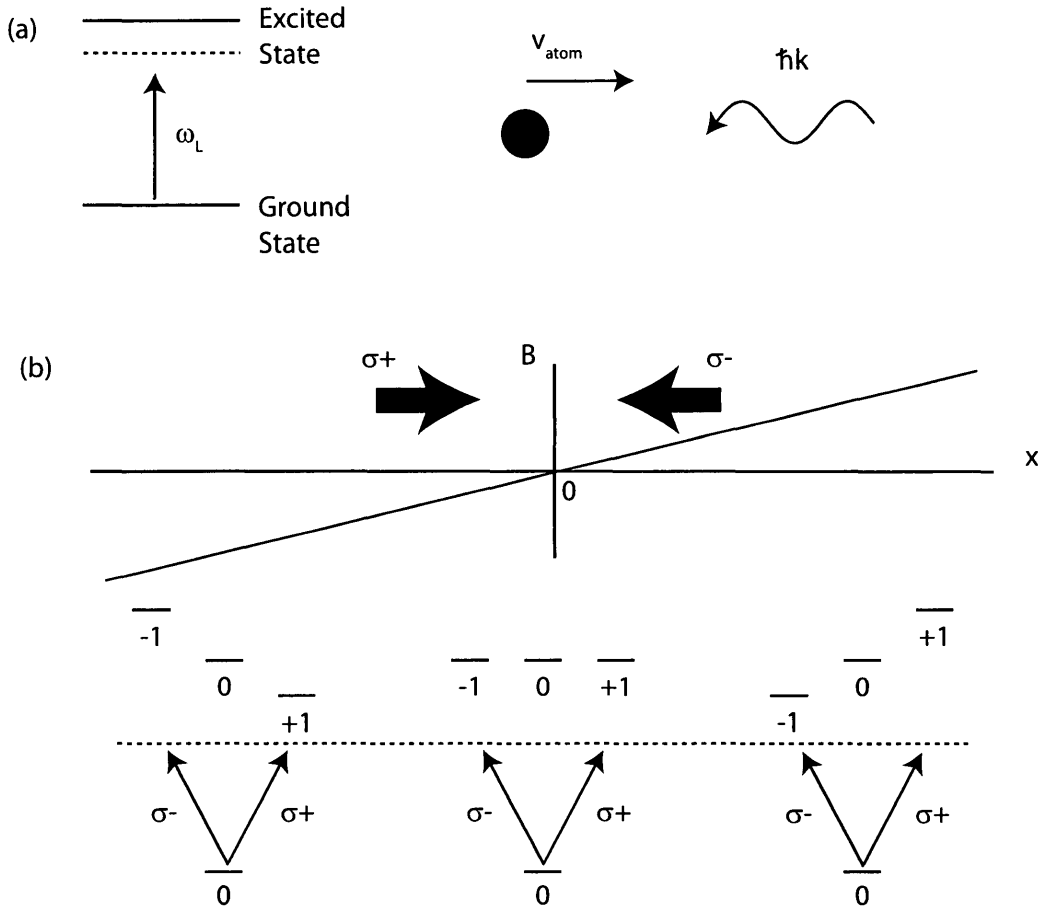

Figure 1.3: (a) A laser detuned below resonance in the lab frame is Doppler shifted closer to resonance in the atom's frame, if an atom travels toward the laser. The same laser frequency is Doppler shifted away from resonance for atoms moving in the direction of the laser. With two counter-propagating beams, there is a net velocity dependent force in the direction opposing the motion of the atom due to the differential Doppler shift in the atom's frame. This net force is responsible for damping the motion of the atoms. (b) The two counterpropagating laser beams are oppositely circularly polarized and tuned below resonance in the presence of a constant magnetic gradient. The Zeeman splitting of the excited state magnetic sublevels is illustrated for an atom with a $J = 0$ ground state and a $J = 1$ excited state. The position dependent Zeeman shift produces a position dependent trapping force due to the differential absorption of photons. The net force pushes the atom toward $x = 0$.

was much lower than the Doppler limit[3] for a two-level atom ($\approx 140\ \mu$K for rubidium). On the basis of theoretical work [54, 55], it was established that the mechanism of polarization gradient cooling was responsible for the sub-Doppler temperatures.

These experiments culminated in the successful demonstration of a MOT using sodium [22]. In this experiment, atoms were slowed from an atomic beam and trapped by laser-cooling in the presence of a magnetic field gradient as described in figure 1.3b. The typical MOT had a much higher sample density of $5 \times 10^9/\text{cm}^3$ compared to an optical molasses. The cloud size extended over a volume of $\approx 1\ \text{cm}^3$ around the zero of the magnetic field, where the Doppler shift associated with cooling could be compensated by the Zeeman shift associated with trapping. Experiments with MOTs became common place following the realization of a vapour-cell loaded trap [23] in which atoms were slowed from background vapour. In these traps, slow atoms in the tail of the Maxwell-Boltzmann speed distribution were successfully trapped.

MOTs have been instrumental in improving a range of precision measurements, such as the atomic fine structure constant [56–59] and atomic linewidths [60]. MOTs have become the starting point for compression of phase space densities in experiments relating to Bose-Einstein condensation (BEC) of atoms [61, 62] and molecules [63]. Other experiments that use MOTs as the starting point include realization of Fermi degeneracy [64] and exploration of Feshbach resonances[4] on collisional rates [65] and

[3]The Doppler limit is the equilibrium temperature for an atom without magnetic sublevel structure. It is realized by balancing the cooling rate due to the laser force with the heating rate due to spontaneous emission. The definition of the Doppler limit is $\hbar\Gamma_N/(2k_B)$.

[4]A Feshbach resonance occurs when the bound state potential energy of a two body "molecule"

scattering lengths [66]. MOTs have also led to the realization of fountain-based atomic clocks that define the time standard of the GPS network [67] as well as a new generation of lattice-based atomic clocks [68].

1.3 Raman Atom Interferometer

The most precise atom-based measurement of gravity relies on matter wave interference between cold atoms released from a MOT. The most widely known atom interferometric technique used in inertial sensing is the Raman atom interferometer (AI) developed at Stanford University [69, 70]. The Raman AI typically manipulates cold atoms between two hyperfine ground states in cesium using optical transitions via an intermediate excited state associated with $6P_{3/2}F' = 5$, as shown in figure 1.4.

Using a combination of optical and RF pulses, the atoms are prepared in the magnetic sublevel $m_F = 0$ of one of the hyperfine ground states to avoid the effects of magnetic fields and magnetic field gradients. Using a series of counter propagating optical pulses, 1/15th of the $m_F = 0$ state selected atoms are velocity selected and launched in an atomic fountain. The width of the velocity distribution of these atoms corresponds to a temperature of ≈ 10 nK along the axis of excitation.

After the atoms are launched, they are excited by a series of excitation pulses shown in figure 1.4 known as Raman pulses. These pulses consist of two off-resonant

is equal to the kinetic energy of the two individual atoms. An external electromagnetic field can be applied to shift the narrow range of energies of this resonant phenomenon. At the Feshbach resonance, there is discontinuous change in the sign of the scattering length.

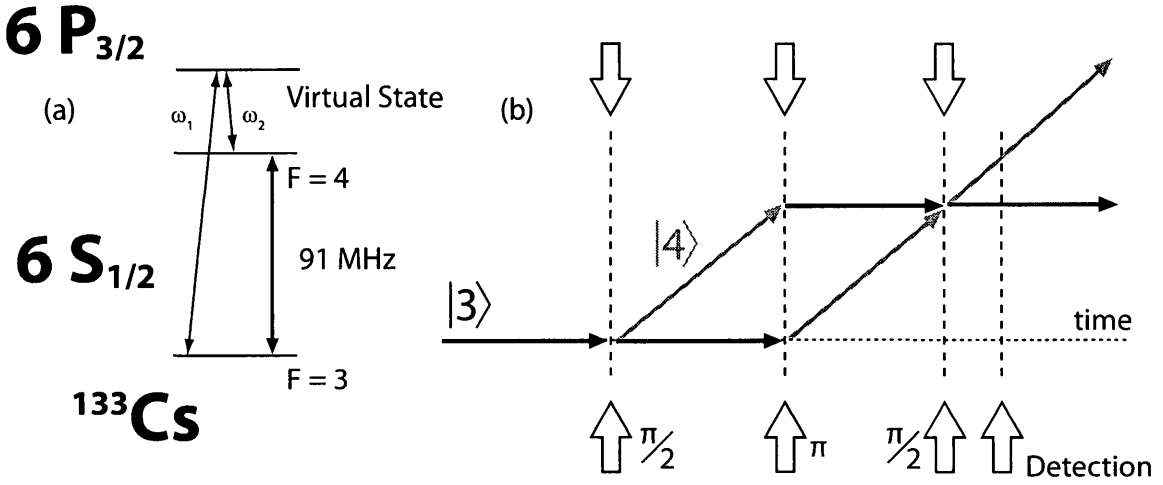

Figure 1.4: (a) Cesium level structure showing the ground states and virtual excited state used in a typical Raman atom interferometer. The two laser frequencies ω_1 and ω_2 resonantly couple the ground states. (b) A $\pi/2 - \pi - \pi/2$ interferometric pulse sequence is shown. The first pulse is used to create a coherent superposition of two ground states of cesium by shifting the Bloch vector an angle of $\pi/2$. The π pulse interchanges the phases of the coherences and the second $\pi/2$ pulse converts the coherences into populations. The detection of populations of both states is accomplished by resonant excitation to an excited state. The time separation between the pulses is T.

laser frequencies that resonantly couple two hyperfine ground states. The first pulse, called a $\pi/2$ pulse[5], splits the atoms into a 50-50 superposition of two ground states corresponding to the $|F = 3\rangle$ and $|F = 4\rangle$ ground states in cesium. The second pulse, a π pulse, applied after a time interval T, interchanges the phases of these two states. The third pulse, which is another $\pi/2$ pulse, is applied at a time T after the second pulse. Its effect is to force the atomic population into one of the two hyperfine states.

[5]A $\pi/2$ pulse refers to a specific area of an electric field envelope. A pulse with this coupling strength will rotate the Bloch vector representing the atomic system though an angle of $\pi/2$ which corresponds to a superposition state.

After the interferometric pulse sequence, the populations of both hyperfine states are detected using another series of three pulses. The first pulse optically excites the $6S_{1/2}F = 4 \rightarrow 6P_{3/2}F' = 5$ transition to measure the population of the $F = 4$ state through fluorescence detection. The second pulse, a resonant microwave π pulse on the $F = 3 \rightarrow F' = 4$ transition optically pumps the atoms in the $F = 3$ ground state to the $F = 4$ ground state. The third pulse again excites the $F = 4 \rightarrow F' = 5$ transition. In this manner, the population of the $F = 3$ state can be inferred from the fluorescence. With these two measurements it is possible to determine the number of atoms in both ground states. The fraction in each state is found by normalizing the signal with the total number of atoms.

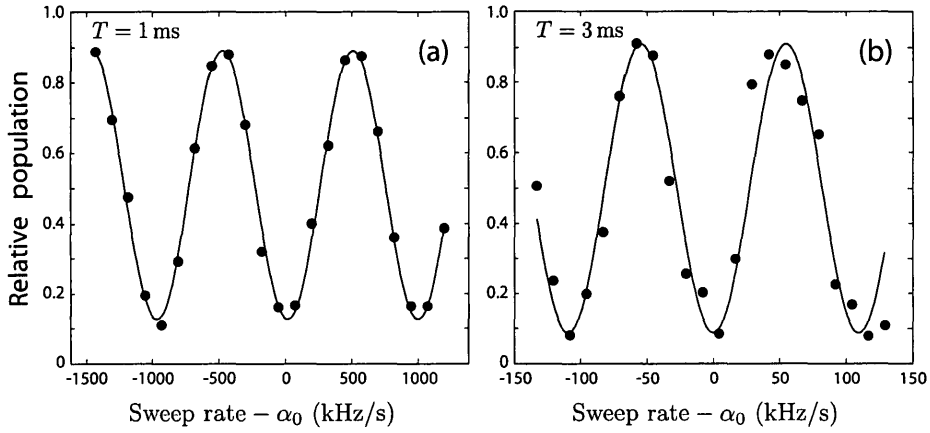

Figure 1.5: Cesium interferometer population fringe pattern at (a) $T = 1$ and (b) $T = 3$ ms. The fringe pattern with $T = 1$ ms is much broader than the fringe pattern with $T = 3$ ms, as can be seen from the horizontal scale. Adapted from reference [71]. The population is measured as a function of chirp rate, where $\alpha_0 = kg/\pi$.

For a measurement of g, the Raman pulse sequence is applied along the vertical. To carry out the experiment, the frequency of the Raman pulses must be chirped,

in order to compensate for the Doppler shift of the two-photon transition frequency due to gravity. Chirping the Raman pulses maintains the two-photon resonance frequency between the ground states. For small values of T, the atomic population as a function of chirp rate α exhibits a very broad fringe, as shown in figure 1.5a [71]. This measurement can be used to define the centre of the fringe pattern if T is incremented. The time separation is progressively increased so that the fringe pattern as a function chirp rate α can be recorded for the largest possible timescale. A typical measurement at progressively larger values of T is shown in figure 1.5.

Due to gravity, the paths of the interfering trajectories in figure 1.4 develop a phase difference $\phi_{\mathrm{AI}} = qgT^2$, where q is the difference in k vectors of the excitation beams. Since the Raman pulses are chirped at a rate α, the minima of the fringe pattern are defined by the condition $(qg - 2\pi\alpha)T^2 = n2\pi$. Therefore, g can be determined precisely from the chirp rate. The Raman AI relies on precisely timed pulses, and a suitably long measurement timescale that is determined primarily by the transit time of atoms across the region of interaction defined by the laser beams. Measurement timescales of 300 ms are possible because the atoms have been cooled to micro-Kelvin temperatures [26–28]. Cooling ensures that the transverse expansion of the atom cloud does not exceed the excitation beam diameter.

However, such an experiment presents many challenges. Magnetic state selection, velocity selection, and detection require an elaborate sequence of RF and optical pulses involving multiple lasers. The number of atoms that contribute to the signal,

a few thousand, is a small fraction of the initial sample size of several billion atoms. The loss in atom number is compensated by scattering up to 2000 photons per atom to ensure adequate signal-to-noise ratio. In addition, the lasers driving the Raman transitions between the hyperfine ground states in cesium must be phase locked with each other to maintain phase stability. The first laser is locked to an atomic resonance, using FM spectroscopy. The beat note between the two lasers is used to generate an error signal that is used to stabilize the frequency of the second laser. These experiments are carried out using a reflecting surface such as a corner cube reflector that determines the nodal position of a standing light field. This optical element serves as an inertial reference frame in which g is measured. The development of both passive and active vibration stabilization methods to isolate the inertial reference frame from sources of noise was crucial for these experiments. In particular, a low noise seismometer was used to measure accelerations of the inertial reference frame and a solenoid actuator was used to physically shift the reflector to compensate for these accelerations.

Pioneering experiments using this AI achieved a measurement of g precise to 3 parts per million (ppm) [69, 70]. Subsequent experiments based on this AI have resulted in the most precise atom-based measurements of g with a precision of 3 ppb [26, 27] in one minute and 8 ppb in one second [28]. These experiments held the record for atom-based measurements of g until very recent measurements where cold atoms were dropped in a 10 m vacuum tube [72]. This experiment achieved two

orders of magnitude improvement in statistical precision.

The sensitivity of Raman AIs to g has been utilized for measurements of G [73,74], tests of general relativity [75, 76], and tests of the equivalence principle [77]. More recently, sensitive measurements of general relativity have been initiated by dropping a BEC in a 100 metre tower [13, 14]. The Raman AI has also produced the best atom-based measurement of gravity gradients [78, 79] and rotation [80, 81].

As a result, this AI has been the basis for mobile payloads used in remote sensing [82–89]. Applications of atom interferometry have focused on building commercial payloads and ground-based portable platforms [90–98].

The sensitivity of the Raman AI stems from the large difference in interfering paths and enclosed area between the arms of the interferometer. A successful method of achieving large momentum transfer in a Raman AI is to use relatively long pulses in the Bragg regime [71,99]. In this regime, the motion of the atoms during the pulse is appreciable compared to the wavelength of light. By transferring large momenta to atoms, it is possible to increase the separation between arms resulting in an increased enclosed area and improved sensitivity. Recently, a Raman AI with Bragg pulses has reported a measurement of g with a statistical precision of 2.7 ppb with 1000 seconds of data acquisition [99]. This experiment used a drop height of 20 cm and a passively vibration stabilized apparatus.

1.4 Bloch Oscillations

An alternative implementation of an AI that can measure g in a compact setup relies on the technique of Bloch oscillations [30, 100–103]. Here, atoms collected in a MOT are adiabatically loaded into an optical lattice generated by a strong blue-detuned beam. After loading atoms in a vertical lattice, the trap depth is continuously modulated in a sinusoidal manner.

When the modulation frequency matches an integer harmonic of the Bloch frequency given by $\nu_B = \frac{Mg\lambda}{2h}$, where M is the atomic mass, λ is the wavelength, and h is Planck's constant, atoms start to tunnel to neighboring lattice sites. This gives rise to a larger vertical spatial distribution of atoms. The resonant Bloch frequency can be measured precisely by fitting the dependence of the cloud size on the modulation frequency as shown in figure 1.6.

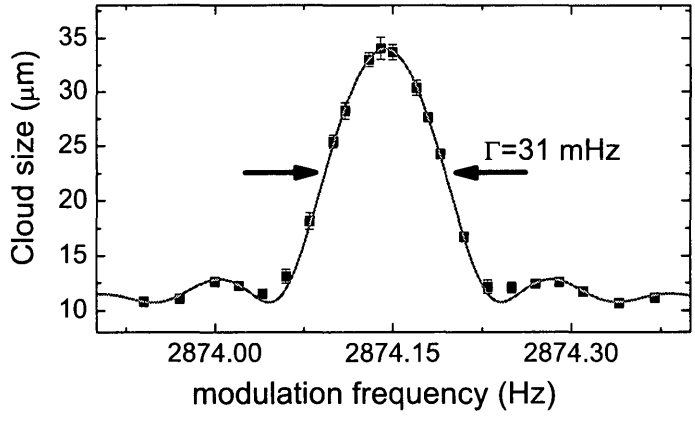

Figure 1.6: Strontium Bloch oscillation fringe pattern adapted from reference [30]. Cloud size measured as a function of the lattice-depth modulation frequency. A fit to a sinc function (of the form $\sin(x)/x$) allows the resonant Bloch frequency to be determined precisely.

A variant of this method is to modulate the lattice in a burst, and observe the evolution of the cloud. The evolution of the atoms gives rise to an interference effect, which produces enhanced visibility of the Bloch oscillation peaks in the time-of-flight images of the atomic cloud. Using this method, the authors of reference [30] have measured g with a statistical precision of 150 ppb in one hour. However, the absolute accuracy relies on the precise knowledge of h [3], which is only known to 44 ppb.

A related technique involving the suspension of atomic wave packets using a multiple pulse AI, as described in reference [103]. This technique has measured g with a statistical precision of 0.1%.

1.5 Time-Domain, Echo-Type, Ground State Interferometer

In this section, we present an overview of two configurations of a distinctive single-state echo interferometer [31–37] that are sensitive to the absolute value of g. Both configurations work in the time-domain and use samples of laser-cooled ^{85}Rb or ^{87}Rb atoms released from a MOT. The apparatus uses only passive vibration stabilization of critical parts of the experiment and all magnetic sublevels of the ground state manifold contribute to the echo signal. In contrast to the Raman AI, the echo AI used in this work manipulates atoms in a single ground state. Therefore, only a single excitation frequency is required. Using a single-state reduces the sensitivity to some systematic effects such as AC Stark shifts and magnetic fields. Another advantage is that the echo technique ensures that velocity selection is not required. Adequate

signal-to-noise ratio is achieved with large samples of relatively dilute atoms and a signal produced by coherent backscattering. As a result of the reduced experimental complexity, this apparatus design has been the basis of an industrial partnership to develop an absolute gravimeter that can be used for independent calibrations of industrial sensors.

1.5.1 Two-Pulse Interferometer

We first discuss the physical principles of the two-pulse AI configuration [31–33] using a recoil diagram followed by a description of signal characteristics.

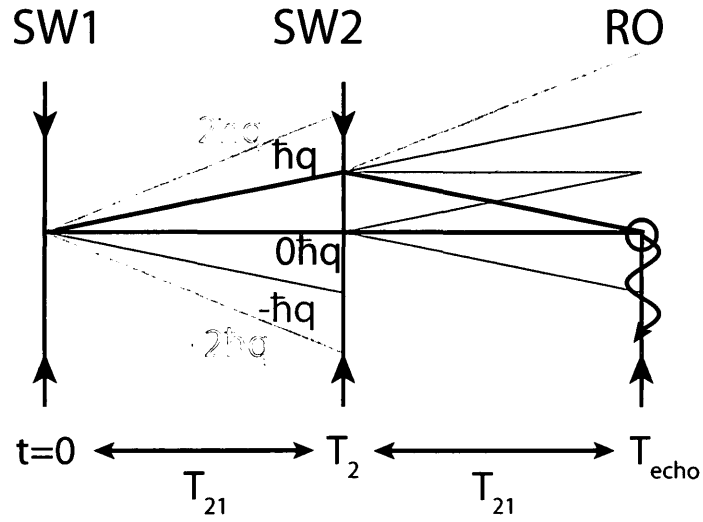

Figure 1.7: Recoil diagram for two-pulse AIs. Only a subset of all trajectories are shown. SW refers to standing wave pulses and RO is a travelling wave read-out pulse. The SW pulses, composed of the two counter-propagating travelling wave components with wavevector $|k|$, diffract atoms into a superposition of momentum states separated by $\hbar q$. The backscattered signal arises from interferences between states differing by $\hbar q$ at the echo time $t = 2T_{21}$.

Figure 1.7 represents the recoil diagram for the two-pulse configuration of the AI.

The recoil diagram represents an AI on the basis of a billiard-ball model [104–106] in which the displacements of centre-of-mass trajectories of wavepackets corresponding to momentum states are depicted as a function of time. A sample of laser-cooled ^{85}Rb or ^{87}Rb atoms is excited along the vertical by two standing wave (SW) pulses separated by a time T_{21}. The SW pulses are composed of two travelling wave components, each carrying a wave vector with wavenumber $k = 2\pi/\lambda$. These travelling wave components are blue detuned with respect to the excited state, as shown in figure 1.8 for two reasons. Firstly, the detuning ensures that spontaneous emission during the excitation pulses can be reduced. Secondly, complications from the rubidium excited state manifold on the signal shapes are avoided[6].

Atoms in each of the magnetic sublevels of the $F = 3$ ground state in ^{85}Rb or the $F = 2$ ground state in ^{87}Rb are diffracted into a superposition of momentum states separated by $\hbar q$ at $t = 0$, as shown in figure 1.7. Here, $q = 2k$ for counter-propagating travelling wave components of the SW excitation. The diffraction into multiple momentum states by a short standing wave pulse is referred to as Kapitza-Dirac scattering [25]. Since the lasers are not on resonance, the transfer of momenta to atoms only occurs in units of $\hbar q$. This process involves the absorption of a photon from one travelling wave component of the standing wave and stimulated emission along the counter-propagating travelling wave component. The duration of the SW pulses

[6]The detected signal is a coherent superposition of electric fields produced by each magnetic sublevel. By detuning above resonance, the signals from the lower hyperfine sublevels of the excited state manifold are much smaller than the contribution from of highest lying hyperfine excited state.

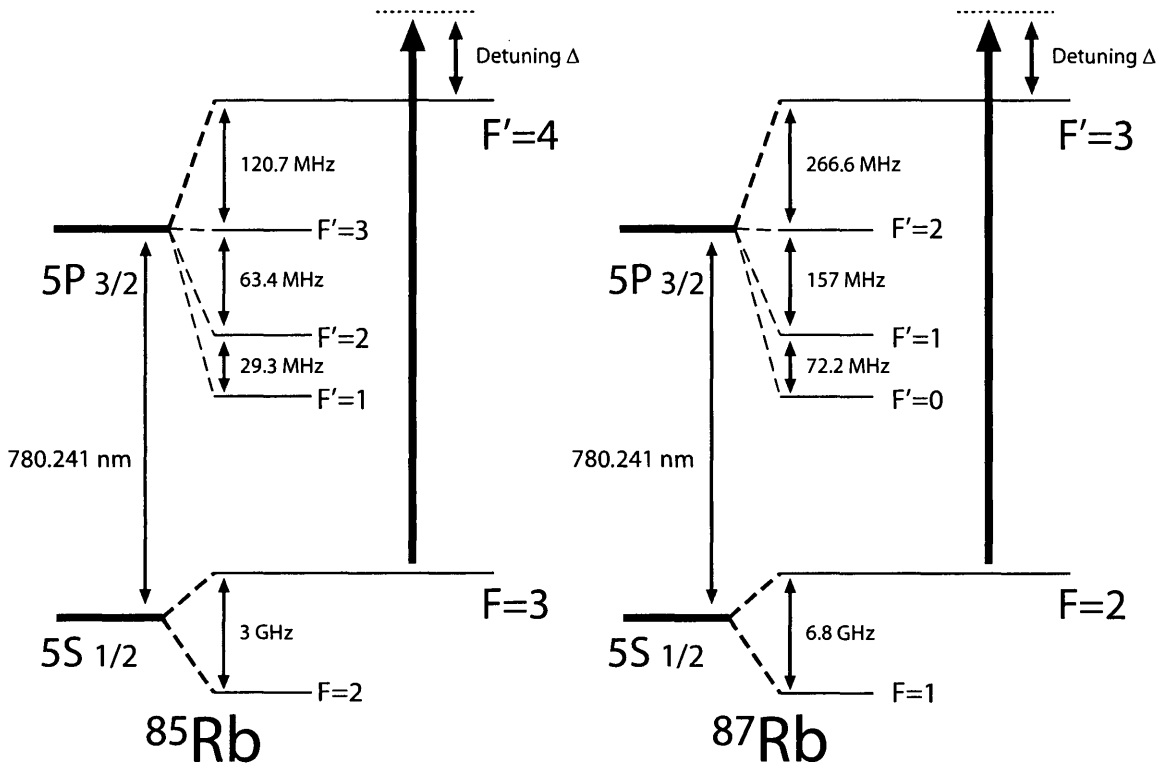

Figure 1.8: Rubidium D2 transition showing $5S_{1/2} \rightarrow 5P_{3/2}$ transition frequencies. The hyperfine splittings between different F-levels are indicated. A "blue" detuning Δ of the excitation beam is shown.

are sufficiently short that they meet the Raman-Nath criterion [107, 108] where the displacement of the atoms due to the momentum transfer from standing wave pulses is small compared to the spacing of the quasi-sinusoidal standing wave potential. For counter-propagating travelling wave components, the wavelength of the potential is $\lambda/2$.

The classical description of the effect of the standing wave interaction is that the atoms are focused toward the nodes of the standing wave potential. The focusing of atoms into the nodes produces a one-dimensional density grating with a period of

$\lambda/2$. In a quantum mechanical description, it is the interference between momentum states that produces this one-dimensional density grating. In this latter description, each of the momentum states in figure 1.7 is modulated at integer multiples of the recoil frequency $\omega_q = \dfrac{\hbar q^2}{2M}$.

The velocity distribution of the cold sample along the SW axis causes the grating to dephase on a timescale of $\tau_{\text{coh}} = 1/(ku)$, where $u = \sqrt{2k_{\text{B}}\mathcal{T}/M}$ is the $1/e$ width of the velocity distribution. Here, $\mathcal{T}$ refers to the temperature of the sample, and k_{B} is the Boltzmann constant. The timescale τ_{coh} represents the time of travel of a typical atom through a distance $\lambda/2$. In practice, a typical sample temperature of 20 μK produces a timescale $\tau_{\text{coh}} \approx 2\mu$s.

A long time T_{21} after the grating has dephased, a second SW pulse is applied to diffract the momentum states. The effect of this SW pulse is to cause the momentum states separated by $\hbar q$ to rephase at the echo time $2T_{21}$. Momentum state interference produces a maximum contrast in the density grating just before and just after the echo time. The re-phasing is reminiscent of a two-pulse photon echo experiment [109] that involves a superposition of ground and excited states. The echo technique is a general method of cancelling Doppler dephasing in an atomic gas. In echo atom interferometry, this technique has been extended to ground states so that velocity selection is not required. The effect of cooling the sample is simply to ensure that the timescale of the experiment is suitably long. Under ideal conditions, the experimental timescale is limited by the transit time of atoms across the excitation beam.

Since the atoms are in the ground state, it is necessary to apply a travelling-wave read-out pulse in the vicinity of the echo time to detect the contrast of the re-phased density grating. The periodic array of atoms formed at the echo time coherently back scatters the read-out pulse. This process is known as Bragg scattering[7]. In this case, the wavelength of the back scattered light λ is matched with the Fourier component of the density grating with spacing $\lambda/2$. The backscattered signal due to the read-out pulse is known as the echo signal.

The backscattering of the read-out pulse is a consequence of the law of conservation of momentum. If an incoming read-out photon is backscattered, then the total momentum delivered to the sample is $\hbar q$. This momentum transfer allows the two arms of the interferometer that differ by $\hbar q$ to recombine. This action of the read-out pulse also creates a coherent superposition of ground and excited states throughout the sample. The total radiation pattern from this system of dipole radiators is phase-matched only along the backward direction.

Experiments in echo interferometry can be designed to detect both the electric field and intensity of the echo signal. Figure 1.9 shows an example of the envelope of the electric field associated with the echo signal. The signal exhibits a characteristic dispersion shape with a zero crossing at $t = 2T_{21}$. The duration of the echo envelope, characterized by τ_{coh}, is determined by the velocity distribution of the sample. The

[7]The grating spacing of $\lambda/2$ causes a total path difference change of λ for light reflecting from adjacent planes of the grating. This effect produces constructive interference since the phase difference of reflections from adjacent planes is 2π.

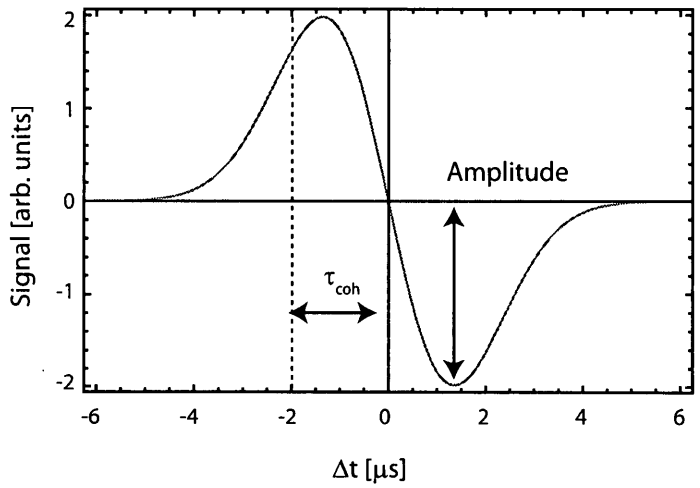

Figure 1.9: The electric field envelope of the two-pulse echo signal in the absence of gravity exhibits a characteristic dispersion shape with a zero crossing near the echo time $t = 2T_{21}$. Here, $\Delta t = t - 2T_{21}$ is the time with respect to the echo time.

shape of the signal indicates that the maximum contrast of the density grating occurs just before and after the echo time $2T_{21}$. The zero crossing at exactly the echo time shows that the absence of density modulation at $t = 0$ is replicated at $t = 2T_{21}$.

A striking feature of this interferometer is that the electric field amplitude of the echo envelope, shown in figure 1.9, exhibits a recoil modulation as a function of T_{21}. The recoil modulation occurs with a period $T_q = \pi/\omega_q = 32.655$ μs, for ^{87}Rb, as shown in figure 1.10a. This figure also shows a phenomenological decay to illustrate the effect of all decoherence mechanisms including the transit time. The physical basis of the recoil period arises from the time in which momentum states that have acquired a recoil velocity of $\hbar q/M$ traverse a distance $\lambda/2$. The contrast of the density grating revives periodically on this timescale. Precise measurements of the recoil frequency based on echo AIs are discussed in references [38,110–113]. Most measurements of the

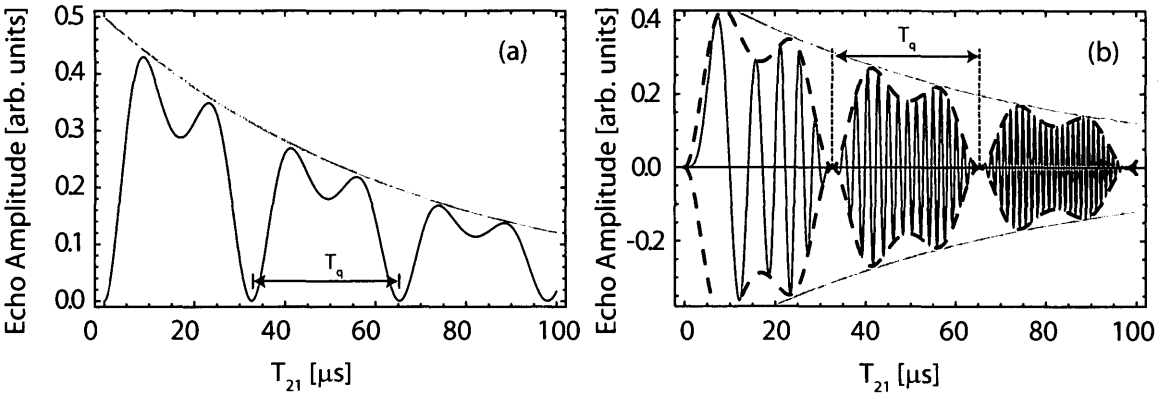

Figure 1.10: (a) Illustration of electric field amplitude (red line) of the two-pulse echo as a function of T_{21} in the absence of gravity. The amplitude is defined by a Bessel function with a sinusoidal argument which produces an amplitude modulation at the frequency $2\omega_q$. An exponential decay (grey line) illustrates signal loss due to decoherence and transit time effects. (b) Electric field amplitude (red line) of the two-pulse echo as a function of T_{21} in the presence of gravity. The recoil modulated amplitude shown in (a) exhibits an additional modulation at an increasing frequency due to g. Again, an exponential decay (grey line) illustrates signal loss due to decoherence and transit time effects. The black dashed line represents the recoil modulated signal without gravity.

recoil frequency using this AI have been carried out by recording only the intensity of the echo signal [111–113].

As shown in figure 1.11, there is no difference in the displacement of the two interfering arms without gravity as shown by the grey lines. With gravity, the two interfering arms shown in black also have no difference in displacement. The path length difference of the two grey arms is equal to the path length difference of the two black arms. However, the interfering trajectories shown in black have been displaced by gravity and there is an overall phase shift that scales as gT_{21}^2 due to the increase in path length compared to the paths in grey. This phase difference can be measured

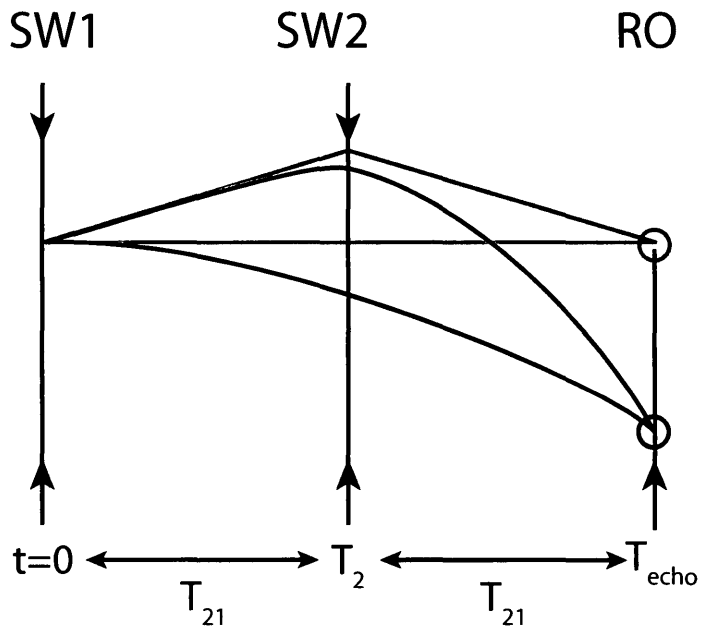

Figure 1.11: Recoil diagram for the two-pulse AI with gravity (black) and without gravity (grey). Only one subset of trajectories that differ by $\hbar q$ are depicted.

with respect to an inertial reference frame. A convenient reference frame is a nodal point of the standing wave, generally defined by a reflecting surface. To measure g, it is necessary to record both the amplitude and phase of the electric field associated with the echo signal.

In the presence of gravity, the recoil modulated signal shown in figure 1.10a exhibits an additional sinusoidal modulation that increases in frequency, as shown in figure 1.10b. The essential characteristic of the two-pulse AI is that the different momentum states that interfere experience a continuously changing relative displacement during the entire experiment. As a consequence, the AI signal exhibits a linear frequency change as a function of T_{21}. The corresponding phase of the echo signal increases quadratically with T_{21}, an appealing scaling law for a precision measure-

ment of g. However, the disadvantage of this technique is that the signal amplitude exhibits a recoil modulation as well as a chirped frequency as a function of T_{21}, resulting in the need for a more complicated fit function to extract g. The frequency chirp associated with this configuration is analogous to the frequency chirp of interference fringes recorded by the falling corner-cube optical interferometer [18].

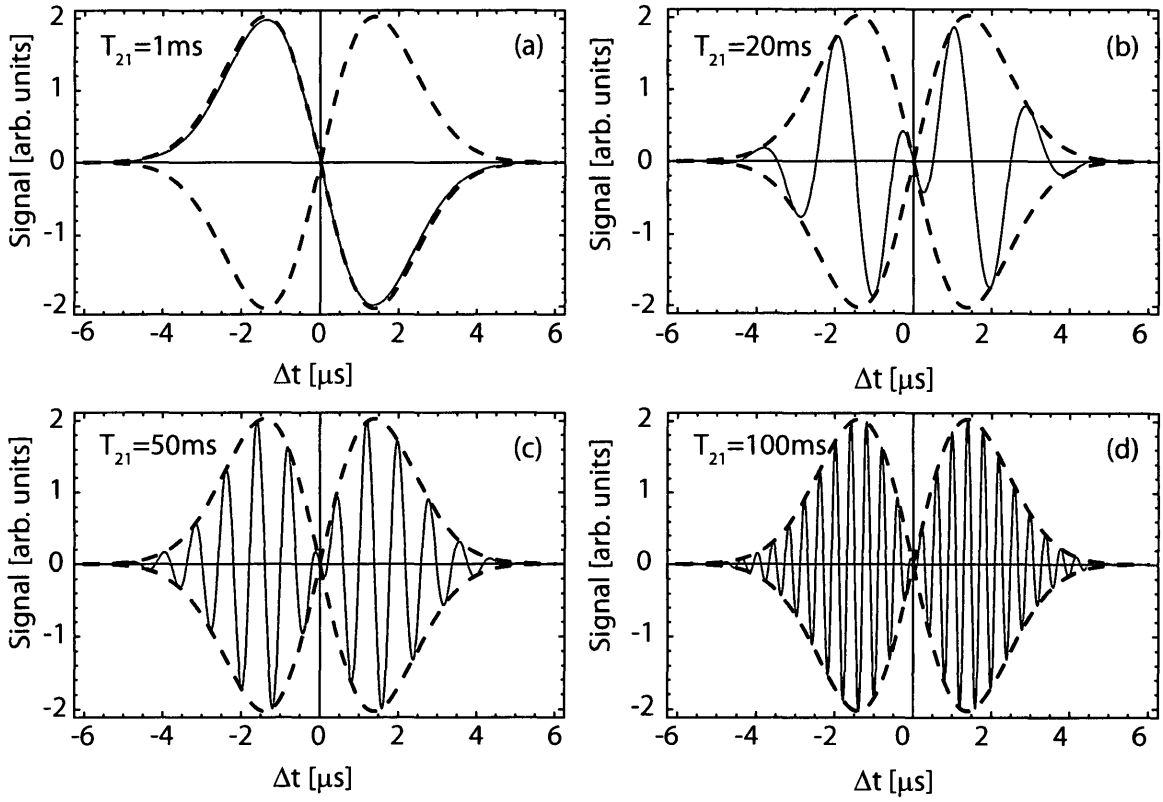

Figure 1.12: The electric field envelope of the two-pulse echo signal in the presence of gravity. As T_{21} is incremented, the oscillation frequency increases due to the motion of the falling density grating. The oscillation frequency can be observed within the signal envelope when the read-out pulse is applied. Here we assume $g = 9.8$ m/s^2.

The chirped accumulation of matter wave fringes shown in figure 1.10b due to gravity also produces a modulation of the echo envelope, as shown in figure 1.12.

These oscillations are associated with the atoms falling through a grating spacing of $\lambda/2$ and accumulating a phase of 2π within a timescale of τ_{coh}.

1.5.2 Three-Pulse Interferometer

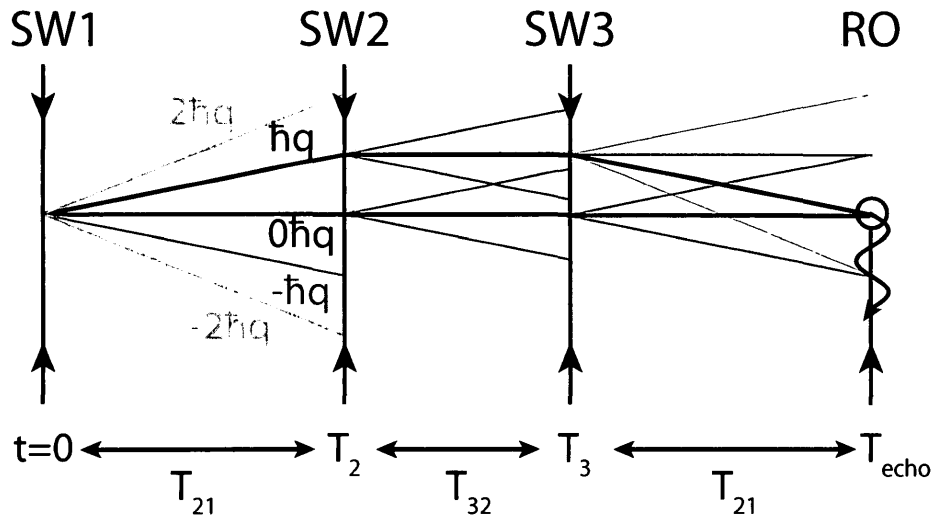

Figure 1.13: Three-Pulse recoil diagram without gravity. Only a subset of all trajectories are shown. SW refers to standing wave pulses and RO is a travelling wave read-out pulse. The second pulse renders a subset of trajectories parallel. The third pulse causes states separated by $\hbar q$ to interfere at the echo time $t = 2T_{21} + T_{32}$. The backscattered signal detected by the read-out pulse arises from interferences between states differing by $\hbar q$ at this echo time.

An alternate configuration involves a three-pulse stimulated echo AI, shown in figure 1.13 [34–37,114]. Again, the first SW pulse creates a superposition of momentum states separated by $\hbar q$. A second SW pulse applied at $t = T_{21}$ selects momentum states that are co-propagating with the same momentum. A third pulse applied at $t = T_{21} + T_{32}$ causes the selected states to interfere at the echo time $t = 2T_{21} + T_{32}$, forming a density grating. Just like the two-pulse AI, the grating formation is asso-

ciated with interference of momentum states separated by $\hbar q$.

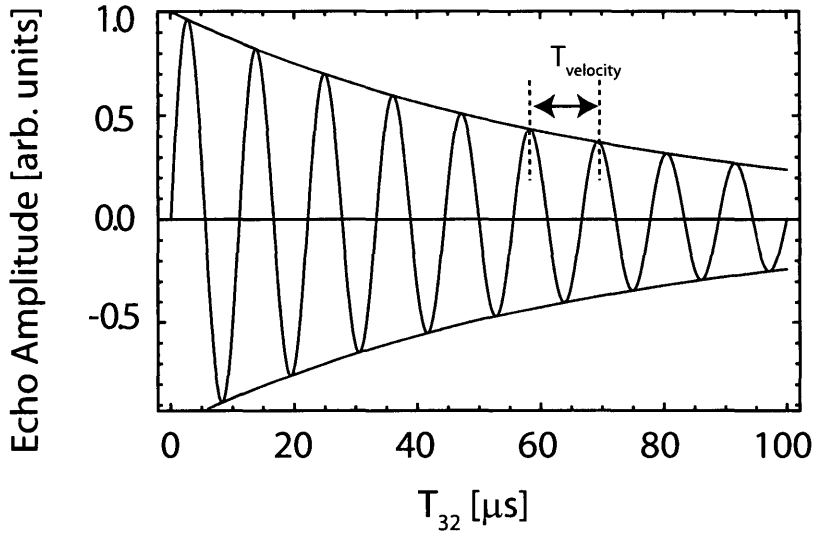

Figure 1.14: Illustration of the electric field amplitude (red line) of the three-pulse echo as a function of T_{32} in the presence of gravity. This signal exhibits a single frequency determined by T_{21} and shows no recoil modulation. An exponential decay (grey line) illustrates signal loss due to decoherence and transit time effects.

For the three-pulse AI, the arms of the interferometer consist of co-propagating arms with no momentum difference during the central time window associated with T_{32} [34,35]. The signal amplitude as a function of pulse separation T_{32} shows no recoil modulation and exhibits a fixed frequency determined by T_{21}, as shown in figure 1.14. This angular frequency, which can be shown to be qgT_{21}, is determined by the velocity gT_{21} the atoms acquire during the time interval T_{21} due to gravity. Therefore, this configuration represents a velocity-sensitive AI. The period of the signal shown in figure 1.14 is given by $T_{\text{velocity}} = \dfrac{\lambda/2}{gT_{21}}$.

The single frequency signal without recoil modulation has beneficial practical consequences for improving the quality of the fits to the data, thereby resulting in in-

creased sensitivity. Since there is no relative displacement between the co-propagating momentum states during the time window T_{32}, the AI exhibits reduced sensitivity to spurious accelerations due to magnetic curvature and mirror vibrations in this time window. This feature allows the overall timescale of the experiment to be increased in comparison to the two-pulse AI, resulting in improved precision. By careful choice of pulse parameters, a suitably long observational window can be made available for the measurement of the fixed frequency. The largest phase accumulation is obtained when $T_{32} = 2T_{21}$. The echo envelope for the three-pulse AI exhibits a modulation frequency due to gravity that is similar to the two-pulse AI. The disadvantage is the loss in signal strength due to the third pulse and the inherent sensitivity to the initial velocity.

The stimulated echo configuration was first developed in reference [115] for collisional studies. Subsequently, an AI based on this configuration was used to study the formation of nanostructures in cold atoms [114]. Reference [34] used an inclined magnetic waveguide to show that this AI exhibits reduced sensitivity to mirror vibrations for measurements of acceleration. The theory of this interferometer was described in detail in reference [35] and predictions were verified using measurements of magnetic field gradients that did not require vibration stabilization.

1.6 Key Developments

At the initial stage of my doctoral work, the two-pulse AI had achieved a statistical precision of 15 ppm over several hours. The experiment relied on hanging a mirror attached to large block of aluminum from the ceiling using surgical tubing. This mirror served as a passively vibration stabilized inertial reference frame. Achieving repeatability on successive measurements proved to be challenging because of inadequate phase stability.

The first task was to achieve a high degree of repeatability using vibration isolation platforms. These platforms were used to stabilize the upper mirror as well as the optical atom interferometry setup placed below the vacuum chamber. The second task was to improve the absolute accuracy of the measurement which was compromised by a highly magnetized 304-stainless steel vacuum chamber. This vacuum chamber was used for three high-precision measurements (atomic recoil, magnetic g-factor ratios and g) and it was particularly challenging to share and switch between setups.

Working with other students, I rebuilt the gravity apparatus using a less magnetic 316L-stainless steel vacuum chamber. Although the timescale of echo experiments immediately improved, the accuracy remained poor because this chamber also acquired a permanent magnetization over the course of a few weeks. I then worked with other graduate students to build two glass vacuum chambers, one for the atomic recoil and g-factor ratio measurements and one for g measurements. Only one of five of these glass cells held vacuum. The failure was primarily caused by stresses on the

thin-walled (3 mm) chambers. Resource constraints were responsible for the delay time in constructing a much thicker-walled glass chamber, which will be used for the forthcoming measurements of g. However, I was constrained to work with the 316L-chamber. I reassembled this vacuum chamber with larger clearance to permit access for alignment. The chamber was placed on floating optical table and key experimental components were stabilized on vibration isolation platforms.

The focus of the work changed toward developing a statistical precision of 25 ppb so that tidal effects could be observed. By comparing tidal variations measured with cold atoms against 1 ppb measurements using an industrial falling corner-cube sensor, we expected to quantify the extent of systematic effects in a controlled manner. However, the eventual statistical precision was 75 ppb so that the study of tidal variations could be achieved only by acquiring data over several days. Therefore, it was not possible to study systematic effects in a controlled manner.

In this dissertation, we explore the characteristics of two-pulse and three-pulse stimulated-echo AIs using a magnetized vacuum chamber[8] [36, 37]. We show that an analysis of the echo envelope produced by both AI configurations, with a duration of a few microseconds, can be used to extract g with a precision of 0.5%. The amplitude of the two-pulse echo is analyzed as a function T_{21} to demonstrate a sensitivity to vertical accelerations at the level of 5 ppm. The $\approx$ 25 ms timescale of this measurement

[8]Optical pumping into the $m_F = 0$ sublevel using laser excitation did not achieve high efficiencies, an effect we attribute to the due to poorly controlled magnetic field environment in the vicinity of the atomic sample. In Chapter 5, we discuss a more suitable method that selects atoms in the $m_F = 0$ sublevel using the combination of RF and optical excitation.

is limited by the magnetization of the apparatus. The amplitude of the three-pulse echo is analyzed as function of T_{32}. An appreciably longer timescale of $\approx$ 70 ms is achieved so that an increased sensitivity to vertical accelerations at the level of 75 ppb is demonstrated. We examine the systematic corrections to these accelerations, which are dominated by g. Based on the signal-to-noise ratio and timescale achieved in recent echo experiments that used a non-magnetized apparatus, we predict that a measurement of g with state-of-the-art sensitivity can be realized in a future experiment.

1.7 Organization of Dissertation

The rest of the dissertation is organized as follows. Chapter 2 describes the theoretical formalism relevant to the experiment. A quantum mechanical derivation of the signal is followed by inferences based on a classical approach. At the end of Chapter 2, we discuss the interpretation of the key results. Chapter 3 contains the experimental details of the optical layout, atom trapping and atom interferometry setups as well as a description of diagnostic measurements relating to the atom trap. This chapter also contains technical details of equipment developed during this dissertation. Chapter 4 presents an overview of the results. Chapter 5 discusses systematic effects and methods of reducing these contributions. In particular, we examine the development of phase stabilization methods to compensate for vibrations and identify methods of improvement. Finally we describe prospects for future work. The appen-

dices consist of a description of the magnetic gradient turn-off circuit, compilations of data acquisition and processing software, and list of publications and conference presentations.

2 Theory

In this chapter, we discuss the quantum mechanical formalism that describes the formation of the two-pulse and three-pulse echoes. The treatment is first carried out in the absence of gravity, to explain the recoil modulated signal. We then extend the treatment to include gravity and explain the signal shape. The theoretical formalism is extended to predict the signal shapes associated with the three-pulse echo. Following the quantum mechanical description, we present a discussion based on the action principle to show the origin of the gravitational phase. The last part of the discussion pertains to the classical description of the gravitational phase.

2.1 Two-Pulse Quantum Mechanical Model

The experiments in this work use standing wave excitation of a laser-cooled sample of rubidium. The travelling wave components of the standing wave are blue detuned from the $5S_{1/2}F = 3 \rightarrow 5P_{3/2}F' = 4$ transition in ^{85}Rb or the $5S_{1/2}F = 2 \rightarrow 5P_{3/2}F' = 3$ transition in ^{87}Rb. We consider the recoil diagram shown in figure 2.1 that describes the two-pulse echo. This diagram is similar to figure 1.7 in Chapter 1. The diagram

shows a subset of momentum states that result in echo formation.

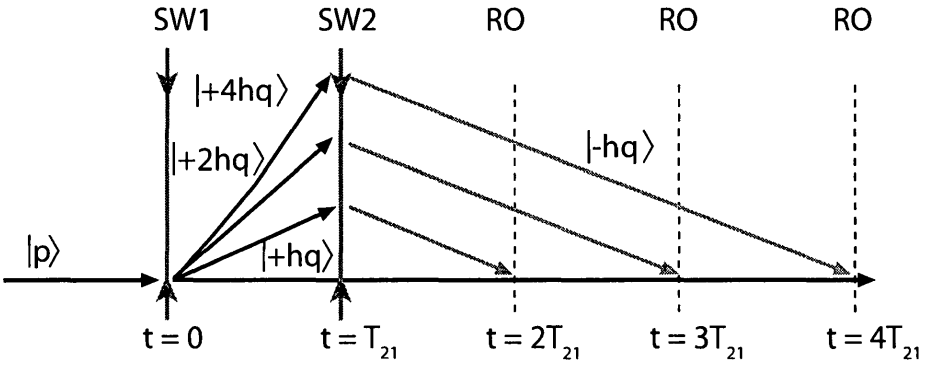

Figure 2.1: Subset of momentum states generated by the two-pulse AI in the absence of gravity. Standing wave excitation and read-out pulses are denoted as SW and RO respectively. The first pulse occurs at $t = 0$, the second pulse at $t = T_{21}$ and the read-out at $T_{\text{echo}} = 2T_{21}$. Examples of higher-order echoes occurring at $t = 3T_{21}$ and $t = 4T_{21}$ are shown.

The first standing wave pulse at $t = 0$ diffracts atoms into a superposition of momentum states that differ by $\hbar q$, where q is the difference between the k vectors of the standing wave components. The dispersing wavepackets are represented by centre-of-mass trajectories of billiard balls following classical trajectories [104–106]. The second standing wave pulse at $t = T_{21}$ diffracts each of the initial trajectories. The relative amplitudes of the momentum states giving rise to echoes can be controlled by the atom-field coupling strength. Trajectories that differ by $\hbar q$ produce interference at the echo time $2T_{21}$. The interference between momentum states produces density gratings with spatial harmonics that are multiples of the fundamental period $\lambda/2$. The fundamental period is detected by coherently backscattering light of wavelength λ. Detection of higher harmonics can be accomplished by using light of different colours.

For example, the $\lambda/4$ harmonic can be detected by coherently backscattering light of wavelength of $\lambda/2$.

Figure 2.1 also shows higher-order echoes occurring at $3T_{21}, 4T_{21}$, etc. associated with momentum states that gain a $(n+1)\hbar q$ momentum during the first pulse, and $-n\hbar q$ during the second pulse, so that their momentum difference at the echo times remains $\hbar q$. In this manner, higher-order spatial harmonics have been converted to lower harmonics that can be detected with light of wavelength λ at the echo times. We now focus on the description of the echo at $t = 2T_{21}$.

We assume that the standing wave pulse durations τ_1, τ_2, are sufficiently short such that the motion of the atoms during the excitation can be ignored (Raman-Nath regime). Following references [31,32,35,111,114], we outline the quantum mechanical calculation of the echo signal. In this treatment, the interaction Hamiltonian acts on the atoms for the duration of the pulses, imparting both energy and momentum to the atoms. After the pulses are turned off, only the free-space evolution of the wavepackets is considered. We now present a version of the theoretical description that ignores spontaneous emission, magnetic sub-level structure, and spatial profile of the laser beam.

We model the atom as a two-level system, as shown in figure 2.2, where ω_0 is the resonant frequency of the atom, ω_L is the laser frequency, and $\Delta = \omega_L - \omega_0$ is the detuning. We take the system to be a linear combination of the ground state $|g\rangle$ and

excited states $|e\rangle$ given by

$$\psi = \begin{pmatrix} |e\rangle \\ |g\rangle \end{pmatrix}. \tag{2.1}$$

2.1.1 First Standing Wave Pulse

The standing wave consisting of two counter-propagating travelling wave components is applied. Atoms undergo two photon transitions that return them to the same ground state through a virtual excited state. As a result, the atoms acquire momentum in multiples of $\hbar q$.

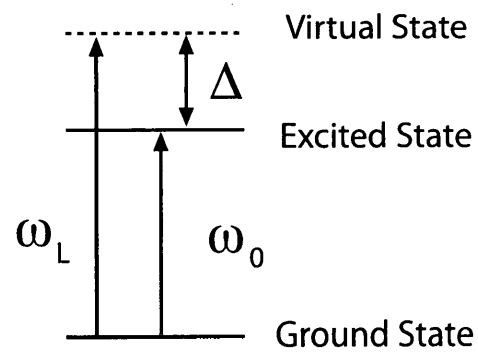

Figure 2.2: States of a two-level atom. The laser frequency is detuned above the atomic resonance by Δ.

During the first interaction pulse, the general form of the Hamiltonian of the system is given by

$$\hat{H} = \frac{\hat{\mathbf{p}}^2}{2M} - \begin{pmatrix} \hbar(\Delta + i\Gamma) & V(\mathbf{r},t) \\ V(\mathbf{r},t) & 0 \end{pmatrix}, \tag{2.2}$$

where $\mathbf{p}$ is the momentum operator, M is the mass of the atom, Γ is the effective radiative decay rate of the atom, and $V(\mathbf{r},t)$ is the interaction potential during the

pulse. Here, the potential has a periodic spatial dependence given by

$$V(\mathbf{r},t) = \mu A_0(t) \cos\left(\frac{\mathbf{q}\cdot\mathbf{r}}{2}\right), \tag{2.3}$$

where $A_0(t)$ is the electric field amplitude, μ is the electric dipole moment of the atom, and $\mathbf{q}$ is the wave vector difference between the two counter propagating beams creating the standing wave potential. Since the standing wave comprises of two counter-propagating components, $q = |\mathbf{k}_1 - \mathbf{k}_2| = 2k$.

We now discuss the form of the potential during the excitation. Since we assume that the Raman-Nath criterion is valid, it is possible to ignore the kinetic energy term of the Hamiltonian during the pulse. Furthermore, we assume the far detuned limit where $\Delta >> \Omega$, where $\Omega = \frac{\mu A_0(t)}{\hbar}$ is the one-photon Rabi frequency. We also assume that the $\Delta >> 1/\tau_1, 1/\tau_2$, which implies the detuning is much greater than the spectral bandwidth of the excitation pulse [116].

With the kinetic energy term ignored, the time-dependent Schrödinger equation is written as

$$i\hbar \begin{pmatrix} \frac{\partial|e\rangle}{\partial t} \\ \frac{\partial|g\rangle}{\partial t} \end{pmatrix} = - \begin{pmatrix} \hbar(\Delta + i\Gamma) & V(\mathbf{r},t) \\ V(\mathbf{r},t) & 0 \end{pmatrix} \begin{pmatrix} |e\rangle \\ |g\rangle \end{pmatrix},$$

which corresponds the two coupled equations

$$i\hbar\frac{\partial|e\rangle}{\partial t} = -\hbar(\Delta + i\Gamma)|e\rangle - V|g\rangle, \tag{2.4}$$

and

$$i\hbar\frac{\partial|g\rangle}{\partial t} = -V|e\rangle. \tag{2.5}$$

Since the laser is far off-resonance ($\Delta + i\Gamma \approx \Delta$), the excited state population stays zero, or $\partial|e\rangle/\partial t = 0$. This simplifies equation 2.4 to

$$0 = -\hbar\Delta|e\rangle - V|g\rangle$$

$$\hbar\Delta|e\rangle = -V|g\rangle$$

$$|e\rangle = -\frac{V|g\rangle}{\hbar\Delta}.$$

Inserting this result into equation 2.5,

$$i\hbar\frac{\partial}{\partial t}|g\rangle = \frac{V^2}{\hbar\Delta}|g\rangle.$$

Therefore, the potential energy is

$$\begin{aligned} U(z) &= \frac{V^2(z)}{\hbar\Delta} \\ &= \frac{[\mu A_0(t)]^2}{\hbar\Delta}\cos^2\left(\frac{\mathbf{q}\cdot\mathbf{r}}{2}\right) \\ &= \frac{[\mu A_0(t)]^2}{\hbar\Delta}\frac{1}{2}\left[\cos\left(qz\right)+1\right]. \end{aligned} \tag{2.6}$$

Ignoring the last term of this equation, which is a positional constant, we obtain

$$U(z) = \frac{\hbar\Omega^2}{2\Delta}\cos(qz). \tag{2.7}$$

Here, the atom-field interaction is described by the two-photon Rabi frequency $\frac{\Omega^2}{2\Delta}$. For one dimensional excitation along the standing wave axis z, the interaction Hamiltonian is

$$\widetilde{H} = \frac{\hbar\Omega^2}{2\Delta}\cos(qz). \tag{2.8}$$

After the standing wave potential is applied for a pulse duration of τ_1 we obtain

$$|\psi(\tau_1)\rangle = e^{i\vartheta_1 \cos(qz)} e^{ik_0 z}, \tag{2.9}$$

where ϑ_1 is the pulse area, which defines the atom-field coupling strength. For a square pulse, $\vartheta_1 = -\frac{\Omega_1^2}{2\Delta}\tau_1$. We note that the general expression for the pulse area is given by

$$\vartheta_1 = \int_{\tau=0}^{\tau_1} \frac{\Omega^2}{2\Delta} d\tau.$$

The integral is typically carried out over a Gaussian temporal envelope.

We now manipulate equation 2.9 using the Jacobi-Anger expansion that expands an exponential in terms of a sum of nth order Bessel functions. The expansion states that

$$e^{ix\cos\theta} = \sum_{n=-\infty}^{\infty} i^n J_n(x) e^{in\theta}.$$

Therefore, the wavefunction after the first standing wave interaction in equation 2.9 can be written as

$$\psi(t=\tau_1) = \sum_{n=-\infty}^{\infty} i^n J_n(\vartheta_1) e^{inqz} e^{ik_0 z}. \tag{2.10}$$

We can re-arrange the wavefunction slightly to obtain

$$\psi(t=\tau_1) = \sum_{n=-\infty}^{\infty} i^n J_n(\vartheta_1) e^{i(n\hbar q + \hbar k_0)z/\hbar}.$$

If we re-label the ground state with the initial momentum $p_0 = \hbar k_0$, this equation can be written as

$$|\psi\rangle = \sum_{n=-\infty}^{\infty} i^n J_n(\vartheta_1) |p_0 + n\hbar q\rangle. \tag{2.11}$$

This manipulation shows that the incoming atomic plane wave can be diffracted into momentum states separated by $\hbar q$, with relative amplitudes controlled by the pulse area ϑ_1.

2.1.2 Time Evolution After First Pulse

After the first standing wave interaction, each individual momentum state undergoes free space evolution with a Hamiltonian given by

$$\widehat{H} = \frac{\widehat{p}^2}{2M}. \tag{2.12}$$

Applying $\widehat{H}$ on $|\psi(\tau_1)\rangle$, we obtain the eigenvalue for $\widehat{H}$

$$\widehat{H}\psi(\tau_1) = \frac{\hbar^2(nq + k_0)^2}{2M}\psi(\tau_1). \tag{2.13}$$

The time evolution operator

$$\widehat{U} = \exp\left[\frac{i}{\hbar}\widehat{H}t\right] = \exp\left[\frac{-i}{\hbar}\frac{\hat{p}^2}{2M}t\right], \tag{2.14}$$

is applied to $|\psi(\tau_1)\rangle$ to calculate the wavefunction as a function of time.

Using the eigenvalues of each momentum state for the operator $\hat{p}$, we obtain

$$\begin{aligned}
\widehat{U}\psi(\tau_1) &= \exp\left[\frac{-it}{\hbar}\frac{(p_0 + n\hbar q)^2}{2M}\right]\psi(\tau_1) \\
&= \exp\left[\frac{-it}{\hbar}\left(\frac{p_0^2}{2M} + \frac{2n\hbar q p_0}{2M} + \frac{(n\hbar q)^2}{2M}t\right)\right]\psi(\tau_1) \\
&= \exp\left[\frac{-it}{\hbar}\frac{\hbar^2 k_0^2}{2M}\right]\exp\left[\frac{-it}{\hbar}\frac{n\hbar q p_0}{M}\right]\exp\left[\frac{-it}{\hbar}\frac{n^2\hbar^2 q^2}{2M}\right]\psi(\tau_1) \\
&= e^{-i\omega_0 t}e^{-inqv_0 t}e^{-in^2\omega_q t}\psi(\tau_1).
\end{aligned} \tag{2.15}$$

Inserting equation 2.10 into equation 2.15, we obtain the time dependent wavefunction [114]

$$\psi(t) = \sum_{n=-\infty}^{\infty} i^n J_n(\vartheta_1) e^{inqz} e^{ik_0 z} e^{-i\omega_0 t} e^{in\mathbf{v}_0\cdot\mathbf{q}t} e^{-in^2\omega_q t}, \tag{2.16}$$

where $\mathbf{v}_0 = \mathbf{p}_0/M$ is the initial velocity of the atom, and $\omega_q = \dfrac{\hbar q^2}{2M}$ is the recoil frequency. This is a crucial result that explains all the features of the atomic evolution after the standing wave diffraction. Each of the momentum states is described by a plane wave, with a relative amplitude controlled by the pulse area ϑ_1 and given by the Bessel function coefficient, $J_n(\vartheta_1)$. We notice that each momentum state acquires a recoil phase given by $n^2\omega_q t$. Each momentum state has also acquired a Doppler phase $nI\mathbf{v}_0 \cdot \mathbf{q}t$.

As shown in reference [117], under BEC conditions (no Doppler dephasing) it is easy to explain the recoil modulated signal shape based on equation 2.16. This is the signal shown in figure 1.10. For BEC conditions, the duration of the signal envelope is sufficiently long that the recoil modulation can be observed over an extended timescale when a read-out pulse is applied. Figure 2.3a shows a plot of the backscattered electric fields produced by interferences associated with $\psi^*\psi$, where ψ is given by equation 2.16.

Each of the momentum states in equation 2.16 oscillates at multiples of the recoil frequency such as ω_q, $4\omega_q$, $9\omega_q$ for $n = 1, 2, 3$, respectively. The relative amplitude of each momentum state is governed by $J_n(\vartheta_1)$. The read-out pulse selects out contributions to the backscattered electric field from pairs of momentum states separated

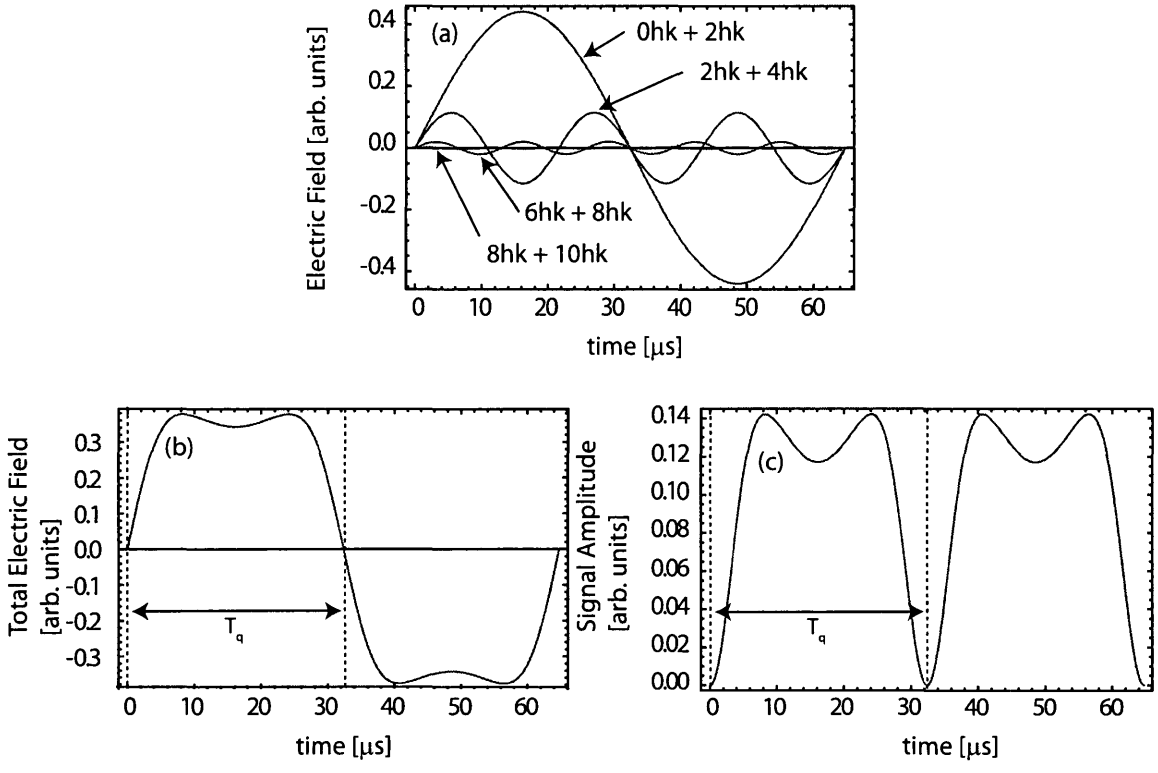

Figure 2.3: (a) Recoil modulated backscattered electric field from pairs of interfering momentum states. (b) The sum of the electric field components in (a) gives the total backscattered electric field. (c) Total signal amplitude given by the square of the electric field in (b).

by $2\hbar k$. These contributions oscillate at multiples of the ω_q such as $(1^2 - 0^2)\omega_q$, $(2^2 - 1^2)\omega_q$, $(3^2 - 2^2)\omega_q$ for different pairs of interfering states. The summation of all these contributions produces the total backscattered field, which is shown in figure 2.3b. The square of the electric field is the total signal amplitude shown in figure 2.3c.

The result in equation 2.16 is valid for a single atom. It shows that there is a spatial modulation in the probability density immediately after standing wave excitation. However, the backscattered signal observed in the experiment comes from an ensemble

of atoms. We now calculate the signal under MOT conditions for a sample of atoms with a velocity distribution. Since the atoms in the experiment are incoherent, the backscattered signal from the ensemble can be calculated by averaging $\psi(t)^*\psi(t)$ over the velocity distribution.

This calculation is fairly tedious, and has been shown elsewhere [118] to be

$$\langle \psi(t)^*\psi(t) \rangle_u \propto \exp\left[-\left(\frac{qut}{2}\right)\right] J_1\left[2\vartheta_1 \sin(\omega_q t)\right]. \tag{2.17}$$

Here, u is the $1/e$ width of the velocity distribution along the axis of the standing wave. A plot of the backscattered signal is shown in figure 2.4.

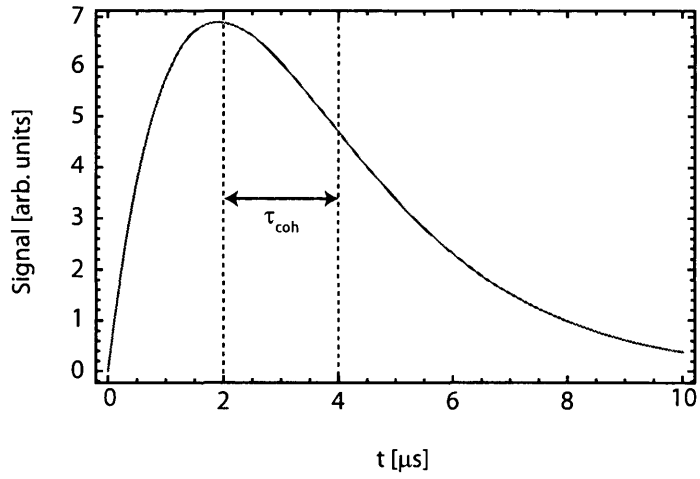

Figure 2.4: Backscattered signal after excitation by a single standing wave pulse. Here, $u = 6$ cm/s, $q = 2k$, $\vartheta_1 = 1$ rad and $\omega_q = 96204$ rad/s. The time τ_{coh} is coherence time due to the velocity distribution.

The signal in figure 2.4 shows the build-up of a one-dimensional density grating immediately after the standing wave excitation. The backscattered signal is a measure of the contrast of this grating. In the classical picture, this is analogous to atoms being channelled into the nodes of the standing wave potential. However, for the case of laser

cooled atoms, this effect is produced by a small modulation of the uniform density distribution that prevailed before excitation. It is possible to infer that modulation in the density is small because the atoms absorbing momentum from the laser fields move a small fraction of the spacing of the standing wave potential during the time in which the density grating builds up in figure 2.4. For example, an atom with a two photon recoil speed $v_{\text{recoil}} = 1.2$ cm/s travels 6 nm during the build-up time, which is much less than the grating spacing, $\lambda/2 = 390$ nm. The signal in figure 2.4 dephases because gratings associated with each velocity class get out of step on a timescale $\tau_{\text{coh}} \approx \lambda/2u$, which is the time for a typical atom to move over a distance of one grating spacing.

Equation 2.17 also predicts that the signal is modulated at the recoil frequency ω_q. However, this modulation cannot be observed directly because $\tau_{\text{coh}} << T_q$, where $T_q = \pi/\omega_q$ is the recoil period.

Equation 2.16 also describes the long term Doppler phase evolution of the momentum states. In an echo experiment, the wavepackets can drift apart by distances considerably larger than the de Broglie wavelength λ_{dB}. For a typical sample temperature of 20 μK, $\lambda_{\text{dB}} \approx 75$ nm. This distance is much smaller than the distance travelled by wavepackets during the echo experiment, which is given by $2T_{21} \times v_{\text{recoil}} =$ 2 (0.025 s)$\times$ (6 mm/s) = 300 μm.

2.1.3 Grating Reformation

In the echo experiment, these momentum states are rephased by a second pulse applied at $t = T_{21}$. The second standing wave pulse is applied with a pulse area ϑ_2. Each of the momentum states associated with the first standing wave is diffracted again into a superposition of partial waves. The wavefunction immediately after the second standing wave is given by

$$\psi(t = \tau_1 + T_{21} + \tau_2) = \sum_{n=-\infty}^{\infty} \sum_{m=-\infty}^{\infty} i^n i^m J_n(\vartheta_1) J_m(\vartheta_2) e^{inqz} e^{ik_0 z} e^{-i\omega_0 t} \times e^{in\mathbf{v}_0 \cdot \mathbf{q}t} e^{-in^2\omega_q t}. \quad (2.18)$$

Since the calculation is carried out in the Raman-Nath regime, the pulse durations τ_1 and τ_2 are much smaller than the time between pulses T_{21}. Therefore, we make the approximation $\tau_1 + T_{21} + \tau_2 \approx T_{21}$ for notational ease.

Using equation 2.15, the free space time evolution of equation 2.18 is given by

$$\psi(t) = \widehat{U}|\psi(T_{21})\rangle = e^{-i\omega_0 t} e^{-imqv_0 t} e^{-in^2\omega_q t} \psi(T_{21}). \quad (2.19)$$

Inserting equation 2.18 into equation 2.19,

$$\psi(t) = \sum_{n=-\infty}^{\infty} \sum_{m=-\infty}^{\infty} i^n i^m J_n(\vartheta_1) J_m(\vartheta_2) e^{ik_0 z} e^{-i\omega_0 T_{21}} e^{i\omega_0 t} e^{i(n+m)qz} e^{i(n^2+m^2)\omega_q T_{21}} e^{i(n+m)qv_0 T_{21}}.$$

To find the density distribution of the ensemble of atoms, we find $\psi^*\psi$ to obtain

$$\psi^*\psi = \sum_{n,m,n',m'=-\infty}^{\infty} J_n(\vartheta_1)J_{n'}(\vartheta_1)J_m(\vartheta_2)J_{m'}(\vartheta_2)i^{n+m}i^{-n'-m'}$$
$$e^{ik_0z}e^{-ik_0z}e^{-i\omega_0T_{21}}e^{i\omega_0T_{21}}e^{i\omega_0t}e^{-i\omega_0t}$$
$$e^{i(n+m)qz}e^{i(n'+m')qz}$$
$$e^{i(n^2+m^2)\omega_qT_{21}}e^{i(n'^2+m'^2)\omega_qT_{21}}$$
$$e^{i(n+m)qv_0T_{21}}e^{i(n'+m')qv_0T_{21}}.$$

We note that the atomic plane wave phases $(k_0z-\omega_0t)$ cancel out when the density distribution is calculated so that

$$\psi^*\psi = \sum_{n,m,n',m'-\infty}^{\infty} J_n(\vartheta_1)J_{n'}(\vartheta_1)J_m(\vartheta_2)J_{m'}(\vartheta_2)i^{n+m-n'-m'}$$
$$e^{i(n+m)qz}e^{i(n'+m')qz}$$
$$e^{i(n^2+m^2)\omega_qT_{21}}e^{i(n'^2+m'^2)\omega_qT_{21}}$$
$$e^{i(n+m)qv_0T_{21}}e^{i(n'+m')qv_0T_{21}} \tag{2.20}$$
$$\tag{2.21}$$

2.1.4 Two-Pulse Echo at $2T_{21}$

For the echo at $t = 2T_{21}$, we only detect the spatial harmonic of the $\lambda/2$ periodic Fourier component of the density distribution. Accordingly, the expression for the

signal can be significantly simplified since it only involves momentum states differing by $\hbar q$. Therefore, equation 2.21 reduces to

$$\psi^*\psi = 2(-1)\cos[q(z - v_0\Delta t)]J_1(2\vartheta_1 \sin(\omega_q \Delta t)J_2(2\vartheta_2 \sin[\omega_q(T_{21} + \Delta t)]), \quad (2.22)$$

where $\Delta t = t - 2T_{21}$ is the time measured with respect to the echo time.

The echo technique ensures that the Doppler phases of momentum states will cancel for all velocities in the sample. By averaging over the Maxwell-Boltzmann velocity distribution of the sample, the velocity-dependent term in equation 2.22 is removed so that the two-pulse echo signal is given by

$$\psi^*\psi \propto \exp\left[-\left(\frac{qu\Delta t}{2}\right)^2\right] J_1(2\vartheta_1 \sin[\omega_q \Delta t])J_2(2\vartheta_2 \sin[\omega_q(T_{21} + \Delta t)]). \quad (2.23)$$

Since $\tau_{\text{coh}} << T_{21}$, the signal is only observed in the immediate vicinity of the echo time. Therefore, $\Delta t \ll 2T_{21}$. We now use the small argument expansion of $J_1(x) \approx x$ and the small angle approximation of $\sin(\omega_q \Delta t) \approx \omega_q \Delta t$ to find the amplitude of the two-pulse echo to be

$$\psi^*\psi \propto (\omega_q \Delta t)\exp\left[-\left(\frac{qu\Delta t}{2}\right)^2\right] J_2[2\vartheta_2 \sin(\omega_q T_{21}]. \quad (2.24)$$

Here, $\tau_{\text{coh}} = 2/qu = 1/ku$.

The backscattered signal amplitude from the sample $E_0^{(2)}(t)$, exhibits the functional form of the $2k$ component of the density distribution. The first two terms are functions of Δt, which represent the dispersion shaped echo signal envelope shown in figure 2.5. This figure can be compared to figure 1.9.

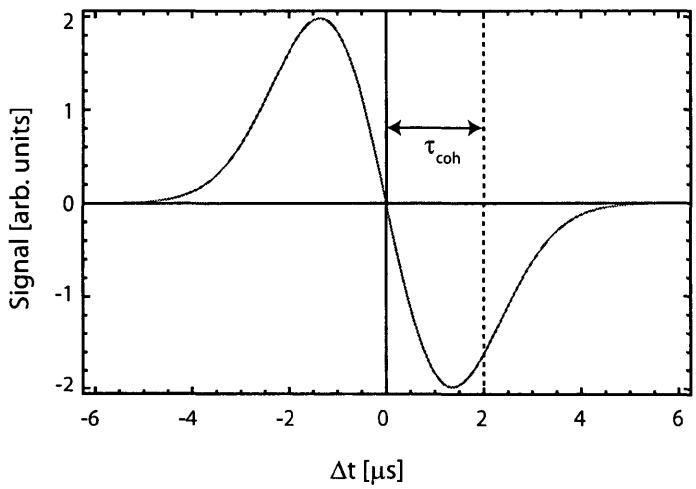

Figure 2.5: Dispersion shaped echo envelope. For atoms with a temperature of 20 μK, the Doppler dephasing time is $\tau_{\text{coh}} = 2$ μs. The signal crosses zero at exactly $2T_{21}$, indicative of the sample having no density grating at the start of the experiment.

The last term in equation 2.24 represents the T_{21}-dependent modulation of the echo signal amplitude, at the frequency $2\omega_q$, shown in figure 2.6. The corresponding period is given by $T_q = \pi/\omega_q$. Since the modulation period $T_q >> \tau_{\text{coh}}$, the recoil modulation can be observed only by varying T_{21} and recording the backscattered signal. Figure 2.6 shows the T_{21} dependence for distinct values of the pulse area ϑ_2. For low pulse area, $\vartheta_2 = 1$ rad, the recoil modulation of the echo amplitude is sinusoidal. As explained in reference [117] and in figure 2.3, this occurs because the signal is dominated by the interference between the 0 and $\hbar q$ momentum states. If the pulse area is increased to $\vartheta_2 = 2$ rad, the contribution of higher-order interferences, such as those between $\hbar q$ and $2\hbar q$, become more apparent. Summing over the backscattered fields from all interferences produces the more complicated signal shape, as shown in figure 2.6. The fringe narrowing near the zeros indicates the presence of these higher harmonics. The

illustrations in figure 2.6 can be compared to the echo signal amplitude in figure 1.10 that included a phenomenological exponential decay.

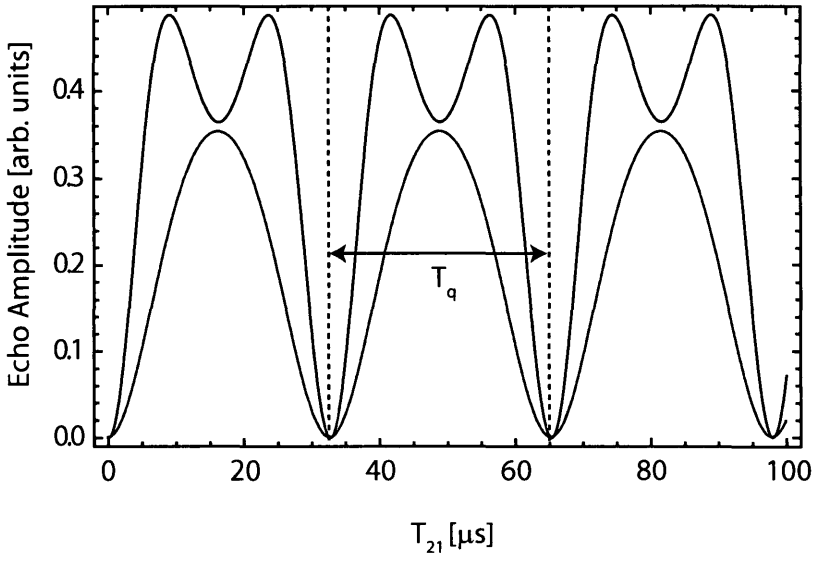

Figure 2.6: Periodicity of echo signal amplitude given by equation 2.24. The echo signal amplitudes with pulse area $\vartheta_2 = 1$ rad is shown in grey, and the amplitude for $\vartheta_2 = 2$ rad is shown in red. The recoil period is $T_q = 32.388$ μs.

2.1.5 Echo AI With Gravity

We now extend the quantum-mechanical calculation of the echo signal to include the presence of gravity. The addition of a gravitational potential adds an extra term to the interaction Hamiltonian during the excitation pulse in equation 2.8. If the coordinate z is in the upward direction, and gravity acts in the negative direction, the Hamiltonian is given by

$$\widetilde{H}_{\text{grav}} = \frac{\hbar\Omega^2}{2\Delta}\cos(qz) + Mgz. \tag{2.25}$$

The two terms in equation 2.25 commute since they both involve the same z

operator. Thus, the gravitational term adds another phase factor to the plane wave wavefunction, which is now given by

$$\Psi(\tau_1) = \sum_{n=-\infty}^{\infty} i^n J_n(\vartheta_1) e^{ik_0 z} e^{inqz} e^{iMgz\tau_1/\hbar}.$$

This expression can be compared to equation 2.10.

Gravity also modifies the free-space evolution Hamiltonian in equation 2.13, which is given by

$$\hat{H}_{\text{grav}} = \frac{\hbar^2 \hat{p}^2}{2M} + Mgz. \tag{2.26}$$

The Hamiltonian now consists of both momentum and position operators that no longer commute. Inserting this Hamiltonian into the time evolution operator, we obtain

$$\hat{U}_{\text{grav}} = \exp\left[\frac{-it}{\hbar}\left(\frac{\hat{\mathbf{p}}^2}{2M} + Mgz\right)\right]. \tag{2.27}$$

We use the Baker-Campbell-Hausdorff formula [119] to write the exponential term in a more useable form. The formula states that

$$e^{t(X+Y)} = e^{tX} e^{tY} e^{-t^2[X,Y]/2} e^{t^3(2[Y,[X,Y]]+[X,[X,Y]])/6} e^{t^4 \ldots} \ldots, \tag{2.28}$$

where X and Y are operators. Furthermore, the Zassenhaus formula [119] states that if the two operators X and Y are chosen such that the commutator $[X,[X,Y]]$ is purely imaginary and $[Y,[X,Y]] = 0$, the above series can be written in closed form as:

$$e^{X+Y} = e^X \; e^Y \; e^{-[X,Y]/2} \; e^{[X,[X,Y]]/6}.$$

We choose $X = \frac{-i}{\hbar}Mgz$ and $Y = \frac{i}{\hbar}\frac{\hat{\mathbf{p}}^2}{2M}$, so that the commutators $[X,Y]$, $[X,[X,Y]]$ and $[Y,[X,Y]]$ are given by

$$\begin{aligned}
[X,Y] &= \left[\frac{-i}{\hbar}Mgz, \frac{-i}{\hbar}\frac{\hat{\mathbf{p}_z}^2}{2M}\right] \\
&= Mg\frac{1}{2M}\left(\frac{-i}{\hbar}\right)^2[z, \hat{\mathbf{p}_z}^2] \\
&= \frac{g}{2\hbar^2}[2i\hbar\hat{p}] \\
&= \frac{i}{\hbar}g\hat{p}, \qquad (2.29)
\end{aligned}$$

$$\begin{aligned}
[X,[X,Y]] &= \left[\frac{-i}{\hbar}Mgz, \frac{i}{\hbar}g\hat{p}\right] \\
&= \left(\frac{-i}{\hbar}\right)^2 Mg^2[z,\hat{p}] \\
&= \frac{1}{\hbar^2}Mg^2i\hbar \\
&= \frac{i}{\hbar}Mg^2, \qquad (2.30)
\end{aligned}$$

and

$$[Y,[X,Y]] \propto [\hat{p}^2,\hat{p}] = 0,$$

respectively. As a result, the gravity modified time evolution operator becomes

$$\hat{U}_{\text{grav}} = \exp\left[\frac{it}{\hbar}\left(\frac{\hat{p}^2}{2M} - Mgz\right)\right] = \exp\left[\frac{-it}{\hbar}Mgz\right] \exp\left[\frac{-it}{\hbar}\frac{\hat{p}^2}{2M}\right] \exp\left[\frac{t^2}{2}\frac{-i}{\hbar}g\hat{p}\right] \exp\left[\frac{t^3}{6}\frac{-i}{\hbar}Mg^2\right].$$

This result shows that the time evolution operation in 2.14 is modified by three exponential factors due to non-commutating operators.

Since the eigenvalues of each of these operators terms are known, applying this operator on $\Psi(\tau_1)$ gives

$$\begin{aligned}\hat{U}_{\text{grav}}\Psi(\tau_1) &= \exp\left[\frac{it}{\hbar}\left(\frac{p^2}{2M} - Mgz\right)\right]\Psi(\tau_1) \\ &= e^{-i\omega_0 t}e^{-inq v_0 t}e^{-in^2\omega_q t} \qquad (2.31) \\ &\quad e^{-iMgzt/\hbar} \\ &\quad \exp\left[\frac{t^2}{2}\left(\frac{-ig(k_0+nq)}{\hbar}\right)\right] \\ &\quad \exp\left[\frac{t^3}{6}\frac{-iMg^2}{\hbar}\right]\Psi(\tau_1). \qquad (2.32)\end{aligned}$$

Comparing this result to equation 2.15, we see that the effect of gravity produces three new phase factors given by the last three terms in equation 2.32.

Based on equation 2.32, at time $t = \tau_1 + T_{21}$, we can write the explicit wavefunction as

$$\Psi(\tau_1 + T_{21}) = \sum_{n=-\infty}^{\infty} i^n J_n(\vartheta_1) e^{ik_0 z} e^{inqz} e^{iMgz\tau_1/\hbar}$$
$$e^{-i\omega_0 T_{21}} e^{-inqv_0 T_{21}} e^{-in^2\omega_q T_{21}}$$
$$e^{-iMgzT_{21}/\hbar}$$
$$\exp\left[\frac{T_{21}^2}{2}\left(\frac{-igk_0}{\hbar}\right)\right] \exp\left[\frac{T_{21}^2}{2}\left(\frac{-ig(nq)}{\hbar}\right)\right]$$
$$\exp\left[\frac{T_{21}^3}{6}\left(\frac{-iMg^2}{\hbar}\right)\right]. \tag{2.33}$$

In the echo experiment, a second pulse with duration τ_2 is applied at time $t = T_{21}$. The second pulse has a pulse area of $\vartheta_2 = \dfrac{-\Omega^2}{2\Delta}$, which produces a similar effect as the first pulse so that new phase factors $e^{imqz} e^{iMgz\tau_2}$ that appear in the wavefunction are given by

$$\Psi(\tau_1 + T_{21} + \tau_2) = \sum_{n=-\infty}^{\infty} \sum_{m=-\infty}^{\infty} i^n J_n(\vartheta_2) i^m J_m(\vartheta_1)$$
$$e^{ik_0 z} e^{inqz} e^{iMgz\tau_1}$$
$$e^{-i\omega_0 T_{21}} e^{-inqv_0 T} e^{-in^2\omega_q T} \left[e^{imqz} e^{iMgz\tau_2}\right]$$
$$e^{-imgzT_{21}/\hbar}$$
$$\exp\left[\frac{T_{21}^2}{2}\left(\frac{-igk_0}{\hbar}\right)\right] \exp\left[\frac{T_{21}^2}{2}\left(\frac{-ig(nq)}{\hbar}\right)\right]$$
$$\exp\left[\frac{T_{21}^3}{6}\left(\frac{-iMg^2}{\hbar}\right)\right]. \tag{2.34}$$

To model free space evolution with gravity, we apply the modified time evolution operator given by equation 2.31 so that

$$\hat{U}_{\text{grav}}\Psi(\tau_1+T_{21}+\tau_2) = \exp\left[\frac{-it}{\hbar}\frac{\hat{p}^2}{2M}\right] \exp\left[\frac{-it}{\hbar}Mgz\right] \exp\left[\frac{t^2}{2}\left(\frac{-ig\hat{p}}{\hbar}\right)\right] \exp\left[\frac{t^3}{6}\left(\frac{-iMg^2}{\hbar}\right)\right]\Psi(\tau_1+T_{21}+\tau_2). \quad (2.35)$$

Inserting the eigenvalues for the four operators and re-arranging gives

$$\Psi(\tau_1+T_{21}+\tau_2+t) = \sum_{n=-\infty}^{\infty}\sum_{m=-\infty}^{\infty} i^n J_n(\vartheta_1) i^m J_m(\vartheta_2) \; e^{ik_0z}e^{inqz}e^{imqz}e^{iMgz\tau_1}e^{iMgz\tau_2} \; e^{-i\omega_0T_{21}}e^{-inqv_0T_{21}}e^{-in^2\omega_qT_{21}} \; e^{-iMgzT_{21}/\hbar} \; \exp\left[\frac{T^2}{2}\left(\frac{-igk_0}{\hbar}\right)\right]\exp\left[\frac{T_{21}^2}{2}\left(\frac{-ig(nq)}{\hbar}\right)\right] \exp\left[\frac{T_{21}^3}{6}\left(\frac{-iMg^2}{\hbar}\right)\right] \; e^{-i\omega_0t}e^{-iMqv_0t}e^{-im^2\omega_qt} \; e^{-iMgzt/\hbar} \; \exp\left[\frac{t^2}{2}\left(\frac{-igk_0}{\hbar}\right)\right]\exp\left[\frac{t^2}{2}\left(\frac{-ig(mq)}{\hbar}\right)\right] \exp\left[\frac{t^3}{6}\left(\frac{-iMg^2}{\hbar}\right)\right]. \quad (2.36)$$

This wavefunction can be compared to equation 2.20 to observe the extra phase terms

due to gravity.

If the density distribution, $\Psi^*\Psi$, is calculated, extra multiplicative terms will be added, but the only terms that will survive are the ones with the indices (m, n). Therefore, we re-arrange the wavefunction to obtain

$$\Psi(\tau_1 + T_{21} + \tau_2 + t) = \sum_{n=-\infty}^{\infty} \sum_{m=-\infty}^{\infty} i^n J_n(\vartheta_1) i^m J_m(\vartheta_2)$$

$$\begin{pmatrix} e^{ik_0 z} e^{-i\omega_0 T_{21}} e^{-i\omega_0 t} e^{iMgz\tau_1} e^{iMgz\tau_2} \\ e^{-iMgzT_{21}/\hbar} e^{-iMgzt/\hbar} \\ \exp\left[\frac{T_{21}^2}{2}\left(\frac{-igk_0}{\hbar}\right)\right] \\ \exp\left[\frac{T_{21}^3}{6}\left(\frac{-iMg^2}{\hbar}\right)\right] \\ \exp\left[\frac{t^2}{2}\left(\frac{-igk_0}{\hbar}\right)\right] \\ \exp\left[\frac{t^3}{6}\left(\frac{-iMg^2}{\hbar}\right)\right] \end{pmatrix}$$

$$e^{inqz} e^{imqz} e^{-inqv_0 T_{21}} e^{-imqv_0 t}$$

$$e^{-in^2\omega_q T_{21}} e^{-im^2\omega_q t}$$

$$\exp\left[\frac{T_{21}^2}{2}\left(\frac{-ig(nq)}{\hbar}\right)\right]$$

$$\exp\left[\frac{t^2}{2}\left(\frac{-ig(mq)}{\hbar}\right)\right].$$

We now calculate $\Psi^*\Psi$. Due to the cancellation of phase factors within the large bracket, we obtain

$$\begin{aligned}\Psi^*\Psi = \sum_{n,m,n',m'-\infty}^{\infty} & J_n(\vartheta_1)J_{n'}(\vartheta_1)J_m(\vartheta_2)J_{m'}(\vartheta_2)i^{n+m-n'-m'} \\ & e^{i(n+m)qz}e^{i(n'+m')qz} \\ & e^{i(n^2+m^2)\omega_q T_{21}}e^{i(n'^2+m'^2)\omega_q T_{21}} \\ & e^{i(n+m)qv_0T_{21}}e^{i(n'+m')qv_0T_{21}} \\ & \exp\left[\frac{T_{21}^2}{2}\left(\frac{-ig(nq)}{\hbar}\right)\right]\exp\left[\frac{T_{21}^2}{2}\left(\frac{ig(n'q)}{\hbar}\right)\right] \\ & \exp\left[\frac{t^2}{2}\left(\frac{-ig(mq)}{\hbar}\right)\right]\exp\left[\frac{t^2}{2}\left(\frac{ig(m'q)}{\hbar}\right)\right].\end{aligned} \tag{2.37}$$

This result can be compared with equation 2.21 to observe the extra phase terms due to gravity.

Since we are interested in the echo near $2T_{21}$, we define $t = 2T_{21} + \Delta t$. As before, we only detect the spatial harmonic of the $\lambda/2$ periodic Fourier component of the density distribution. Therefore, after velocity averaging, the resulting expression simplifies [32] to

$$\begin{aligned}\Psi^*\Psi = & \exp\left[-\left(\frac{qu\Delta t}{2}\right)^2\right] J_1(2\vartheta_1\sin[\omega_q\Delta t])J_2(2\vartheta_2\sin[\omega_q(T_{21}+\Delta t)]) \\ & \times\cos\left(qz + \frac{qg}{2}\left[2T_{21}^2 + (2\tau_2+4\Delta t)T_{21} + 2\Delta t(\tau_1+\tau_2) + \Delta t^2\right]\right).\end{aligned} \tag{2.38}$$

This equation is identical to equation 2.23, previously derived without gravity, except for the last multiplicative cosine term.

The argument of the cosine term is

$$\phi = qz + q\left(\frac{g}{2}\left[4T_{21}\Delta t + 2\Delta t(\tau_1+\tau_2) + \Delta t^2\right]\right) + qgT_{21}^2.$$

The term qz is an arbitrary constant phase factor that does not change as a function of the variables that pertain to the gravity experiment, namely, T_{21} and Δt. Therefore, it is useful to define the gravitational phase as

$$\phi_g^{(2)} = q\left(\frac{g}{2}\left[4T_{21}\Delta t + 2\Delta t(\tau_1+\tau_2) + \Delta t^2\right]\right) + qgT_{21}^2. \tag{2.39}$$

Since $\tau_{\text{coh}} << T_{21}$, the signal is only observed in the immediate vicinity of the echo time. Therefore, $\Delta t \ll 2T_{21}$. We now use the small argument expansion of $J_1(x) \approx x$ and the small angle approximation of $\sin(\omega_q \Delta t) \approx \omega_q \Delta t$ to find the amplitude of the two-pulse echo in the presence of gravity to be

$$\begin{aligned}\Psi^*\Psi \propto & (\omega_q\Delta t)\exp\left[-\left(\frac{qu\Delta t}{2}\right)^2\right] J_2(2\vartheta_2\sin(\omega_q T_{21})) \\ & \times\cos\left(q\left(\frac{g}{2}\left[4T_{21}\Delta t + 2\Delta t(\tau_1+\tau_2) + \Delta t^2\right]\right) + qgT_{21}^2\right).\end{aligned} \tag{2.40}$$

With the definitions of the signal amplitude,

$$E_0^{(2)} = \omega_q\Delta t\exp\left[-\left(\frac{qu\Delta t}{2}\right)^2\right] J_2(2\vartheta_2\sin(\omega_q T_{21}) \tag{2.41}$$

and the gravitational phase $\phi_g^{(2)}$ in equation 2.39, the two-pulse signal can be written as

$$\Psi^*\Psi \propto E_0^{(2)}\cos(\phi_g^{(2)}). \tag{2.42}$$

2.1.6 Interpretation of Two-Pulse AI Theory

It is useful to write equation 2.43 in terms of an exponential phase factor because the experiment detects the in-phase and in-quadrature components of $E_g^{(2)}$. In what follows, we explore the dependence of one of these components on experimental parameters.

The backscattered electric field from the density grating $E_g^{(2)}$ is proportional to $\Psi^*\Psi$ so that an equivalent expression for equation 2.42 can be written as

$$E_g^{(2)} = E_0^{(2)} e^{i\phi_g^{(2)}}, \tag{2.43}$$

where the electric field amplitude $E_0^{(2)}$ in the small angle approximation is given by

$$E_0^{(2)} \propto E_{\mathrm{RO}} \times \Delta t e^{-(\Delta t/\tau_{\mathrm{coh}})^2} J_2\left[2\vartheta_2 \sin\left(\omega_q T_{21}\right)\right] e^{-(2T_{21}+\Delta t)/\tau_{\mathrm{decay}}}, \tag{2.44}$$

where E_{RO} is the electric field of the read-out pulse and

$$\phi_g^{(2)} = q\left(\frac{g}{2}\left[4T_{21}\Delta t + 2\Delta t(\tau_1+\tau_2) + \Delta t^2\right]\right) + qgT_{21}^2. \tag{2.45}$$

The expression for the $E_0^{(2)}$ contains a phenomenological exponential decay term with a time constant τ_{decay} that models the effect of signal loss due to all decoherence mechanisms as well as the transit time of cold atoms through the interaction zone defined by the excitation beams. The expression for $\phi_g^{(2)}$ is dependent on the time separation between excitation pulses T_{21}, the time measured with respect to the echo time, $\Delta t = t - 2T_{21}$, and pulse width parameters τ_1, τ_2.

To interpret the results in equation 2.43, it is useful to separate the electric field amplitude and phase into terms that are dependent on Δt from terms dependent

exclusively on T_{21} as

$$E_g^{(2)} = E_{\mathrm{RO}} \times E_0^{(2)}(\Delta t) e^{i\phi_{\mathrm{D}}^{(2)}} \times E_0^{(2)}(T_{21}) e^{i\phi_{\mathrm{AI}}^{(2)}}. \tag{2.46}$$

In this manner, it is possible to explore the behaviour of the echo envelope on the timescale Δt and the echo signal amplitude as a function of T_{21}.

2.1.7 Dependence on Δt

The electric field of the echo envelope $E_g^{(2)}(\Delta t)$ is given by

$$E_g^{(2)}(\Delta t) = E_0^{(2)}(\Delta t) e^{i\phi_{\mathrm{D}}^{(2)}}, \tag{2.47}$$

where

$$E_0^{(2)}(\Delta t) \propto \Delta t e^{-(\Delta t/\tau_{\mathrm{coh}})^2}, \tag{2.48}$$

and the Doppler phase is

$$\phi_{\mathrm{D}}^{(2)} = qg(2T_{21}\Delta t + \Delta t^2/2). \tag{2.49}$$

The solid lines in figure 2.7 show the total signal amplitude $E_g^{(2)}(\Delta t)$. These shapes are generated by choosing a convenient value of T_{21} in the second term of equation 2.44 to maximize the recoil modulated signal. As the value of T_{21} is incremented in the Doppler phase term as described in equation 2.49, the envelope exhibits an increasing oscillation frequency. This is the effect shown earlier in figure 1.12. The physical explanation for this effect is that atoms are falling through a grating spacing of $\lambda/2$, resulting in a phase increment of 2π. This effect can also be described as

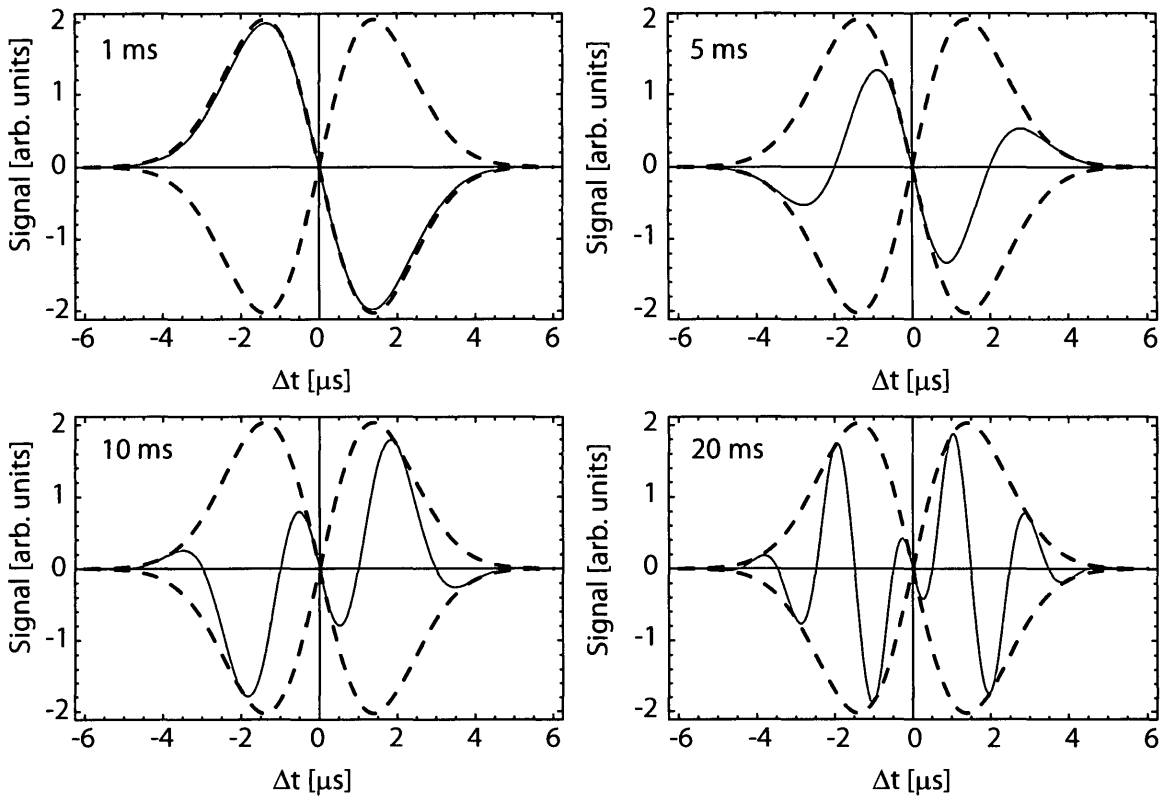

Figure 2.7: Plots of the in-phase component of equation 2.47 as a function of Δt at specified values of T_{21}. We have used $g = 9.8$ m/s^2, $\tau_{\text{coh}} = 2$ μs, and $q = 2k$. The signal envelope (solid line) exhibits an increase in the oscillation frequency due to the influence of gravity on the Δt dependent Doppler phase in equation 2.47. The dashed lines are the two terms in equation 2.48 which predict the signal envelope without gravity.

a Doppler shift of the frequency of the backscattered field due to the motion of the falling grating. The dashed lines in figure 2.7 show the overall amplitude $E_0^{(2)}(\Delta t)$ by equation 2.48.

The angular frequency of the oscillations inside the echo envelope $\omega_D^{(2)}$ can be determined by taking the derivative of the Doppler phase with respect to Δt,

$$\omega_D^{(2)} = \frac{\partial \phi_{\text{D}}^{(2)}}{\partial \Delta t} = qg(2T_{21} + \Delta t). \tag{2.50}$$

The frequency is mainly dependent on T_{21} since $T_{21} \gg \Delta t$. By varying T_{21} and fitting the echo envelope to a constant frequency, it is possible to measure the linear dependence of $\omega_D^{(2)}$ on T_{21}. However, it is generally difficult to observe the Δt dependence since the change in oscillation frequency over the timescale of the echo envelope is much smaller than the frequency of oscillation.

2.1.8 Dependence on T_{21}

The electric field of the echo signal as a function of the pulse spacing T_{21}, $E_0^{(2)}(T_{21})$ is given by

$$E_g^{(2)}(T_{21}) = E_0^{(2)}(T_{21})e^{i\phi_{\mathrm{AI}}^{(2)}}, \tag{2.51}$$

where

$$E_0^{(2)}(T_{21}) \propto J_2\{2\vartheta_2 \sin[\omega_q(T_{21})]\}e^{-2T_{21}/\tau_{\mathrm{decay}}}, \tag{2.52}$$

and the AI phase

$$\phi_{\mathrm{AI}}^{(2)} = qgT_{21}^2 \tag{2.53}$$

depends solely on T_{21}.

By analyzing the total signal amplitude defined as the square root of the sum of the squares of the in-phase and in-quadrature components

$$E_0^{(2)} = \sqrt{\left(E_0^{(2)}\cos\phi_{\mathrm{AI}}\right)^2 + \left(E_0^{(2)}\sin\phi_{\mathrm{AI}}\right)^2}, \tag{2.54}$$

we obtain the decaying recoil modulated signal shown in figure 2.8a. This is the same result as in figures 1.10 and 2.6. As described in Chapter 1, the period of the signal in

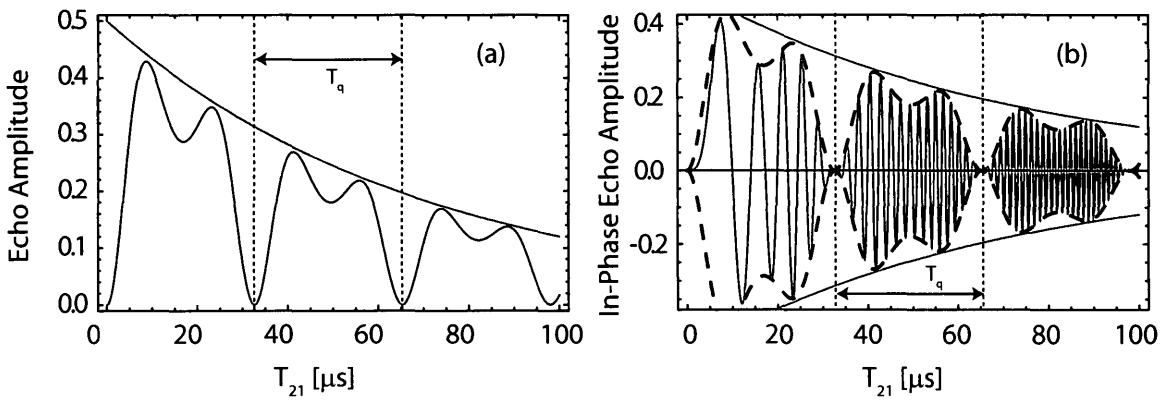

Figure 2.8: (a) Decaying amplitude of the recoil modulated two-pulse signal in equation 2.52 as a function of T_{21}. (b) Gravity induced amplitude oscillations of the in-phase component of the electric field in equation 2.51 bounded by the decaying recoil modulated amplitude shown by the dashed lines. The grey line is the exponential decay. We have used $g = 980$ m/s^2, $\tau_{\text{decay}} = 70$ μs, $\vartheta_2 = 1$ rad for illustration. The vertical axes are in arbitrary units.

figure 2.8a is given by $T_q = \dfrac{\lambda/2}{2\hbar k/M}$. To detect gravity, we plot one component of the electric field as shown in figure 2.8(b) as a function of T_{21}. This result shows a linearly increasing frequency. This effect is the matter-wave analog of the chirped frequency of fringes recorded by an optical falling corner cube Mach-Zehnder interferometer [18]. This result was qualitatively described in figure 1.10.

The angular oscillation frequency ω_{AI} can be calculated by taking the derivative of the AI phase with respect to T_{21},

$$\omega_{AI}^{(2)} = \frac{\partial \phi_{\text{AI}}^{(2)}}{\partial T_{21}} = 2qgT_{21}. \tag{2.55}$$

In practice, the experiment measures one component of the electric field as a function of T_{21} across four widely separated observational windows. The value of gravity is inferred by using a multi-parameter fit function that models the frequency

chirp of the form

$$\sin(2qgT_{21}^2 + qv_0T_{21} + \phi_0), \tag{2.56}$$

where v_0 is a parameter with velocity units and ϕ_0 is constant. For this analysis, the in-phase and in-quadrature components are normalized by the total signal amplitude to remove the recoil modulation and decay terms so that the fit function is simplified.

2.2 Quantum Mechanical Model of the N-Pulse AI

A general approach for calculating the echo signal in the presence of a constant force $\mathcal{F}$ is described in reference [35]. We quote the key results of reference [35] to obtain the signals produced by the three-pulse stimulated echo. These results include the effects of the magnetic sublevel structure and spontaneous emission so that they can also be applied for describing the two-pulse echo in the most general case.

Based on references [32, 35, 112–114], the electric field of the back-scattered light after N excitation pulses is given by a function that is dependent on pulse times $\{T\}$, the time Δt, pulse durations τ and the quantum number of atomic states m_F:

$$E^{(N)}(T, \Delta t, \tau) = \sum_{m_F} E_{m_F}^{(N)} e^{im_F\phi^{(N)}} \tag{2.57}$$

where $\phi^N(t)$ is the phase of the grating due to the linear force $\mathcal{F}$, given by

$$\phi = \frac{q\mathcal{F}}{2M} \sum_{j=1}^{N} (T_{j+1}^2 - T_j^2). \tag{2.58}$$

When the force is due to gravity, $\mathcal{F} = Mg$, the phase is given by

$$\phi = \frac{qg}{2} \sum_{j=1}^{N} l_j (T_{j+1}^2 - T_j^2). \tag{2.59}$$

The phase of the grating is imprinted on the phase of the backscattered electric field $E_{m_F}^{(N)}(t)$ given by

$$E_{m_F}^{(N)}(t) \propto E_{\mathrm{RO}}|\alpha_{m_F}|^2 C \begin{pmatrix} F & 1 & F+1 \\ m_F & q_L & m_F+q_L \end{pmatrix} \sum_{l_1,l_2,l_3,\ldots,l_{N-1}} e^{-\left[(t-t_{\mathrm{echo}}^{(N)})/\tau_{\mathrm{coh}}\right]^2} e^{iqv_0(t-t_{\mathrm{echo}}^{(N)})} \times \prod_{j=1}^{N} J_{l_j-l_{j-1}}\left(2\vartheta_{m_F}^{(j)}\sqrt{\sin(\varphi_j-\theta)\sin(\varphi_j+\theta)}\right)\left(\frac{\sin(\varphi_j-\theta)}{\sin(\varphi_j+\theta)}\right)^{(l_j-l_{j-1})/2}, \tag{2.60}$$

where $|\alpha_{m_F}|^2$ is the population of the state $|F, m_F\rangle$, $C \begin{pmatrix} F & 1 & F+1 \\ m_F & q_L & m_F+q_L \end{pmatrix}$ represents the Clebsh-Gordan coefficients, q_L defines the photon momentum, ± 1, $\{l_1, l_2, l_3, ..., l_N\}$ is the set of momentum states that interfere after the pulse sequence, l_j is the difference between interfering momentum states (in units of $\hbar q$) after pulse j, J_{l_j} are Bessel functions of the first kind, $\vartheta_{m_F}^{(j)}$ is the pulse area for a specific transition from an m_F sublevel, $\theta = \arctan\left(-\frac{\Gamma}{2\Delta}\right)$ is the spontaneous emission parameter, Γ is the radiative rate of the excited state, Δ is the detuning, and the recoil phases are given by

$$\varphi_j = \omega_q \sum_{k=j}^{N} l_k (T_{k+1} - T_k),$$

and the echo times are defined as

$$t_{\mathrm{echo}}^{(N)} = T_N - \frac{1}{N}\sum_{j=1}^{N-1} l_j (T_{j+1} - T_j). \tag{2.61}$$

2.3 Quantum Mechanical Model of the Three-Pulse AI

The recoil diagram for this AI is shown in figure 2.9. For this AI, the arms of the interferometer consist of co-propagating wavepackets with no momentum difference during the central time window associated with T_{32} [34,35]. We show that the signal amplitude as a function of pulse separation T_{32} shows no recoil modulation and exhibits a fixed angular frequency determined by qgT_{21}. Therefore, this AI is sensitive to the velocity of the atoms gT_{21}. The constant frequency and the absence of recoil modulation have beneficial practical consequences for improving the quality of the fits to the data, thereby resulting in increased timescale and precision. Since there is no relative displacement between the co-propagating momentum states during T_{32}, the AI exhibits reduced sensitivity to uncorrelated spurious accelerations due to magnetic curvature and mirror vibrations during the T_{21} time windows [34]. This feature allows the total timescale of the experiment to be increased in comparison to the two-pulse AI [35], resulting in improved precision. By careful choice of pulse parameters, a suitably long observational window can be made available for the measurement of the fixed frequency.

We use the equations for the general N pulse interferometer in the previous section with a few simplifications to obtain the amplitude and phase of the $N = 3$-pulse interferometer. We choose a single m_F state, ignore spontaneous emission, ($\theta = 0$), and absorb the population and Clebsh-Gordan coefficients into a constant of proportionality.

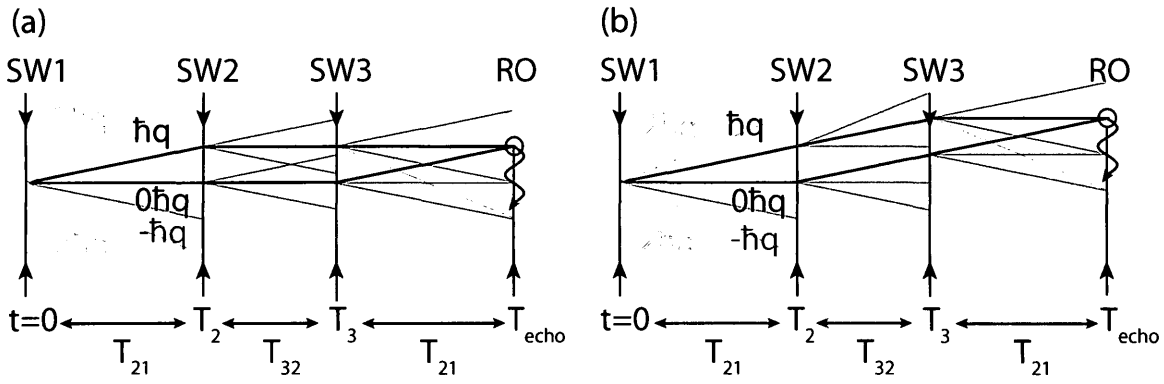

Figure 2.9: Two recoil diagrams for the three-pulse AI in the absence of gravity. Only a subset of all trajectories are shown. SW refers to standing wave pulses and RO is a travelling wave read-out pulse. The backscattered signal arises from interferences between states differing by $\hbar q$ at the echo time.

In the presence of gravity, the backscattered electric field for the three-pulse AI can be written on the basis of equations in section 2.3 as

$$E_g^{(3)} = E_0^{(3)} e^{i\phi_g^{(3)}}. \tag{2.62}$$

The three-pulse amplitude is given by

$$E_0^{(3)} \propto E_{\mathrm{RO}} \times e^{-(\Delta t/\tau_{\mathrm{coh}})^2} J_1\left[2\vartheta_1 \sin(\omega_q \Delta t)\right] J_1\{2\vartheta_2 \sin\left[\omega_q T_{21}\right]\} J_1\{2\vartheta_3 \sin\left[\omega_q T_{21}\right]\} \tag{2.63}$$

Here, $\vartheta_1, \vartheta_2, \vartheta_3$ are the pulse areas of the first, second and third excitation pulses. This signal also exhibits a recoil modulation as a function of T_{21}. It is interesting that the recoil modulation is *not* a function of T_{32}.

The gravitational phase is given by

$$\begin{aligned}\phi_g^{(3)} &= \frac{qg}{2}\left[-(T_2^2 - T_1^2) + (t^2 - T_3^2)\right] \\ &= \frac{qg}{2}\left[-(T_{21}^2 - 0) + (2T_{21} + T_{32} + \Delta t)^2 - (2T_{21} + T_{32})^2\right] \\ &= \frac{qg}{2}(2T_{21}^2 + 2T_{21}T_{32} + 2T_{32}\Delta t + 4T_{21}\Delta t + \Delta t^2). \end{aligned} \tag{2.64}$$

Here, the time measured with respect to the echo time $\Delta t = t - 2T_{21} - T_{32}$. Equations 2.63 and 2.64 reduce to the corresponding two-pulse equations if $T_{32} = 0$.

2.3.1 Three-Pulse AI Δt Dependence

To interpret the results in equation 2.62, it is useful to separate the electric field amplitude and phase into terms that are dependent on Δt from terms dependent exclusively on pulse spacings T_{21} and T_{32} as

$$E_g^{(3)} = E_{\mathrm{RO}} \times E_g^{(3)}(\Delta t) \times E_g^{(3)}(T_{32}, T_{21}). \tag{2.65}$$

In this manner, it is possible to explore the behaviour of the echo envelope on the timescale Δt and the echo signal amplitude as a function of pulse spacings T_{21} and T_{32}.

The electric field of the echo envelope $E_g^{(3)}(\Delta t)$ as a function of Δt is given by:

$$E_g^{(3)}(\Delta t) \propto E_0^{(3)}(\Delta t) e^{i\phi_{\mathrm{D}}^{(3)}}, \tag{2.66}$$

where

$$E_0^{(3)}(\Delta t) \propto \Delta t e^{-(\Delta t/\tau_{\mathrm{coh}})^2}, \tag{2.67}$$

and the Doppler phase is given by

$$\phi_{\mathrm{D}}^{(3)} = \frac{qg}{2}(2T_{32}\Delta t + 4T_{21}\Delta t + \Delta t^2). \tag{2.68}$$

The effect of the Doppler phase term is to produce oscillations within the echo envelope. Equation 2.68 becomes identical to equation 2.49 if the definition of the echo time T_{echo} is written as $2T_{21}$ for the two-pulse AI, and as $2T_{21}+T_{32}$ for the three-pulse AI. Therefore, there is no difference in the shapes of the echo envelopes generated by the two AI configurations. The echo envelopes are identical to the shapes shown in figure 2.7. However, for the two configurations, different oscillation frequencies can be observed by varying either T_{21} *or* T_{32}.

The frequency of the oscillations within the envelope $\omega_D^{(3)}$ can be calculated by taking the derivative of the Doppler phase with respect to Δt,

$$\omega_D^{(3)} = \frac{\partial \phi_{\mathrm{D}}^{(3)}}{\partial \Delta t} = qg(T_{32} + 2T_{21} + \Delta t). \tag{2.69}$$

The frequency is mainly dependent on T_{21} and T_{32} since $T_{21}, T_{32} \gg \Delta t$. By varying either T_{21} or T_{32} and fitting the echo envelope to a constant frequency, it is possible to measure the linear dependence of $\omega_D^{(3)}$ on T_{21} and T_{32}. The rate of frequency increase as a function of T_{21} is twice the rate of frequency increase as a function of T_{32}. However, it is generally difficult to observe the Δt dependence as the change in oscillation frequency over the timescale of the echo envelope is much smaller than the frequency of oscillation.

2.3.2 Dependence on T_{21} and T_{32}

The electric field of the echo signal as a function of pulse spacings T_{21} and T_{32}, $E_g^{(3)}(T_{21}, T_{32})$ is given by

$$E_g^{(3)}(T_{21}, T_{32}) \propto E_0^{(3)}(T_{21}, T_{32}) e^{i\phi_{\mathrm{AI}}^{(3)}}, \tag{2.70}$$

where

$$E_0^{(3)}(T_{21}, T_{32}) \propto J_1\{2\vartheta_2 \sin[\omega_q T_{21}]\} J_1\{2\vartheta_3 \sin[\omega_q T_{21}]\} e^{-(2T_{21}+T_{32}+\Delta t)/\tau_{\mathrm{decay}}}, \tag{2.71}$$

and the AI phase is given by

$$\phi_{\mathrm{AI}}^{(3)} = \frac{qg}{2}(2T_{21}^2 + 2T_{21}T_{32}) \tag{2.72}$$

depends on T_{21} and T_{32}.i

By analyzing the total signal amplitude defined as the square root of the sum of the squares of the in-phase and in-quadrature components, we obtain the decaying recoil modulated signal predicted by equation 2.71 and shown in figure 2.10a as a function of T_{21}. In the experiment, the second and third excitation pulses are chosen to have the same pulse area. Hence the $J_1(2\vartheta_2)$ and $J_1(2\vartheta_3)$ terms are equal. Since $[J_1(2\vartheta_2)]^2$ is functionally similar to $J_2(2\vartheta_2)$, the recoil modulated signal resembles the two-pulse results in figure 2.8. Figure 2.10b shows a plot of one component of equation 2.70 as a function of T_{21}. These plots are similar to the two-pulse results in figure 2.8.

The angular oscillation frequency ω_{AI} can be calculated by taking the derivative of the AI phase with respect to T_{21},

$$\omega_{AI}^{(3)} = \frac{\partial \phi_{\mathrm{AI}}}{\partial T_{21}} = qg(2T_{21} + T_{32}). \tag{2.73}$$

For a fixed value of T_{32}, it is possible to determine the chirped frequency using four widely spaced observational windows, similar to the two-pulse AI. The frequency measured by varying T_{21} is offset by the T_{32} term. If T_{32} is set to zero, the two-pulse result is recovered. However, the three-pulse AI offers a much simpler method of determining g.

By analyzing the total signal amplitude, we obtain the decaying signal predicted by equation 2.71 and shown in figure 2.10c as a function of T_{32}. The electric field does not exhibit recoil modulation because the recoil terms are independent of T_{32}. This allows the freedom to record the signal envelope as a function T_{32} for an optimized value of T_{21}. Figure 2.10d shows a plot of one component of equation 2.70 as a function of T_{32}. Since $\phi_{\mathrm{AI}}^{(3)}$ exhibits a linear dependence on T_{32}, the signal amplitude exhibits a modulation at a fixed frequency defined by T_{21}. This angular oscillation frequency can be calculated by taking the derivative of the AI phase with respect to T_{32} so that

$$\omega_{AI}^{(3)} = \frac{\partial \phi_{\mathrm{AI}}}{\partial T_{32}} = qgT_{21}. \tag{2.74}$$

As noted in Chapter 1, the period of the signal is given by $T_{\mathrm{velocity}} = \dfrac{\lambda/2}{gT_{21}}$. Since the angular frequency, qgT_{21}, is constant, a measurement of g can be carried out with high precision by recording one of the signal components as a function of T_{32} across

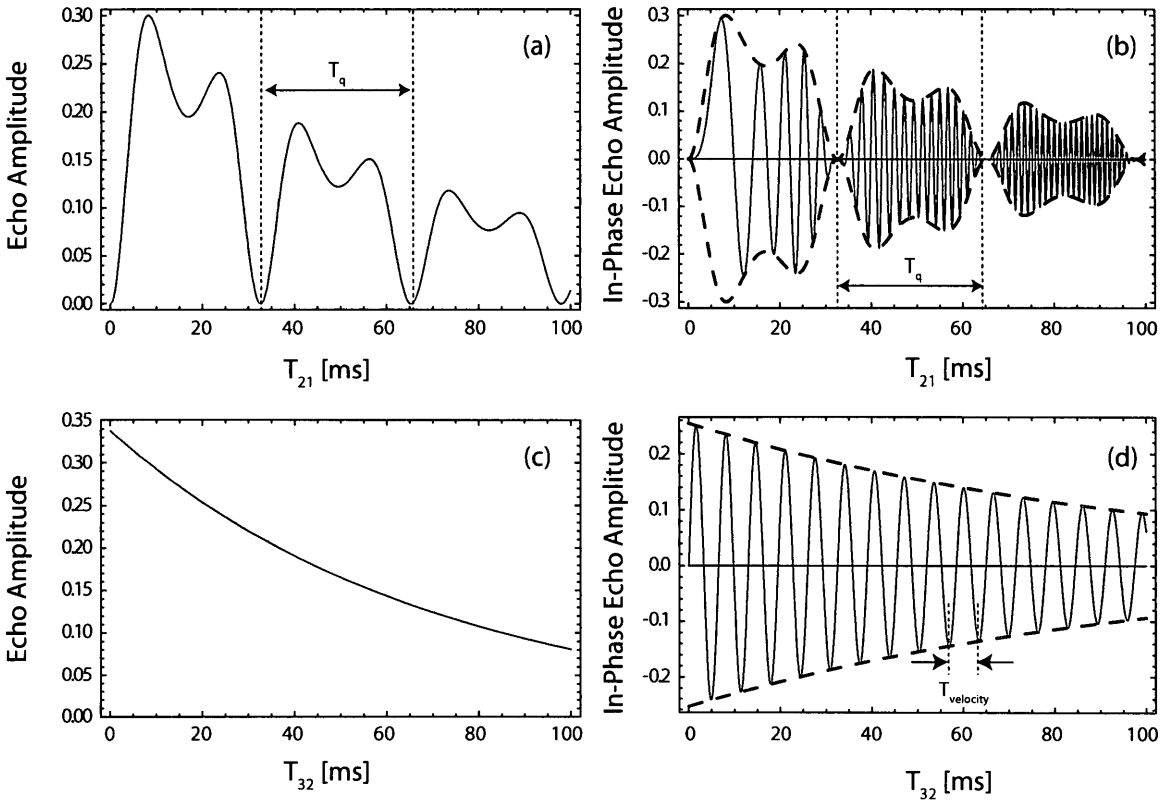

Figure 2.10: (a) Plot of equation 2.71 as a function of T_{21} for a fixed T_{32}. The total signal amplitude is recoil modulated. (b) Gravity induced amplitude oscillations of the in-phase component of the electric field in equation 2.70 as a function of T_{21} for a fixed T_{32} bounded by corresponding decaying recoil modulated amplitude shown by dashed lines. (c) Plot of equation 2.71 as a function of T_{32} for a fixed T_{21}. The signal does *not* exhibit recoil modulation. (d) Gravity induced amplitude oscillations of the in-phase component of the electric field in equation 2.70 as a function of T_{32} bounded by the decaying recoil modulated amplitude shown by dashed lines for fixed T_{21}. The frequency of oscillation is a constant determined by T_{21}. The grey line is the exponential decay. We have used $g = 980$ m/s^2, $\tau_{\text{decay}} = 70$ μs, $\vartheta_2 = 1$ rad for illustration.

two widely-separated observational windows. The maximum ϕ_{AI} occurs for a total timescale of $2T_{21} + T_{32}$ if $T_{32} = 2T_{21}$.

2.4 Two-Pulse AI Based on Action Principle

The action principle can also be applied to the classical trajectories of the atoms to show the origin of both recoil modulation and the effect of gravity. The classical action $\mathcal{S}$ is defined as

$$\mathcal{S} = \int_{t'=0}^{t'=t} (\mathcal{L}(z(t'), \dot{z}(t'))\, dt', \tag{2.75}$$

where t is the real time, t' is the integration variable, and $\mathcal{L}$ is the Lagrangian, equal to the difference of kinetic and potential energies,

$$\mathcal{L} = \frac{p^2}{2M} + Mgz. \tag{2.76}$$

The phase accumulation of the trajectories is given by $\mathcal{S}/\hbar$.

To carry out this calculation, it is necessary to calculate the phase difference due to the path and the phase imparted by the interaction with the light fields.

2.4.1 Phase Difference due to Path

We consider the effects of initial momentum $p_0 = Mv_0$ and gravity on the action with the trajectories shown in figure 2.11.

Although these trajectories are curved due to gravity, it is convenient to use an illustration with rectilinear paths. The derivation for curved paths is presented in Appendix A.

The Lagrangian of the undiffracted atom is $\mathcal{L} = \frac{p_0^2}{2M} + Mgz$ for all time, and so the action is then

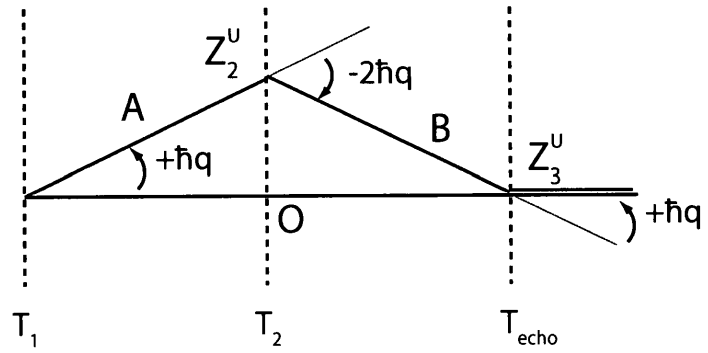

Figure 2.11: One set of recoil trajectories in a triangle configuration. The diffracted upper path is shown in red, and the undiffracted Path O is shown in black.

$$\mathcal{S}_0 = \int_{t'=0}^{t'=2T_{21}} \left(\frac{p_0^2}{2M} + Mgz\right) dt' \tag{2.77}$$

$$= \left(\frac{p_0^2}{2M} + Mgz\right) 2T_{21}. \tag{2.78}$$

The diffracted atom has two separate parts. During the first leg A, the kinetic energy of the atom is $\frac{(p_0+\hbar q)^2}{2M}$, so the Lagrangian is

$$\mathcal{L}_A = \frac{(p_0+\hbar q)^2}{2M} + Mgz,$$

and the action $\mathcal{S}_A$,

$$\mathcal{S}_A = \int_{t'=0}^{t'=T_{21}} \left(\frac{(p_0+\hbar q)^2}{2M} + Mgz\right) dt' \tag{2.79}$$

$$= \left(\frac{p_0^2 + (\hbar q)^2 + 2p_0\hbar q}{2M} + Mgz\right) T_{21}. \tag{2.80}$$

During the second leg B, the kinetic energy of the atom is $\frac{(p_0-\hbar q)^2}{2M}$, so the Lagrangian is

$$\mathcal{L}_B = \frac{(p_0 - \hbar q)^2}{2M} + Mgz,$$

and the action $\mathcal{S}_B$,

$$\mathcal{S}_B = \int_{t'=0}^{t'=T_{21}} \left(\frac{(p_0 - \hbar q)^2}{2M} + Mgz \right) dt' \tag{2.81}$$

$$= \left(\frac{p_0^2 + (\hbar q)^2 - 2p_0\hbar q}{2M} + Mgz \right) T_{21}. \tag{2.82}$$

The phase difference between these paths is

$$\Delta\phi_{\text{path}} = \frac{\mathcal{S}_A + \mathcal{S}_B - \mathcal{S}_0}{\hbar}, \tag{2.83}$$

$$= 2\left(\frac{p_0^2 + (\hbar q)^2}{2M} + Mgz \right) T_{21} - \left(\frac{p_0^2}{2M} + Mgz \right) 2T_{21},$$

$$= \frac{\hbar q^2}{2M} 2T_{21},$$

$$= 2\omega_q T_{21}. \tag{2.84}$$

This allows us to understand the origin of the recoil modulation. It is clear that the expression for $\Delta\phi_{\text{path}}$ does not show a gravitational phase shift because the change in potential energy is identical along both paths.

2.4.2 Light Interaction Phase

We now calculate the phase contributions due to the interaction with the light fields. When an atom interacts with a light field, it is necessary to add a phase term of the

form

$$\phi_{\text{interaction}} = k_{\text{eff}} z_i - \omega_{\text{eff}} t, \tag{2.85}$$

where $k_{\text{eff}} = \pm q$ is the total effective momentum transfer to the atom and ω_{eff} is the difference between the optical frequencies of the excitation pulses. Since we use standing wave pulses, there is no difference in the optical frequencies so that $\omega_{\text{eff}} = 0$. The undiffracted arm of the interferometer does not acquire an interaction phase since the atom did not interact with the light field.

Taking the initial position as zero, the upper arm of the interferometer acquires an interaction phase given by

$$\phi^{\text{U}}_{\text{interaction}} = -2qz^{\text{U}}_2 + qz^{\text{U}}_3. \tag{2.86}$$

With gravity, the position of the vertices are given by

$$\begin{aligned} z^{\text{U}}_2 &= \left(v_0 + \frac{\hbar q}{M}\right) T_{21} - \frac{1}{2} g T^2_{21} \\ z^{\text{U}}_3 &= (v_0 T_{21} + \frac{\hbar q}{M} T_{21} - \frac{1}{2} g T^2_{21}) + \left(v_0 - g T_{21} - \frac{\hbar q}{M} T_{21}\right) T_{21} - \frac{1}{2} g T^2_{21}. \end{aligned} \tag{2.87}$$

Since the echo envelope occurs over a time interval around the echo time $2T_{21}$, we add the parameter Δt at the echo time so that

$$\begin{aligned} z^{\text{U}}_3 &= \left(v_0 T_{21} + \frac{\hbar q}{M} T_{21} - \frac{1}{2} g T^2_{21}\right) + \left(v_0 - g T_{21} - \frac{\hbar q}{M} T_{21}\right)(T_{21} + \Delta t) - \frac{1}{2} g (T_{21} + \Delta t)^2 \\ &= 2v_0 T_{21} - 2g T^2_{21} + \frac{\hbar q}{M} 2T_{21} + \left(v_0 - \frac{\hbar q}{M} - g T_{21}\right) \Delta t + g T_{21} \Delta t + \frac{1}{2} g \Delta t^2. \end{aligned} \tag{2.88}$$

The phase difference is calculated from equation 2.86 to be

$$\begin{aligned}\Delta\phi_{\text{interaction}} &= qg\left(T_{21}^2 + 2T_{21}\Delta t + \frac{\Delta t^2}{2}\right) + \frac{\hbar q^2}{M}2T_{21} - q\left(v_0 - \frac{\hbar q^2}{M}\right)\Delta t \\ &= qg\left(T_{21}^2 + 2T_{21}\Delta t + \frac{\Delta t^2}{2}\right) + 4\omega_q T_{21} - q\left(v_0 - \frac{\hbar q}{M}\right)\Delta t \end{aligned} \tag{2.89}$$

Since the echo signal involves an average over the velocity distribution, the velocity dependent term $q\left(v_0 - \hbar q/M\right)\Delta t$ does not contribute. Therefore

$$\Delta\phi_{\text{interaction}} = qg\left(T_{21}^2 + 2T_{21}\Delta t + \frac{\Delta t^2}{2}\right) + 4\omega_q T_{21}. \tag{2.90}$$

Adding $\Delta\phi_{\text{path}}$ in equation 2.86 and $\Delta\phi_{\text{interaction}}$ in equation 2.90 we obtain

$$\Delta\phi_{\text{total}} = qg\left(T_{21}^2 + 2T_{21}\Delta t + \frac{\Delta t^2}{2}\right) + 6\omega_q T_{21}. \tag{2.91}$$

This equation predicts the same gravitational phase as the quantum mechanical result for the two-pulse AI given in equation 2.39 in the limit of instantaneous pulses, $\tau_1 = \tau_2 = 0$. We note that the recoil modulation phase will occur at integer multiples of $\omega_q T_{21}$ for different closed paths.

2.5 Three-Pulse AI Based on Action Principle

We now apply the action principle to the three-pulse AI. Figure 2.12 shows an example of the interfering trajectories.

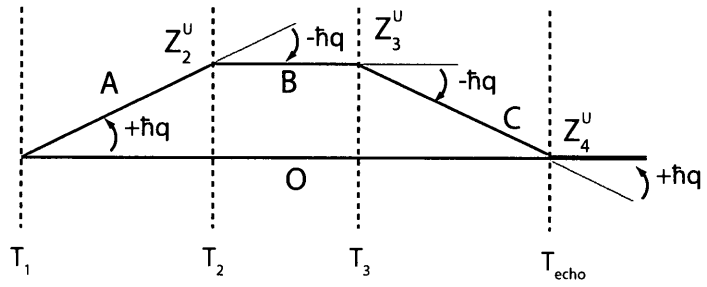

Figure 2.12: One set of recoil trajectories for the three-pulse AI. The diffracted atom travels along the upper paths A, B, and C shown in red, and the undiffracted atom travels along path O shown in black.

2.5.1 Phase Difference due to Path

We consider the effects of initial momentum $p_0 = Mv_0$ and gravity on the action. We now calculate the action along the paths shown in figure 2.12.

The Lagrangian of the undiffracted atom which follows path O is $\mathcal{L} = \frac{p_0^2}{2M} + Mgz$ for all time, and so the action is given by

$$\mathcal{S}_0 = \int_{t'=0}^{t'=2T_{21}+T_{32}} \left(\frac{p_0^2}{2M} + Mgz\right) dt' \tag{2.92}$$

$$= \left(\frac{p_0^2}{2M} + Mgz\right)(2T_{21} + T_{32}). \tag{2.93}$$

The diffracted atom follows three paths A, B, and C. During the first leg, the kinetic energy of the atom is $\frac{(p_0+\hbar q)^2}{2M}$, so the Lagrangian is

$$\mathcal{L}_A = \frac{(p_0+\hbar q)^2}{2M} + Mgz, \tag{2.94}$$

and the action $\mathcal{S}_A$,

$$\begin{aligned}\mathcal{S}_A &= \int_{t'=0}^{t'=T_{21}} \left(\frac{(p_0^2 + \hbar q)^2}{2M} + Mgz \right) dt' \\ &= \left(\frac{p_0^2 + (\hbar q)^2 + 2p_0\hbar q}{2M} + Mgz \right) T_{21}. \end{aligned} \tag{2.95}$$

During the second leg B, the kinetic energy of the atom is $\frac{p_0^2}{2M}$, so the Lagrangian is

$$\mathcal{L}_B = \frac{p_0^2}{2M} + Mgz, \tag{2.96}$$

and the action $\mathcal{S}_B$,

$$\begin{aligned}\mathcal{S}_B &= \int_{t'=0}^{t'=T_{32}} \left(\frac{p_0^2}{2M} + Mgz \right) dt' \\ &= \left(\frac{p_0^2}{2M} + Mgz \right) T_{32}. \end{aligned} \tag{2.97}$$

During the third leg C, the kinetic energy of the atom is $\frac{(p_0 - \hbar q)^2}{2M}$, so the Lagrangian is

$$\mathcal{L}_C = \frac{(p_0 - \hbar q)^2}{2M} + Mgz, \tag{2.98}$$

and the action $\mathcal{S}_C$ is given by,

$$\begin{aligned}\mathcal{S}_C &= \int_{t'=0}^{t'=T_{21}} \left(\frac{(p_0^2 - \hbar q)^2}{2M} + Mgz \right) dt' \\ &= \left(\frac{p_0^2 + (\hbar q)^2 - 2p_0\hbar q}{2M} + Mgz \right) T_{21}. \end{aligned} \tag{2.99}$$

The phase difference between these paths is

$$\Delta\phi_{\text{path}} = \frac{\mathcal{S}_A + \mathcal{S}_B + \mathcal{S}_C - \mathcal{S}_0}{\hbar}, \tag{2.100}$$

$$= 2\left(\frac{p_0^2 + (\hbar q)^2}{2M} + MgzT_{21}\right) - \left(\frac{p_0^2}{2M} + Mgz\right)T_{32} - \left(\frac{p_0^2}{2M} + Mgz\right)(2T_{21} + T_{32})$$

$$= \frac{2\hbar q^2}{M}T_{21},$$

$$= 4\omega_q T_{21}. \tag{2.101}$$

Again, this calculation only gives rise to recoil modulation.

2.5.2 Light Interaction Phase

We now calculate the phase contributions due to the interaction with the light fields. Taking the initial position of the atoms as zero, the upper arm of the interferometer acquires an extra phase

$$\phi^{\text{U}} = -qz_2^{\text{U}} - qz_3^{\text{U}} + qz_4^{\text{U}}, \tag{2.102}$$

while the bottom arm of the interferometer acquires no extra phase. Without gravity, $z_1^{\text{U}} = z_4^{\text{U}} = 0$, and $z_2^{\text{U}} = z_3^{\text{U}}$. Therefore there is no phase difference between the two arms.

In the presence of gravity, the vertices in figure 2.12 are given by

$$
\begin{aligned}
z_2^{\mathrm{U}} =& z_1^{\mathrm{U}} + \left(v_0 + \frac{\hbar q}{M}\right) T_{21} - \frac{1}{2} g T_{21}^2 \\
=& \left(v_0 + \frac{\hbar q}{M}\right) T_{21} - \frac{1}{2} g T_{21}^2 \qquad (2.103) \\
z_3^{\mathrm{U}} =& z_2^{\mathrm{U}} + v_0 T_{32} - \frac{1}{2} g T_{32}^2 \\
=& \left(v_0 T_{21} + \frac{\hbar q}{M} T_{21} - \frac{1}{2} g T_{21}^2\right) + (v_0 - g T_{21}) T_{32} - \frac{1}{2} g T_{32}^2 \qquad (2.104) \\
z_4^{\mathrm{U}} =& z_3^{\mathrm{U}} + \left(v_0 - \frac{\hbar q}{M} - g(T_{21} + T_{32})\right) T_{21} - \frac{1}{2} g T_{21}^2 \\
=& \left(v_0 (T_{21} + T_{32}) + \frac{\hbar q}{M} T_{21} - \frac{1}{2} g T_{21}^2\right) + (v_0 - g T_{21}) T_{32} - \frac{1}{2} g T_{32}^2 \\
&+ \left(v_0 - \frac{\hbar q}{M} - g(T_{21} + T_{32})\right) T_{21} - \frac{1}{2} g T_{21}^2 \qquad (2.105)
\end{aligned}
$$

Since the echo envelope occurs over a time interval around the echo time $2T_{21} + T_{32}$, we add the parameter Δt at the echo time so that

$$
\begin{aligned}
z_4^{\mathrm{U}} =& \left(v_0 (T_{21} + T_{32}) + \frac{\hbar q}{M} T_{21} - \frac{1}{2} g T_{21}^2\right) + (v_0 - g T_{21}) T_{32} - \frac{1}{2} g T_{32}^2 \\
&+ \left(v_0 - \frac{\hbar q}{M} - g(T_{21} + T_{32})\right) (T_{21} + \Delta t) - \frac{1}{2} g (T_{21} + \Delta t)^2 . \qquad (2.106)
\end{aligned}
$$

The phase difference can now be calculated from equation 2.102 to be

$$
\Delta\phi_{\mathrm{interaction}} = qg \left[T_{21}^2 + 2T_{32}T_{21} + 2gT_{32}\Delta t + 4gT_{21}\Delta t + \frac{1}{2}\Delta t^2 + \left(2v_0 - \frac{\hbar q}{M}\right)\Delta t\right] . \qquad (2.107)
$$

Since the echo signal involves an average over the velocity distribution, the velocity dependent term $q\,(2v_0 - \hbar q/M)\,\Delta t$ does not contribute. The sum of the $\Delta\phi_{\mathrm{path}}$ in

equation 2.101 and $\Delta\phi_{\text{interaction}}$ in equation 2.107 gives

$$\Delta\phi_g^{(3)} = qg\left(T_{21}^2 + 2T_{21}T_{32} + (T_{32} + 2T_{21})\Delta t + \frac{1}{2}\Delta t^2\right) + 6\omega_q T_{21}. \tag{2.108}$$

Once again, the gravitational phase calculated from the action is exactly the same as the quantum mechanical result in equation 2.64. The origin of $\Delta\phi_g^{(3)}$ is again seen to be governed by the imprint of the light interaction optical phase on the system dynamics. As for the case of the two-pulse AI in equation 2.91, different sets of closed paths will give different recoil phases.

2.6 Classical Analogies

From the action calculations, it is evident that the $k_{\text{eff}}z$ term in the interaction phase $\Delta\phi_{\text{interaction}}$ was responsible for the gravitational phase terms in equations 2.90 and 2.101. The gravitational phase terms from the action calculation agree with the quantum mechanical calculations. This should not be surprising because both methods calculate the energy imparted to atoms. It is tempting to think of these results as a strict analogy to the classical picture.

2.6.1 Point Particle Optical Phase

This comparison can be made evident by considering the displacement of a point particle with an initial velocity v_0 in a gravitational field over a time $t = 2T_{21}$ in the absence of any interaction with light fields.

In this case, the displacement is given by

$$\Delta z = z_0 + v_0 2T_{21} - \frac{1}{2} g \left(2T_{21}\right)^2 , \tag{2.109}$$

where z_0 is the initial position.

If the displacement is mapped onto the phase of a light field, the corresponding optical phase change $k\Delta z$, is given by

$$\phi = kz_0 + kv_0 2T_{21} - 2kgT_{21}^2.$$

This is not quite the same as the two-pulse AI phase! If the phase shifts of a velocity distribution of particles are considered, then the classical phase will resemble the $\phi_{\mathrm{AI}}^{(2)}$ in equation 2.53. However, the gravitational phase $\phi_g^{(2)}$ in equation 2.45 is the sum of both ϕ_{AI} and ϕ_{D}, whereas equation 2.6.1 is only ϕ_{AI} because of the absence of the ϕ_{D} terms that affect the signal envelope.

To make an analogy with the three-pulse AI, we consider the displacement of a point particle with an initial velocity v_0 in a gravitational field over a time $t = 2T_{21} + T_{32}$.

In this case, the displacement is given by

$$\Delta z = z_0 + v_0(2T_{21} + T_{32}) - \frac{1}{2} g \left(2T_{21} + T_{32}\right)^2 . \tag{2.110}$$

The corresponding optical phase change is $k\Delta z$, which is equal to

$$\phi = kz_0 + kv_0(2T_{21} + T_{32}) - \frac{1}{2} kg(4T_{21}^2 + 4T_{21}T_{32} + T_{32}^2).$$

This expression is also not the same as the three-pulse AI phase in equation 2.64, even after velocity averaging! So we can conclude that the classical picture does

not contain all the details that represent the quantum mechanical interferometer. This is not surprising because a velocity distribution of falling particles is not an interferometer.

2.6.2 Moving Mirror Reflection

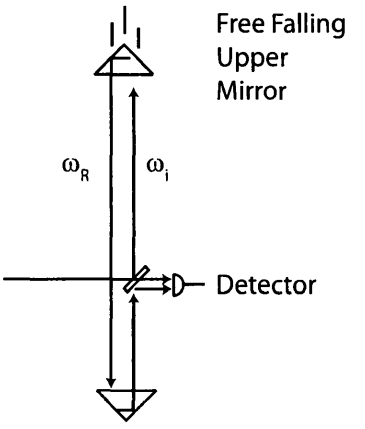

Figure 2.13: Falling corner cube gravimeter. This optical interferometer resembles a Michelson interferometer in which one arm falls in gravity. The incident light has a frequency ω_i and the reflected light has a frequency ω_R.

Since the two-pulse AI is the classical analog of a falling corner cube interferometer shown in figure 2.13 [18], it is instructive to compare the two systems. Assuming no launch velocity, the phase difference between the two arms of the classical interferometer is given by $2\pi/\lambda \times z(t)$, where $z(t) = z_0 + \frac{1}{2}gt^2$. Since $k = 2\pi/\lambda$, the accumulation of fringes is given by

$$\phi = \phi_0 + \frac{kg}{2}t^2. \tag{2.111}$$

The light incident on the mirror with frequency ω_i is Doppler shifted by the moving mirror so that the frequency of the back reflected light is ω_R.

Since this light is re-emitted, the light recorded by the detector will have contributions from two multiplicative Doppler shift terms so that

$$\begin{aligned}\omega_R &= \omega_i \sqrt{\frac{1+v/c}{1-v/c}} \sqrt{\frac{1+v/c}{1-v/c}} \\ &= \omega_i \left(1+\frac{v}{c}\right)\left(1+\frac{v}{c}\right) - \frac{1}{2!}\left(\frac{v}{c}\right)^2 + \frac{1}{3!}\left(\frac{v}{c}\right)^3 \ldots.\end{aligned}$$

Ignoring terms of order $(v/c)^2$ and higher, we obtain

$$\omega_R \approx \omega_i \left(1+2\frac{v}{c}\right). \tag{2.112}$$

The phase shift between the reference beam and the Doppler shifted reflection is:

$$\begin{aligned}\Delta\phi &= (\omega_i - \omega_R)t \qquad (2.113)\\ &= \left[\omega_i - \omega_i\left(1+2\frac{v}{c}\right)\right]t \\ &= 2v\frac{\omega_i}{c}t \\ &= 2(gt)(k)t \\ &= 2kgt^2. \qquad (2.114)\end{aligned}$$

Therefore the chirped accumulation of fringes can also be understood as arising from the Doppler shift. Once again, we see that the signal from the classical optical interferometer is analogous to ϕ_{AI} given by equation 2.53 but not to ϕ_g given by equation 2.45 for the two-pulse AI.

3 Experimental Setup

This chapter contains the experimental details of the optical setup, hardware considerations, and diagnostic measurements. As in most cold atom experiments, this project requires a range of components such as lasers, vacuum systems, optics, analog and digital electronics. The block diagram of the experimental system is shown in figure 3.1. We begin by describing the laser setup located on the laser table as shown in figure 3.2, and then describe the operation of the MOT and its properties. We also describe the atom interferometric setup and the detection method. This chapter also contains technical details of systems that were developed during the course of this experiment. At the end of the chapter, a discussion of methods of phase control and data reduction routines is presented. Figure 3.2 shows the major components of the experiment located on the Laser Table.

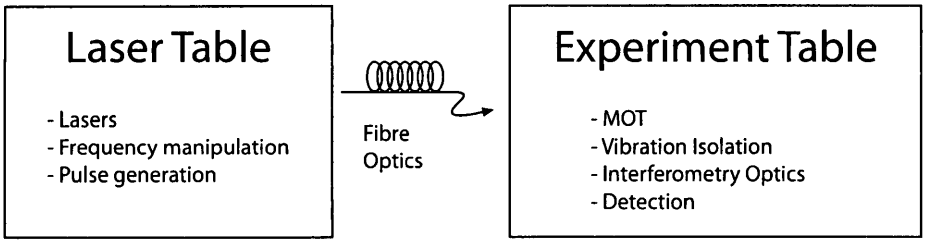

Figure 3.1: Block diagram of the major experimental components.

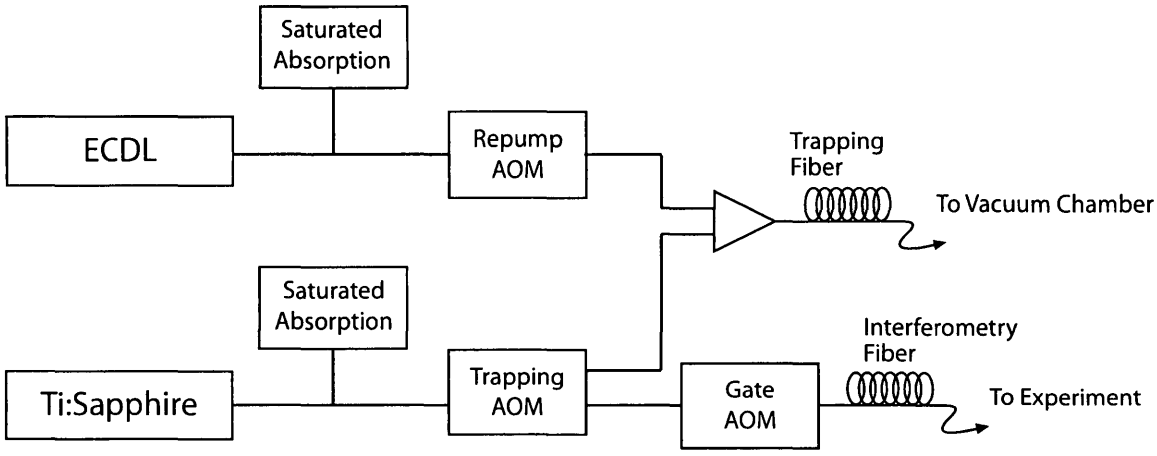

Figure 3.2: Block diagram of setup for frequency generation and amplitude modulation on the Laser Table.

3.1 Lasers

We used a number of laser systems including a Titanium:Sapphire (Ti:Sapphire) ring laser, diode lasers, and a semiconductor tapered amplifier (TA) system. Both commercial and home-built units were used in the experiment.

The master laser for the experiment is a Coherent 899 Ti:Sapphire ring laser operating near 780 nm. This laser system consists of three stages to produce the light used in the experiment. First, diode laser bars produce 800 nm light that enters an Erbium doped optical fibre, producing 1.064 μm light. This is sent to a lithium triborate (LiB_3O_5) frequency-doubling crystal, producing 10 W of light near 532 nm. This light pumps a ring laser with a Ti:Sapphire crystal, producing up to 1.3 W of 780 nm light with a linewidth of approximately 1 MHz. This light was used for atom trapping and atom interferometry.

A commercially manufactured external cavity diode laser (ECDL) is also used to produce repump light[9]. This unit consists of a grating-stabilized ECDL with a power output of 100 mW at 780 nm. The external grating is arranged in a Littrow configuration, where the zero-th order diffraction is the output beam and the first-order diffracted beam is sent back along the incident beam, seeding the diode with a range of selected wavelengths. In this configuration, $\approx$ 20% of the light from the free-running diode is fedback to narrow the laser linewidth, and the remaining 80% of the optical power represents the output of the laser. As a result of the optical feedback from the external cavity, the linewidth of the laser narrows to less than 1 MHz. A modular temperature controller maintains the temperature to a specified value with a long-term drift of less than 2 mK. A separate current controller module ensures that the current to the diode is stable to within 10 μA. A piezo controller allows the laser frequency to be scanned over several GHz, as well as fine-adjusted to within 1 MHz. A feed-forward circuit synchronously varies the current and grating position allowing single-mode operation over the tuning range.

In addition, a home-built ECDL unit uses 785 nm laser diodes often found in compact disc (CD) drives. This laser is again run in a Littrow configuration. This home-built laser produced a typical output power of 30 mW. The temperature controller stabilized temperature fluctuations to within 50 mK, and the current controller

[9]The repump laser is the terminology used to describe the laser that optically pumps atoms from the $F = 2$ ground state to the $F = 3$ ground state in ^{85}Rb through excited states. Similarly, the repump laser pumps atoms out of the $F = 1$ ground state into the $F = 2$ ground state in ^{87}Rb through excited states. Atoms that are optically pumped into these upper ground states will interact with the trapping laser light

stabilized currents to within 50 μA. The home-built ECDL was used to generate off-resonant probe light in the experiment.

Both commercial and home-built Tapered amplifier (TA) systems are used to boost the optical power of several laser beams.

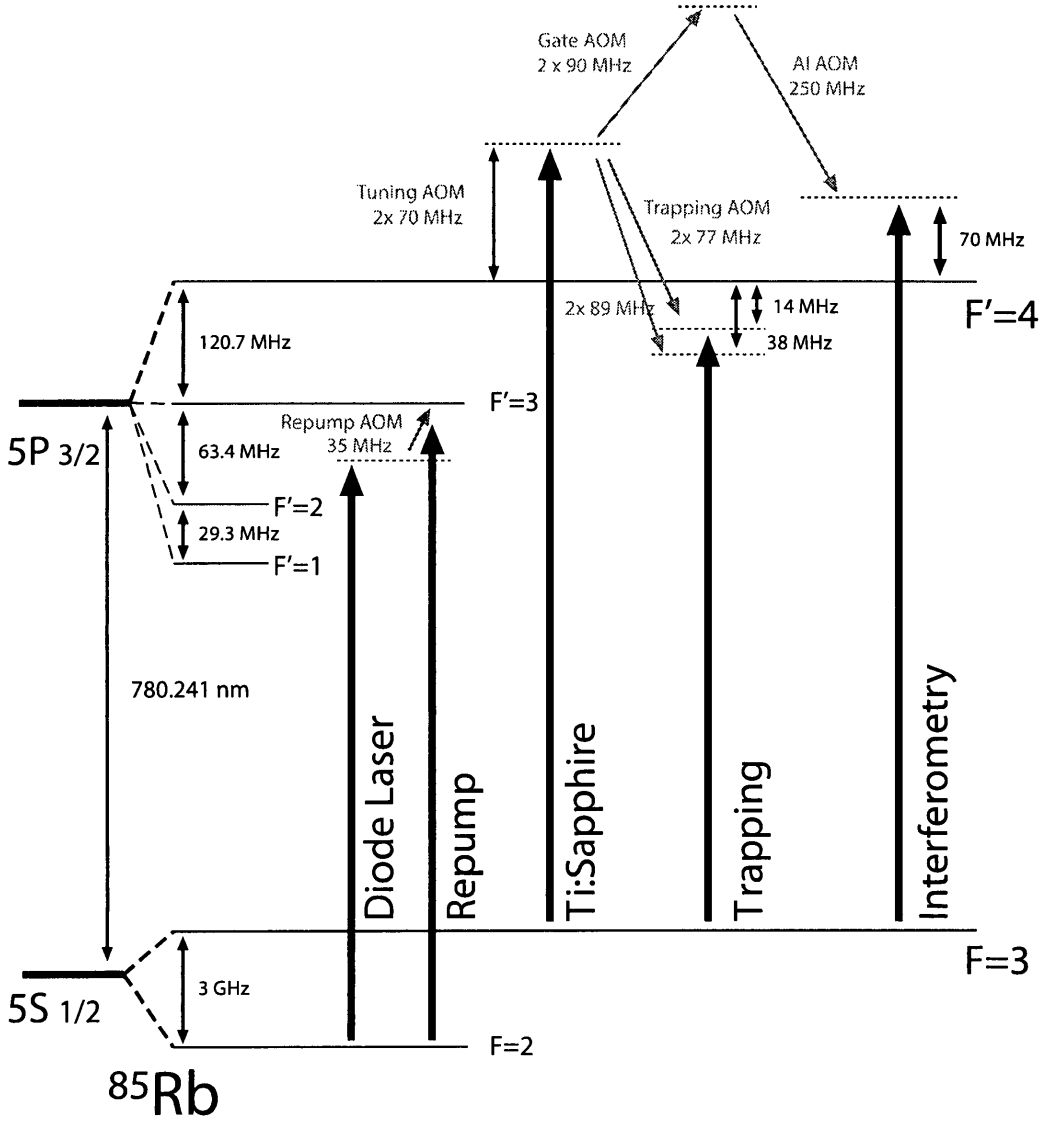

Figure 3.3: Laser frequencies used in the experiment for ^{85}Rb. Laser frequencies generated for atom trapping and interferometry are indicated. Typical AOM drive frequencies are shown in grey.

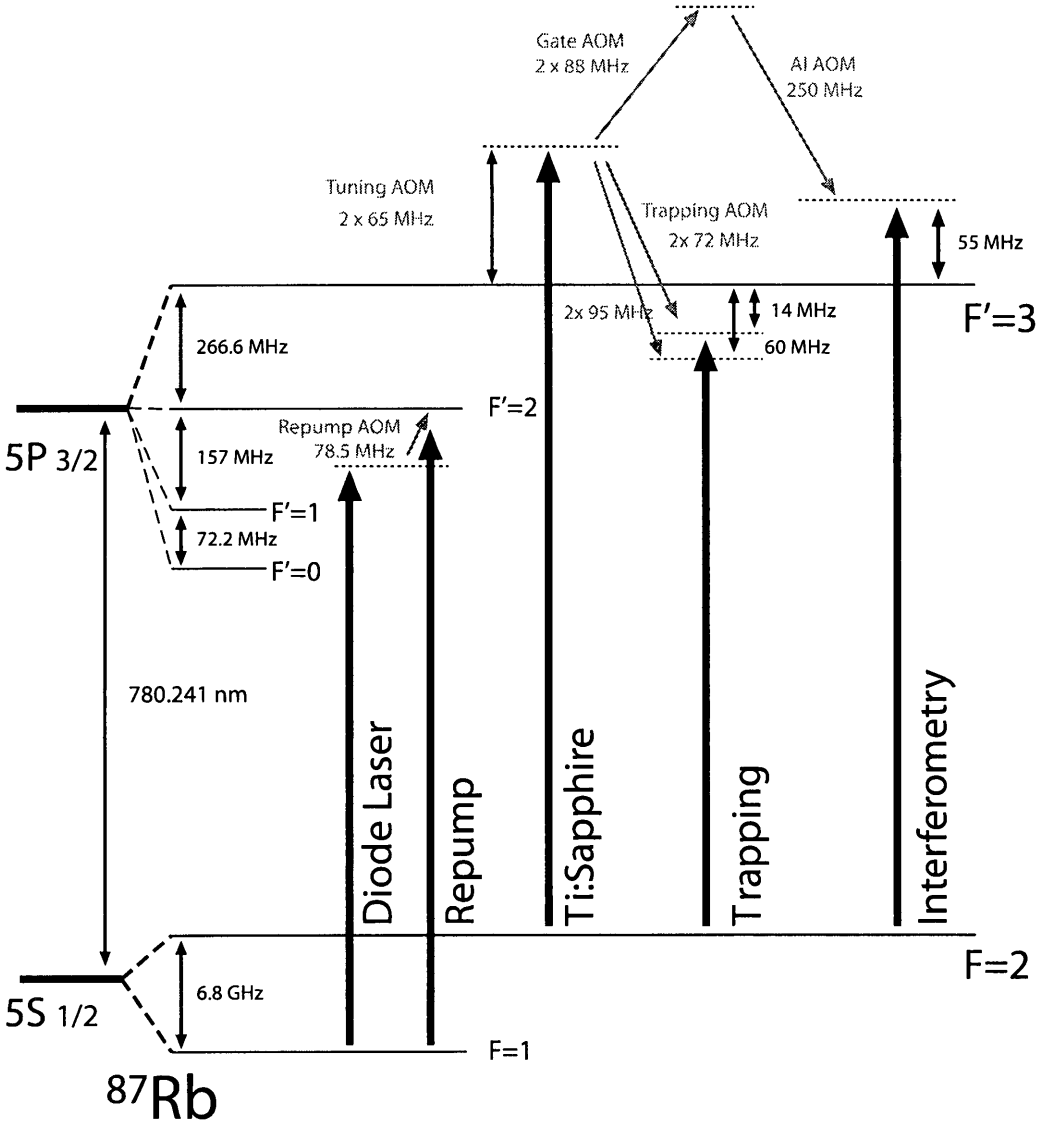

Figure 3.4: Laser frequencies used in the experiment for ^{87}Rb. Laser frequencies generated for atom trapping and interferometry are indicated. Typical AOM drive frequencies are shown in grey.

3.1.1 Trap Laser

An overview of the laser frequencies and tuning elements for the experiment is given in figure 3.3 for ^{85}Rb and in figure 3.4 for ^{87}Rb.

Approximately 35 mW of power from the Ti:Sapphire laser is split off and sent to a saturated absorption setup shown in figure 3.5. This light is sent to the dual-pass Tuning acousto-optic modulator (AOM). Lenses focus the beam into the Tuning AOM and recollimate the twice-diffracted output beam. A quarter-wave plate is placed at the retro-reflecting mirror so that the polarization of the return beam is rotated by 90°, thereby allowing the twice-diffracted beam to reflect off of the second cube. The twice-downshifted beam is incident on a thick glass plate. Two weak probe beams from the front- and back-surface reflections are generated, while the rest of the laser power is transmitted through the plate. The probe beams are sent through a rubidium vapour cell. The strong beam passing through the glass plate is directed to counter-propagate with one of the weak probe beams. The absorption of the probe in the presence of the counter-propagating pump beam shows Doppler-free resonances and crossover peaks, as shown in figure 3.5. The absorption of the single probe beam shows only the Doppler background. Two photodiodes, one running in forward bias and the second running in reverse bias, detect the probe beams. These two signals are summed together by home-built operational-amplifier circuits to remove the Doppler-broadened background. The laser can be locked to a convenient spectral peak. The central frequency of the Tuning AOM can be used to change the overall frequency of the beam directed to the experiment in figure 3.5.

The saturated-absorption setup is used to frequency-lock the Ti:Sapphire to the $F = 3 \rightarrow F' = 4$ transition in ^{85}Rb or the $F = 2 \rightarrow F' = 3$ transition in ^{87}Rb. The

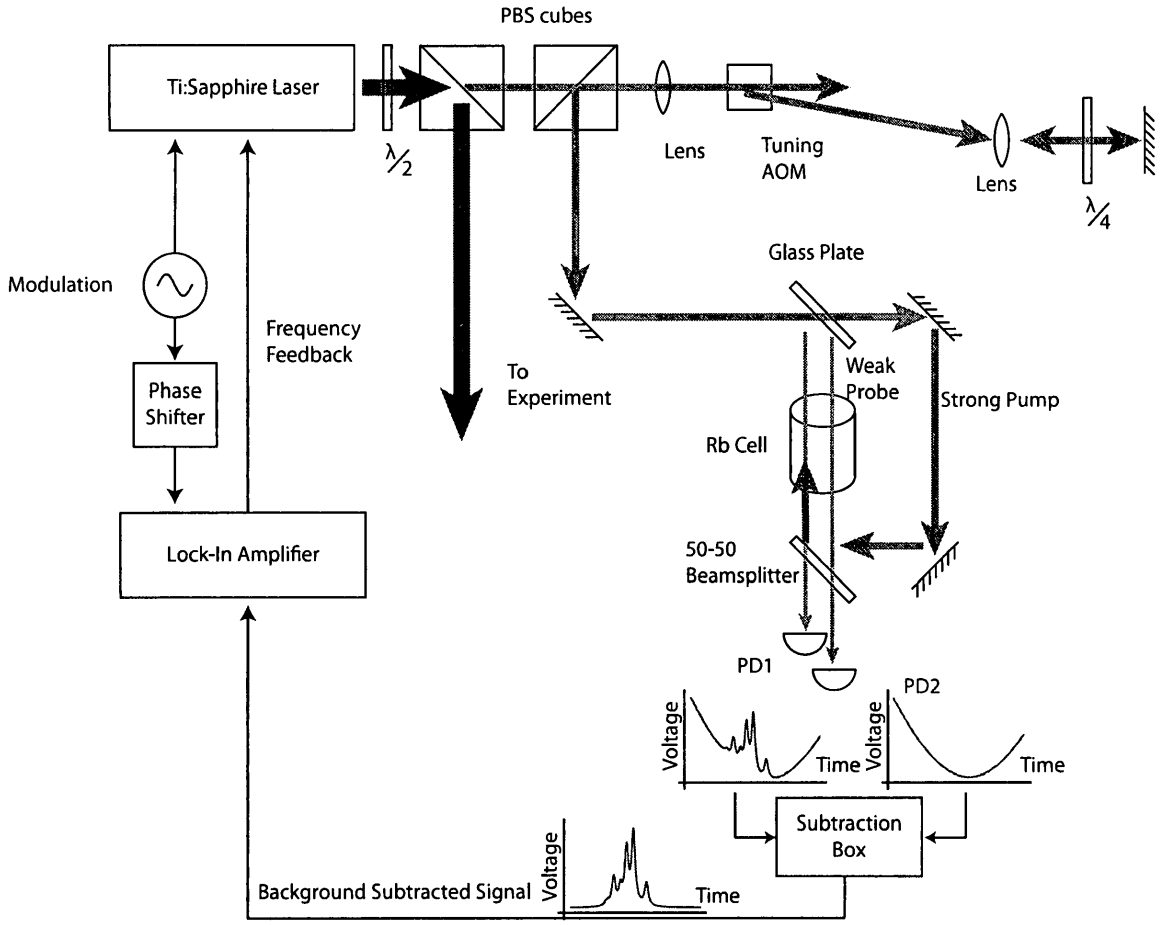

Figure 3.5: Ti:Sapphire saturated absorption setup. The Tuning AOM is driven continuously in the range 65-70 MHz. The downshifted diffracted beam is retro-reflected into the AOM, creating a dual pass setup. The twice downshifted beam is sent to a standard saturated absorption setup. Photodiode 1 (PD1) detects the background Doppler-broadened transitions and Photodiode 2 (PD2) detects the saturated absorption signal. The laser is locked to the $F = 3 \rightarrow F' = 4$ transition in ^{85}Rb or to the $F = 2 \rightarrow F' = 3$ transition in ^{87}Rb.

locking is accomplished using a lock-in amplifier. The Ti:Sapphire laser frequency is modulated by a voltage applied to a piezo-actuated mirror and a scanning Brewster plate that change the path length of the lasing cavity. The frequency of modulation is typically 5 kHz. The amplitude of the modulation is adjusted so that the typical

frequency excursion of the laser is up to 500 kHz. The modulated signal from the photodiode in the saturated absorption setup is mixed down to DC with modulation voltage sent to the laser using a lock-in amplifier. The lock-in amplifier generates an error signal that is fed back to the laser. The typical stability of the laser lock is about 500 kHz, as inferred by the variation in the absorption of the laser beam in the vapour cell used for saturated absorption. This locking scheme ensures that the laser beam directed to the experiment in figure 3.5 is tuned to $\omega_0 + 140$ MHz for ^{85}Rb or $\omega_0 + 130$ MHz for ^{87}Rb.

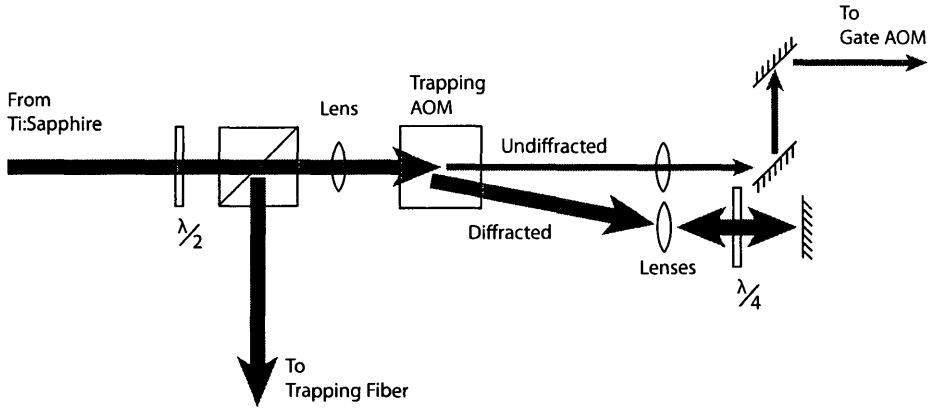

Figure 3.6: The Trapping AOM is operated in dual-pass mode at 77 MHz for ^{85}Rb and 72 MHz for ^{87}Rb. The twice downshifted beam is sent to the trapping fibre. A telescope placed in the input beam for the setup increases the efficiency of the AOM in the Bragg regime. The undiffracted beam is sent to the Gate AOM. This light is available for atom interferometry after the Trapping AOM is turned off.

Most of the Ti:Sapphire laser output is sent to the Trapping AOM, as shown in figures 3.2 and 3.6. This AOM operates in a dual-pass configuration and imposes a total downshift on the input beam to generate an output beam ≈ 14 MHz below the cycling transition ($F = 3 \rightarrow F' = 4$ transition in ^{85}Rb or $F = 2 \rightarrow F' = 3$ transition

in ^{87}Rb). The output beam is detuned by approximately twice the natural linewidth Γ_N to maximize the laser cooling force and the number of atoms loaded into the atom trap. The typical efficiency of the dual-pass AOM setup is 50%. Another purpose of the Trapping AOM is to amplitude-modulate the trapping beams. The output beam is sent to the coupling optics for the trapping fibre.

3.1.2 Repump Laser

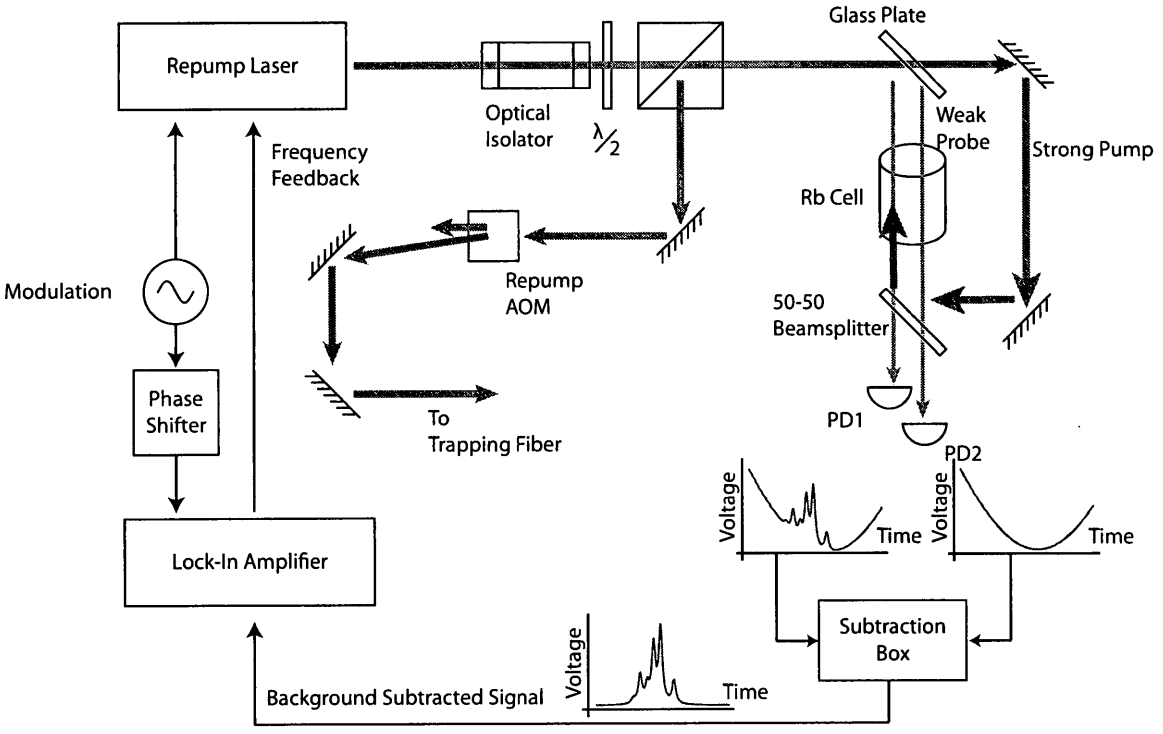

Figure 3.7: Repump laser setup. An ECDL is used as the repump laser. An optical isolator is placed at the laser output to protect the laser from back reflections. A small portion of the laser light is sent to a standard saturated absorption setup. Most of the laser light is sent to the Repump AOM operating at 35 MHz for ^{85}Rb, or 78.5 MHz for ^{87}Rb. The upshifted beam, which is on resonance with the $F = 2 \rightarrow F' = 3$ transition in ^{85}Rb or the $F = 1 \rightarrow F' = 2$ transition in ^{87}Rb, is combined with trapping light on an optical fibre.

In ^{85}Rb, atoms excited into the $F' = 3$ excited state by the trapping beams may decay into the $F = 2$ ground state, in which case they will no longer be addressed by the trapping laser. Similarly, in ^{87}Rb, atoms excited into the $F' = 2$ excited state by the trapping beams may decay into the $F = 1$ ground state, in which case they will no longer be addressed by the trapping laser.

A separate laser is required to cycle atoms out of the lower ground state. This is achieved by using a commercially-available ECDL tuned to the $F = 2 \rightarrow F' = 3$ transition in ^{85}Rb or the $F = 1 \rightarrow F' = 2$ transition in ^{87}Rb. The excited states of these transitions can decay back to the ground states of the cycling transitions. This laser is referred to as the repump laser. This laser produces a typical output power of 60 mW.

For frequency locking purposes, a small portion of the repump beam is coupled into a saturated absorption setup. The saturated absorption setup is identical to the saturated absorption setup for the Ti:Sapphire laser. The repump laser is locked to the $F = 2 \rightarrow F' = 2, 3$ crossover peak in ^{85}Rb or to the $F = 1 \rightarrow F' = 1, 2$ crossover peak in ^{87}Rb. The laser frequency is modulated by driving both the current and grating at a typical frequency of 1.2 kHz. The typical stability of the laser lock is about 1 MHz, as inferred by the variation of the absorption in the vapour cell used for saturated absorption.

Most of the repump light is sent to the Repump AOM, as shown in figure 3.7. This AOM operates at 35 MHz for ^{85}Rb and 78.5 MHz for ^{87}Rb, upshifting the

repump beam directly onto resonance with the $F = 2 \rightarrow F' = 3$ transition in ^{85}Rb or the $F = 1 \rightarrow F' = 2$ transition in ^{87}Rb. The purpose of the Repump AOM is to amplitude-modulate the output, which is combined with the trapping beam on an optical fibre.

3.1.3 Tapered Amplifiers

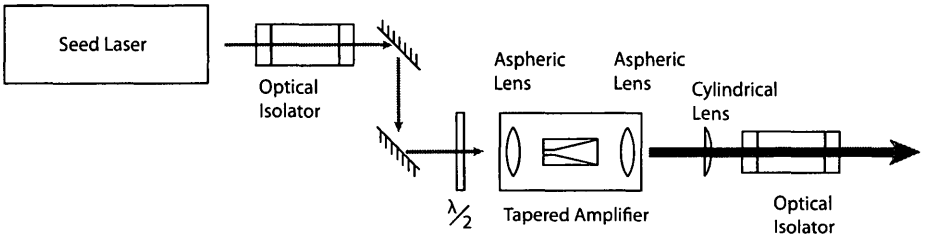

Figure 3.8: Tapered amplifier setup. The seed beam can originate from any narrow linewidth laser as the TA does not change the coherence properties of the beam. The half-wave plate before the TA is used to mode match the polarization of the seed beam to the TA cavity. The output aspheric lens collimates the beam along one axis, and the cylindrical lens collimates the beam along the perpendicular. A second optical isolator is used to protect the TA from unwanted back reflections.

Semiconductor tapered amplifiers (TAs) were used to boost the power of various beams. Typical TA gains are of the order of 15 dB, or 30 fold, with an injection current of 2 A and a seed power of 30 mW. This system provides a typical power output of 700 mW with the same wavelength and linewidth characteristics as the seed beam. Both commercial and home-built TAs were used. An example of a typical setup is shown in figure 3.8. The half-wave plate is adjusted to match the polarization acceptance of the TA cavity. The seed beam is focused into the TA chip

by a very short focal length aspheric lens, and the output is collimated in one axis by a second identical aspheric lens. However, the increase in power comes at a cost since the output divergences along the axes perpendicular to the direction of propagation are no longer equal, and the beam profile is highly distorted.

An aspheric lens collimates the output of the TA cavity in one axis and a second cylindrical lens is used to collimate the perpendicular axis. Even if the input to the TA is a Gaussian beam, the output of the TA has a square shape and a flat-top diffraction pattern. Furthermore, the beam has a diffuse and spectrally broad background due to amplified spontaneous emission from the TA waveguide. Characteristics of the home-built units are summarized in figure 3.9.

Figure 3.9a shows the thermal characteristics of a home-built unit. A thermo-electric cooler moves heat from the TA chip assembly to a large thermal mass heat sink. Water cooling is applied to the heat sink to increase the removal of heat from the laser system. The higher the injection current, the more power the cooling system draws to maintain a steady temperature. Figure 3.9b shows the amplified spontaneous emission output power of a TA system as a function of injection current without seeding the TA. The amplified spontaneous emission constitutes a spectrally broad, spatially diffuse background. The power law dependence of the output amplified spontaneous emission shows a characteristic nonlinear behaviour in figure 3.9b. Figure 3.9c shows a histogram of the output power of a TA. Typical output power stability of

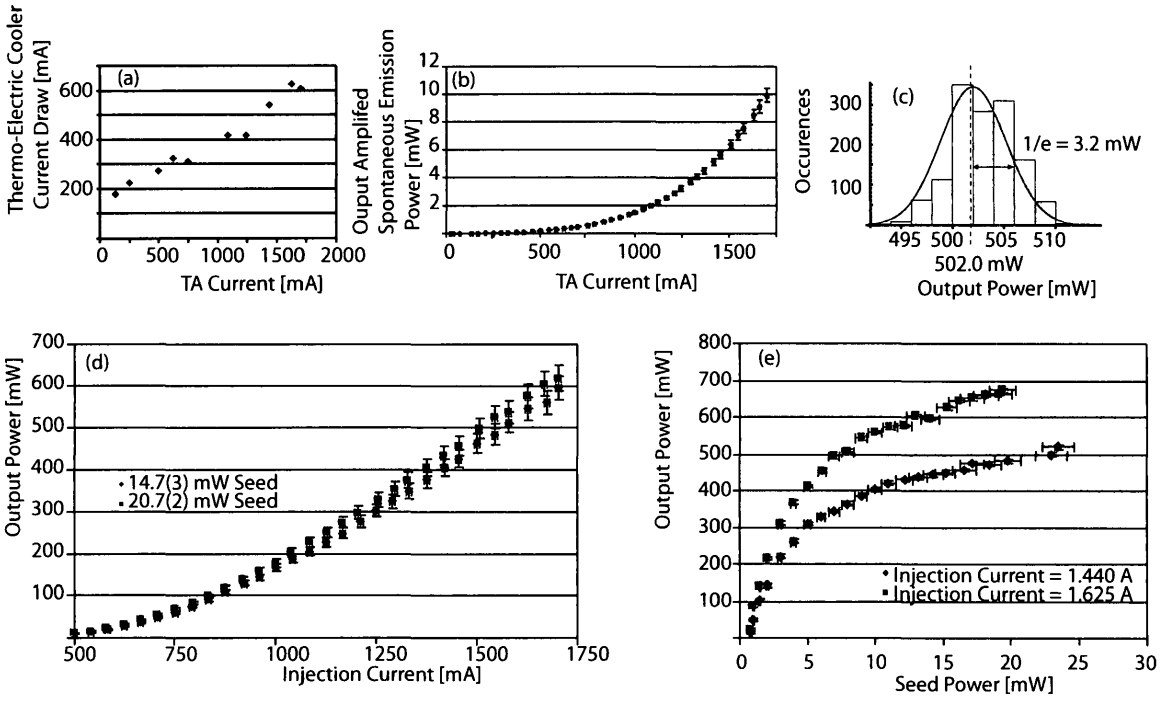

Figure 3.9: The home-built TAs used Eagle-Yard EYE-TPA-0780 waveguides. The characterization for chip serial DA-01151 is shown here. (a) Thermal characteristics of a home-built TA system. The higher the injection current, the higher the cooling system power required. (b) Typical amplified spontaneous emission output power of a TA system as a function of injection current. (c) Typical power stability of 0.6% over 50 s with an input power fluctuation of 0.5%. (d) Typical output power of a TA system as a function of injection current. (e) Typical output power of a TA system as a function of seed power.

a TA system over 50 s is 0.6% with an input power stability of 0.5%[10]. This data set was acquired with a 250 Hz sample rate. Figure 3.9d shows the output power of a TA system as a function of injection current. Two seed powers are shown: 14.7(3) mW in blue diamonds, and 20.7(2) mW in red squares. The minimum current is set to 500 mA to avoid damage as the chip becomes transparent only when current is

[10]The variances in power of the input beam and output beam were measured separately at different times.

flowing. The marginal increase in power per unit injection current is highest at higher currents. The maximum current characterized was limited to 1.75 A to stay well below the damage threshold of 2 A. Figure 3.9e is a plot of the typical output power of a TA system as a function of seed power. Two injection currents are shown: 1.44 A in blue diamonds, and 1.625 A in red squares. The square root type dependency of output power as a function of seed power gives reduced marginal increases in power at high seed powers. The maximum seed power was chosen to be 25 mW to stay well below the damage threshold 40 mW.

3.2 Magneto-Optical Trapping

3.2.1 Trapping Beams

The trapping and repump beams are combined on a beam splitter and coupled into a commercially fabricated, angle-cleaved, anti-reflection (AR) coated optical fiber as shown in figure 3.10.

Each beam passes through a separate telescope to adjust the beam size and divergence for optimal fibre coupling. These two beams are cross polarized by half-waveplates and combined on a polarizing cube beam splitter. The fibre is a non-polarization-maintaining, single-mode optical fibre. As such, the fibre accepts any transverse polarization with a typical coupling efficiency of 50%. The typical output power is 300 mW for the trapping beam and 25 mW for the repump beam. The fibre maintains the cross polarization of the beams, but not the initial orientation of the

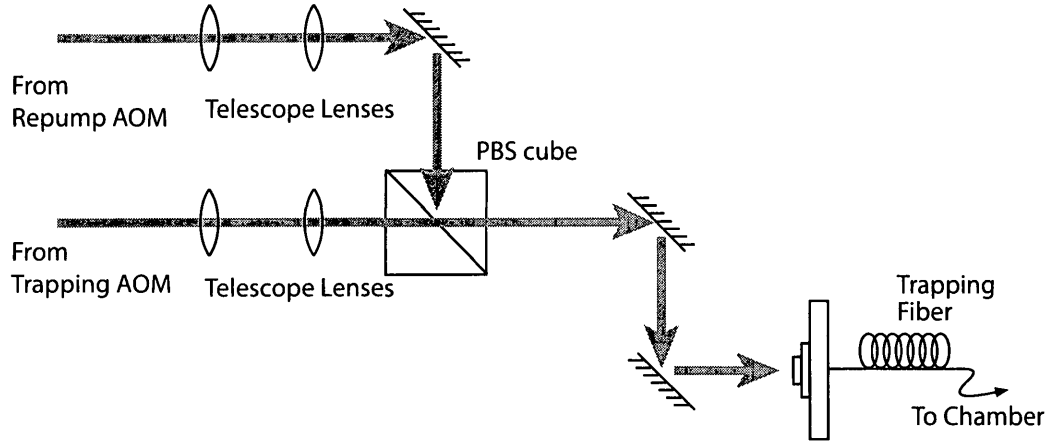

Figure 3.10: Trapping and repump laser beam combination. Two separate telescopes match the divergences of the lasers for maximum coupling efficiency into the trapping fibre. The trapping beam is transmitted through a polarizing beam splitting cube, and the repump beam is reflected off a polarizing beam splitting cube to ensure cross polarized beams.

polarization.

As shown in figure 3.1, the fibre guides the light from the Laser Table to the Experiment Table. The setup near the vacuum chamber is shown in figure 3.11. The fibre output is collimated to a diameter of 5 cm, and a half-wave plate resets the polarization of the trapping beams. The fibre output is evenly split into three orthogonal axes and routed to the trapping chamber. Unfortunately, the trapping beams become elliptical with an aspect ratio of $\sqrt{2}$ due to the orientation and sizes of the steering mirrors. Nevertheless, the average diameter of the trapping beams is greater than 4 cm. Quarter-wave plates are used to produce circularly polarized incident beams. The beams are aligned through the chamber with AR-coated view-ports and then pass through $\lambda/4$ plates. These beams are retro-reflected to create

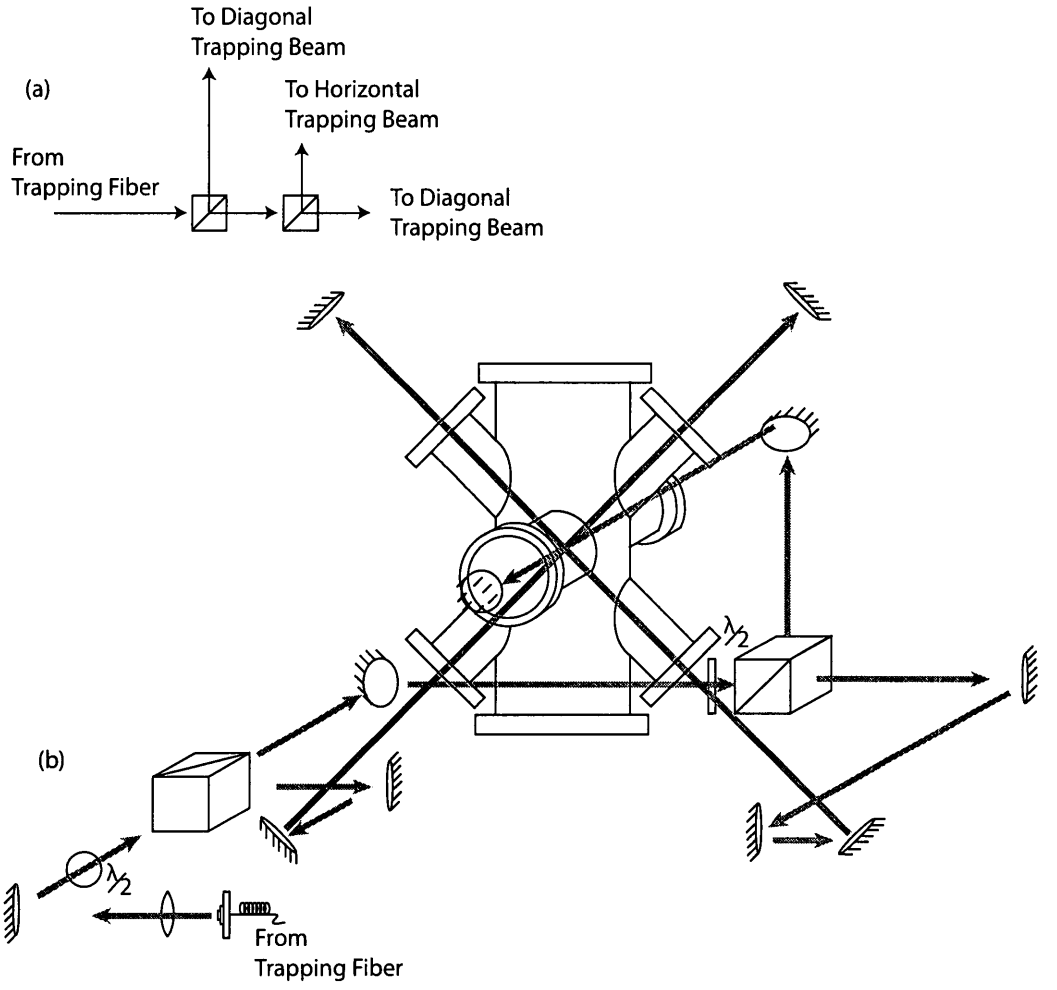

Figure 3.11: (a) Schematic describing power split of the trapping beams. (b) Trapping laser beam configuration. Light from the combination optics in figure 3.10 is guided to a separate optical table by a fibre. The fibre output is collimated by a two inch diameter lens. Half-wave plates and polarizing beam-splitting cubes divide the trapping laser light into three beams. Mirrors direct these three beams along orthogonal axes. Quarter-wave plates (not shown) at the entrances of the vacuum chamber circularly polarize the beam.

three pairs of counter-propagating beams. Each pair of counter-propagating beams consists of circularly polarized travelling waves with opposite angular momentum.

3.2.2 Vacuum Hardware

The vacuum chamber is made from 316 L stainless steel, with optical access, as shown in figure 3.12. Eight viewports are equally spaced at 45° intervals along the horizontal plane. Two sets of 4.5 inch diameter ConFlat (CF) viewports with 2.5 inch viewing diameters are used for the trapping beams. The four remaining viewports in the horizontal plane, which have 2.5 inch diameters and 1.5 inch viewing diameters, are used to monitor the trap. A CCD camera monitors the position and orientation of the trap, and the number of atoms is inferred by detecting fluorescence from atoms using a photomultiplier tube (PMT).

The vertical viewports with 6 inch viewing diameters provide optical access for atom interferometry. Two coils, each with 285 turns, are wound on a tapered form fitted to the vertical axis of the chamber and connected in an anti-Helmholtz configuration, where the centers of the coils are placed at a distance equal to the radius of the coil to provide the magnetic gradient required for trapping atoms. The average radius of the coils is 7.5 cm, and the vertical separation between the closest ends of the tapered forms is 7.1 cm. The typical operating gradient is 11.6 G/cm.

The vacuum is maintained by an ion pump with a pumping speed of 270 L/s. The pump is located at a distance of 1 m from the trapping chamber to reduce the effect of magnetic fields from the pump magnets. A rubidium ampoule is mildly heated above room temperature to provide rubidium vapour.

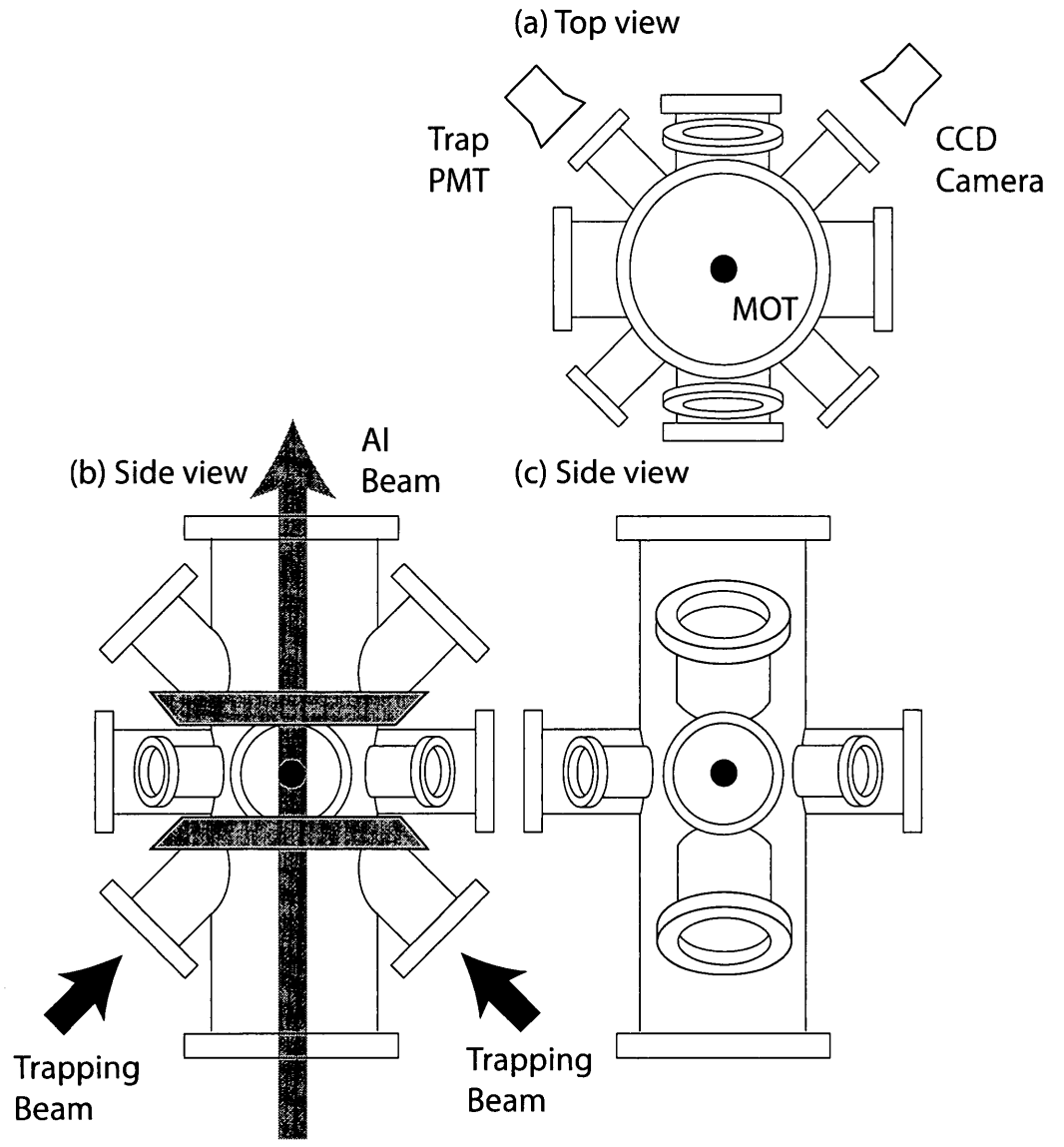

Figure 3.12: Diagram of the vacuum chamber used in the experiment. It is made from 316 L steel and optical access is provided through numerous viewports. The outline of the tapered forms of the anti-Helmholtz coils is shown in (b).

The number of atoms loaded into the trap, N, obeys the differential equation

$$\frac{dN}{dt} = R - \gamma N, \tag{3.1}$$

where R is the loading rate from the background vapour and γ is the collisional rate

for hot background atoms colliding with cold atoms. The solution of this differential equation is $N(t) = N_{SS}(1 - e^{-\gamma t})$, where N_{SS} is the steady-state number of atoms, so that γ can be identified as the collisional rate of background atoms. The collisional rate is given by

$$\gamma = n\sigma v. \tag{3.2}$$

Here, the number density of the background vapour n is given by the ideal gas law,

$$n = \frac{N}{V} = \frac{P}{k_B \mathcal{T}}, \tag{3.3}$$

where P is the pressure and $\mathcal{T}$ is the temperature of the background gas. The relative velocity of the colliding atoms v is overwhelmingly determined by the speed of the background atoms, and $\sigma \approx 3 \times 10^{-17}$ m^2 [120] is the cross sectional area for collisions.

The vapour pressure of rubidium at room temperature is 3×10^{-7} Torr. Typically, the entire vacuum system equilibrates at a rubidium vapour pressure of approximately 5×10^{-9} Torr. The observed loading time of the trap under these conditions is ≈ 5 s. Under these conditions, the calculated rate for Rb_{hot} - Rb_{cold} collisions is of order one per second per atom. Under these conditions, the effect of collisions is not significant during the 100 ms time scale of the experiment.

The chamber is surrounded by three pairs of magnetic field and magnetic gradient cancelling coils with an orientation as shown in figure 3.13. Another set of coils consisting of three pairs are wound on the same frames with oppositely directed currents and used for magnetic gradient cancellation. There are 120 turns for the vertical field cancelling coils and 60 turns of the horizontal field cancelling coils.

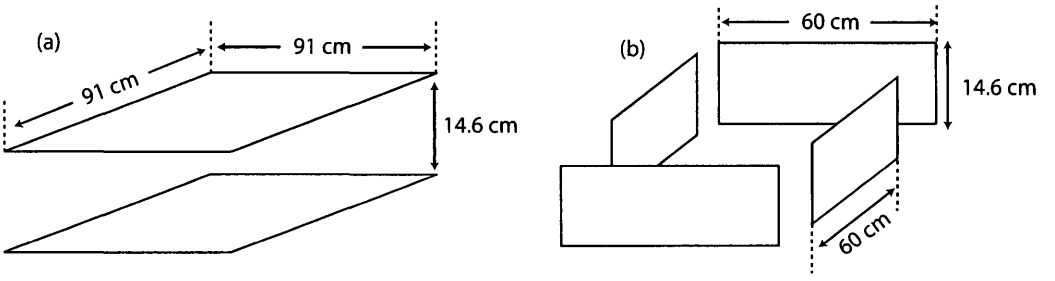

Figure 3.13: Orientation of (a) vertical and (b) horizontal magnetic cancelling coils surrounding the vacuum chamber. Both field and gradient coils are wound on the same frames.

There are 40 turns in all gradient cancelling coils.

3.2.3 Trap Timing

We load approximately 5×10^8 ^{85}Rb atoms in the MOT in 300 ms and turn off the trapping magnetic gradient in 0.4 ms using an IGBT[11] switching circuit. We then turn off the trapping beams in 100 ns and perform the AI experiment while the atoms expand and fall in gravity. The repetition rate for this procedure varies from 0.8 to 3 Hz. The trapping pulse sequence is shown in figure 3.14.

Optical pulses are generated by pulsing the RF used to drive the AOMs using digital delay generators. The electronic pulse sequence shown in figure 3.14 is produced by a single delay generator. The initial loading of the MOT is carried out for 300 ms with the trapping beams at a frequency $2\Gamma_N$ below resonance, where $\Gamma_N = \Gamma/2\pi \approx 6$ MHz. The magnetic field gradient is turned off by an IGBT module

[11] An IGBT combines the ease of voltage control of a MOFSET and the high current handling capabilities of a transistor in a single package.

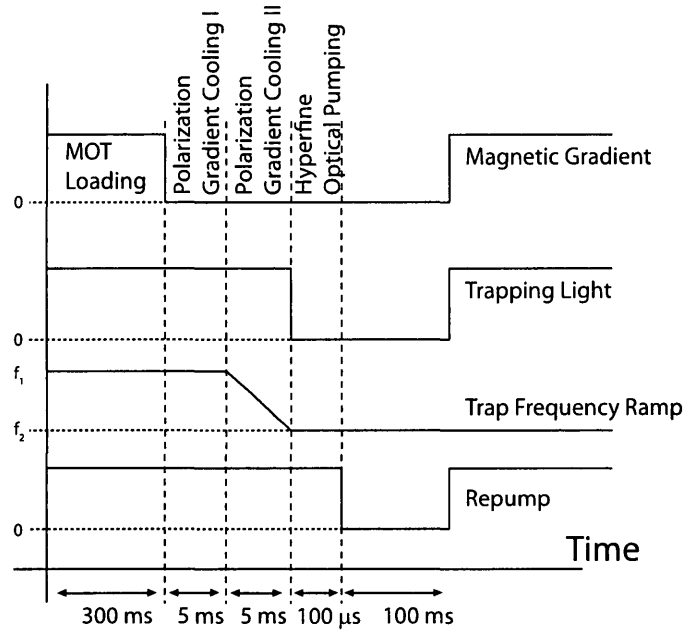

Figure 3.14: Schematic of trapping pulse sequence. The MOT loading stage occurs during the first 300 ms time window. The magnetic gradient coils are turned off, further cooling the atoms in an optical molasses in the first stage of polarization gradient cooling. Then the frequency of the trapping beams is ramped further off resonance to further cool the atoms in the second stage of polarization gradient cooling. The trapping beams are extinguished and the repump light remains on for a further 100 μs to ensure that the atoms are optically pumped into the upper hyperfine ground state.

with a switching time of less than 500 μs. Details of the IGBT module are shown in Appendix B. After the turn-off of the magnetic gradient, the atoms in the MOT are cooled in an optical molasses for 5 ms. Next, the Trap AOM frequency is ramped further below resonance by $5 - 10\Gamma_N$ to cool atoms further in the optical molasses for another 5 ms. After this phase, the trapping laser is extinguished, and the repump laser remains on for 100 μs to ensure that the atoms are fully pumped into the $F = 3$ ground state in ^{85}Rb or $F = 2$ ground state in ^{87}Rb.

The RF electronics used to generate the trapping AOM drives consist of tunable,

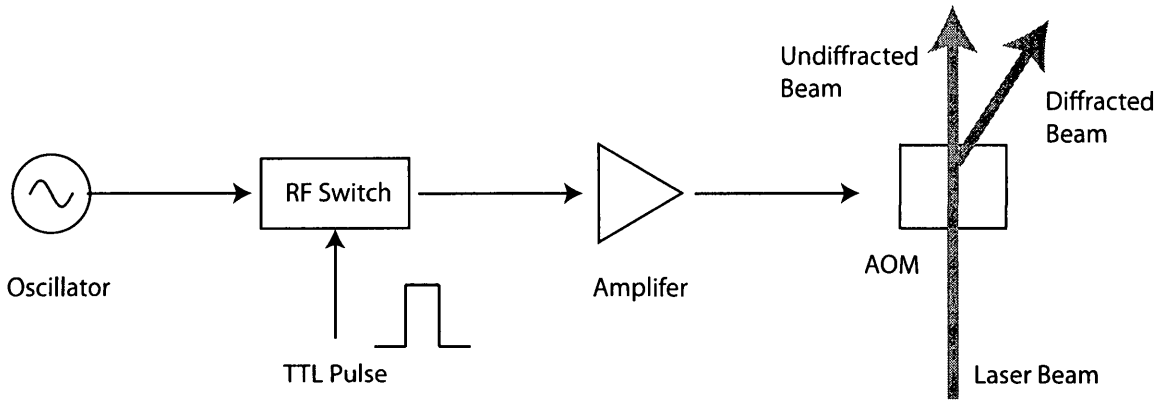

Figure 3.15: Schematic of RF and light pulse generation. The RF switch gates the output of the continuous oscillator to send a pulse of RF to the amplifier. The pulse of RF is sent to the AOM, which in turns generates a pulse of light along the diffracted beam.

free-running voltage-controlled oscillators (VCOs) and TTL switches, as shown in figure 3.15. Powered, high-isolation, TTL switches were used to produce RF pulses with an on/off power ratio of 10^9. The RF pulses were amplified, and used to drive the AOMs, creating RF pulses with rise times of less than 10 ns. The corresponding optical pulses have extinction ratios of greater than 10^6 and rise times of order 10 ns.

3.2.4 Trap Imaging

A CCD camera monitors the position and orientation of the trap. A PMT detects the fluorescence from trapped atoms, giving a measurement of the number of trapped atoms.

The CCD can be operated in a 60 Hz continuous mode as well as in a triggered mode. The continuous video stream is sent to a TV monitor to provide visual monitoring of the trap. The triggered mode of the camera is used to obtain images of the

trap at specific times. The trigger pulse opens the electronic shutter of the CCD and the exposure time is controlled by the pulse length. The trigger pulse is also sent to a computer, signaling the electronics to accept the next incoming frame. An example of an image is shown in figure 3.16. By measuring the trap radius as a function of the free expansion time of the atomic sample, the temperature of the trap can be inferred. The temperature of the cloud, determined by photographing the time-of-flight expansion using a CCD camera, is typically 20 μK [121].

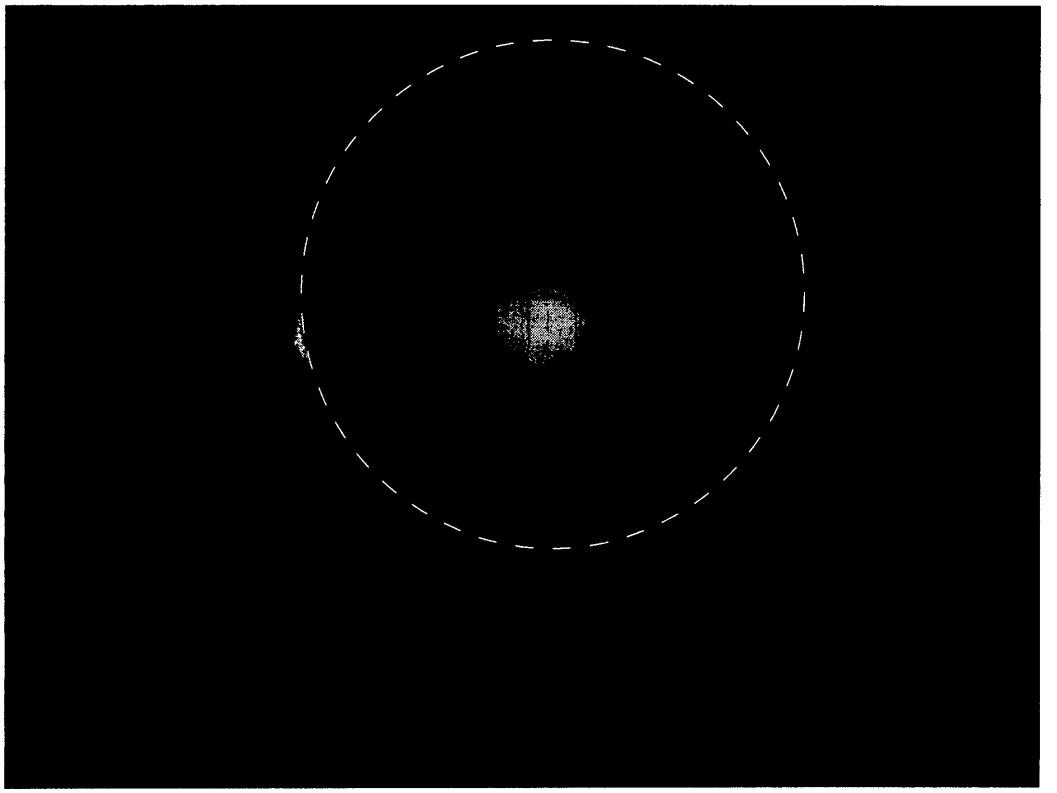

Figure 3.16: Image of the MOT obtained after 1 ms of expansion. The typical diameter of the MOT at this time is 3 mm. The shadow of the viewport is shown as a dashed ring around the cloud of atoms.

A series of time-of-flight images was acquired after the trapping beams were extin-

guished. For each of these images, the free expansion time was varied. The trapping and repump beams were turned on again at the same time the camera was triggered for less than 50 μs. This allowed the trap to be imaged via fluorescence. The images were averaged four times and stacked to obtain the final image.

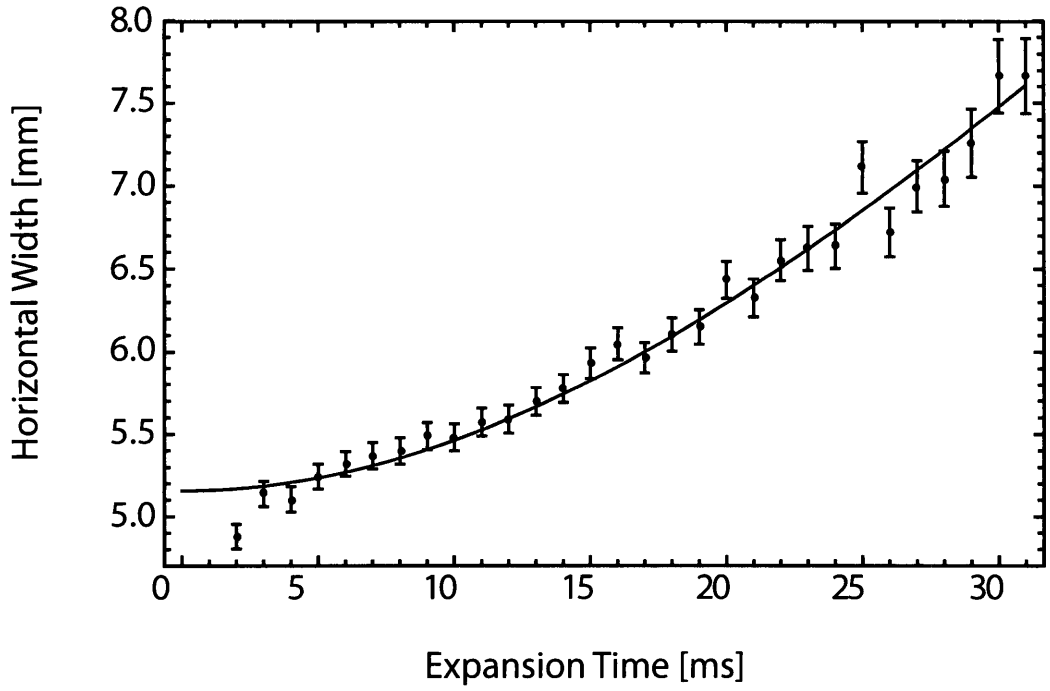

Figure 3.17: $1/e$ radius of the atomic cloud as a function of expansion time. The fit to the data is used to extract the initial trap size and the most probable speed of the atoms. A fit to the form $\sqrt{R_0^2 + (v_0 t)^2}$ gives the parameters $R_0 = 3.9(1)$ mm and $v_0 = 9.2(2)$ cm/s, resulting in a temperature of 20 μK.

The cloud radius was extracted by fitting the spatial profile of the trap with a Gaussian function. The expansion of the cloud in the horizontal direction is shown in figure 3.17. A fit to the hyperbolic form

$$R(t) = \sqrt{R_0^2 + (v_0 t)^2}$$

was used to extract the initial size of the cloud, R_0, and the most probable speed of the atoms, v_0. The temperature $\mathcal{T}$ is determined using the equipartition theorem as

$$\mathcal{T} = \frac{M v_0^2}{k_B}.$$

3.2.5 Atom Counting

A lens with focal length f was placed at a distance $2f$ from the trap to image the MOT on a PMT placed at a distance $2f$ from the lens. By using this technique, the field of view of the PMT is limited to a small volume around the trap, thereby minimizing background light. The radiative rate of the cycling transition in rubidium can be used to infer the rate of photons scattered from the trap per second. Using the geometrical solid angle subtended by the imaging lens, the detector gain, and collection efficiencies, it is possible to calculate the number of atoms in the trap.

The fraction of atoms excited by the trapping beams f is given by

$$f = \frac{1}{2} \frac{I/I_{\rm sat}}{1 + \frac{I}{I_{\rm sat}} + \left(\frac{2\Delta}{\Gamma}\right)^2},$$

where I is the intensity of the trapping beams, and $I_{\rm sat}$= 3.895 mW/cm^2 is the saturation intensity for equally populated ground state sublevels. For the $F = 2 \rightarrow F' = 3$ cycling transition, the atomic cloud is excited by three pairs of $\sigma^+ - \sigma^-$ beams. The polarization of the light is isotropic with respect to any quantization axis. Therefore we use the saturation intensity corresponding to equally populated sublevels. Typically 300 mW of power distributed over the the elliptical shape of the incident trapping beams and retro-reflected beams gives an intensity of 42 mW/cm^2.

The detuning of 15 MHz and the radiative rate of 3.61×10^7 rad/s gives the fraction of atoms excited to be $\approx 23\%$.

The collection of the photons emitted by the trap is limited by the geometry of the detection system. The smallest aperture at a distance of 9 cm along the axis of the PMT has a diameter of 2.54 cm. Therefore the fraction of photons collected, $\mathcal{F}$, is 0.4%. An independent calibration of the PMT gives a responsivity of $R = 2.4$ MV/W (or 2.4 A/W with 1 MΩ termination).

Combining these results, the signal S (in volts) from N atoms is given by

$$Nf\frac{hc}{\lambda}\Gamma\mathcal{F}R = S.$$

This procedure gives a calibration of 321×10^6 atoms/Volt. A typical reading of 1.6 V on the PMT corresponds to 0.5 billion atoms. The variation of the beam intensity across the trap, along with the uncertainties of other dimensional measurements combine in quadrature for an estimate of the uncertainty of the atom number to be $\pm 10\%$.

3.3 Atom Interferometer

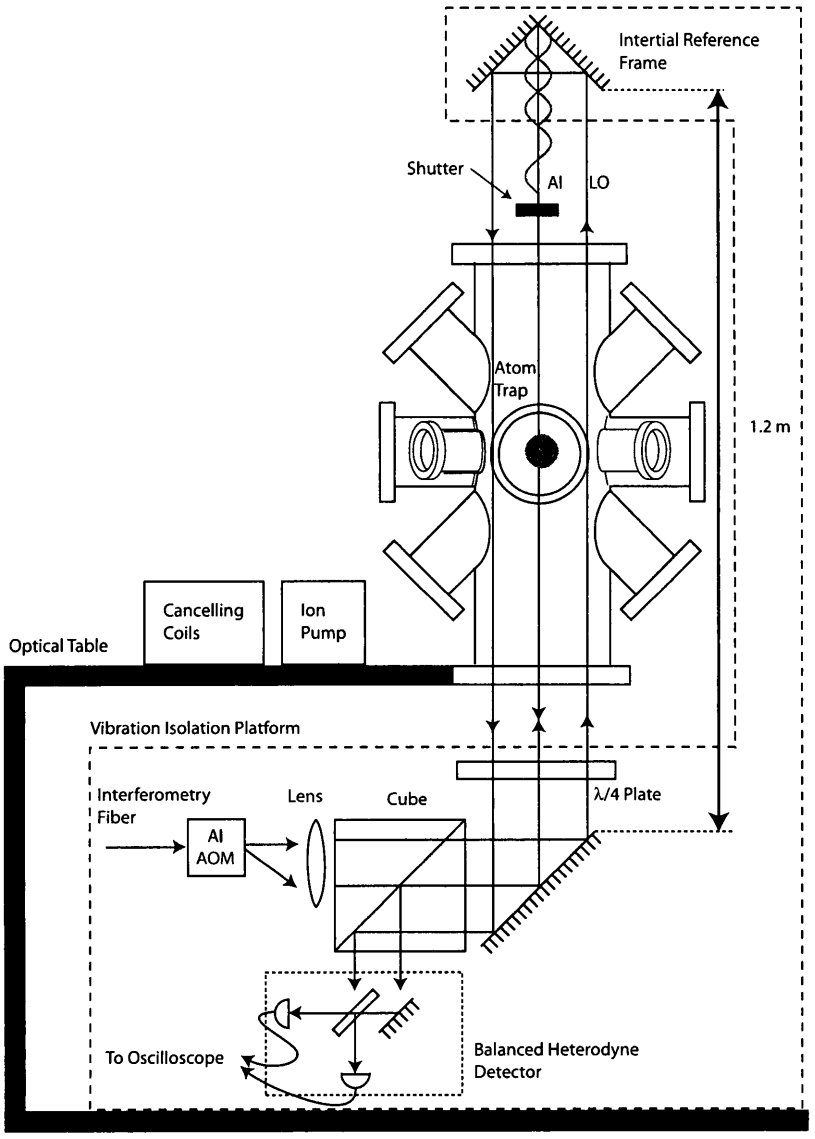

Figure 3.18: Schematic of the experimental setup. The lower detection optics and the upper corner cube are anchored together and placed on a vibration isolation platform. The vacuum chamber and vibration isolation platform rest on an optical table supported by pneumatic legs. The photodiodes detect a 250 MHz beat note as the frequency difference between the AI and LO beams. The ion pump, cancelling coils and anti-Helmholtz coils are not shown so that the optical setup can be clearly illustrated. These elements are anchored to the optical table.

3.3.1 Beam Path

When the Trap AOM is turned off, the undiffracted light is used for atom interferometry. This beam is routed to a dual pass Gate AOM, as shown in figures 3.2 and 3.6, which upshifts the laser frequency two times. The frequency of the Gate AOM can be changed to alter the overall detuning of the interferometry beams with respect to the $F = 3 \rightarrow F' = 4$ resonance in ^{85}Rb or the $F = 2 \rightarrow F' = 3$ resonance in ^{87}Rb, as illustrated in figures 3.3 and 3.4. The typical drive frequency of the Gate AOM ranges between 50-90 MHz.

The output of the Gate AOM is coupled into a fibre to bring light to the Experiment Table shown in figure 3.1. This table is an optical table with pneumatic supports. The pneumatic supports and the optical table are effective in suppressing vibrations greater than 1 kHz. The optical elements of the interferometer are aligned on a vibration isolation platform placed on the optical table, as shown in figure 3.18. The vibration isolation platform uses tuned damping and has a resonant frequency of 1 Hz, providing passive vibration isolation to optimally attenuate sources of vibration with frequencies 1-100 Hz. Fiber coupling ensures that the interferometer is decoupled from the relative motion between the two pneumatically supported optical tables shown in figure 3.1.

The output of the interferometry fibre enters the AI AOM shown in figure 3.18. This single-pass AOM imposes a frequency downshift of 250 MHz. The AI AOM is operated in the Bragg regime so that the diffraction efficiency of the first-order

diffracted beam is greater than 50%. Circuit elements driving this AOM pulse the RF using TTL switches just like the arrangement shown in figure 3.15. By pulsing the RF drive to the AI AOM, the first-order diffracted beam is pulsed, generating the excitation beams for atom interferometry.

The diffracted beam from the AI AOM has an average diameter of 0.8 cm and is circularly polarized. It is aligned along the vertical through the MOT, as shown in figure 3.18. The beam is aligned through the centre of a corner-cube reflector so that there is no displacement of the reflected beam. The retro-reflected beam from the corner-cube reflector produces standing-wave excitation of the laser-cooled sample. The corner cube is used to reduce phase shifts due to torsional motion and tilts associated with a retro-reflecting surface. If a mirror were used, any tilt motion not centred on the point of incidence changes the path of the reflected beam, thereby changing the phase of the standing wave. Furthermore, any tilt of the mirror used would cause the incident angle to change, and the phase of the reflected beam changes as a function of incident angle. By using a corner-cube reflector, the beam is reflected twice, producing the same total phase change, which is independent of the path through the corner cube.

As shown in figure 3.18, the optical table is used to support the vacuum chamber and the ion pump. The vibration isolation platform provides additional passive isolation for the AI optics and the corner-cube reflector. The main disadvantage of this setup is that only critical components of the experiment have been well shielded

from vibrations.

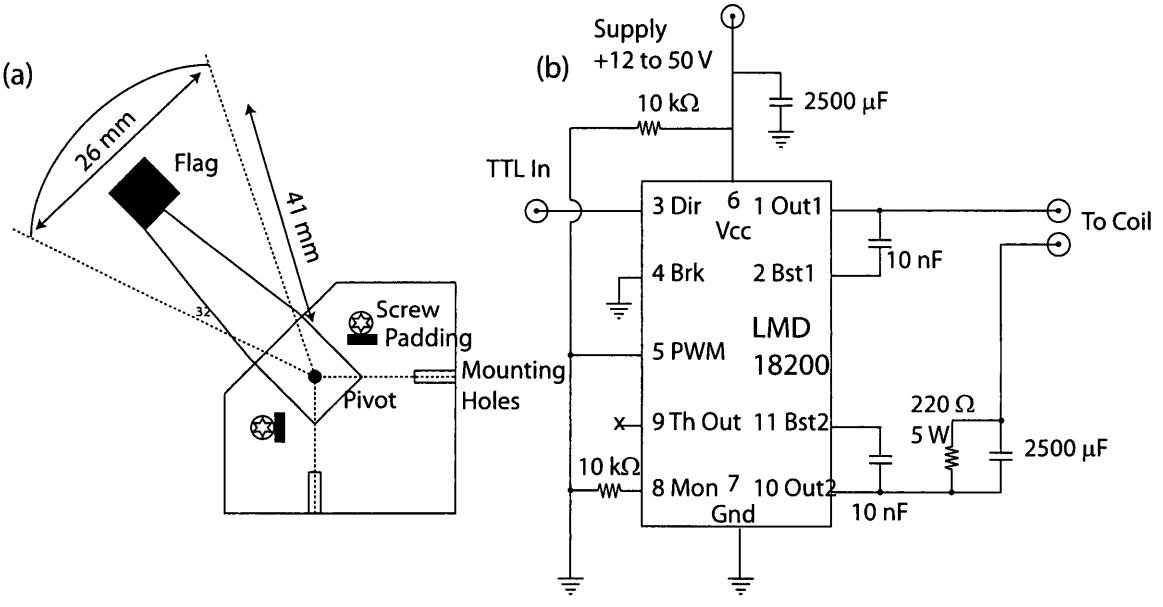

Figure 3.19: (a) Diagram of the hard drive shutter arm. The maximum speed of the shutter arm reaches is 28.5 m/s. Padding is required to cushion the shutter arm to reduce vibrations. (b) Hard drive control circuitry is based on the LMD 18200 CMOS H-Bridge chip. The direction of the output is defined by the directional selector pin 3.

A lab-built mechanical shutter [122] based on the voice-coil[12] actuator arm of a computer hard drive is located in the interferometry beam path. Drive electronics and schematics are shown in figure 3.19. At the time of the read-out pulse, the shutter blocks the retro-reflection of the excitation beam in less than 1 ms to produce a travelling wave.

The benefit of this shutter is to realize an aperture-less design, allowing for any reasonably sized beam to be physically blocked in a short amount of time by the flag.

[12]The hard drive actuator arm has a coil of wire that is often called a "voice-coil". The coil on the arm is placed in a magnetic field due to permanent magnets, so that the application of current through this coil creates a force that moves the arm.

The maximum continuous repetition rate is 40 Hz. The total 35° angular travel of the arm is limited by the size of the constraining magnet and by the hard stop of the screws. Bypassing the hard drive control electronics and applying the current directly to the coil on the arm allows for faster response. The 2500 μF output capacitor must not be polarized as this capacitor discharges in both directions to accelerate the arm. The 220 Ω resistor is used to limit the current used to hold the arm in the terminal positions.

The undiffracted beam from the AI AOM, serving as an optical local oscillator (LO), is aligned through the same optical elements as the excitation beam to minimize the impact of relative phase changes due to vibrations. The centres of the two beams are separated by 2.5 cm. The LO is physically displaced upon reflection by the corner cube, as shown in figure 3.18. The excitation and LO beams are combined on a beam splitter and sent to a balanced heterodyne detector.

3.3.2 Timing and Synchronization

We use a 10 MHz Rubidium Reference Clock (Stanford Research Systems PRS10 with an Allan variance of 10^{-12} in 100 seconds [123]) as the master time base for the experiment. This provides a stable common time base for the delay generators with a relative accuracy of $\pm 5 \times 10^{-11}$ [123]. A 250 MHz voltage-controlled oscillator (VCO) is phase locked to the reference clock with an update rate of 200 kHz. By phase locking the VCO to the clock, the stability characteristics of the clock are transferred

to the 250 MHz signal, which drives the AI AOM in figure 3.18.

Several pulse generators (Stanford Research Systems DG535) produce the TTL pulses used to generate the RF and optical pulses. These generators can use either the internal crystal oscillator clock, or an external 10 MHz source for their timebase. The internal clock of these generators is accurate to 25 ppm, whereas if slaved to an external reference clock signal, the time base is accurate to the external clock accuracy plus 0.2 ppb [124]. We slave the timebase of these generators to the master time base in order to obtain better accuracy and drift characteristics through all generators. For the largest time delays of $\approx$ 100 ms, this translates to delay time accuracies better than 50 ps. In this setup, the drifts and jitter between the pulses generated by separate generators is comparable to the delay-time accuracy.

A further complication arises since the pulse generators can be triggered either internally or externally. The internal trigger point of the pulse generators may fall anywhere within one cycle of the master 10 MHz clock signal. Thus, each TTL and RF pulse may occur with a phase shift compared to the previous sequence. To avoid this problem, we externally trigger a 'master' pulse generator on the reference clock, thereby fixing the phase of the trigger point. This 'master' delay generator sends a synchronization pulse to the other generators. The duration of the pulse sequence of the 'master' delay generator is set much larger than the period of the 10 MHz reference so that the next trigger point continues to be phase locked to the 10 MHz reference.

The pulse sequence and typical pulse durations are shown in figure 3.20. To reduce the amount of background light entering the apparatus during the AI pulse sequence, the Gate AOM was pulsed on only when the AI AOM was turned on. Therefore, light entered the setup only during the interferometry pulses. The undiffracted LO beam from the AI AOM is 320 MHz above resonance, which is within the Doppler broadened spectral envelope of the room temperature background atoms in the vacuum chamber. If the Gate AOM is not pulsed, the scattered light from the Doppler-broadened vapour inside the trapping chamber can decohere the signal, thereby reducing the timescale of the experiment.

3.3.3 Magnetic Field Characterization

Before assembling the vacuum chamber, the magnetic field at the center was characterized with a Hall probe as a function of position. After the chamber was pumped down to hold vacuum, we had to rely on the signals from cold atoms to infer the magnetic field since it is non-trivial to obtain real-time measurements with a magnetic probe in ultra-high vacuum. It is not possible to use properties of the echo interferometer to measure constant magnetic fields since the signal is associated with a single atomic ground state. However, we were able to use the properties of echo signals to characterize magnetic field gradients in the vicinity of the sample, as described in Chapter 5.

The magnetic environment was influenced by the magnetic field of the external

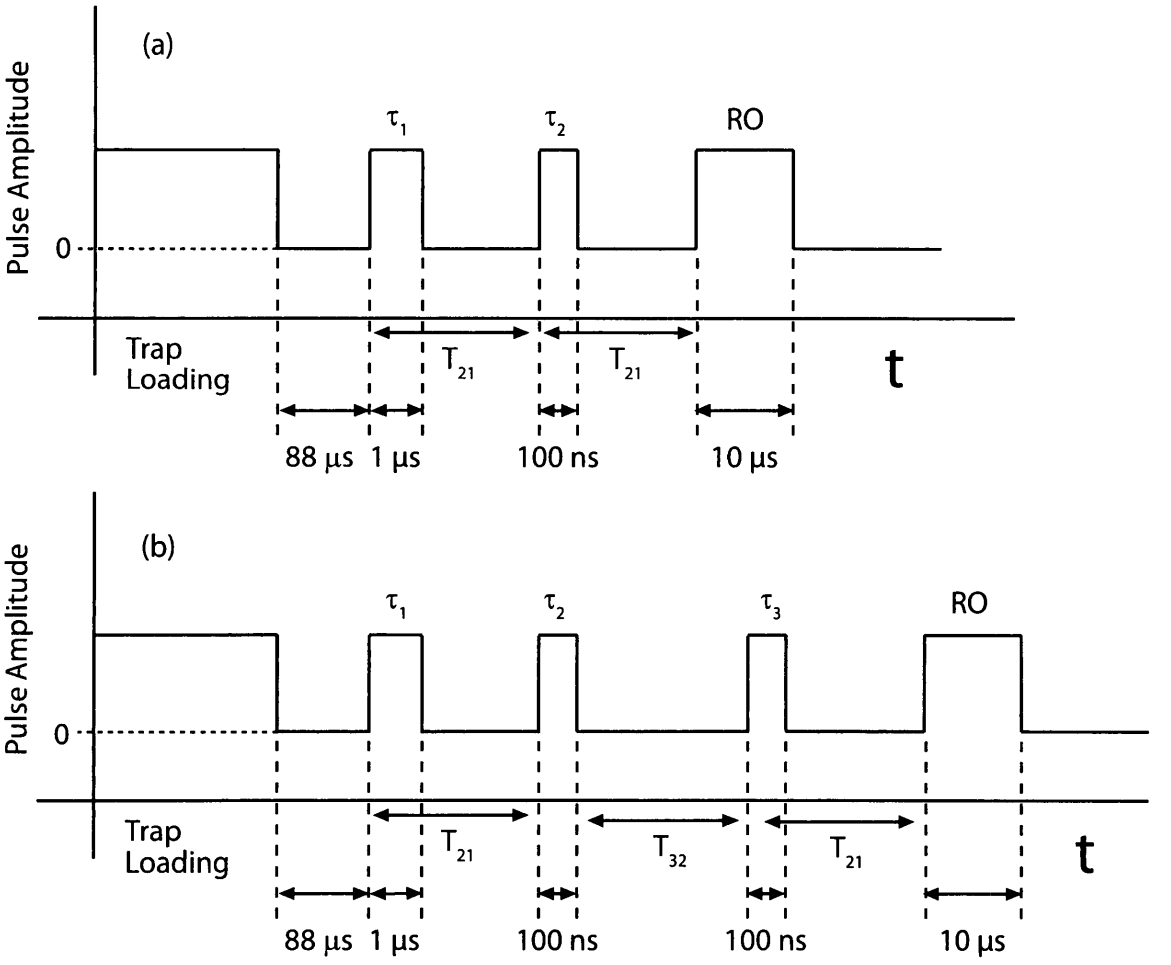

Figure 3.20: (a) Two-pulse AI pulse sequence and typical pulse durations. (b) Three-pulse AI pulse sequence and typical pulse durations. RO refers to the read-out pulse.

coils, the magnetization of the vacuum chamber due to the constant pulsing of the anti-Helmholtz coils, and by ambient magnetic fields. The combined effects of these sources resulted in significant magnetic gradients and curvature, as per the estimates in Chapter c.

Attempts to de-magnetize the vacuum chamber using degaussing techniques were only partially successful. The first attempt involved applying a ramped current with a

frequency of 60 Hz to the anti-Helmholtz coils. However, each time this procedure was completed, the settings on both the magnetic field and magnetic gradient cancellation coils required to obtain a MOT as well as long lived echo signals were significantly different suggesting the magnetic field in the vicinity of the atoms was still non-zero.

In a more sophistical method of degaussing the chamber, the current was ramped up and down with a period of two seconds to avoid inductive effects. A high-current relay switched the direction of the current, and the ramp process was repeated. A computer controlled program allowed the amount of current being delivered to the coils to be progressively reduced after each repetition. After this procedure, the settings of the cancellation coils required to obtain a MOT as well as long lived echo signals were consistently near zero, suggesting the magnetic field in the vicinity of the atoms was near zero. However, shortly after the commencement of the pulsing of the trapping coils, the chamber became magnetized.

3.3.4 LabVIEW Interface and Data Analysis

The entire pulse sequence for the experiment was controlled though a LabVIEW interface, shown in Appendix E. The pulses for atom interferometry are controlled by the highest-precision delay generators in the lab, which are slaved to the rubidium clock. A less precise delay generator is used to control the pulse sequence for atom trapping. For measurement of the AI signals, the LabVIEW program allows the pulse delays to be randomized to avoid systematic effects that may depend on the sequential

ordering of pulses.

The LabVIEW program also allows data to be acquired from a number of oscilloscopes. Electronic mixing down, background subtraction, and slicing discussed later in this chapter were implemented using C++ code, presented in Appendix C. Curve fitting and some batch processing were carried out in Mathematica. See Appendix D for the source code.

3.3.5 Isolation and Shielding

The corner-cube retro-reflector, AI AOM, and associated optics are anchored to the vibration isolation platform, as shown in figure 3.18. This platform has a resonance frequency of 1 Hz. The optical table of the experiment is supported by pneumatic, laminar flow legs. The optical table is effective in suppressing vibration frequencies above 1 kHz, whereas the vibration isolation platform is much more effective in suppressing frequencies in the range of $1 - 100$ Hz. The mechanical shutter is separately anchored to the ceiling of the laboratory to reduce vibrational coupling. In this manner, critical components of the experiment are passively isolated with the vibration platform and optical table. Phase detection in the apparatus is sensitive enough to detect effects such as the motion of building elevators and people walking in the lab so that further precautions were necessary. These included flush mounting of the optics, and surrounding the optical table with acoustic shielding, which also reduced air currents. Car batteries were used to power the photodiodes to reduce power supply

noise, RF pickup, and crosstalk.

3.4 Detection and Measurement

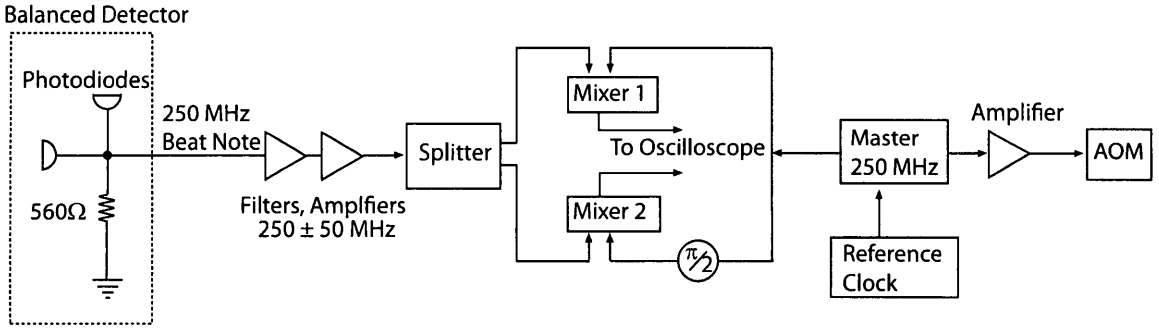

Figure 3.21: Detection electronics for analog mixing down to DC. The master oscillator operating at 250 MHz drives the AI AOM and provides the reference RF for mixing down to DC.

Signal detection in the AI experiment uses an optical heterodyne detection technique. The optical local oscillator (LO) required for this method of detection is derived from the undiffracted beam from AI AOM. This beam is spatially separated from the interferometry beam. The beam diameter of the LO is comparable to the size of the interferometry beam.

The AI and LO beams are turned on continuously, in order to align the AI beam through the atom trap, as shown in figure 3.18. Both beams travel up through the central region of the chamber, reflect off the corner cube reflector, and return downward. The AI beam is centred on the cube so that the reflected beam is overlapped with the incident beam, but the LO beam is laterally displaced. Upon returning to the floating vibration isolation platform below the trap, the excitation and LO beams

are combined on a beam splitter and sent to a balanced heterodyne detector setup, shown in figure 3.18. This detector measures a beat signal at 250 MHz, which is the frequency difference between the AI and LO beams. The balanced detector consists of two oppositely biased Si photodiodes with rise-times of 1 ns and responsivities of 0.45 A/W. The heterodyne optics are rigidly mounted to the vibration isolation platform to reduce relative path difference drifts between the AI and LO beams.

The heterodyne signal is detected on a photodiode as a 250 MHz beat note. The beat note can have a DC offset due to background LO light. By using a balanced heterodyne detector consisting of two oppositely biased silicon photodiodes, this offset can be removed. The output current of the photodiodes are electronically summed to give a heterodyne signal with twice the amplitude of a single photodiode and near zero offset. This arrangement of photodiodes cancels the DC component of the photodiode signal, but the beat notes from the detectors add constructively.

The heterodyne signal recorded by the balanced detector is amplified by an RF amplifier, with a 26 dB gain (400 times), then notch filtered at 250 ± 50 MHz, as shown in figure 3.21. The heterodyne beat note is compared to the master oscillator at 250 MHz to determine the phase. This comparison is accomplished by mixing the beat note and master oscillator signals on a RF mixer to derive the DC components of the signal. These are the so called in-phase and in-quadrature components of the signal. We now review the details of the heterodyne detection.

3.4.1 Heterodyne Detection

The interferometry excitation beam has an optical frequency ω_{AI} and the LO beam has an optical frequency ω_{LO}, with a well-defined frequency difference ω_{RF} given by $\omega_{\mathrm{RF}} = (\omega_{\mathrm{LO}} - \omega_{AI})$. To explain the principle of detection, we assume the LO to be a perfectly phase-stable beam as compared to the interferometry beam.

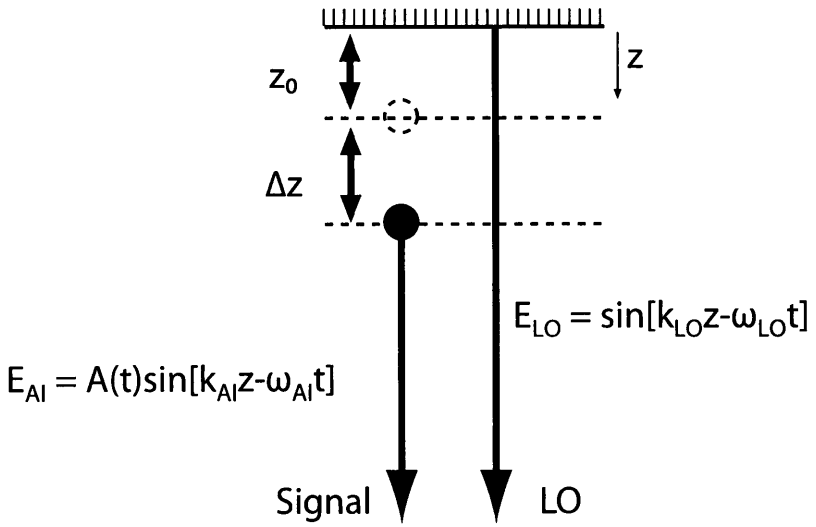

Figure 3.22: Positional phase between heterodyne beams.

The electric field of the LO can be written as $E_{\mathrm{LO}} = \sin(k_{\mathrm{LO}} z_{\mathrm{LO}} - \omega_{\mathrm{LO}} t)$. The electric field of the backscattered light signal can be written as

$$E_{AI} = A(t)\sin(k_{\mathrm{AI}} z_{\mathrm{AI}} - \omega_{\mathrm{AI}} t), \tag{3.4}$$

as shown in figure 3.22. Here $A(t)$ is the time varying envelope of the echo signal.

The heterodyne beat note measured by a photodiode can be written as $I = (E_{\mathrm{LO}} + E_{\mathrm{AI}})^2$. Inserting the respective electric fields, we obtain

$$I = (\sin[k_{\mathrm{LO}} z_{\mathrm{LO}} - \omega_{\mathrm{LO}} t] + A(t) \sin[k_{\mathrm{AI}} z_{\mathrm{AI}} - \omega_{\mathrm{AI}} t])^2$$

$$= \sin^2[k_{\mathrm{LO}} z_{\mathrm{LO}} - \omega_{\mathrm{LO}} t] + A^2(t) \sin^2[k_{\mathrm{AI}} z_{\mathrm{AI}} - \omega_{\mathrm{AI}} t)$$

$$+ 2A(t) \sin[k_{\mathrm{LO}} z_{\mathrm{LO}} - \omega_{\mathrm{LO}} t] \sin[k_{\mathrm{AI}} z_{\mathrm{AI}} - \omega_{\mathrm{AI}} t].$$

Since $\frac{1}{\omega_{\mathrm{LO}}}, \frac{1}{\omega_{\mathrm{LO}}} \ll \tau_{\mathrm{rise}} = 1$ ns, we ignore terms oscillating at the optical frequency, so that we are left with the cross term:

$$I = 2A(t) \sin[k_{\mathrm{LO}} z_{\mathrm{LO}} - \omega_{\mathrm{LO}} t] \sin[k_{\mathrm{AI}} z_{\mathrm{AI}} - \omega_{\mathrm{AI}} t].$$

We convert this product into a sum via the trigonometric identity $\sin A \sin B = \frac{1}{2}[\cos(A - B) - \cos(A + B)]$, so that

$$I = A(t)[\cos[k_{\mathrm{LO}} z_{\mathrm{LO}} - k_{\mathrm{AI}} z_{\mathrm{AI}} - (\omega_{\mathrm{LO}} - \omega_{\mathrm{AI}})t] - \cos[k_{\mathrm{LO}} z_{\mathrm{LO}} - k_{\mathrm{AI}} z_{\mathrm{AI}} - (\omega_{\mathrm{LO}} + \omega_{\mathrm{RF}})t].$$

Again discarding the high frequency optical term, we obtain the heterodyne beat note:

$$I = A(t)[\cos[k_{\mathrm{LO}} z_{\mathrm{LO}} - k_{\mathrm{AI}} z_{\mathrm{AI}} - (\omega_{\mathrm{LO}} - \omega_{\mathrm{AI}})t]. \tag{3.5}$$

The term $\Delta\phi = k_{\mathrm{LO}} z_{\mathrm{LO}} - k_{\mathrm{AI}} z_{\mathrm{AI}}$ is the phase difference between the AI beam and the LO beam caused by gravity. Equation 3.5 can therefore be written as

$$I = A(t)[\cos[\Delta\phi - (\omega_{\mathrm{LO}} - \omega_{\mathrm{AI}})t]. \tag{3.6}$$

Figure 3.23 shows a calibration of the heterodyne system. The output of the balanced detector is found as a function of AI beam power. The LO beam power was

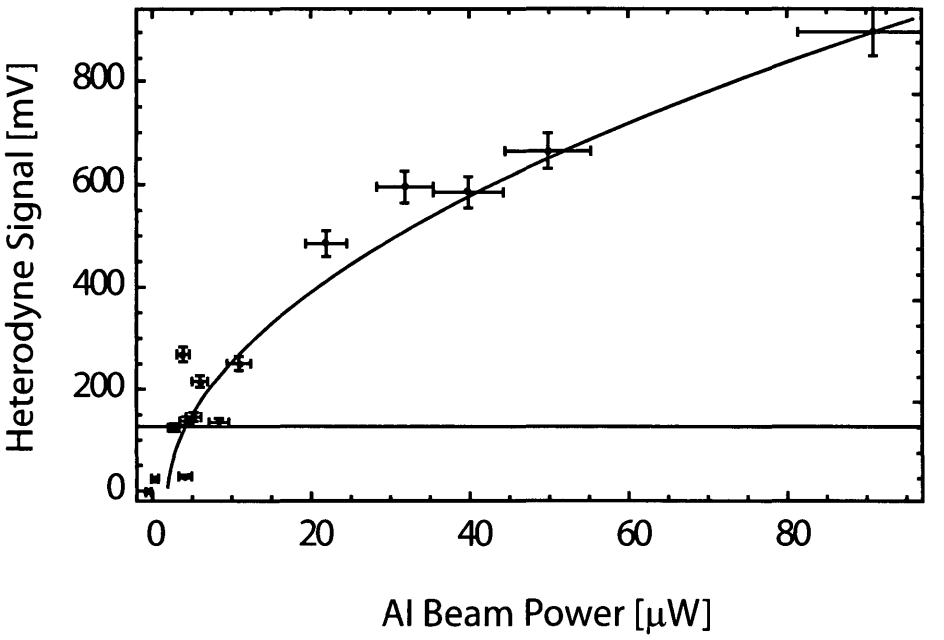

Figure 3.23: Heterodyne calibration curve. The data set is fit to a square root function, as shown in red. The black line is the largest signal from the atoms corresponding to a peak power of 2.5 μW.

fixed at 25 mW and the AI beam power was varied up to 80 μW. This calibration curve allows a measurement of the energy of the pulse of light backscattered by the atoms.

The phase of the signal was initially determined by using discrete RF components to mix the heterodyne beat note with the 250 MHz RF. The in-phase component of the signal was obtained by mixing the heterodyne beat note with the RF, phase shifted by 0 degrees. The in-quadrature component of the signal was obtained by mixing the heterodyne beat note with a 90 degree phase shifted RF signal. The propagation speed of an electro-magnetic wave through an RG-58 co-axial cable occurs at approximately 2/3 of the speed of light so that one wavelength of the 250 MHz signal is approximately

80 cm. So, a 90 degree phase shift can be achieved using an extra length (20 cm) of coaxial cable. Alternatively, a 60 cm cable can also be used to obtain a phase shift of 270 degrees (-90 degrees). Measurement of the relative phase between the original and phase shifted RF was accurate to 1%, as determined by varying the phase of the input RF and fitting the DC output of the mixer. The mixed output was low-pass filtered through a 10 MHz filter to remove the high frequency components, resulting in the DC components of the signal.

A high-bandwidth oscilloscope (Tektronix TDS 7000 series) became available at the later stages of the experiment. Using this oscilloscope, it was possible to directly record the master oscillator signal and the beat note from the balanced detector with sufficient point density (5 points/cycle) so that mixing down was carried out in post-processing. This procedure reduced cross-talk between components, RF pickup noise and also preserved the high temporal resolution of the signal. Furthermore, errors due to the phase shifts associated with mixing down to DC were eliminated. This oscilloscope had the added benefit of enabling higher data transfer rates so that a high resolution trace could be recorded without sacrificing acquisition time.

The detection system allowed any change in relative phase between the LO and AI beams due to mirror motion or atomic motion to be detected as a phase change.

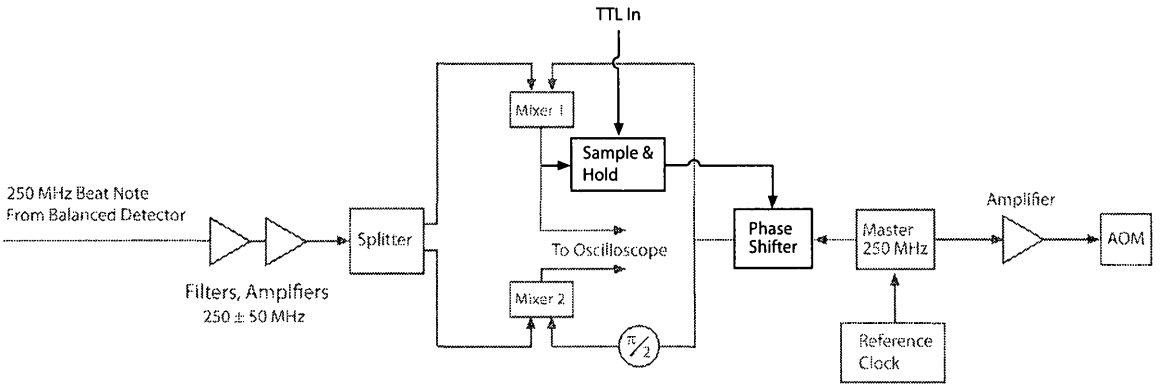

Figure 3.24: Detection electronics for analog mixing down to DC with phase shifter and sample and hold circuit. This circuit is designed to sample when the TTL input is high and to hold when the TTL input is low. The voltage from the mixer is sent to a phase shifter to correct for shifts from vibrations.

3.4.2 Sample and Hold

We used a sample and hold method to stabilize the RF signal used for mixing down the signal to DC. The feedback loop shown in figure 3.24 was essential for partially compensating for optically induced phase shifts that could affect the phase difference between the AI and LO beams.

During trap loading, an attenuated excitation beam aligned through the MOT is turned on to record a 250 MHz beat note that serves as a monitor of the real-time phase changes due to motion of the optical elements.

The DC voltages from this measurement are sent to a sample-and-hold circuit, shown in figure 3.25, that allows switching between active sampling and holding the phase. The first stage of this circuit is a non-inverting amplifier. The second stage either samples or holds the input signal as determined by whether the TTL input is

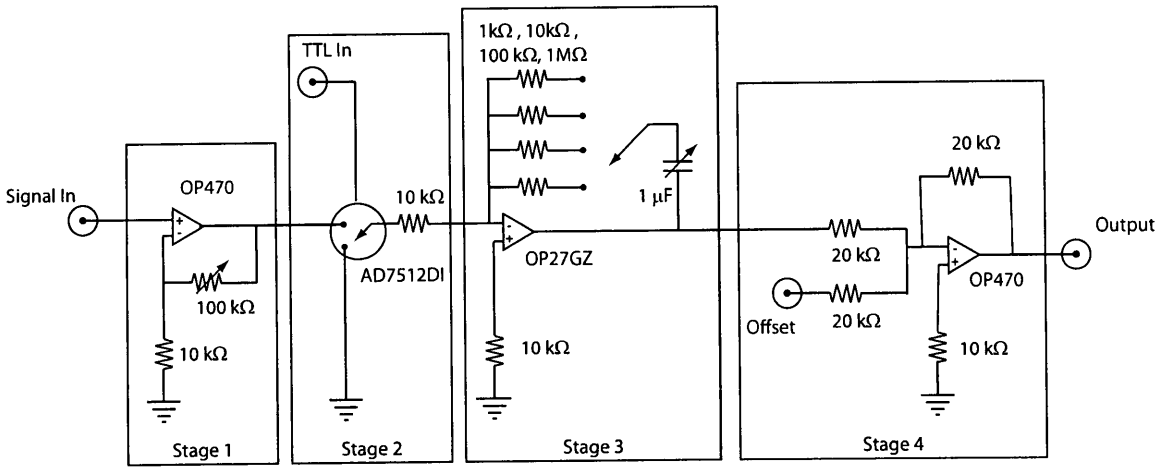

Figure 3.25: Electrical schematic of the sample-and-hold circuit used in the experiment.

high or low. The third stage is the integrator and low-pass filter for the signal. The bank of resistors is chosen to span a large 1/RC time constant range. The fourth and last stage is an adder to shift the offset of the signal.

The output of the sample-and-hold circuit is sent to RF phase shifters to re-initialize the RF phase used to mix the signal down to DC. Each phase shifter produces a linear change in RF phase as a function of voltage. The range of each phase shifter is 90 degrees. The maximum phase shift that could be produced by the linear array of phase shifters is 900 degrees, which is greater than the phase variation due to the motion of the apparatus[13]. The phase-shifted RF is used to mix the heterodyne signal down to DC. This procedure ensures that the relative phases between the excitation beam and the LO are the same at the start of the experiment.

At the end of trap loading, the probe beam is turned off and the last measured

[13]The relative changes in path lengths travelled by the LO and AI beams was measured as a phase shift that ranged between ±450°

value of the phase was held constant during the interferometer pulse sequence. In this arrangement, we could not detect any phase changes during the experiment due to any mirror motion associated with the entire apparatus, or the motion of the corner cube reflector. The sampling period re-commenced as soon as the pulse sequence ended for the next repetition. In this manner, it was ensured that the phase difference between the LO and AI beams was the same at the start of every repetition of the experiment.

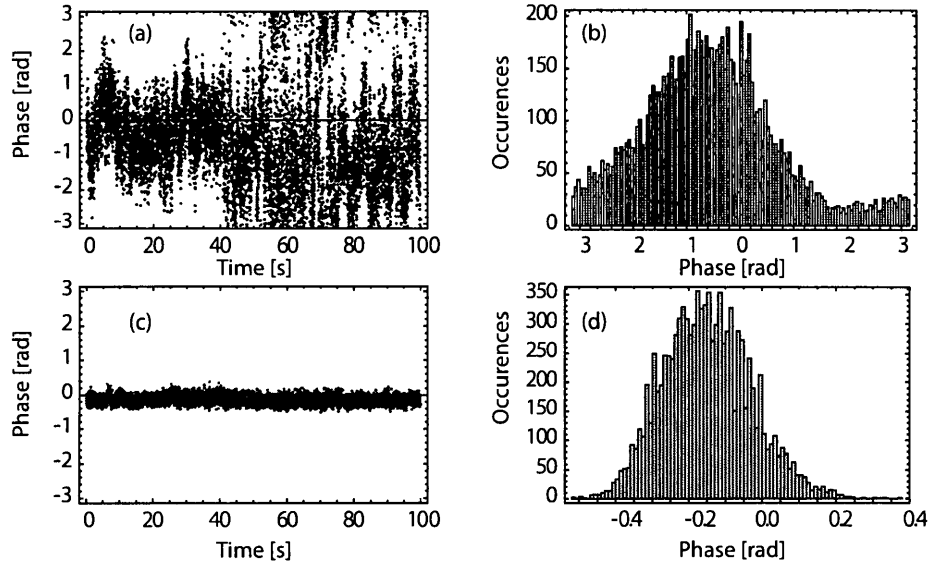

Figure 3.26: Phase feedback effectiveness (a) without correction, and (c) with continuous correction. The histograms of the data set are shown in (b) and (d). The standard deviation without correction is 1.3 rad and with correction 0.1 rad.

The effectiveness of this method can be seen in figures 3.26 and 3.27. In figure 3.26, the phase is displayed with and without the feedback loop engaged. For these measurements, the probe beam was on continuously. The histograms of the phase show that the distribution is significantly narrowed with the feedback loop. In figure 3.27, the phase distribution width is shown in pulsed mode. Here, the optical phase

was measured after a variable hold time following the last correction. Again, the width of the phase distribution significantly decreased with phase feedback. However, the method breaks down after $\approx$ 25 ms, as vibrations continue to couple into the system.

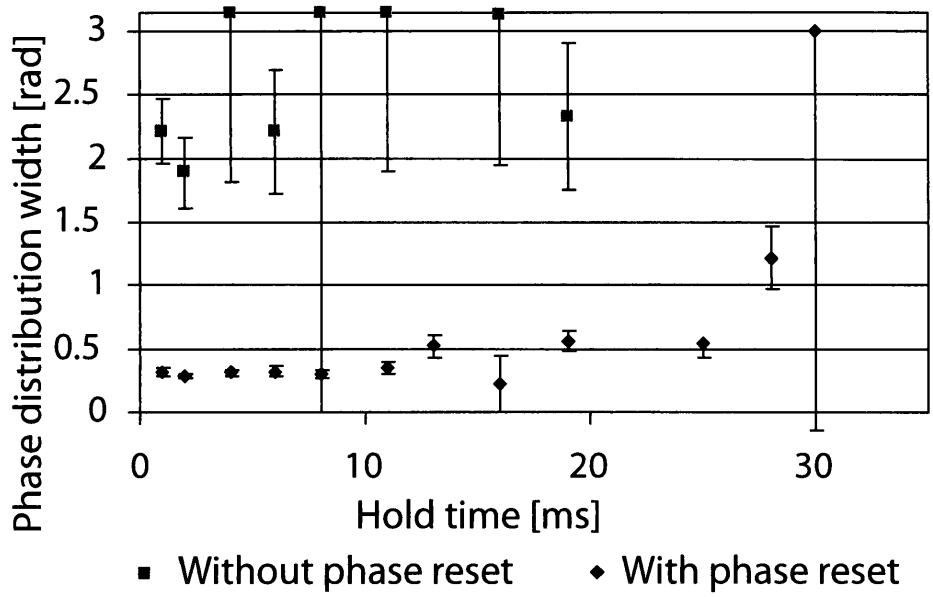

Figure 3.27: Sample-and-hold method of phase stabilization. Pink squares denote no phase feedback; blue diamonds denote phase feedback.

3.4.3 Optical Probe

To ensure that we have knowledge of the phase at all times, we used a second Probe AOM also driven by the same 250 MHz RF oscillator to generate a continuous heterodyne signal. This Probe AOM is anchored to the same vibration isolation platform as shown in figure 3.28. The AI beams are physically separated from the probe beams. However, the two beams from the probe are aligned along nearly the same path as the AI beam. The 250 MHz beat note from the probe beams is used to mix the echo

signal down to DC.

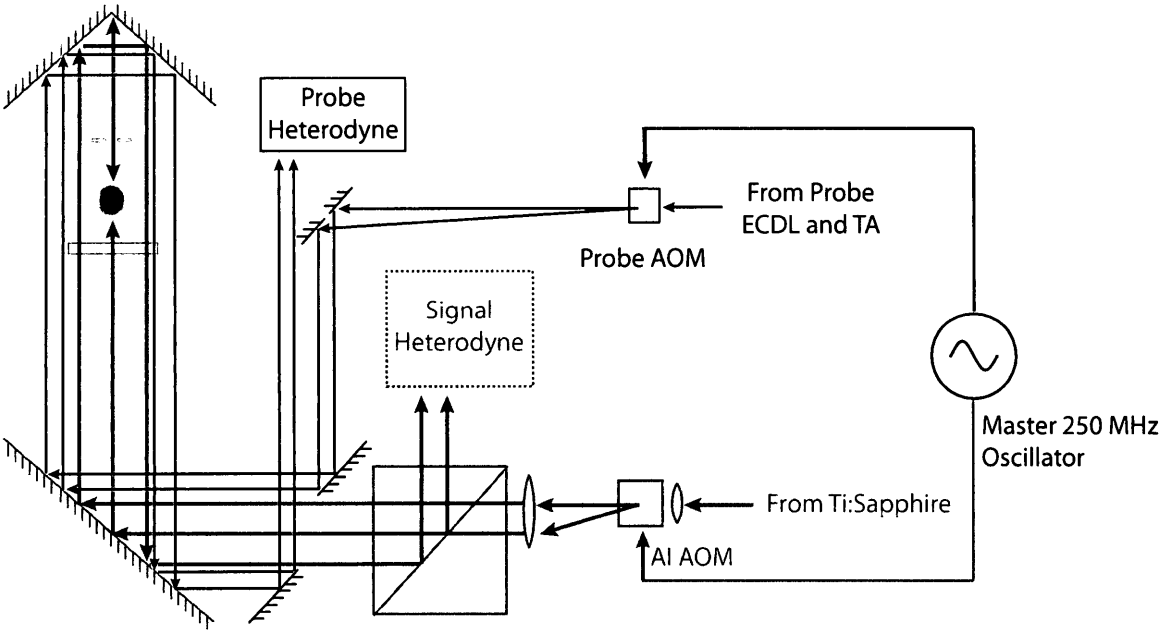

Figure 3.28: Experimental setup showing Probe and AI AOMs with two separate lasers. This setup allows optical phase changes to be monitored continuously.

The choice of wavelength of the probe laser requires some consideration. Using the same wavelength light as the AI beams is not ideal as resonant scattering from the background light decoheres the atomic sample and reduces the AI signal. Therefore, a 60 mW, 785 nm diode laser amplified by a TA was used since this wavelength can be transmitted through the AR coatings on mirrors and viewports and yet remain sufficiently off resonance so as not to interact with the atoms. However, the probe beams cannot be directly overlapped with the 780 nm beams, since a suitable narrow band dichroic beam splitter was not available. Thus, the 785 nm beam travels through a similar path as the 780 nm beams, as shown in figure 3.28. The probe laser used in this setup was a home-built ECDL with a linewidth of $\approx$ 1 MHz.

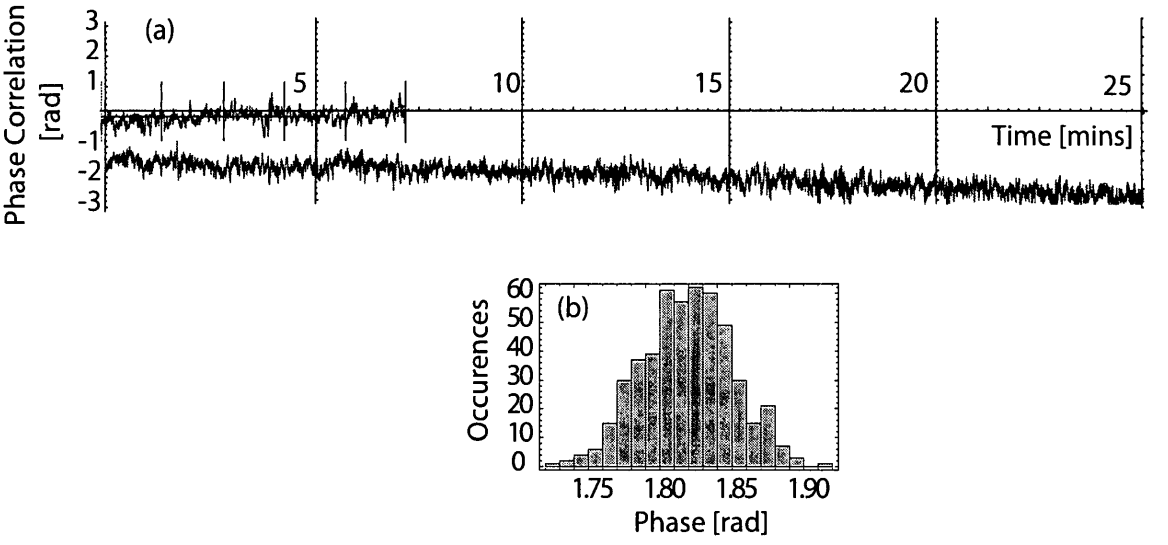

Figure 3.29: (a) Phase correlation between the 250 MHz beat note from the AI beams and the probe beams in figure 3.28 recorded with active feedback. Both sets of beams are continuously on. (b) Histogram variations of the signal over 100 ms. The standard deviation is 0.03 rad.

The experiment relies on passive isolation of critical components. In this arrangement, the AI signal is determined by beating the backscattered light from atoms with the optical LO. This beat note can be mixed down to DC using the 250 MHz beat note from the continuous wave probe beams. For this arrangement to work, the two beat note signals must be highly correlated.

Figure 3.29a shows the phase correlation between these beat note signals. As shown in figure 3.24, the optical phase of the AI beam is measured as a 250 MHz beat note during the trap loading. This information is sent to a phase shifter which periodically resets the Master Oscillator phase for each repetition of the experiment.

The phase is held constant during the experiment. The maximum hold time is 100 ms. Figure 3.29b shows the histogram of the phase correlations between the AI beat note and the Probe beat note on a 100 ms timescale. The typical standard deviation of 0.03 rad shows that this set of beat notes is highly correlated. If the AI experiment had no other phase fluctuations, one would expect the AI phase to be determined with comparable precision. However, a variety of optical phase changes due to vibrational coupling and the motion of the inertial reference frame limited the precision of the AI phase measurement, as discussed in Chapters 4 and 5.

3.5 Data Reduction

Detection of the phase of the electric field of the echo signal is accomplished by mixing the RF drive signal with the heterodyne beat note. Initially, discrete RF components were used to obtain the in-phase and in-quadrature components. These signals were averaged in real-time on an oscilloscope and stored. This method was initially used to reduce data taking and data reduction time. This method was used during the setup and optimization of the signal.

Alternatively, high-resolution traces of the 250 MHz signals from the balance detectors can be directly recorded by the oscilloscope and the data transferred on each repetition of the experiment. This procedure allowed mixing down in post-processing, resulting in reduced noise and allowing single shot data to be compared to the averaged signal. This technique resulted in a 100-fold increase in file size and

increased processing time. However, this latter method was preferred since it was possible to investigate improvements in post-processing.

3.5.1 Gravitational Phase Detection

We begin by mathematically describing the in-phase components of the signal S_{IP}, obtained by mixing the beat note from the balanced detector down to DC with the RF used to drive the AI AOM. We obtain

$$\begin{aligned} S_{\mathrm{IP}} &= A(t)\cos(\Delta\phi + \omega_{\mathrm{RF}}t)\cdot\sin(\omega_{\mathrm{RF}}t) \\ &= \frac{A(t)}{2}\left(\sin[\Delta\phi + \omega_{\mathrm{RF}}t - \omega_{\mathrm{RF}}t] + \sin[\Delta\phi + \omega_{\mathrm{RF}}t + \omega_{\mathrm{RF}}t]\right). \end{aligned}$$

The high frequency component is removed by a low-pass filter so that the DC component:

$$S_{\mathrm{IP}} = A(t)\sin\left(\Delta\phi\right). \tag{3.7}$$

The in-quadrature component S_{QUAD}, is given by

$$\begin{aligned} S_{\mathrm{QUAD}} &= A(t)\cos(\Delta\phi + \omega_{\mathrm{RF}}t)\cdot\cos(\omega_{\mathrm{RF}}t) \\ &= \frac{A(t)}{2}\left(\cos[\Delta\phi + \omega_{\mathrm{RF}}t - \omega_{\mathrm{RF}}t] + \cos[\Delta\phi + \omega_{\mathrm{RF}}t + \omega_{\mathrm{RF}}t]\right). \end{aligned}$$

After low-pass filtering, the high frequency component is removed, leaving the DC component

$$S_{\mathrm{QUAD}} = A(t)\cos\left(\Delta\phi\right). \tag{3.8}$$

In this manner, the in-phase and in-quadrature components of the AI signal amplitude can be determined.

A gravity measurement consists of measuring the phase of the AI signal as a function of T_{21} or T_{32}. We note that $\Delta\phi$ accounts for an overall positional phase. For measuring gravity, $\Delta\phi$ corresponds to $\phi_g^{(2)}$ for the two-pulse AI or $\phi_g^{(3)}$ for the three-pulse AI, depending on the configuration of the pulses.

The phase due to gravity can be extracted directly by finding the ratio of the amplitude of the in-phase and in-quadrature components so that

$$\tan(\Delta\phi) = \frac{S_{\mathrm{IP}}}{S_{\mathrm{QUAD}}}. \tag{3.9}$$

Another method of measuring $\Delta\phi$ involves obtaining the component signal amplitudes given by equations 3.7 and 3.8 by mixing down to DC. Each data point in the traces representing the amplitude components was squared and summed. The square root of the sum gives the total signal amplitude, with the sign assigned arbitrarily so that

$$A(t) = \sqrt{S_{\mathrm{IP}}^2 + S_{\mathrm{QUAD}}^2}. \tag{3.10}$$

A more precise version of the above mentioned technique for extracting $A(t)$ and hence $\Delta\phi$ involves fitting the echo signal envelope to the form

$$A(t - t_0)e^{-(t-t_0)^2/2\tau}\sin[\omega(t - t_0)] + D, \tag{3.11}$$

where A, τ, ω, t_0, and D are free parameters. Here, A defines the amplitude, τ defines the duration of the signal envelope, ω is the frequency of oscillation within the en-

velope, t_0 is the temporal offset and D is the vertical offset. However, this method was dependent on iterative searches for initial fit parameters and the fitting routine proved time consuming.

For the two-pulse AI, the total signal amplitude exhibits recoil modulation as a function of T_{21} and decay due to incoherence, transit time effects, breakdown of the two-photon resonance condition as the atoms accelerate due to gravity. For the three-pulse AI, the amplitude decays as a function of T_{32} due to the aforementioned reasons. The total signal amplitude can be used to normalize equations 3.7 and 3.8 to divide out the amplitude co-efficient and extract the gravitational phase.

4 Results

4.1 Doppler Phase Measurements

We first present data showing that the characteristics of the signal envelope can be used to extract the effective acceleration along the axis of excitation, a. Although the value of a is dominated by g, we make this distinction because the experiment has significant systematic effects. Equation 2.49 for the two-pulse AI and equation 2.68 for the three-pulse AI show that the Doppler phase ϕ_D produces a similar modulation of the signal envelope for the two configurations of the AI.

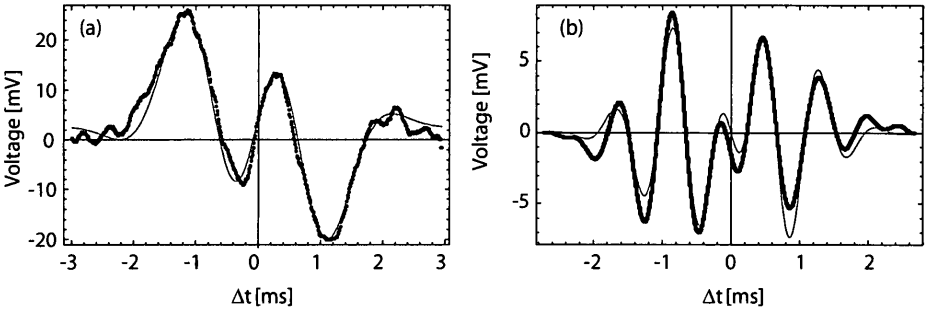

Figure 4.1: (a) Example of fit to the in-phase component of the two-pulse echo signal obtained on a single acquisition for $2T_{21} = 9.3$ ms using a sample of ^{85}Rb. (b) Example of fit to the in-phase component of the three-pulse echo signal obtained on a single acquisition for $2T_{21} + T_{32} = 45.1$ ms using a sample of ^{87}Rb.

If T_{21} and T_{32} are small, the signal envelope has a simple dispersion shape, which is shown in figure 2.5, and predicted by equation 2.24. As T_{21} and T_{32} are incremented, the effect of gravity produces oscillations in the signal shape, as shown in figure 4.1a and 4.1b. These figures show the in-phase component of the signal envelope obtained on a single acquisition for two-pulse and three-pulse configurations of the experiment, respectively. The effect of a is apparent for the echo time $2T_{21} = 9.3$ ms in figure 4.1a. In figure 4.1b, the echo time $2T_{21} + T_{32} = 45.1$ ms with $T_{21} = 1.5$ ms. Therefore, the effect of gravity produces an increased modulation frequency within the signal envelope.

For the analysis of the echo envelope, we assume that the Doppler modulation frequency across the signal envelope is a constant. The data set is fit to the form

$$A(t - t_0)e^{-(t-t_0)^2/2\tau} \sin[\omega(t - t_0)] + D, \tag{4.1}$$

as explained in section 3.5. This fit function is based on equations 2.47 and 2.66 that define the signal envelope. The fit shown in figure 4.1a is used to infer the frequency $\omega_{\mathrm{D}}^{(2)}$ given by equation 2.50, and the fit shown in figure 4.1b is used to infer the frequency $\omega_{\mathrm{D}}^{(3)}$ given by equation 2.69.

Figures 4.2a and 4.2b show the expected linear increase in frequency as a function of T_{21} for the two-pulse AI and as a function of T_{32} for the three-pulse AI, respectively. In these graphs, the frequency is determined by the weighted average of eight repetitions, and the error bar represents the standard deviation of the distribution.

Based on equation 2.50, the two-pulse angular frequency is given by $\omega_D^{(2)} =$

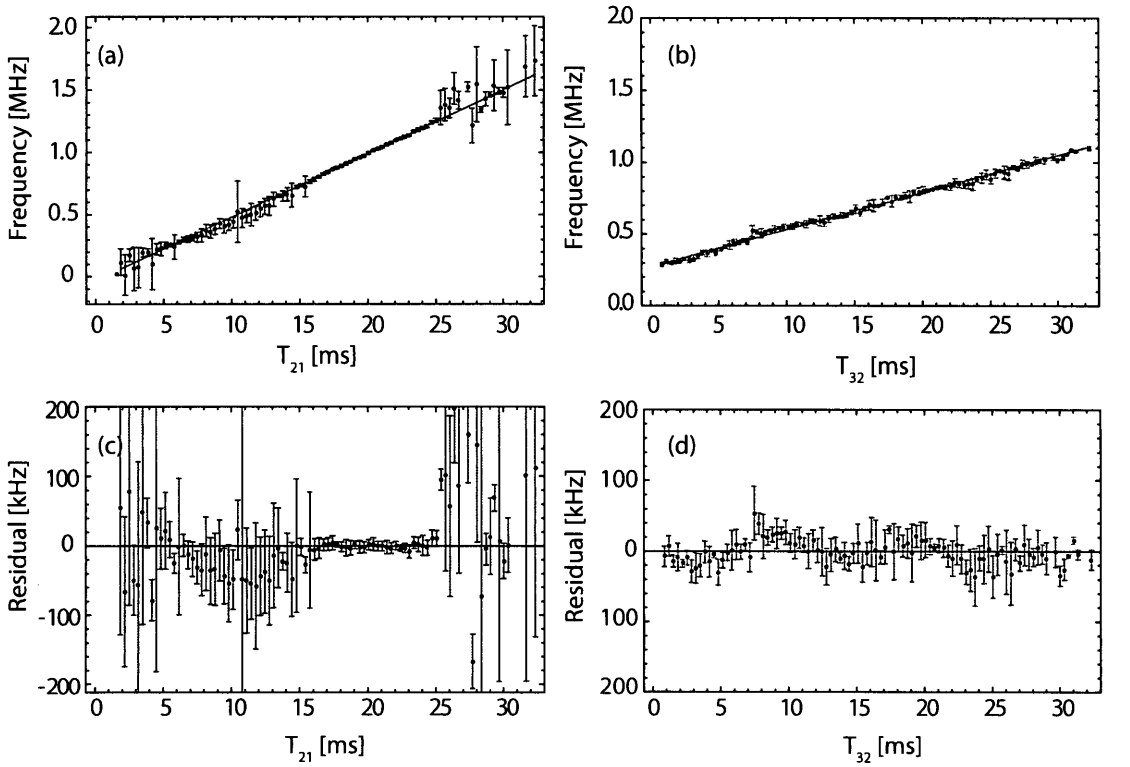

Figure 4.2: (a) Two-pulse Doppler phase measurement of a by varying T_{21} using a sample of ^{85}Rb. The slope of the line is 50.9(3) MHz/s with a corresponding statistical precision of 0.6%. The χ^2_{R} for this fit is 1.4. (b) Three-pulse Doppler phase measurement of a by varying T_{32} at a fixed $T_{21} = 7.5$ ms. Here we use a sample of ^{87}Rb. The slope of the line is 25.4(2) MHz/s, with a corresponding statistical precision of 0.8%. The χ^2_{R} for this fit is 0.94. (c) Residuals of the two-pulse linear fit. (d) Residuals of the three-pulse linear fit. Here $\tau_1 = 0.95$ μs, $\tau_2 = \tau_3 = 90$ ns. The intensity of the AI pulses is 50 mW/cm^2 and $\Delta = 55$ MHz.

$qg(2T_{21} + \Delta t) \approx qg(2T_{21})$ since $T_{21} \gg \Delta t$. Similarly, based on equation 2.69, the three-pulse angular frequency is given by $\omega_D^{(3)} = qg(2T_{21} + T_{32} + \Delta t) \approx qg(2T_{21} + T_{32})$ since $T_{21}, T_{32} \gg \Delta t$. Linear least squares fits to the two-pulse and three-pulse data sets show the slopes are 50.9(3) MHz/s and 25.4(2) MHz/s, respectively. The corre-

sponding uncorrected values of a are 9.93(6) and 9.91(4) m/s^2, respectively[14]. The results confirm that the slope for the two-pulse AI is twice the slope for the three-pulse AI and that these values are within statistical uncertainty. We note that the value of a determined from both AI configurations exhibits a significant dependence on the fit function used to model the echo envelope. The variation of a due to the fit function is at the level of $\pm 1\%$. Therefore, the values of a obtained from the Doppler phase are suitable for a relative comparison between the AI configurations, but not for an absolute measurement of acceleration.

The size of the statistical uncertainty is limited mainly by the relatively small temporal duration of the signal envelope, which is a few microseconds. An additional challenge is associated with fitting to the complicated signal shapes in equations 2.47 and 2.66. This is illustrated by the residuals for these data sets shown in figures 4.2c and 4.2d. Both the error bars and residuals are larger for the two-pulse AI. There are a number of factors that contribute to the characteristics of the residuals. For small T_{21}, the frequency of the two-pulse signal tends to zero and there are very few oscillations across the signal envelope, leading to a large uncertainty. In contrast, for the three-pulse AI, T_{21} was fixed at 7.5 ms, giving rise to a discernible oscillation frequency even if T_{32} is small, which leads to a reduced uncertainty for this range of T_{32}. The signal amplitude decreases as a function of T_{21} for the two-pulse AI. Although

[14]This uncorrected value of a is larger than the expected value of g. The sensitivity of the fit parameters produces a variation in the value in a as discussed at the end of this chapter. The corrections that need to be applied to extract g are discussed in Chapter 5.

the overall signal amplitude for the three-pulse AI is about 50% smaller, the signal decays more gradually as a function of T_{32}. Reduction in signal amplitude is caused by transit time losses, the Doppler shift due to falling atoms that prevents resonant two-photon excitation, and decoherence effects due to magnetic field curvature. Due to the reduced sensitivity to the last mentioned effect, the signal-to-noise ratio is generally higher for the three-pulse AI for large T_{32} resulting in reduced error bars.

It should be emphasized that vibrations and magnetic field curvature affect the signal amplitude and phase for both configurations of the AI. Since the longest timescale of three-pulse AI of 45 ms is attained with $T_{21} = 7.5$ ms, we expect the three-pulse AI to be much less sensitive to these effects than the two-pulse AI. In comparison, the longest timescale for the two-pulse AI of 64 ms is obtained with $T_{21} = 32$ ms. Therefore the three-pulse AI gives better fits to the signal envelope. The longest timescale for the three-pulse AI ($2T_{21} + T_{32} = 45$ ms) is attained with $T_{21} = 7.5$ ms, whereas the longest timescale of the two-pulse AI is attained with $T_21 = 32$ ms. Because of the smaller T_{21}, we expect the three-pulse AI to be much less sensitive to these effects than the two-pulse AI, giving better fits to the echo envelope. Accordingly, the overall size of the error bars in figure 4.2c are larger than in figure 4.2d.

The predicted dependence of ω_D on Δt in equations 2.50 and 2.69 can be measured in a longer timescale experiment, as shown later in this section. Although the three-pulse results may appear to be more precise, the statistical precision from both AI configurations is about the same since the three-pulse frequency spans a smaller range.

Another aspect of the two-pulse data is that the size of the error bars and residuals is noticeably smaller near $T_{21} = 6$ ms and 20 ms. This effect is not fully understood and we speculate that there are resonant responses to certain vibrational frequency bands.

For this discussion, we analyzed the modulation frequency of the signal envelope as a function of T_{21} and T_{32} to verify the predicted dependence of the Doppler phase in equations 2.49 and 2.68. We note that the change in modulation frequency can also be observed by varying the onset of the AI experiment with respect to the turn off of trapping beams. In practice, such an experiment can be performed by varying the 'dead time' T_1 between the end of the molasses stage and the onset of the AI pulse sequence.

4.2 Two-Pulse AI Phase Measurement

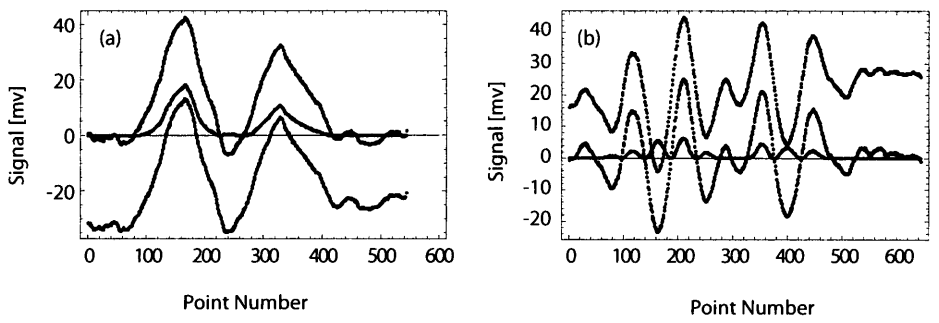

Figure 4.3: Examples of the "raw" echo envelope (blue traces) using a sample of ^{85}Rb at the echo time (a) $2T_{21} = 11$ ms and (b) $2T_{21} + T_{32} = 41$ ms . The corresponding background subtracted data set is shown in red. The square of the points is shown in green after scaling.

As noted in section 3.5, the in-phase and in-quadrature component amplitudes can be used directly to measure a. To obtain the in-phase component amplitude, the signal is background subtracted, and the points are squared and summed over the duration of the echo signal, as shown in figure 4.3. This method of analysis is particularly sensitive to background subtraction.

In general, fitting to the signal shape, as in figure 4.1a and 4.1b, and extracting the amplitude avoids this problem if the fits are of good quality. However, as shown in figure 4.1, amplitude extraction does not produce consistently good results because the signal shape is complicated and the corresponding form of the fit function is complex.

Using the square-sum method, the component amplitude extracted from raw data is shown in the left column of figure 4.4 as a function of T_{21}. The quadrature sum of the component amplitudes gives the total signal amplitude in the centre column. Each of the component amplitudes are normalized by the total signal amplitude $E_0^{(2)}$ to obtain the normalized signal amplitudes $\cos(\phi_{\mathrm{AI}}^{(2)})$ and $\sin(\phi_{\mathrm{AI}}^{(2)})$, shown in the right column of figure 4.4.

Figure 4.5 shows a measurement of a using the non-linear dependence of $\phi_g^{(2)}$ on T_{21}, as predicted by equation 2.53. Here, the best statistical precision was obtained with the upper corner-cube reflector placed on a vibration isolation platform and the lower AI optical setup placed on separate, uncoupled vibration isolation platform, with both platforms resting on the pneumatically supported optical table. The

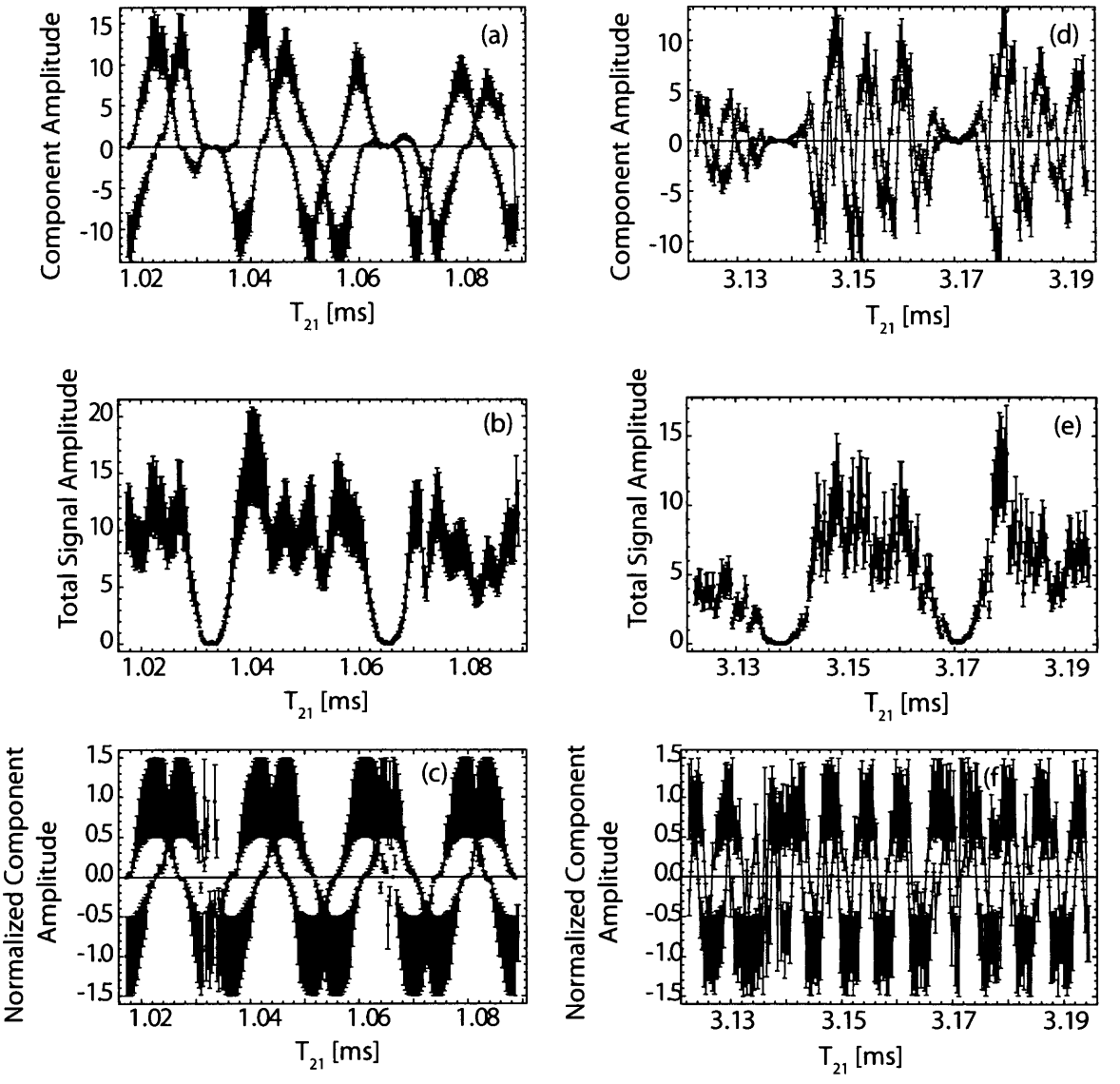

Figure 4.4: Examples of raw amplitude as a function of T_{21} showing recoil modulation at (a) 1 ms and (d) 3 ms using a sample of ^{85}Rb. The in-phase component is in blue, and the in-quadrature is in purple. Total signal amplitude $A(t) = \sqrt{S_{\mathrm{IP}}^2 + S_{\mathrm{Q}}^2}$ as a function of T_{21} at (b) 1 ms and (e) 3 ms. Normalized signal amplitude as a function of T_{21} at (c) 1 ms and (f) 3 ms.

amplitude of the in-phase component is recorded as a function of T_{21} using four observational windows in a data-acquisition time of one hour. Each window consists of

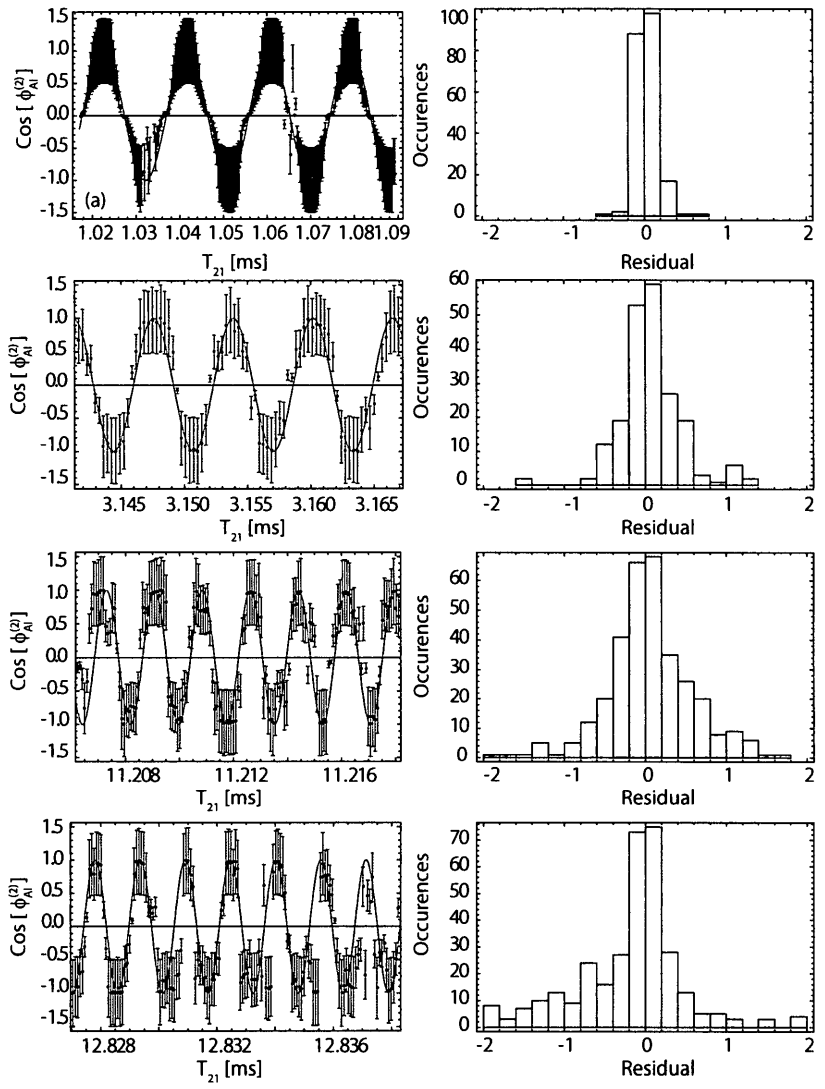

Figure 4.5: Left: Four observational windows showing the amplitude of the in-phase component for the two-pulse AI as a function of T_{21} using a sample of ^{85}Rb. The angular frequency $\partial\phi_{\mathrm{AI}}^{(2)}/\partial T_{21}$ increases linearly as a function of T_{21}. Here, $\tau_1 = 0.8$ μs, $\tau_2 = 90$ ns. The most statically precise fit was obtained with the points weighted equally. Right: Histogram of the residuals. The standard deviations of the residuals for the four windows are 0.13, 0.39, 0.60, and 0.73, respectively. Here, the intensity of the AI pulses is 50 mW/cm^2 and $\Delta = 55$ MHz.

about 200-325 points acquired in randomized order. Each data point is obtained by analyzing the signal envelope averaged over 16 repetitions. The error bars represent

the statistical uncertainty of these repetitions. The overall time window was limited to $T_{21} = 12.8$ ms because of the gradual breakdown of the periodically reset RF phase shown in figure 3.27.

Figure 4.5 shows the expected chirped sinusoidal dependence of $\cos(\phi_{\mathrm{AI}}^{(2)})$ on T_{21}. The data set for the in-phase component is fit to a multi-parameter fit function of the form $\cos(qaT_{21}^2 + qv_0T_{21} + \phi_0)$ to extract $a = 9.791\ 19(8)$ m/s^2. This measurement represents a statistical uncertainty of 8 ppm. Both the in-phase and in-quadrature components were obtained by mixing down the same photodiode signal with RF signals that have phase shifts of 0 and $\pi/2$. Similarly, we obtain $a = 9.791\ 35(8)$ m/s^2 from the in-quadrature component, which represents a statistical uncertainty of 8 ppm. From a weighted average of the in-phase and in-quadrature components, we obtain a statistical precision of 6 ppm. In this analysis, v_0 models a velocity parameter for the atoms, and ϕ_0 is the initial phase of the grating with respect to the nodal point on the inertial reference frame (corner-cube reflector). The typical value of v_0 was 0.107(1) mm/s. The physical origin of this effect associated with v_0 is not clear since the initial velocity does not contribute to the two-pulse AI phase. It is possible that intensity imbalances in the two standing wave components can produce this effect. In fact, centroid tracking of the atom cloud showed launch velocities of as high as 2 mm/s along the vertical. We speculate that intensity imbalances in the two standing wave components can produce this effect.

Figure 4.6a shows a sample of the residuals as a function of T_{21} for the time win-

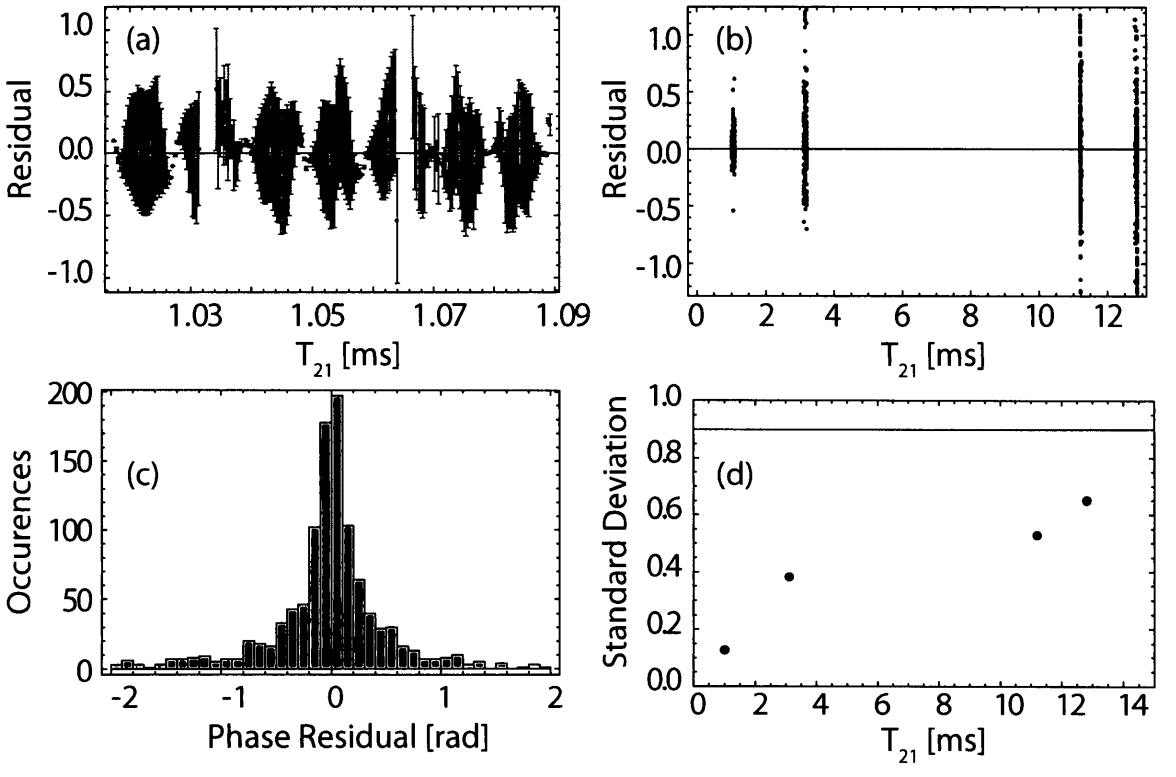

Figure 4.6: (a) Residuals of the fit shown in figure 4.5 in a single time window near $T_{21} = 1.05$ ms. (b) Residuals as a function of T_{21} for all windows in the data set. (c) Histogram of residuals for the entire data set. (d) Standard deviation of the residual in each window as a function of T_{21}. The red line corresponds to the standard deviation of a random distribution.

dow near $T_{21} = 1.05$ ms in figure 4.5. Figure 4.6b shows the residuals as a function of T_{21} for the time windows in figure 4.5. The standard deviations of the residuals for all four windows are smaller than the standard deviation for a random distribution. The increasing size of the residuals for $T_{21} > 10$ ms illustrates the sensitivity of the two-pulse AI to vibrations and other decoherence effects such as magnetic field curvature. The sensitivity to vibrations can be inferred since the best statistical precision was obtained by supporting the upper reflector and the AI optical setup below the

vacuum chamber on uncoupled vibration isolation platforms. In comparison, the distribution of the residuals was significantly smaller for the three-pulse AI when critical components were supported by a single vibration isolation platform. The residuals can be converted to phase to enable a more effective comparison. Figure 4.6c shows a histogram of the phase residuals for the entire data set obtained from figure 4.6b. The standard deviation of the phase residuals for the entire data set is 0.7 rad out of a total phase accumulation of 2.5×10^4 rad. Figure 4.6c shows that the standard deviation of the residuals for each window are smaller than the expected value for a random distribution.

Another indication that the two-pulse AI was more sensitive to vibrations is that the best statistical precision was obtained by adding an additional vibration isolation platform to support the upper reflector. In comparison, it was possible to obtain much better statistical precision for the three-pulse AI, as shown later in this section, by using a single vibration isolation platform to isolate the AI optics and corner-cube reflector in figure 3.18.

4.3 Three-Pulse AI Phase Measurement

We now discuss the data obtained with the three-pulse AI. The relative insensitivity of the three-pulse AI to vibrations compared to the two-pulse AI allows us to avoid the two previously mentioned analysis techniques, namely fitting to the echo envelope as well as the faster square-sum method. Instead, we use a slicing technique, in which

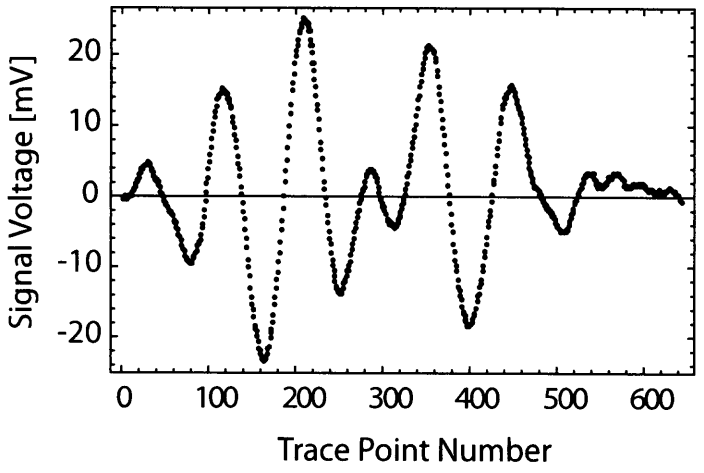

Figure 4.7: Trace of echo envelope acquired using a sample of ^{87}Rb at the echo time $2T_{21} + T_{32} = 41$ ms. An example of a time slice is indicated in red.

the instantaneous amplitude of the background subtracted data set is found from a single time slice, as shown in figure 4.7. The best statistical precision in the following results was obtained with 200 slices, each with a temporal duration of 10 ns. This slice duration was chosen since there is effectively no change in the signal amplitude over this timescale. The average amplitude of each slice was determined by averaging 16 repetitions.

Figure 4.8a and figure 4.8b show $\cos(\phi_g^{(3)})$ as a function of T_{32} for a single slice shown in figure 4.7 with T_{21} fixed at 7.5 ms. This data set was recorded with 100 points in each window acquired in randomized order in one hour. We note that the greatest phase accumulation for the three-pulse AI is obtained with $2T_{21} = T_{32}$, suggesting the ideal value of $T_{21} = 11$ ms. However, we choose to operate with $T_{21} = 7.5$ ms due to the reduced effect of vibrations and decoherence mechanisms. As predicted by equation 2.72, the signal exhibits a single frequency that can be precisely determined

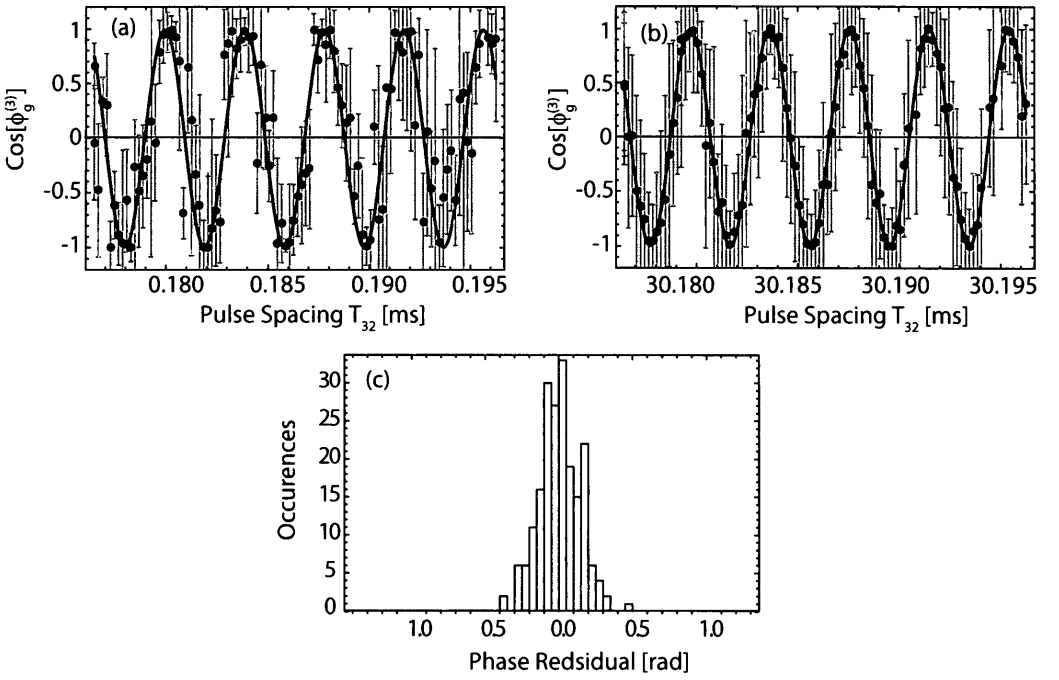

Figure 4.8: Two observational windows of the amplitude of the in-phase component for the three-pulse AI with T_{32} in the range of (a) 0.2 ms and (b) 30 ms using a sample of ^{87}Rb. This data set corresponds to a single time slice and exhibits a constant frequency as a function of T_{32}. Here, $T_{21} = 7.5$ ms. (c) Histogram of phase residuals for the data in (a) and (b). The frequency extracted from the fit is 187 324.75(8) Hz.

using two observational windows spaced widely apart.

The in-phase and in-quadrature components $\cos(\phi_g^{(3)})$ and $\sin(\phi_g^{(3)})$ were obtained by following the same normalization protocol as for the two-pulse AI. This means that each component amplitude is normalized by the total signal amplitude $E_0^{(3)}$ to obtain the normalized signal amplitudes $\cos(\phi_{\rm AI}^{(3)})$ and $\sin(\phi_{\rm AI}^{(3)})$. Using a single slice, the frequency given by equation 2.74, as $\omega_{AI}^{(3)} = qaT_{21}$ allows a to be determined. Here we obtain $a = 9.833\ 245(4)$ m/s^2, which represents a statistical precision of 0.4 ppm. This statistical precision can be compared to the 6 ppm statistical uncertainty for the

two-pulse AI.

The enhancement in precision can be attributed to several effects. Firstly, the analysis involves fitting to a single frequency in the absence of recoil modulation. Secondly, the measurement time scale has also been significantly extended in comparison to the two-pulse AI since this data set represents a total timescale $2T_{21}+T_{32} = 45$ ms while limiting the value of T_{21} to 7.5 ms[15]. Therefore there is reduced sensitivity to the effects of magnetic curvature and vibrations. The insensitivity to these effects also leads to a more gradual decay of the signal amplitude. As a result, we obtain a similar standard deviation of the phase residuals (≈ 0.2 rad) in each observational window, as shown in figure 4.8c. In comparison, the overall standard deviation is 0.7 rad for the two-pulse AI. Indeed, the slicing technique cannot be expected to work without good phase stability.

A further improvement to this statistical uncertainty can be achieved by processing the frequency of all time slices across the echo envelope. Figure 4.9a shows the frequency of each time slice as a function of Δt. The data set confirms the linear dependence of the angular frequency on Δt predicted by

$$\omega_a^{(3)} = \frac{\partial \phi_g^{(3)}}{\partial T_{32}} = qa(T_{21} + \Delta t), \tag{4.2}$$

similar to equation 2.69. Each data point in figure 4.9a has a typical error bar of 1 ppm (one of the best data sets is presented in figure 4.8). The reduced error bar

[15]Although theoretically $T_{32} = 2T_{21}$ for the greatest phase accumulation, we found that $T_{21} = 7.5$ ms resulted in better statistical precision than $T_{21} = 11$ ms. This could be due to better vibrational shielding for certain timescales as noted in Section 4.1.

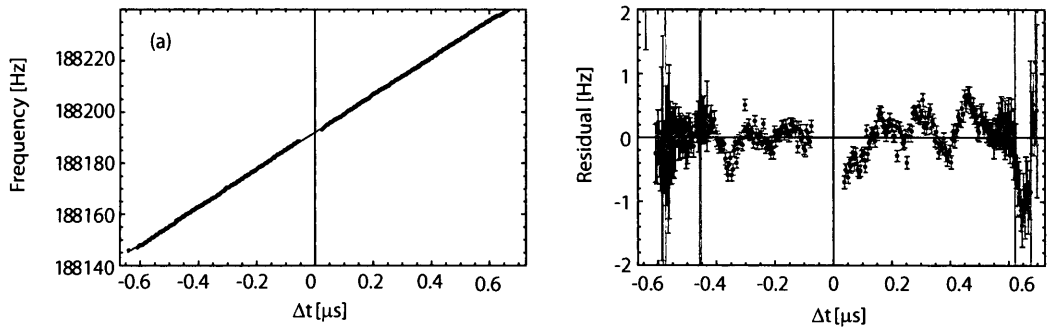

Figure 4.9: (a) Measurement of frequencies across the signal envelope using 200 time slices. The χ^2_R for this fit is 0.94 (b) Residuals of the linear fit. The intercept of the line is 188 192.095(17) Hz giving an uncorrected value of $a = 9.877\ 445\ 8(9)\ \mathrm{m/s^2}$. Similar analysis of the in-quadrature component gives a value of 188 158.67(4) Hz, which reduces the final statistical error to 75 ppb.

in comparison to the two-pulse AI results is a consequence of the 30 ms timescale spanned by the two observational windows. The resulting sensitivity allows the Δt dependent frequency change across the signal envelope predicted by equation 2.69 to be observed. In contrast, for the data in figure 4.1, we assume a constant frequency across the signal envelope since the observational window is only a few microseconds long and the measurement does not have the desired sensitivity.

For the data in figure 4.9a, the limited timescale of the echo envelope and the scatter lead to an overall statistical error in the slope that is appreciable (600 ppm) despite the relatively small statistical error in each of the points (1 ppm). The scatter is attributed to magnetic effects described in the next section. However, the error in the frequency intercept is much more tightly constrained since the data points are closely clustered near $\Delta t = 0$. Based on equation 4.2, the frequency intercept is qaT_{21}. A linear fit allows this frequency intercept to be determined as 188 192.095(17) Hz.

The corresponding value of a is 9.877 445 8(9) m/s^2, which represents a statistical precision of 90 ppb. A weighted average of the measurements from the in-phase and in-quadrature components gives a final statistical precision of 75 ppb. Figure 4.9b shows the residuals to the straight line fit in figure 4.9a. The residuals increase in size in the regions where the signal is small such as in the extremities and in the vicinity of $\Delta t = 0$.

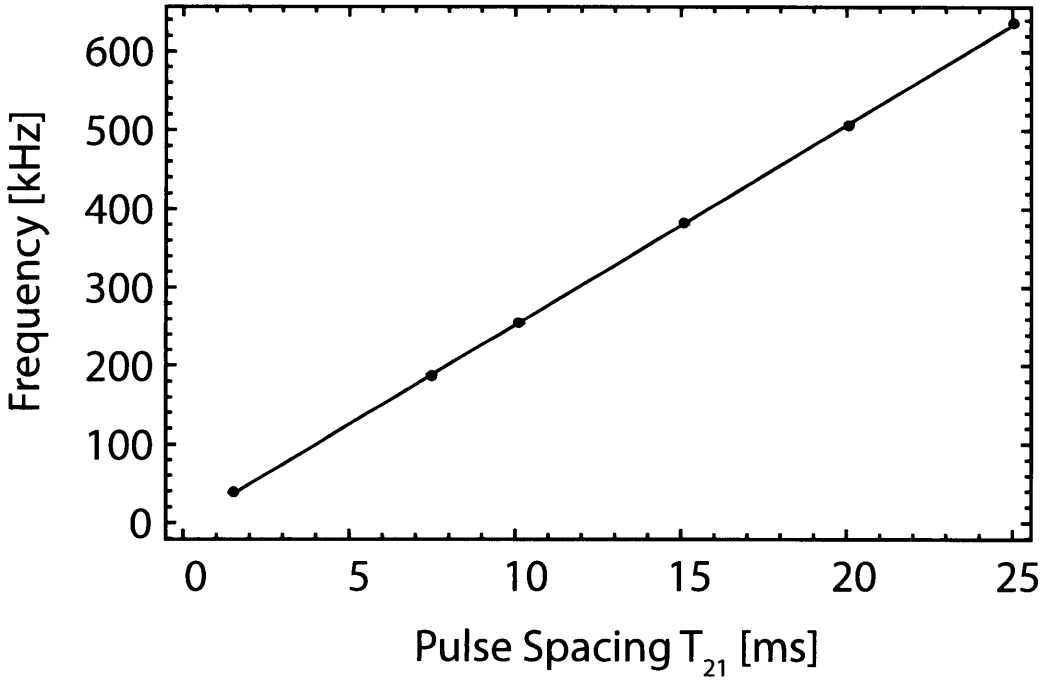

Figure 4.10: Frequency change of the three-pulse AI as a function of T_{21} acquired using a sample of ^{87}Rb. The size of the vertical error bars (90-150 ppb) are too small to be seen. The slope of the linear fit is 25.41(6) MHz/s. The corresponding value of a is 9.91(2) m/s^2.

In figure 4.10, we investigate the frequency of the three-pulse AI signal as a function of T_{21}. For this data set, the total experiment time, $2T_{21} + T_{32}$, is fixed but the time window over which the atoms are most sensitive to accelerations, T_{21}, is varied.

For each value of T_{21}, the frequency is determined from the intercept, as in figure 4.9a. The data set shows the linear dependence of the frequency on T_{21}, as predicted by equation 2.74. The slope of the linear fit is $2ka = 25.41(6)$ MHz/s. Although each data point has an error bar of 90-150 ppb, the overall error in the slope is 0.2% due to the scatter in the points. This scatter can be ascribed to magnetic field effects due to the magnetized vacuum chamber and influence of curvature from external cancelling coils and the variation in the initial velocity of atoms for different repetitions of the experiment. We note that the primary systematic effects caused by magnetic effects and trap launch are generally not controllable in the current setup.

4.4 Summary

Table 4.1 summarizes the values of a obtained using the different techniques outlined in this chapter. The value of a extracted from the data set has been corrected for two controllable systematic effects. The first is the angle of the excitation beam θ with respect to the vertical, which produces a correction $a' = a/\cos\theta$. The typical value of θ for the results in table 4.1 is 15 mrad.

The second correction only applies to velocity-dependent measurement in figures 4.8 and 4.9. Therefore this correction applies to the three-pulse amplitude velocity dependent measurement entry in table 4.1. In all these velocity-dependent measurements, the excitation pulse sequence was applied 88 μs after the extinction of the trapping beams. Thus, the velocity acquired during this 'dead time' has to be con-

Method	Extracted a [m/s^2]	Corrected a [m/s^2]	Uncertainty compared to baseline g	Notes
Two-Pulse Envelope	9.93(6)	9.93(6)	1.3%	Angle Only
Three-Pulse Envelope	9.91(4)	9.91(4)	1.1%	Angle Only
Two-Pulse Amplitude	9.791 19(8)	9.792 29(8)	0.1%	Angle Only
Three-Pulse Amplitude	9.877 445 8(9)	9.816 237 2(9)	0.1%	Angle and Temporal Offset
Slope from Fig. 4.10	9.91(2)	-	1.1%	

Table 4.1: Summary of the extracted value of a with the methods described in this dissertation.

sidered when extracting a, as explained in more detail in Chapter 5.

The measurements in table 4.1 can be compared to the absolute value of g determined by a falling corner cube optical interferometer (Scintrex model FGL) located in the research lab. This baseline value of $g = 9.804\ 165\ 15(5)$ m/s^2 is obtained with an overall precision of 5 ppb (sum of statistical and systematic uncertainties) by subtracting the effect of tides and the Earth's gravity gradient, which was assumed to be 300 ppb of g per metre. The last two corrected values in the table agree with the baseline value of g at the level of 0.1%. This represents a satisfactory level of agreement since the maximum extent of the uncontrolled systematic effects discussed in Chapter 5 is of order 630 ppm for the two-pulse AI and 2.2% for the three-pulse AI. Other representative methods of extracting a, such as from the slope in figure 4.10, will be discussed in Chapter 5.

The first two entries in this table also agree with the baseline value of g if all the systematic effects are included. However, as previously noted in this chapter, the value of a based on the determination of the Doppler phase is sensitive to the nature of the fit functions. Therefore, great caution should be exercised in using these values for comparison or for absolute measurements of g.

In summary, we have demonstrated a statistically precise measurement of the acceleration a along the axis of standing wave excitation can be obtained using different techniques. Analysis of the signal envelope resulted in a statistical precision of 0.5%. Analysis of the signal amplitude and phase of the two-pulse AI resulted in a statistical precision of 5 ppm. By exploiting the advantages of the three-pulse AI, an improved statistical precision of 75 ppb was achieved. The values of a quoted in this chapter were affected by significant systematic effects, which are discussed in the next chapter.

5 Discussion and Future Work

The measurements reported in Chapter 4 of this dissertation represent significant improvements in statistical precision for measurements of g using echo techniques. The two-pulse AI was used to obtain a statistical precision of 100 ppm in reference [31] on a 1 ms timescale. Elimination of decoherence effects due to collisions and background light resulted in measurement timescales of ≈ 20 ms and led to a statistical precision of 15 ppm in several hours of data acquisition [32]. The timescale of the experiments described in reference [32] and the measurements in this dissertation were principally limited by a magnetized vacuum chamber. Operational constraints permitted the vibration isolation of only critical components of the experiment. Nevertheless, these improvements coupled with better data analysis techniques allowed the two-pulse AI to operate with a statistical precision of 6 ppm. The three-pulse AI was developed to reduce the impact of magnetic curvature and vibrations so that measurement timescales of 50 ms could be achieved, resulting in a statistical precision of 75 ppb.

Recent experiments relating to measurements of magnetic interactions [39], magnetic gradients [35], and atomic recoil [38] utilized a low-cost, non-magnetic apparatus and achieved measurement timescales of up to 220 ms. However, these experiments

relied on measurements of the signal intensity and did not require vibration isolation. Therefore, the aforementioned non-magnetic apparatus was not suitable for measurements of gravity.

In this chapter, we discuss the main sources of systematic uncertainties, which are predominantly due to the magnetized vacuum chamber. This is followed by a discussion of phase noise due to vibrations, timescale, signal size, and methods of improving the phase stability. Based on the improved signal-to-noise ratio and timescale obtained in the non-magnetic apparatus, we project the measurement sensitivity for gravitational measurements that can be realized with adequate vibration stabilization. We discuss how such an experiment can be realized by (i) magnetic state selection into an $m = 0$ sublevel to further suppress magnetic effects, (ii) improved passive isolation, (iii) active stabilization of the inertial reference frame, and (iv) improved detection techniques. The proposed measurement is currently underway in my research group based on the efforts of another graduate student.

At the end of the chapter, we present simulations of the signal-to-noise ratio for the improved experiment and review relevant experimental techniques to achieve the goals of the proposed experiment.

5.1 Systematic Effects

Table 5.1 shows the typical values of the major systematic effects that must be used to correct a.

Systematic	Estimate	Shift
Verticality	$\vartheta_\perp = 15$ mrad	+ 110 ppm
Index of Refraction	$n = 0.9999955$	- 4.5 ppm
Diffraction	$\vartheta_{\mathrm{Div}} = 0.8$ mrad	± 0.35 ppm
Magnetic gradient	∇ B = 8 mG/cm	± 520 ppm
Magnetic curvature	∇^2B = 4.3 mG/cm^2	± 340 ppm
Three-Pulse Time Offset	$T_1 = 88$ μs	- 2000 ppm
Three-Pulse $T_{21} = 7.432$ ms Launch Velocity	$v_L = 2$ mm/s	± 22 000 ppm

Table 5.1: Summary of dominant systematic effects on a currently limiting the experiment.

5.1.1 Angle Correction

Based on equations 2.39 and 2.64, the uncertainty in a is linearly dependent on the uncertainty in q. The flatness of the corner-cube retro-reflector ensures that the two-travelling wave components of each SW pulse deviate from 180° by no more than θ = 3 arcseconds. Since $q = 2k\cos(\theta)$, a small angle approximation gives $\Delta q = 2k\frac{\theta^2}{2}$. This corresponds to a 0.1 ppb deviation in q, which is negligible compared to other sources of uncertainty.

A larger systematic uncertainty occurs due to the deviation of the AI beam axis from the vertical. At the beginning of the experiment, the standing-wave components were aligned to within 1 mrad of the vertical by suspending a ring[16] of aluminum with

[16] A ring was used so that the laser beam could pass through and illuminate the plumb-line defining the vertical.

thread attached to the ceiling. An iris was used to reduce the size of the AI beam to 1 mm, and the beam was aligned along the plumb line created by the string and ring. The diameter of the thread was less than 1 mm and the laser beam was aligned so that the thread was illuminated for a distance greater than 1 m. This angle corresponds to a deviation of 1 mrad from the vertical. However, when the corner-cube reflector is introduced, the weight distribution on the vibration-isolation platform changes. Thus, the alignment of the excitation beam along the vertical is compromised, leading to a typical deviation from the vertical as large as 15 mrad. The projection of g on the laser beam axis is $g\cos(\theta) \approx g(1+\theta^2/2)$. Therefore the maximum correction $\Delta g/g$ = 110 ppm.

5.1.2 Index Correction

Additionally, the index of refraction of the sample also imposes a correction to q. The index of refraction n is dependent on both the sample density and the detuning of the excitation [125] and is given by

$$\eta = \sqrt{1 - \frac{n\mu_{21}^2}{\epsilon_0 \hbar \Gamma^2} \frac{\Delta/\Gamma}{1+(\Delta/\Gamma)^2}}, \tag{5.1}$$

where n is the number density of the atoms, $\mu_{21} = 3.584(4) \times 10^{-29}$ C·m is the dipole matrix element corresponding to the ground state-excited state transition, $\epsilon_0 = 8.85 \times 10^{-12}$ F/m is the permittivity of free space, $\Gamma = 2\pi \cdot 6.066\,6(18) \times 10^6$ rad/s is the radiative rate of the excited state, and $\Delta = 2\pi \cdot 50 \times 10^6$ rad/s is the detuning of the excitation beam in angular units.

The number density, n, of the atoms calculated with the typical number of atoms 0.5×10^9 and the typical $1/e^2$ radius of the trap, 3 mm, gives $n = 4.4\times10^9$ atoms/cm^3. With this density, we have estimated the index correction based on typical conditions to be 4.5 ppm.

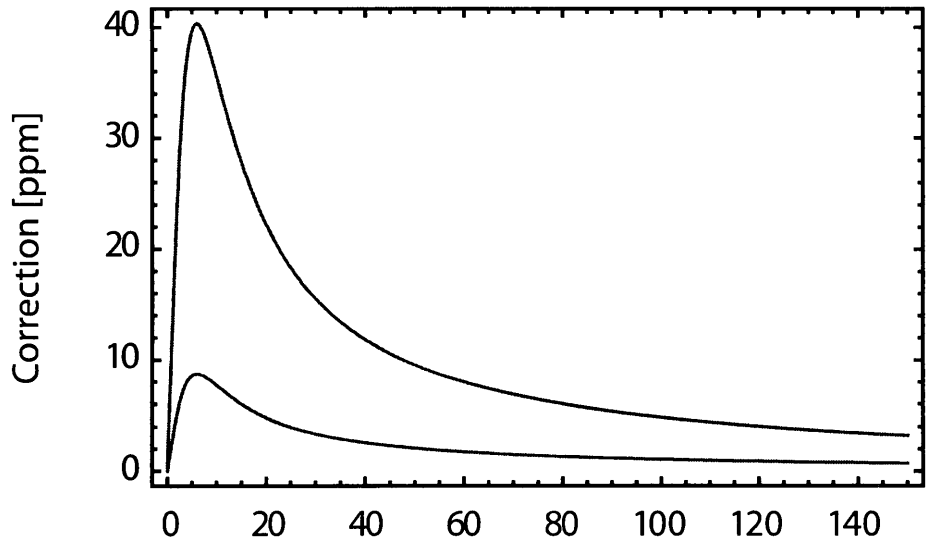

Figure 5.1: Range of index of refraction correction as a function of detuning Δ. The upper trace corresponds to a number density of 4.4×10^9 atoms/cm^3 and the lower trace corresponds to a number density of 1×10^9 atoms/cm^3.

However, the number density changes as a function of time as the cloud undergoes thermal expansion. The predicted change in the index of refraction for typical densities is shown in figure 5.1 for the positive detunings used in the experiment. With a typical trap temperature of 20 μK, 50 ms of expansion would increase the trap radius to 5 mm, and reduce the corresponding density to 1×10^9 atoms/cm^3. Therefore, the index of refraction correction is reduced to 2 ppm.

5.1.3 Magnetic Gradient Correction

This AI manipulates atoms in a single hyperfine ground state with an undetermined distribution of populations in the different magnetic sublevels. Therefore, the AI signal has contributions from all magnetic sublevels. As a result, magnetic gradients and magnetic field curvature introduce much larger systematic shifts than the effect of uniform magnetic fields.

The magnetic gradient in the vicinity of the atom cloud is significantly influenced by the magnetized stainless steel vacuum chamber. Since it is not possible to place a magnetic field sensor inside the vacuum chamber, we use the well-understood dependence of the echo signals on magnetic gradients to infer the gradient sampled by the atoms.

Gradient cancelling coils are used to reduce the average gradient so that the timescale of the experiment is maximized. Based on references [32] and [35], it is known that the echo signal exhibits amplitude oscillations with a phase

$$\phi_M = \frac{q m_F g_F \mu_b \nabla B}{2M} \Upsilon \tag{5.2}$$

in the presence of a magnetic gradient ∇B, where $\Upsilon = T_{21}^2$ for the two-pulse AI, and $\Upsilon = T_{21}^2 + T_{32}T_{21}$ for the three-pulse AI, g_F is the Landé g factor, and μ_b is the Bohr magneton. Similar to gravity induced amplitude modulation, the signal shape for the three-pulse AI is governed by the expression $E_0^{(3)}(T_{21}, T_{32})\cos(\phi_M)$, where $E_0^{(3)}(T_{21}, T_{32})$ is given by equation 2.71. The frequency of the magnetic gradient

induced amplitude oscillations for the three-pulse AI is given by

$$\frac{\partial \phi_M}{\partial T_{32}} = \frac{q m_F g_F \mu_b T_{21}}{2M} \nabla B. \tag{5.3}$$

The first zero of the oscillation occurs at the phase $\phi_M = \pi/2$, or, at a magnetic gradient of

$$\nabla B = \frac{2\pi M}{q g_F \mu_b \Upsilon}. \tag{5.4}$$

Examples of the two-pulse and three-pulse decays are shown in figure 5.2. The measured $1/e^2$ timescale for the two-pulse AI is $\approx$ 11 ms and the $1/e^2$ timescale for the three-pulse AI is $\approx$ 28 ms. This is much shorter than the expected transit time of 250 ms because of a number of limitations. To obtain such a transit-time-limited timescale, it is necessary to work in a non-magnetic apparatus with no magnetic curvature. It is also necessary to chirp the frequencies of the travelling-wave components of the standing-wave excitation to maintain the two-photon resonance condition as the atoms fall in gravity, as in references [32] and [38]. However, the need for a frequency chirp is reduced if the excitation pulse bandwidths are sufficiently large ($1/\tau_2$ = 10 MHz), as is the case for this work.

Inserting the estimated value of the timescale factor $\Upsilon = 0.011^2$ in equation 5.4, the magnetic gradient is calculated to be ∇B = 12 mG/cm. For the three-pulse AI, the T_{32} dependent $1/e^2$ timescale is 28 ms for a T_{21} of 5.5 ms. Inserting these values for the timescale into the expression for Υ, we obtain a magnetic gradient ∇B = 7.5 mG/cm. These measurements give the estimated range of gradients sampled by

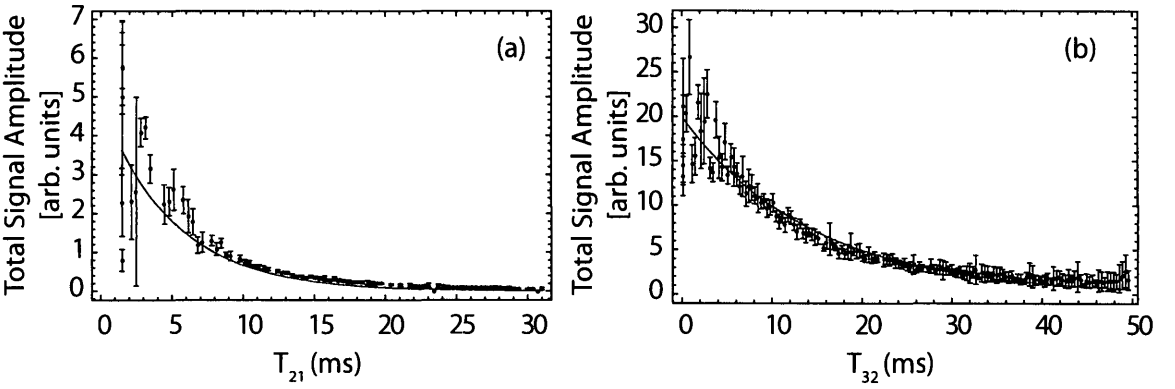

Figure 5.2: (a) Plot of total signal amplitude for the two-pulse AI as a function of T_{21}. (b) Plot of total signal amplitude for the three-pulse AI as a function of T_{32}. In both cases, the data points are the average of 16 repetitions, with the error bar being the standard deviation of these repetitions. The data set is fit to a decaying exponential to extract the $1/e^2$ time constant of 11 ms in (a) and the $1/e^2$ time constant of 28 ms in (b). We note that the amplitude of the two-pulse and three-pulse signals are expressed in scaled units and cannot be directly compared. In general, the three-pulse signal is about two times smaller than the two-pulse signal.

the atoms[17].

A more direct estimate for the magnetic gradient sampled by the atoms is shown in figure 5.3. Here, the frequency of amplitude oscillations is measured as a function of the magnetic gradient and extrapolated to find the magnetic gradient for the lowest observed oscillation frequency as in reference [32]. Using the three-pulse AI, the results from figure 5.3 give the magnetic gradient $\nabla B = 8.5$ mG/cm which is comparable to the measurement using the timescale.

The systematic error in a due to magnetic effects is the ratio of the phase caused

[17]These two measurements were obtained after a considerable time gap of several months during which the chamber was repeatedly de-magnetized. Therefore, it is not surprising that the magnetic field has changed during this interval.

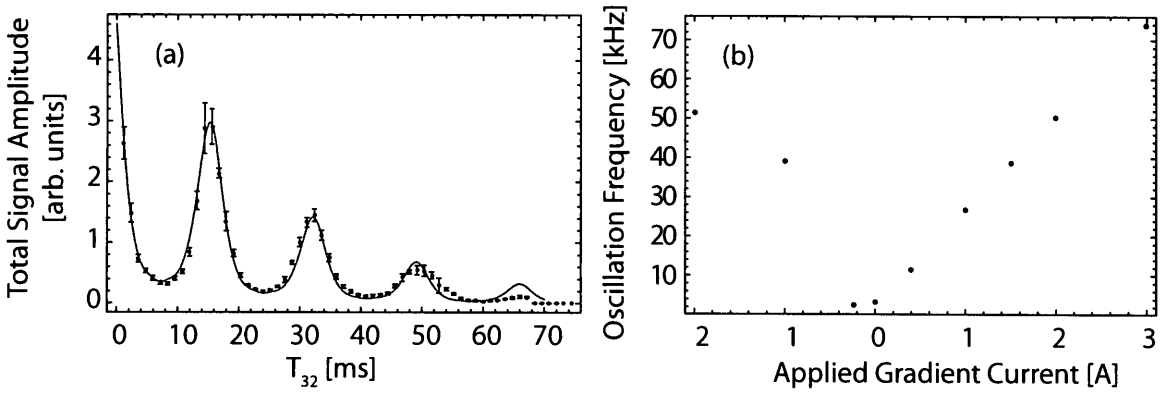

Figure 5.3: Studies of the magnetic gradient induced amplitude modulation as a function of T_{32}. (a) Plot of total signal amplitude as a function of T_{32} in the presence of an external gradient. From (a), the frequency of the magnetic gradient induced amplitude oscillations is extracted, and plotted in (b) as a function of applied current in the gradient cancelling coils. From the graph, the frequency of the magnetic gradient induced amplitude oscillation frequency can be found from the applied cancelling current.

by the magnetic gradient divided by the phase caused by gravity,

$$\Delta g = \frac{m_F g_F \mu_b \nabla B \Upsilon}{M g \Upsilon}. \tag{5.5}$$

Although the time dependent factor Υ is different for the two-pulse and three-pulse AIs, equation 5.5 is the same for both configurations. For an atom in the $m_F = 2$ sublevel, we assume a typical gradient of $\nabla B = 8$ mG/cm[18], to estimate the correction to the phase, and the resulting correction to a is 520 ppm.

The size of this correction is comparable to an estimate based on an independent characterization of the AI. In this experiment, the value of g was measured using the three-pulse AI with T_{21} fixed at 5.5 ms and the AI frequency determined with two

[18]This is the average of 7.5 mG/cm determined by decay time measurements and 8.5 mG/cm determined from amplitude oscillations.

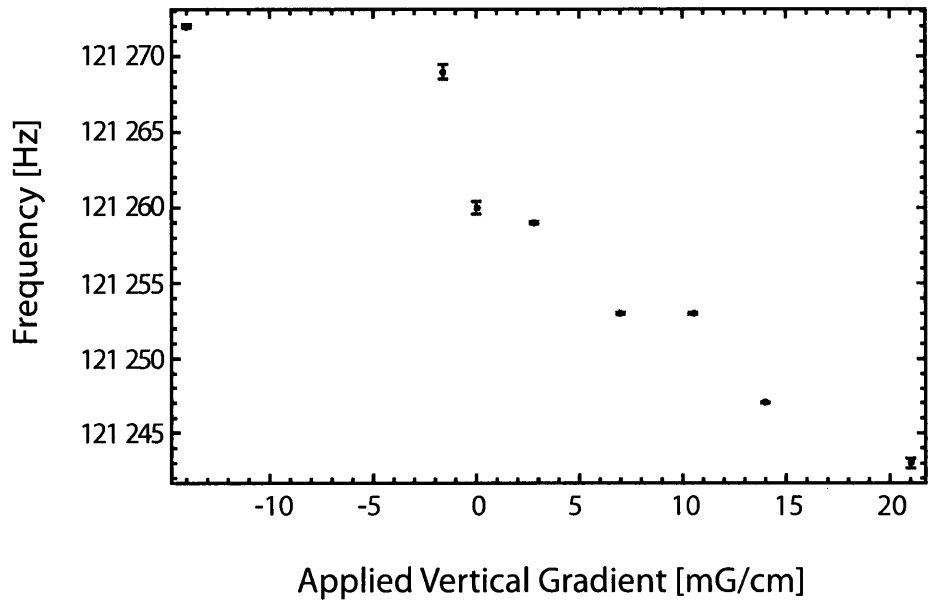

Figure 5.4: Plot of the frequency of the three-pulse AI as a function of current in the set of coils that is used to adjust the vertical magnetic gradient. Error bars represent the statistical precision of the measured frequency. The values for $T_{21} = 5.5$ ms and $T_{32} = 50$ ms. The total change of frequency is 25 Hz, a 240 ppm change in a.

observational windows separated by 50 ms in a manner similar to figure 4.8. Figure 5.4 shows the AI frequency obtained in this manner as a function of the current in the magnetic gradient cancelling coils. The graph shows a 240 ppm change suggesting that the estimated correction is reasonable.

5.1.4 Magnetic Curvature Effects

Another large systematic error appears to arise from the curvature of the magnetic field cancelling coils. From the geometry of the cancelling coils, the curvature of the magnetic field across the atoms is estimated to be 4.3 mG/cm^2. For atoms falling for 50 ms, the maximum correction to a is estimated to be 340 ppm.

This estimate was obtained by rewriting equation 5.5 as

$$\Delta g = \frac{m_F g_F \mu_b (\nabla^2 B \Delta z)}{g}. \tag{5.6}$$

and inserting the drop height for 50 ms, given by $\Delta z = \frac{g}{2}(0.050)^2 = 1.2$ cm.

In the presence of magnetic field curvature, the gradient sampled by the interfering momentum states will have a spatial variation. The phases of the momentum states change as a function of spatial location resulting in systematic correction to a. As shown in figure 4.10, the statistical variation in the slope (which represents a variation in a) is at the level of 2000 ppm if T_{21} is varied. Changing T_{21} implicitly changed the spatial region sampled by the momentum states. Therefore it is possible that the observed statistical change of 2000 ppm is strongly influenced by the curvature and gradient corrections.

The origin of the field curvature is difficult to isolate since it has contributions from the cancelling coils, magnetized vacuum chamber, and ion pump magnets. We have estimated this effect based solely on the properties of the cancelling coils.

5.1.5 Differential m_F-level phase shift

The gradient systematic can be predicted on the basis of numerical simulations for arbitrary m_F population distributions. The differential m_F-level shift has the same physical origin as the magnetic gradient effect. Based on references [117, 126], it is possible to describe the total backscattered electric field as a superposition of electric field amplitudes from individual sublevels. These contributions are weighted by pulse

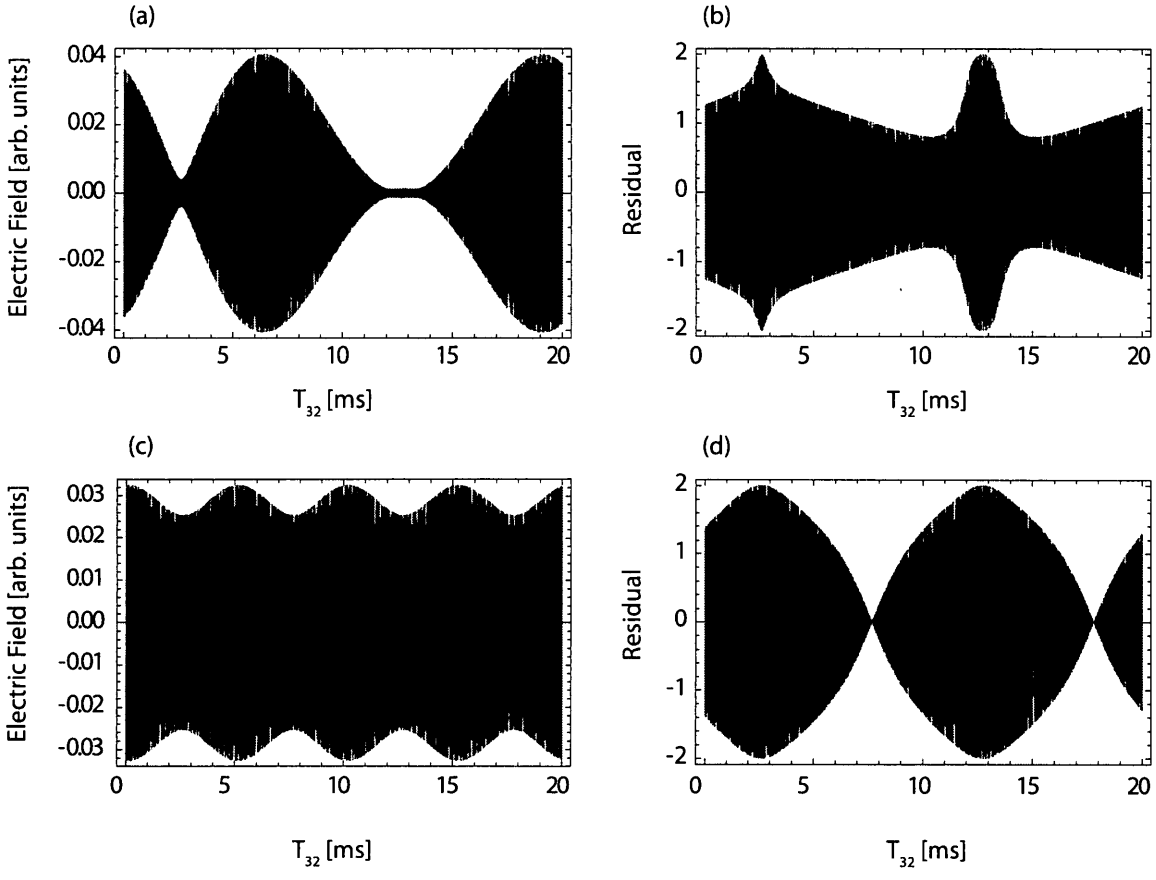

Figure 5.5: (a) The un-normalized total electric field emitted from an equal population distribution in m_F-levels. (b) The residual of the normalized total electric field of (a) compared to a $m_F = 0$ pumped population. (c) The total electric field emitted from a population distribution in the $m_F = -2$ and $m_F = +2$ levels. (d) The residual of the normalized total electric field of (c) compared to a $m_F = 0$ pumped population.

areas and Clebsch-Gordan coefficients.

The total backscattered electric field is a weighted sum given by

$$E = \sum_{n=-F}^{+F} \rho_n \left(C^{J_{GR}\ 1\ J_{EX}}_{m_{GR}\ q_L\ m_{EX}}\right)^2 J_F\left(2\vartheta \left(C^{J_{GR}\ 1\ J_{EX}}_{m_{GR}\ q_L\ m_{EX}}\right)^2 \sin[\omega_q T]\right) e^{i(\phi_g+\phi_M)}, \qquad (5.7)$$

where $\left(C^{J_{GR}\ 1\ J_{EX}}_{m_{GR}\ q_L\ m_{EX}}\right)$ is the Clebsh-Gordan coefficient of the $|J_{GR}, m_{GR}\rangle$ ground state and $|J_{EX}, m_{EX}\rangle$ excited state, q_L is the angular quantum number of the photon, ρ_n

is the population fraction in the $m_F = n$ state, J_F is the Bessel function of the first kind, ϕ_g is the gravitational phase and ϕ_M is the magnetic phase.

Using an overall pulse area $\vartheta = 1$, the signal from each of the m_F-levels in the ground state manifold was simulated on the basis of equation 5.7 for ^{87}Rb. The Clebsh-Gordan coefficients for the different m_F-levels and the individual pulse areas for the independent two-photon transitions from each sublevel produces characteristic modulation in the total electric field amplitude.

Figure 5.5a shows the results for uniformly populated sublevels. Figure 5.5c shows the results for the extreme state pumping into the -2 and +2 sublevels. A system optically pumped into a single m_F level will produce a pure sinusoid. If this m_F level corresponds to $m_F = 0$, the sinusoid can be used as a reference. For all other distributions, each m_F contributes an independent sinusoid. The total electric field of the backscattered light was computed in figure 5.5 by summing the individual electric fields from each sublevel. This electric field was normalized and fit to the expected frequency for the three-pulse AI based on an assumed value of g. This frequency was compared to the frequency obtained for the system pumped into $m_F = 0$ to calculate the differential m_F-level shift.

For the three-pulse AI involving ^{87}Rb, the simulations confirm that a gradient of 8 mG/cm will result in a maximum correction of 520 ppm for atoms pumped into the $m_F = 2$ sublevel and that other population distributions produce smaller effects.

5.1.6 Temporal Offset

The two-pulse AI measurement in figure 4.5 is independent of the initial velocity of the sample because the technique is only sensitive to the change in velocity during the AI pulse sequence. In contrast, the three-pulse measurements in figure 4.8 and figure 4.9 are sensitive to the initial velocity of the sample at the beginning of the pulse sequence.

For all these results, there was an overall dead time of $T_1 = 88$ μs before the start of the AI pulse sequence with respect to the end of the molasses cooling stage. Since the atoms have acquired an initial velocity during this delay time because of gravity, there is a systematic offset in the frequency measured for every slice. To understand this effect, we note that the AI frequency for a single point on the echo envelope is given by equation 2.73. To include the effect of the envelope, it is necessary to use the Doppler frequency in equation 2.69. This equation is in turn modified by the effect of the 'dead time' T_1 so that

$$\omega_D^{(3)} = qg(T_1 + T_{21} + T_{32} + T_{21} + \Delta t). \tag{5.8}$$

This effect leads to a -2000 ppm shift in the value of a in table 5.1 for the three-pulse AI.

5.1.7 Launch Velocity

The launch velocity of the cloud, v_L, is another parameter that affects the three-pulse AI results. In this case, the frequency $\omega_D^{(3)}$ in equation 5.8 is modified by a constant

shift of qv_L.

Typically, v_L is sensitive to a number of effects such as power imbalances in the laser beams, imperfect circular polarization of the trapping beams, and background magnetic fields. The CCD camera method of measuring the trap temperature monitors both the spatial profile and centroid of the atom cloud [121]. Although the spatial position of the cloud cannot be measured in real-time during the AI experiment, periodic checks showed that v_L along the vertical direction can vary by as much as ± 2 mm/s over several hours. For the three-pulse AI, with $T_{21} = 7.5$ ms, this effect produces a correction of $\pm 2.2\%$. Since the data set in figure 4.10 was taken over 10 hours, we expect this effect to impact both the statistical error in the slope of $\pm 0.2\%$ as well as the absolute error in the value of a extracted from the slope of 1.1%. The importance of measuring and controlling v_L is likely to be one of the crucial considerations for accurate, high-precision measurements of g using this technique.

5.1.8 Total Correction due to Dominant Systematic Effects

It is notable that the quadrature sum of the systematic errors is 2.2% for the three-pulse AI and 630 ppm for the two-pulse AI. These corrections satisfactorily explain the discrepancy between the baseline value of g and the value of a shown in Table 4.1 for the three-pulse AI. For the two-pulse AI, the estimated systematic corrections are not sufficient to explain the discrepancy. We attribute this discrepancy to the lack of independent control over the magnetic gradient and curvature effects, and the

Systematic	Estimate	Shift
Counterpropagation	$\theta = 3$ arcseconds	- 0.1 ppb
AC Stark Shift	I = 50 mW/cm^2	- 6 ppb
Laser Linewidth	1 MHz	$\pm$ 3 ppb
Zeeman Shift	100 mG	$\pm$ 0.4 ppb
Wavefront Curvature	$w_0 = 3$ mm	$\pm$ 3 ppb

Table 5.2: Summary of estimates of systematic effects on a that will limit the experiment in the future. Here we assume a typical background magnetic field, a collimated beam with intensities and detunings used in the experiment.

inability to directly measure the variation of the magnetic field in the current setup. Other effects that have not been characterized include the dependencies on pulse widths. Furthermore, the effect of the read-out pulse intensity, which can affect the slope of the straight line in figure 4.9, has also not been characterized. Although the major sources of systematic errors have been described, a precision measurement of g using echo interferometers will require the control of several other systematic shifts. Some of these effects, estimated under well controlled conditions, are summarized in Table 5.2. The relatively small sizes of these effects suggest that the main challenge will be associated with suppressing the effects in Table 5.1.

5.1.9 Corrections Due to Minor Systematic Effects

We now examine different physical effects that result in much smaller systematic errors, which nevertheless should be address in future work.

5.1.10 AC Stark Shift

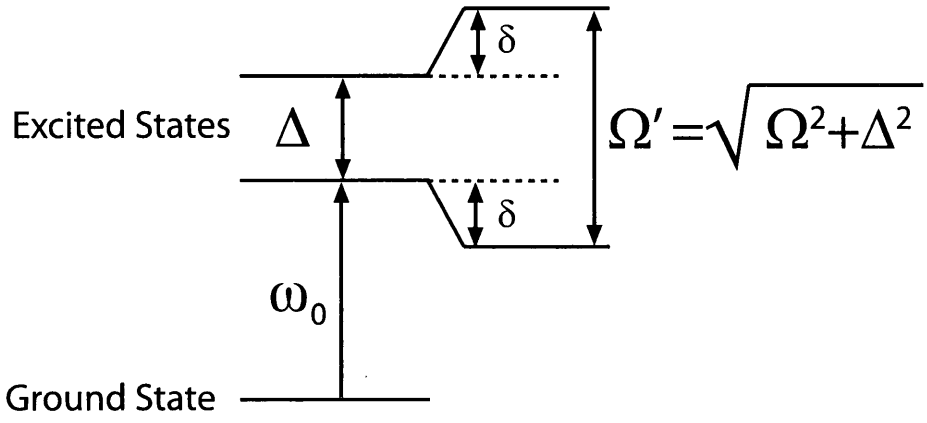

Figure 5.6: Dressed atom interpretation of the AC Stark shift. The detuning Δ is replaced by the generalized Rabi frequency $\Omega' = \sqrt{\Omega^2 + \Delta^2}$.

Since the initial and final states of the atom are the same for the echo AI, the AC Stark shift is considerably reduced compared to Raman AIs. Nevertheless, this effect must still be taken into account. The shift in the energy levels due to the AC Stark effect can be viewed as a change of the detuning Δ, which in turn changes the value of k and affects a. From the dressed state picture as shown in figure 5.6, the steady-state AC Stark shift δ is given by

$$\delta = \frac{\Omega' - \Delta}{2}, \tag{5.9}$$

where the generalized Rabi frequency, $\Omega' = \sqrt{\Omega^2 + \Delta^2}$. The Rabi frequency can be written as

$$\Omega = \sqrt{\frac{I}{2I_{\text{sat}}}}\Gamma, \tag{5.10}$$

where I is the intensity, I_{sat} is the saturation intensity, and Γ is the radiative rate, 1/27.72 ns. Using the saturation intensity of the $F = 2 \rightarrow F' = 3$ transition in ^{87}Rb

of $I_{\text{sat}} = 3.576$ mW/cm^2 and typical values for $\Delta = 55$ MHz, and $I = 100$ mW/cm^2, the generalized Rabi frequency becomes $\Omega' = 2\pi \cdot 23$ MHz. The shift $\delta = 2.3$ MHz. The transition frequency is 384 THz, giving a fractional shift of 6 ppb.

5.1.11 Laser Linewidth

The laser linewidth results in an uncertainty in the value of k, which in turn changes a. For a laser linewdith of 1 MHz, and a transition frequency of 384 THz, we estimate the fractional correction to be 1 MHz/384 THz = 3 ppb.

5.1.12 First-Order Zeeman Shift

The Zeeman effect lifts the degeneracy of magnetic sublevels of the states in the presence of a magnetic field. This shift changes the value of k, which in turn changes g. The energy shift due to a uniform magnetic field is given by

$$\Delta E = \mu_B g_F m_F B, \tag{5.11}$$

where μ_B is the Bohr magneton, B is the magnetic field, and g_F is the Landé g factor given by the relations

$$g_F = g_J \frac{F(F+1) + J(J+1) - I(I+1)}{2F(F+1)}, \tag{5.12}$$

$$g_J = 1 + \frac{J(J+1) + S(S+1) - L(L+1)}{2J(J+1)}. \tag{5.13}$$

Here, L, S, and J are the quantum numbers for the orbital, spin, and total angular momenta respectively, and I, F are the quantum numbers for the nuclear spin and the coupled nuclear spin and total angular momenta.

The total shift in the transition energy between the ground state $m_F = 2$ and the excited state $m_F = 3$ is given by

$$\begin{aligned} \Delta E &= \mu_B B(g_F - g_{F'}) \\ &= \mu_B B(2 \cdot 1/2 - 3 \cdot 2/3) \\ \Delta E &= -\mu_B B. \end{aligned} \tag{5.14}$$

Although magnetic field cancelling coils are used in the experiment, there is no direct measurement of the magnetic field at the location of the atoms. Assuming a maximum magnetic field of 1 Gauss, (approximate ambient magnetic field of earth), the total energy shift is 9.27×10^{-28} J, or a 4 ppb change of the photon energy.

5.1.13 Laser Diffraction

In the current experiment, light for the interferometry beams are collimated to a small size at the output of the fiber giving rise to strong diffraction effects. Due to space constraints, the excitation beam was not ideally collimated. The beam diameter increases from 6 mm to 12 mm over the total distance travelled of 2.4 m (see figure 3.18 for scale) giving a maximum angular spread of $\theta = 0.8$ mrad. This causes a $\theta^2/2$ change of the wavevector, a 350 ppb change.

5.1.14 Wavefront Curvature and Gouy Phase

The spread in k vectors across a curved wavefront is given by [127]

$$k_{\text{eff}} = k - \frac{2}{kw(z)^2} + \frac{2r_{\text{trap}}^2}{kw(z)^4}\left(1 - \frac{z^2}{z_R^2}\right), \tag{5.15}$$

where $w(z)$ is the beam waist as a function of z, r_{trap} is the radius of the trap, and z_R is the Rayleigh range,

$$z_R = \frac{2\pi}{\lambda}\frac{w_0^2}{2},$$

where w_0 is the minimum beam waist. The initial beam size after the fiber is 1 mm[19] and the corresponding Rayleigh range is 4 m, still larger than the total path travelled by the beams. This estimate is related to the strong diffraction in the previous subsection. The radius of the interferometry beam is 3 mm, and the radius of the trap is 1.5 mm. This corresponds to a correction of 3 ppb in the second term of equation 5.15, and a correction of 0.6 ppb in the third term of equation 5.15.

5.2 Phase Noise and Vibration Stabilization

The measurement of a is obtained from coupled measurements of amplitude and phase of the backscattered light from the grating. In practice, this is accomplished by measuring a signal of the form $S = A\cos(\phi_g)$ and $A\sin(\phi_g)$ where A is the amplitude and ϕ_g is the gravitational phase. The inertial reference frame for these measurements

[19]The 1 mm beam size was used due to the space constraints of the optical path. With a longer optical path available for the next generation of experiment, the beam size can be enlarged, thereby reducing diffraction.

is the nodal point of the standing wave excitation beam at the location of the corner cube reflector. Since we use a heterodyne technique, we assume that the nodal point is faithfully represented by the optical phase of the LO. Although the LO and AI beams are aligned through the same optical elements, vibrations still cause relative phase changes between the beams. This dissertation focused mainly on minimizing the phase differences between the AI and LO beams using passive isolation of critical experimental components.

The development of methods to stabilize the phase in the experiment was a significant part of the experimental work. Due to the constraints of limited resources, only incremental changes to the experiment were possible. In reference [99], a two-pulse Raman AI that relied only on passive vibration isolation of the entire apparatus obtained measurements of g that are statistically precise to a 2.7 ppb. Since only critical components in the experiment were passively isolated, it is not surprising that the statistical error for the two-pulse AI is only 6 ppm.

Furthermore, the accelerations of the motion of the corner cube reflector due to vibrations will cause an error in the measured value of g. The best way to avoid this error is to actively stabilize the motion of the corner cube. This is a challenging endeavor that has so far been addressed by only the Chu and Müller groups at Stanford University [26–28] by using an accelerometer placed on the corner cube to measure and correct the position using a solenoid actuator[20]. It should be noted

[20]The accelerometer measures the real time vibrations and the solenoid actuator can physically shift the corner-cube reflector to counteract environmental vibrations, thereby reducing the phase

that the experimental configuration used in this dissertation was not designed to be sensitive to the motion of the corner cube reflector. This is evident from figure 3.18 since the continuous wave probe heterodyne signal was generated by sending two probe beams aligned through the same optics (as the signal heterodyne beams) to the upper reflector and back down.

In the final stages of this work, only one of the probe beams (see figure 3.28) was sent to the corner cube whereas the second was confined to the bottom optics platform. The resulting beat note was sensitive to the motion of the corner cube position with respect to the lower platform. The optical phase of this probe beat note was subtracted from the optical phase of the signal heterodyne beat note (see figure 3.28) in post processing in an attempt to reduce the phase error. However, this method did not yield improvements, an effect that we attribute to the common motion of the lower platform and the corner cube.

To avoid potential phase errors due to the RF electronics, we replaced the probe AOM with a 50-50 beam splitter. In this arrangement, one beam travelled to the corner cube and returned and the second beam was again confined to the lower platform. The resulting interference signal also allowed a measurement of the relative motion of the lower platform and corner cube reflector. Again, post-processing the signal heterodyne beat note with phase information from the probe interference signal did not yield improvements. Therefore, our understanding that the common motion

error.

of the corner cube and lower platform contributed to the inability to carry out phase subtraction in post-processing appears to be correct.

5.3 Future Work

We now discuss improvements to the experiment that can be realized in a new setup with the goal of achieving a statistical precision of 1 ppb with adequate control over systematic effects. Such an effort is currently underway.

5.3.1 Timescale and Signal Size

The Raman AI in reference [98] and the hybrid Raman AI based on large momentum transfer Bragg pulses in reference [99] relied on state selection to a $m_F = 0$ sublevel, measurement timescales of 100 ms, and passive isolation to achieve statistical precision of a few ppb in 1000 s of averaging. In comparison, the statistical precision achieved in this work is limited both by the timescale due to the magnetized apparatus and low signal-to-noise ratio due to the photodiode based detection technique and phase stability.

In measurements of magnetic gradients [35] and atomic recoil [38], we have successfully used echo AIs and a non-magnetic apparatus to achieve measurement timescales of $\approx$ 130 ms with the two-pulse AI, and $\approx$ 220 ms for the three-pulse AI without magnetic state selection due to better control of magnetic effects and the use of chirped standing wave pulses to compensate for Doppler shifts. The non-magnetic apparatus

used in these experiments allowed better molasses cooling and resulted in a ten-fold increase in atom number. The well controlled magnetic environment in the glass cell has also allowed atoms to be routinely cooled to less than 5 μK thereby limiting cloud expansion. Such an apparatus will also allow much better control of the launch velocity of the atom cloud.

These experiments relied on a ten-fold increase in atom number and a gated PMT to realize an overall 50-fold increase in signal size. However, these experiments did not require vibration isolation since they measured only the signal intensity, and are therefore unsuitable for measurements of g. These glass cell results suggest that a vibration stabilized, non-magnetic apparatus, and a heterodyne detection system using PMTs can result in the suitably long timescales and adequate signal-to-noise ratio required to achieve competitive measurements of g using echo AIs.

The combined effects of the larger atom number and PMT based heterodyne detection is an expected 50-fold increase in the signal-to-noise ratio compared to the results in this dissertation. If atoms are state selected to a $m_F = 0$ level, a three-fold loss in signal-to-noise-ratio is expected. Therefore the overall improvement in signal-to-noise is expected to be a factor of 17 with respect to the current work.

Magnetic state selection into an $m_F = 0$ sublevel is expected to increase the timescales of both AI configurations from the current timescale in the glass cell (130 ms for the two-pulse AI, 220 ms for the three-pulse AI) to the transit time limit of $\approx$ 220 ms with a 2.54 cm beam diameter. This is similar to the long-lived

timescales achieved using Raman AIs [26–28].

To reduce phase error in such a setup, we plan to passively isolate the entire apparatus using a vibration isolation platform that supports all elements of the experiment including the ion pump, vacuum chamber and optics. Under these conditions, the phase error is expected to be reduced from the current level of 0.7 rad to .01 rad for the two-pulse AI based on the results in reference [99]. The newly designed apparatus will use a Michelson interferometer to measure the relative motion between the corner cube reflector and optics platform. Additionally, the motion of the corner cube reflector that serves as the inertial reference frame will be actively stabilized using an accelerometer and solenoid actuator. Under these conditions, the phase error is expected to be further reduced.

Another consideration for a long-timescale echo interferometer is the necessity of maintaining the two-photon resonance condition to compensate for the gravity-induced Doppler shift. In the long-timescale echo experiments in references [35, 38], both travelling wave components were chirped, whereas in reference [99], only one travelling component was chirped at twice the required rate. In this work, the standing wave pulses were not chirped since the pulse duration of $50 - 100$ ns provided sufficient bandwidth to maintain the two-photon resonance condition. A model for the two-photon transition probability as a function of the pulse width confirms these expectations. For our pulse parameters, this model shows that although the resonance condition is maintained for > 100 ms, the signal size is appreciably reduced.

An increase in signal size can be achieved by using longer pulses and compensating for the gravitational Doppler shift by chirping the frequency.

5.4 Control of Systematic Effects

5.4.1 State Preparation

State preparation of the atoms in the $m_F = 0$ sublevel will be an essential requirement to eliminate systematic effects due to magnetic gradient and curvature. So far, efforts to pump the atoms into the $m_F = 0$ sublevel with high efficiency with laser excitation have not been successful in the stainless-steel chamber. Accordingly, we propose to state select the atoms using RF and optical excitation. To achieve state selection the atoms can be optically pumped into the lower $F = 1$ hyperfine ground state. A linearly polarized RF pulse in the presence of a bias magnetic field can be used to selectively excite the $F = 1, m_F = 0 \rightarrow F' = 2, m_{F'} = 0$ transition. The remaining atoms in the $F = 1$ ground state can be pushed out of the interaction region by a laser tuned to the $F = 1 \rightarrow F' = 2$ transition. Selection into a single m_F-level will also eliminate the effect of differential phase shifts between sublevels.

The expected three-fold loss of signal strength due to state selection can be compensated by pre-loading the atoms into a one-dimensional optical lattice, as in recent echo experiments [128].

Whereas the peak reflectivity of the gratings for the experiments described here is $\approx 0.2\%$, the work in reference [129] suggests that the reflectivity of order unity can

be realized if the atoms are channelled into the nodes of a far-detuned, optical dipole force potential. This argument suggests that the signal size can increase by a factor of 500.

The reflectivity of the grating depends on the read-out pulse intensity. Therefore, it is an approximate indicator of signal-to-noise ratio. A more transparent argument to predict the signal size is based on the momentum conservation argument presented in Chapter 1 that suggests that each atom should backscatter no more than one photon. The typical atom number in this experiment is 5×10^8, Based on reference [130], it is possible to predict that in the absence of spontaneous emission, $\approx$50% of the atoms will participate in the two-pulse AI. Thus, the maximum number of signal photons should be 2.5×10^8. In comparison, the maximum number of photons detected in this work is 10^7.

Since the atom number is expected to increase by a factor of 10 in a non-magnetic apparatus, the maximum number of photons for the two pulse AI should be $\approx 2.5 \times 10^9$ if only 50% of the atoms contribute. With lattice loading, it may be possible to have most atoms contribute to the signal, boosting the photon number to 5×10^9. Thus the argument based on momentum conservation also suggests that the signal size can show a $\approx$ 500-fold improvement.

These arguments suggest that with lattice loading and RF state selection into the $m_F = 0$ magnetic sublevel can produce a 170-fold increase in signal strength.

5.4.2 Beam Properties

The index of refraction systematic can be addressed by working at much larger detunings. However, this will require more power in the excitation beams to achieve higher atom-field coupling strengths. The development of a new family of high-power fiber amplified lasers [95, 131] makes it practical to achieve the desired coupling strengths. Since fibre lasers have a linewidth of 50 kHz, the linewidth systematic can be reduced to below the desired level. Another possibility is to operate the AI at a detuning where the combined index correction due to all transitions in the $F = 2 \rightarrow F' = 1, 2, 3$ manifold sum to zero [38]. However, studies remain to be carried out to determine the extent of suppression of the index correction.

Decreasing systematic effects such as wavefront curvature and diffraction can be accomplished by increasing the size of the beams in the optical setup. Such a setup will allow the use of more collimated beams and reduce diffraction, as well as reduce wavefront curvature effects. However, this change will require a larger experimental optical breadboard and corresponding increase in the load capacity and size of vibration isolators.

Better control of the verticality of the laser beams such that the associated systematic effect is below 1 ppb is ideal for high accuracy measurements. This can be accomplished by aligning the vertical beam by relying on the flatness of the meniscus of a liquid, a procedure that has been adopted in industrial gravimeters. By choosing a liquid with sufficiently high index of refraction, it is possible to increase the amount

of light reflected from the meniscus so that the alignment is straightforward.

Finally, the three-pulse echo experiment will require better control of the launch velocity and a more precise characterization of any dead time. Recent experiments in a glass cell [35, 38, 39] indicate that the molasses cooling is highly efficient, routinely producing temperatures of ≈ 1 μK. These results suggest that imbalances in the intensities of trapping beams and magnetic field effects are well controlled. Under these conditions, we expect that the launch velocity can be sufficiently controlled so the effect of this systematic can be characterized.

5.4.3 Simulations of Signal-to-Noise Ratio

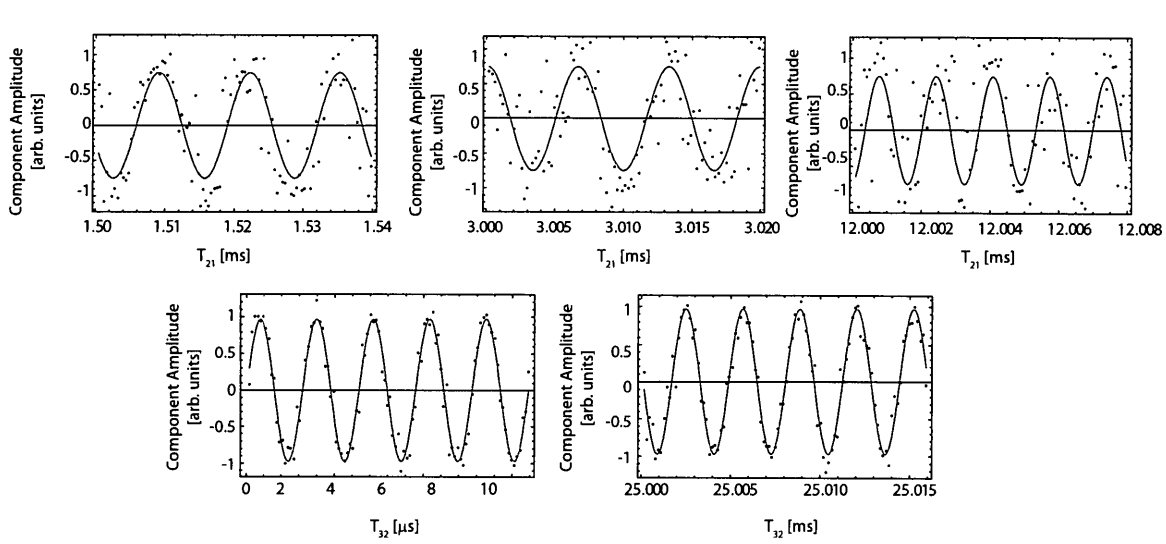

Figure 5.7: Top row: Simulation of the two-pulse AI with phase noise of 0.7 rad, amplitude noise of 10% and a timescale of $T_{21} = 12$ ms gives a statistical precision of 4 ppm. Bottom row: Simulation of the three-pulse AI with phase noise of 0.2 rad, amplitude noise of 10%, and a total timescale of 50 ms produces a statistical precision of 470 ppb. The $1/e$ time constant for the decay is 16.7 ms.

Figure 5.7 shows simulations of the two-pulse and three-pulse AIs with current signal-to-noise ratio and phase noise. The simulated precision of 4 ppm for the two-pulse AI and the simulated precision of 470 ppb for the three-pulse AI closely match the results in this dissertation. These simulations incorporate the decay of the signal that can arise from effects such as the transit time.

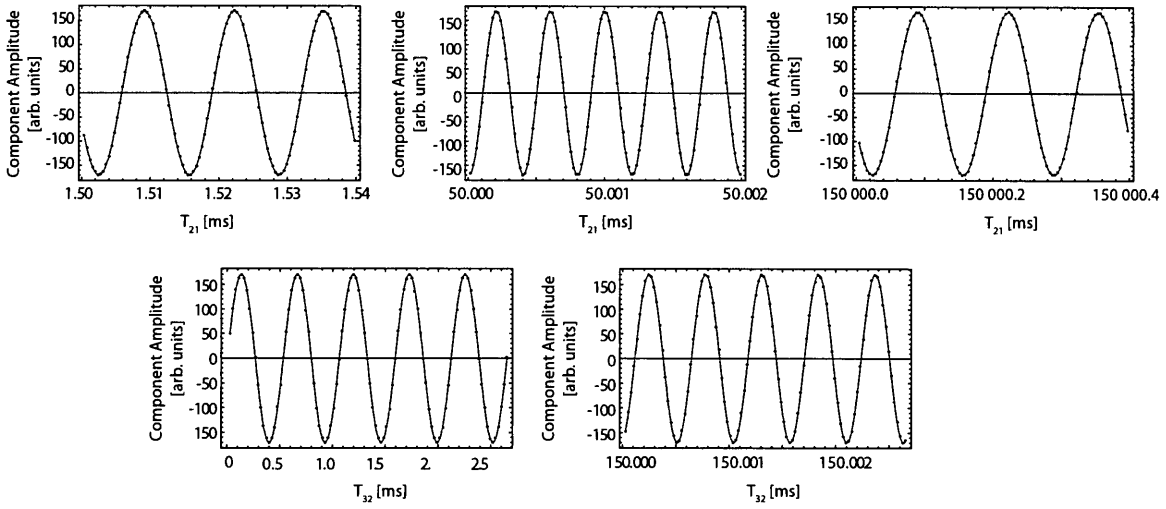

Figure 5.8: Top row: Simulation of the two-pulse AI with phase noise of 0.01 rad, a factor of 170 increase in signal-to-noise ratio, and a timescale of $T_{21} = 150$ ms produces a statistical precision of 0.3 ppb. Bottom row: Simulation of the three-pulse AI with phase noise of 0.01 rad, a factor of 170 increase in signal-to-noise ratio and a total timescale of 300 ms produces a statistical precision of 0.6 ppb. The $1/e$ time constant for the decay is 50 ms.

Figure 5.8 shows simulations of the two-pulse and three-pulse AIs with a 170 fold increase in signal-to-noise ratio and a reduction of phase noise to 0.01 rad for a total experimental timescale of 300 ms. The simulated precision is 0.3 ppb for the two-pulse AI and 0.6 ppb for the three-pulse AI. With active stabilization of the inertial reference frame, it appears that further improvements in the statistical precision are

achievable.

The code used to simulate the experiment is included in Appendix D.

5.4.4 Experimental Methods

Introducing the frequency chirp of excitation beams in the time-domain experiments discussed here is equivalent to performing the measurement in a reference frame that moves with free-falling atoms. Since the time domain experiments described here would be insensitive to g in this configuration, one must vary either the phase of the read-out pulse or the chirp rate of all pulses to measure g as in experiments with Raman AIs [99]. In such an experiment, the value of the pulse spacing between frequency chirped pulses will be progressively increased. For each value of the pulse spacing, the frequency chirp rate α will be adjusted to reduce the frequency of Doppler phase oscillations within the echo envelope. At the highest value of pulse spacing, the amplitude of the in-phase and in-quadrature component of the signal will be measured as a function of the phase of the read-out pulse to determine the minima of the fringe pattern. The value of g can be determined using the condition $(qg - 2\pi\alpha)T^2 = n2\pi$.

An alternative technique applicable to echo experiments could rely on measuring a gravitational phase shift using a Ramsey fringe pattern in the frequency domain [110].

Another priority will be the reduction in measurement time, which can be achieved with a higher signal-to-noise ratio by recording under sampled fringe patterns [132]. Optimizing data acquisition with respect of the number of fringes recorded and the

distribution of points within an observation window will need to be investigated.

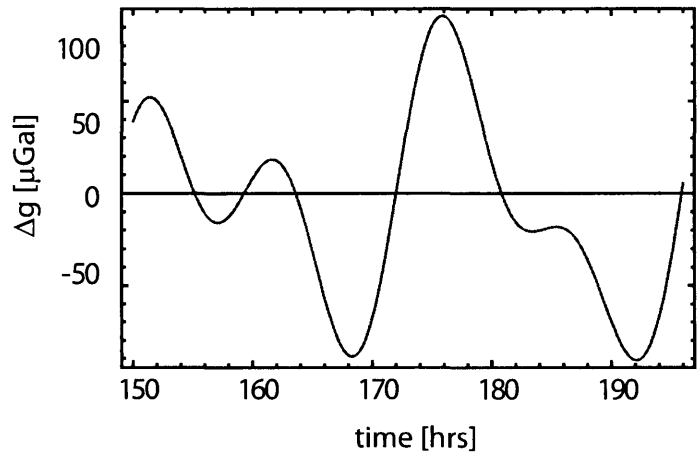

Figure 5.9: Prediction of tidal variation of gravity due to the sun and the moon. The input parameters are the latitude and longitude of the observer, height above sea level, and the date. The results plotted here correspond to Toronto: 43.77° N, 79.37° W, 100 m above sea level. The time is the number of hours after 9 AM, 14 May 2013.

If all the statistical errors are well controlled, is it possible to set the appropriate pulse parameters and measure the displacement of the maximum of the fringe pattern to monitor relative changes in g.

The next generation experiment in a glass chamber will incorporate all the aforementioned improvements. Such an experiment will allow tidal variations to be measured in real-time. A particularly valuable method of analyzing systematic effects will be to compare data from the cold atom experiment with real-time data from a portable industrial gravimeter. The effect of tides on the baseline value of gravity in the lab is illustrated on the basis of proprietary simulations from Scintrex Ltd. in figure 5.9. The simulation inputs are the location of the observer on the Earth and

the date and time. The model primarily incorporates the motion of the sun and the moon.

5.5 Summary

In summary, we have developed and explored techniques for measuring g using two-pulse and three-pulse echo interferometers. Analysis of the Doppler phase oscillations of the echo envelope resulted in measurements statistically precise to 0.5%. Experiments with the amplitude and phase of the two-pulse AI yielded a statistical uncertainty of 6 ppm. Experiments with the three-pulse AI have demonstrated the best statistical precision of 75 ppb.

Simulations suggest that an improved experiment in a non-magnetic chamber will be capable of realizing a statistical precision of 0.6 ppb for the three-pulse AI and a statistical precision of 0.3 ppb for the two-pulse AI. We have discussed techniques to reduce dominant systematic errors. However, more work will be required to verify that the systematic errors can be reduced to the level of the statistical error.

A table-top experiment such as the proposed next generation experiment should be able to provide an independent method of calibrating industrial sensors, which is a long term goal for this project. Recently, a much larger scale Raman AI experiment of g using a 10 m tall enclosure has achieved a sensitivity of 6.7×10^{-12} [72]. Although competing with projects on such a scale is not a realistic goal, a 1 ppb measurement of g with good control of systematic effects using echo AIs is likely to attract considerable

interest given the reduced experimental complexity of this approach.

A Action of Curved Trajectories

The z direction points upward, with gravity acting on the negative z direction. The potential energy is given by $U_g = +Mgz$, and the kinetic energy is $KE = \frac{1}{2}Mv^2$.

The classical action $\mathcal{S}$ is defined as

$$\mathcal{S} = \int_{t'=0}^{t'=t} (\mathcal{L}(z(t'), \dot{z}(t'))\, dt', \tag{A.1}$$

where t is the real time, t' is the integration variable, and $\mathcal{L}$ is the Lagrangian, equal to the difference of kinetic and potential energies,

$$\mathcal{L} = \frac{1}{2}Mv^2 - Mgz. \tag{A.2}$$

The phase accumulation of the trajectories is given by $\mathcal{S}/\hbar$.

A.1 Two-Pulse Action

In this section, we calculate the action along curved trajectories shown in figure A.1.

The Lagrangian of the undiffracted atom is $\mathcal{L}_A = M\left(\frac{1}{2}v^2 - gz\right)$ for all time, where $z = -\frac{1}{2}gt^2 + v_0 t$ and corresponding velocity, $v = \frac{dz}{dt} = -gt + v_0$. Inserting the position and velocity of the atom,

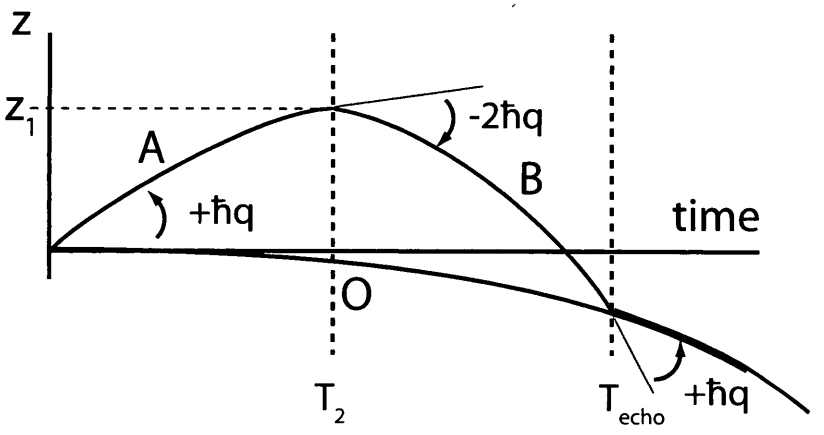

Figure A.1: Curved trajectories of the two-pulse AI due to gravity.

$$\begin{aligned}\frac{\mathcal{L}_0}{M} &= \frac{1}{2}(v_0 - gt)^2 + \frac{1}{2}g^2t^2 - v_0gt \\ &= \frac{1}{2}\left(v_0^2 - 2v_0gt + g^2t^2\right) + \frac{1}{2}g^2t^2 - v_0gt \\ &= \frac{1}{2}v_0^2 - 2v_0gt + g^2t^2 \end{aligned} \tag{A.3}$$

The action is then

$$\begin{aligned}\frac{\mathcal{S}_0}{M} &= \int_{t'=0}^{t'=2T_{21}} \left(\frac{1}{2}v_0^2 - 2v_0gt + g^2t^2\right) dt' \\ &= \left[\frac{1}{2}v_0^2t - v_0gt^2 + \frac{1}{3}g^2t^3\right]_{t'=2T_{21}} \\ &= v_0^2T_{21} - 4v_0gT_{21}^2 + \frac{8}{3}g^2T_{21}^3. \end{aligned} \tag{A.4}$$

The diffracted atom has two separate parts. During the first leg A, the position of the atom is $z = \frac{-1}{2}gt^2 + \left(v_0 + \frac{\hbar q}{M}\right)t$ and the corresponding velocity is $v = \frac{dz}{dt} = -gt + v_0 + \frac{\hbar q}{M}$. Inserting the position and velocity of the atom,

$$\begin{aligned}\frac{\mathcal{L}_A}{M} &= \left(\frac{1}{2}\left[v_0+\frac{\hbar q}{M}\right]-gt\right)^2+\frac{1}{2}g^2t^2-\left(v_0+\frac{\hbar q}{M}\right)gt \\ &= \frac{1}{2}\left(v_0+\frac{\hbar q}{M}\right)^2-\left[v_0+\frac{\hbar q}{M}\right]gt+\frac{1}{2}g^2t^2+\frac{1}{2}g^2t^2-\left(v_0+\frac{\hbar q}{M}\right)gt \\ &= \frac{1}{2}\left(v_0+\frac{\hbar q}{M}\right)^2-2\left[v_0+\frac{\hbar q}{M}\right]gt+g^2t^2 \qquad \text{(A.5)}\end{aligned}$$

The action is calculated to be

$$\begin{aligned}\frac{\mathcal{S}_A}{M} &= \int_{t'=0}^{t'=T_{21}}\left(\frac{1}{2}v_0^2-2v_0gt+g^2t^2\right)dt' \\ &= \left[\frac{1}{2}\left(v_0+\frac{\hbar q}{M}\right)^2t-\left(v_0+\frac{\hbar q}{M}\right)gt^2+\frac{1}{3}g^2t^3\right]_{t=T_{21}} \\ &= \frac{1}{2}\left(v_0^2+2v_0\frac{\hbar q}{M}+\left[\frac{\hbar q}{M}\right]^2\right)T_{21}-\left[v_0+\frac{\hbar q}{M}\right]gT_{21}^2+\frac{1}{3}g^2T_{21}^3. \qquad \text{(A.6)}\end{aligned}$$

At the end of leg A, the position of the atom is $z_1=-\frac{1}{2}gT_{21}^2+\left(v_0+\frac{\hbar q}{M}\right)T_{21}$.

During the second leg B, the position of the atom is $z=-\frac{1}{2}gt^2+(v_0-gT_{21})\,t+z_1$ and the corresponding velocity is $v=\frac{dz}{dt}=-gt+\left(v_0-gT_{21}-\frac{\hbar q}{M}\right)$. Inserting the position and velocity of the atom,

$$\begin{aligned}\frac{\mathcal{L}_B}{M} &= \left[\frac{1}{2}\left(v_0-gT_{21}-\frac{\hbar q}{M}\right)-gt\right]^2+\frac{1}{2}g^2t^2-\left(v_0-\frac{\hbar q}{M}-gT_{21}\right)gt-gz_1 \\ &= \frac{1}{2}\left(v_0-gT_{21}-\frac{\hbar q}{M}\right)^2-\left(v_0-gT_{21}-\frac{\hbar q}{M}\right)gt+\frac{1}{2}g^2t^2 \\ &\quad +\frac{1}{2}g^2t^2-\left(v_0-gT_{21}-\frac{\hbar q}{M}\right)gt-gz_1 \qquad \text{(A.7)} \\ &= \frac{1}{2}\left(v_0-gT_{21}-\frac{\hbar q}{M}\right)^2-gz_1-2\left(v_0-gT_{21}-\frac{\hbar q}{M}\right)gt+g^2t^2. \qquad \text{(A.8)}\end{aligned}$$

The action is calculated to be

$$\begin{aligned}
\frac{\mathcal{S}_B}{M} &= \int_{t'=0}^{t'=T_{21}} \left\{ \frac{1}{2}\left(v_0 - gT_{21} - \frac{\hbar q}{M}\right)^2 - gz_1 - 2\left(v_0 - gT_{21} - \frac{\hbar q}{M}\right) gt + g^2t^2 \right\} dt' \\
&= \left\{ \left[\frac{1}{2}\left(v_0 - gT_{21} - \frac{\hbar q}{M}\right)^2 - gz_1 \right] t - \left(v_0 - gT_{21} - \frac{\hbar q}{M}\right) gt^2 + \frac{1}{3}g^2t^3 \right\}\Bigg|_{t=T_{21}} \\
&= \left\{ \frac{1}{2}v_0 - \frac{\hbar q}{M} - v_0 gT_{21} + \frac{\hbar q}{M}gT_{21} + \frac{1}{2}\left(\frac{\hbar q}{M}\right)^2 + \frac{1}{2}gT_{21}^2 + \frac{1}{2}gT_{21}^2 - v_0 gT_{21}^2 - \frac{1}{2}gT_{21}^2 gT_{21} \right\} T_{21} \\
&\quad - v_0 gT_{21}^2 + \frac{\hbar q}{M}gT_{21}^2 + g^2T_{21}^3 + \frac{1}{3}g^2T_{21}^3 \\
&= \left[\frac{1}{2}v_0^2 - v_0\frac{\hbar q}{M} + \frac{1}{2}\left(\frac{\hbar q}{M}\right)^2 \right] T_{21} \\
&\quad + \left[-v_0 + \frac{\hbar q}{M} - v_0 + \frac{\hbar q}{M} - v_0 - \frac{\hbar q}{M} \right] gT_{21}^2 \\
&\quad + \left[\frac{1}{2} + \frac{1}{2} + 1 + \frac{1}{3} \right] g^2T_{21}^2 \\
&= \left[\frac{1}{2}v_0^2 - v_0\frac{\hbar q}{M} + \frac{1}{2}\left(\frac{\hbar q}{M}\right)^2 \right] T_{21} + \left[-3v_0 + \frac{\hbar q}{M} \right] gT_{21}^2 + \frac{7}{3}g^2T_{21}^3. \qquad \text{(A.9)}
\end{aligned}$$

The total action of the upper path is the sum of equations A.6 and A.6,

$$\begin{aligned}
\frac{\mathcal{S}_A + \mathcal{S}_B}{M} &= \left[\frac{1}{2}v_0^2 + v_0\frac{\hbar q}{M} + \frac{1}{2}\left(\frac{\hbar q}{M}\right)^2 + \frac{1}{2}v_0^2 - v_0\frac{\hbar q}{M} + \frac{1}{2}\left(\frac{\hbar q}{M}\right)^2 \right] T_{21} \\
&\quad + \left[-v_0 - \frac{\hbar q}{M} - 3v_0 + \frac{\hbar q}{M} \right] gT_{21}^2 + \left[\frac{1}{3} + \frac{7}{3} \right] gT_{21}^2 \\
&= \left[v_0^2 + \frac{\hbar q}{M} \right] T_{21} + -4v_0 gT_{21}^2 + \frac{8}{3}g^2T_{21}^3. \qquad \text{(A.10)}
\end{aligned}$$

Subtracting the action of the lower path in equation A.4, only one term remains:

$$\frac{\Delta\mathcal{S}}{M} = \frac{\mathcal{S}_A + \mathcal{S}_B - \mathcal{S}_0}{M} = \left(\frac{\hbar q}{M}\right)^2 T_{21}. \qquad \text{(A.11)}$$

The phase difference between these paths is

$$\begin{aligned}\Delta\phi_{\text{path}} &= \frac{\Delta\mathcal{S}}{\hbar} = \frac{M}{\hbar}\left(\frac{\hbar q}{M}\right)^2 T_{21} \\ &= \frac{\hbar q^2}{M} T_{21} \\ &= 2\omega_q T_{21}. \end{aligned} \tag{A.12}$$

This is identical to the phase difference of rectilinear paths giving rise to only recoil modulation.

A.2 Three-Pulse Action

In this section, we calculate the action along curved trajectories shown in figure A.2.

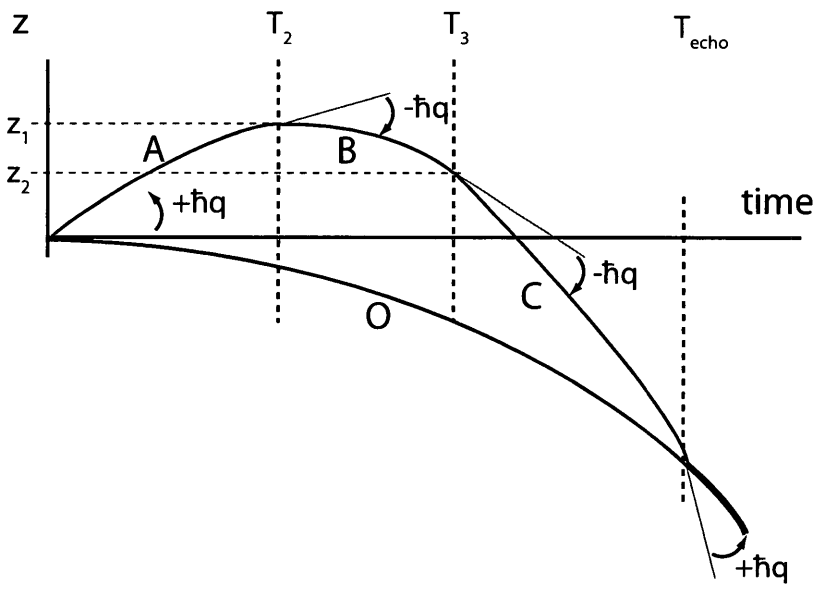

Figure A.2: Curved trajectories of the three-pulse AI due to gravity.

The Lagrangian of the undiffracted atom is $\mathcal{L}_A = M\left(\frac{1}{2}v^2 - gz\right)$ for all time, where $z = -\frac{1}{2}gt^2 + v_0 t$ and corresponding velocity, $v = \frac{dz}{dt} = -gt + v_0$. Inserting the position and velocity of the atom,

$$\begin{aligned}\frac{\mathcal{L}_0}{M} &= \frac{1}{2}(v_0 - gt)^2 + \frac{1}{2}g^2t^2 - v_0gt \\ &= \frac{1}{2}\left(v_0^2 - 2v_0gt + g^2t^2\right) + \frac{1}{2}g^2t^2 - v_0gt \\ &= \frac{1}{2}v_0^2 - 2v_0gt + g^2t^2 \end{aligned} \tag{A.13}$$

The action is then

$$\begin{aligned}\frac{\mathcal{S}_0}{M} &= \int_{t'=0}^{t'=2T_{21}+T_{32}} \left(\frac{1}{2}v_0^2 - 2v_0gt + g^2t^2\right) dt' \\ &= \left[\frac{1}{2}v_0^2 t - v_0gt^2 + \frac{1}{3}g^2t^3\right]_{t'=2T_{21}+T_{32}} \\ &= \frac{1}{2}v_0^2(2T_{21} + T_{32}) - v_0g\left(4T_{21}^2 + 4T_{21}T_{32} + T_{32}^2\right) \\ &\quad + \frac{1}{3}g^2\left[8T_{21}^3 + 12T_{21}^2T_{32} + 6T_{21}T_{32}^2 + T_{32}^3\right] \\ &= v_0^2 2T_{21} + \frac{1}{2}v_0^2T_{32} \\ &\quad - 4v_0gT_{21}^2 - 4v_0gT_{21}T_{32} - v_0gT_{32}^2 \\ &\quad + \frac{8}{3}g^2T_{21}^3 + 4g^2T_{21}^2T_{32} + 2g^2T_{21}T_{32}^2 + \frac{1}{3}g^2T_{32}^3 \end{aligned} \tag{A.14}$$

The diffracted atom has three separate parts. During the first leg A, the position of the atom is $z = -\frac{1}{2}gt^2 + \left(v_0 + \frac{\hbar q}{M}\right)t$ and the corresponding velocity is $v = \frac{dz}{dt} = -gt + v_0 + \frac{\hbar q}{M}$. Inserting the position and velocity of the atom,

$$\begin{aligned}\frac{\mathcal{L}_A}{M} &= \left(\frac{1}{2}\left[v_0+\frac{\hbar q}{M}\right]-gt\right)^2+\frac{1}{2}g^2t^2-\left(v_0+\frac{\hbar q}{M}\right)gt \\ &= \frac{1}{2}\left(v_0+\frac{\hbar q}{M}\right)^2-\left[v_0+\frac{\hbar q}{M}\right]gt+\frac{1}{2}g^2t^2+\frac{1}{2}g^2t^2-\left(v_0+\frac{\hbar q}{M}\right)gt \\ &= \frac{1}{2}\left(v_0+\frac{\hbar q}{M}\right)^2-2\left[v_0+\frac{\hbar q}{M}\right]gt+g^2t^2 \end{aligned} \tag{A.15}$$

The action is calculated to be

$$\begin{aligned}\frac{\mathcal{S}_A}{M} &= \int_{t'=0}^{t'=T_{21}}\left(\frac{1}{2}v_0^2-2v_0gt+g^2t^2\right)dt' \\ &= \left[\frac{1}{2}\left(v_0+\frac{\hbar q}{M}\right)^2t-\left[v_0+\frac{\hbar q}{M}\right]gt^2+\frac{1}{3}g^2t^3\right]_{t=T_{21}} \\ &= \frac{1}{2}\left(v_0^2+2v_0\frac{\hbar q}{M}+\left[\frac{\hbar q}{M}\right]^2\right)T_{21}-\left[v_0+\frac{\hbar q}{M}\right]gT_{21}^2+\frac{1}{3}g^2T_{21}^3. \end{aligned} \tag{A.16}$$

At the end of leg A, the position of the atom is $z_1 = -\frac{1}{2}gT_{21}^2+\left(v_0+\frac{\hbar q}{M}\right)T_{21}$.

During the second leg B, the position of the atom is $z = -\frac{1}{2}gt^2+(v_0-gT_{21})\,t+z_1$ and the corresponding velocity is $v = \frac{dz}{dt} = -gt+(v_0-gT_{21})$. Inserting the position and velocity of the atom,

$$\begin{aligned}\frac{\mathcal{L}_B}{M} &= \left[\frac{1}{2}(v_0-gT_{21})-gt\right]^2+\frac{1}{2}g^2t^2-(v_0-gT_{21})\,gt-gz_1 \\ &= \frac{1}{2}(v_0-gT_{21})^2-(v_0-gT_{21})\,gt+\frac{1}{2}g^2t^2+\frac{1}{2}g^2t^2-(v_0-gT_{21})\,gt-gz_1 \\ &= \frac{1}{2}(v_0-gT_{21}-gt)^2-gz_1-2(v_0-gT_{21})\,gt+g^2t^2. \end{aligned} \tag{A.17}$$

The action is calculated to be

$$\begin{aligned}
\frac{\mathcal{S}_B}{M} &= \int_{t'=0}^{t'=T_{32}} \left\{ \frac{1}{2}\left(v_0 - gT_{21}\right)^2 - gz_1 - 2\left(v_0 - gT_{21}\right)gt + g^2t^2 \right\} dt' \\
&= \left\{ \left[\frac{1}{2}\left(v_0 - gT_{21}\right)^2 - gz_1 \right] t - \left(v_0 - gT_{21}\right)gt^2 + \frac{1}{3}g^2t^3 \right\} \Big|_{t=T_{32}} \\
&= \frac{1}{2}v_0^2T_{32} - v_0gT_{21}T_{32} + \frac{1}{2}g^2T_{21}^2T_{32} + \frac{1}{2}g^2T_{21}^2T_{32} - g\left(v_0 + \frac{\hbar q}{M}\right)T_{21}T_{32} \\
&\quad - \left(v_0 - gT_{21}\right)gT_{32}^2 + \frac{1}{3}g^2T_{32}^3 \\
&= \frac{1}{2}v_0^2T_{32} - 2v_0gT_{21}T_{32} - g\frac{\hbar q}{M}T_{21}T_{32} + g^2T_{21}^2T_{32} \\
&\quad - g\left(v_0 + \frac{\hbar q}{M}\right)T_{21}T_{32} - \left(v_0 - gT_{21}\right)gT_{32}^2 + \frac{1}{3}g^2T_{32}^3 \qquad \text{(A.18)}
\end{aligned}$$

At the end of leg B, the position of the atom is $z_2 = -\frac{1}{2}gT_{32}^2 + v_0T_{32} - gT_{21}T_{32} - \frac{1}{2}gT_{21}^2 + \left(v_0 + \frac{\hbar q}{M}\right)T_{21}$.

During the third leg C, the position of the atom is $z = -\frac{1}{2}gt^2 + \left(v_0 - gT_{21} - gT_{32} - \frac{\hbar q}{M}\right)t + z_2$ and the corresponding velocity is $v = \frac{dz}{dt} = -gt + (v_0 - gT_{21} - gT_{32} - \frac{\hbar q}{M})$. Inserting the position and velocity of the atom,

$$\begin{aligned}
\frac{\mathcal{L}_C}{M} &= \left[\frac{1}{2}\left(v_0 - gT_{21} - gT_{32} - \frac{\hbar q}{M}\right) - gt \right]^2 + \frac{1}{2}g^2t^2 - \left(v_0 - gT_{21} - gT_{32} - \frac{\hbar q}{M}\right)gt - gz_2 \\
&= \frac{1}{2}\left(v_0 - gT_{21} - gT_{32} - \frac{\hbar q}{M}\right)^2 - \left(v_0 - gT_{21} - gT_{32}\right)gt + \frac{1}{2}g^2t^2 + \frac{1}{2}g^2t^2 \\
&\quad - \left(v_0 - gT_{21} - gT_{21}\right)gt - gz_2 \\
&= \frac{1}{2}\left(v_0 - gT_{21} - gT_{32}\right)^2 - gz_2 - 2\left(v_0 - gT_{21} - gT_{32}\right)gt + g^2t^2. \qquad \text{(A.19)}
\end{aligned}$$

The action is calculated to be

$$
\begin{aligned}
\frac{\mathcal{S}_C}{M} &= \int_{t'=0}^{t'=T_{21}} \left\{ \frac{1}{2}\left(v_0 - gT_{21} - gT_{32}\right)^2 - gz_2 - 2\left(v_0 - gT_{21} - gT_{32}\right)gt + g^2t^2 \right\} dt' \\
&= \left\{ \left[\frac{1}{2}\left(v_0 - gT_{21} - gT_{32}\right)^2 - gz_2 \right] t - \left(v_0 - gT_{21} - gT_{32}\right)gt^2 + \frac{1}{3}g^2t^3 \right\} \Bigg|_{t=T_{21}} \\
&= \frac{1}{2}v_0^2T_{21} - v_0gT_{21}T_{21} - v_0gT_{32}T_{21} - v_0\frac{\hbar q}{M}T_{21} + \frac{1}{2}g^2T_{21}^2T_{21} + g^2T_{21}T_{32}T_{21} + \frac{\hbar q}{M}gT_{21}T_{21} \\
&\quad + \frac{1}{2}T_{32}^2T_{21} + \frac{\hbar q}{M}T_{32}T_{21} + \frac{1}{2}\left(\frac{\hbar q}{M}\right)^2 T_{21} \\
&\quad \frac{1}{2}g^2T_{32}^2T_{21} - v_0gT_{32}T_{21} + g^2T_{21}T_{21}T_{21} + \frac{1}{2}g^2T_{21}^2T_{21} - \left(v_0 + \frac{\hbar q}{M}\right)gT_{21}T_{21} \\
&\quad - \left(v_0 - gT_{21} - gT_{32}\right)gT_{21}^2 + \frac{1}{3}g^2T_{21}^3 \\
&= \left[\frac{1}{2}v_0^2 - v_0\frac{\hbar q}{M} + \frac{1}{2}\left(\frac{\hbar q}{M}\right)^2 \right] T_{21} \\
&\quad + \left[-v_0 + \frac{\hbar q}{M} - v_0 - \frac{\hbar q}{M} - v_0 + \frac{\hbar q}{M} \right] gT_{21}^2 \\
&\quad + \left[-v_0 + \frac{\hbar q}{M} - v_0 \right] gT_{21}T_{32} \\
&\quad + \left[\frac{1}{2} + \frac{1}{2} + \frac{1}{2} + \frac{1}{3} \right] g^2T_{21}^3 + \left[1 + 1 + 1\right] g^2T_{21}^2T_{32} + \left[\frac{1}{2} + \frac{1}{2} \right] g^2T_{21}T_{32}^2,
\end{aligned}
$$

and collecting like terms,

$$
\begin{aligned}
\frac{\mathcal{S}_C}{M} &= \left[\frac{1}{2}v_0^2 - v_0\frac{\hbar q}{M} + \frac{1}{2}\left(\frac{\hbar q}{M}\right)^2 \right] T_{21} \\
&\quad + \left[-3v_0 + \frac{\hbar q}{M} \right] gT_{21}^2 + \left[-2v_0 + \frac{\hbar q}{M} \right] gT_{21}T_{32} \\
&\quad + \frac{7}{3}g^2T_{21}^3 + 3g^2T_{21}^2T_{32} + g^2T_{21}T_{32}^2. \qquad \text{(A.20)}
\end{aligned}
$$

Subtracting the action of the undiffracted atom from the total action of the upper path,

$$\begin{aligned}\frac{\mathcal{S}_A+\mathcal{S}_B+\mathcal{S}_C-\mathcal{S}_0}{M} &= \left[\frac{1}{2}v_0^2 - v_0\frac{\hbar q}{M} + \frac{1}{2}\left(\frac{\hbar q}{M}\right)^2 + \frac{1}{2}v_0^2 - v_0\frac{\hbar q}{M} + \frac{1}{2}\left(\frac{\hbar q}{M}\right)^2 - v_0\right]T_{21} \\ &+ \left[\frac{1}{2}v_0^2 - \frac{1}{2}v_0^2\right]T_{32} \\ &+ \left[-v_0 - \frac{\hbar q}{M} - 3v_0 + \frac{\hbar q}{M} - 4v_0\right]gT_{21}^2 \\ &+ \left[-\frac{1}{2}v_0^2 + \frac{1}{2}v_0^2\right]T_{32}^2 \\ &+ \left[-2v_0 - \frac{\hbar q}{M} - 2v_0 + \frac{\hbar q}{M} + 4v_0\right]gT_{21}T_{32} \\ &+ \left[\frac{1}{3} + \frac{7}{3} - \frac{8}{3}\right]g^2T_{21}^3 + [1+3-4]\,g^2T_{21}^2T_{32} \\ &+ [1+1-2]\,T_{21}T_{32}^2 + \left[\frac{1}{3} - \frac{1}{3}\right]g^2T_{32}^2,\end{aligned}$$

leaving only one term,

$$\frac{\Delta\mathcal{S}}{M} = \left(\frac{\hbar q}{M}\right)^2 T_{21}. \tag{A.21}$$

The phase difference between these paths is

$$\begin{aligned}\Delta\phi_{\text{path}} &= \frac{\Delta\mathcal{S}}{\hbar} = \frac{M}{\hbar}\left(\frac{\hbar q}{M}\right)^2 T_{21} \\ &= \frac{\hbar q^2}{M}T_{21} \\ &= 2\omega_q T_{21}.\end{aligned} \tag{A.22}$$

This is identical to the phase difference of rectilinear paths giving rise to only recoil modulation.

B IGBT Switching Circuit

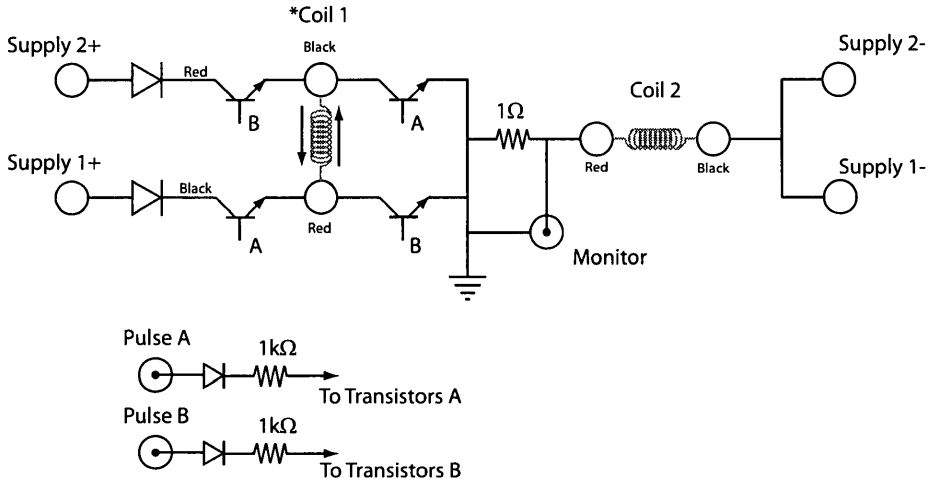

Figure B.1: Electrical schematic of the IGBT current direction switching module. This module allows the current in one of the anti-Helmholtz coils to be reversed so that it operates in the Helmholtz configuration. The two sets of IGBTs labelled A and B, linked to the inputs A and B, create an "H" configuration. The current flowing through Coil 1 changes the direction, while the current flows through Coil 2 in the same direction. The Monitor port measures the voltage across a 1Ω high-power resistor. The benefit of using car ignition IGBT chips is that they can be driven at standard TTL voltages. The maximum electrical power through the IGBT is well below the 85 W damage threshold.

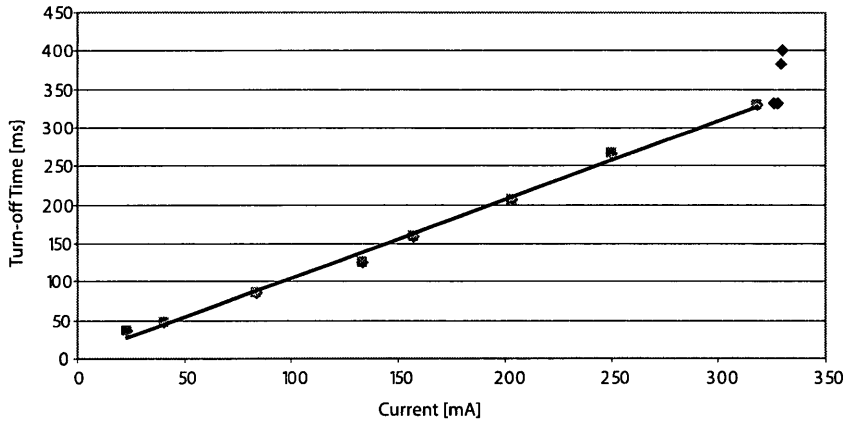

Figure B.2: IGBT current turn-off time as a function of current for the circuit shown in figure B.1. The typical turn-off time of 1 μs/mA is due to the number components. The inductance of the coils slows the fast action of the IGBT chips. A single IGBT chip circuit is used in the AI experiment to turn off the anti-Helmholtz coils. This circuit is shown later in this section.

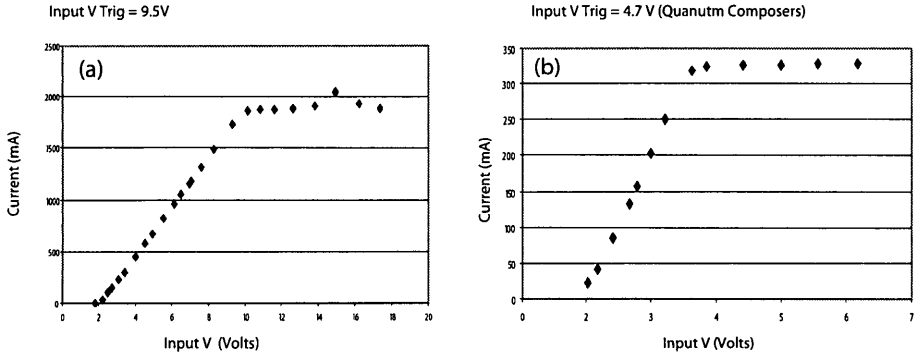

Figure B.3: IGBT current flow as a function of input trigger voltage for the circuit shown in figure B.1. (a) Input trigger of 9.5 V is applied to the IGBT. The power supply voltage is changed to find the current and resistance of the system. (b) Input trigger of 4.7 V is applied to the IGBT. The maximum current the IGBT provides is linked to the input trigger voltage. In the experiment, the trigger input voltage allowed the current supplied to the trapping magnetic gradient coil to be controlled.

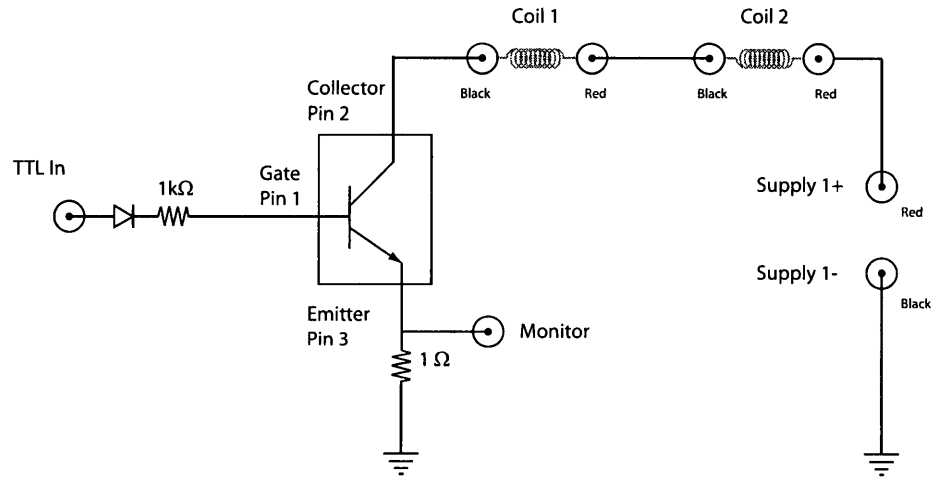

Figure B.4: Electrical schematic of the IGBT current switching module. This circuit was used to turn off the anti-Helmholtz coils for the AI experiment. A single IGBT stops current flow through both coils. The Monitor port measures the voltage across a 1Ω high-power resistor. The benefit of using car ignition IGBT chips is that they can be driven at standard TTL voltages. The maximum electrical power through the IGBT is well below the 85 W damage threshold.

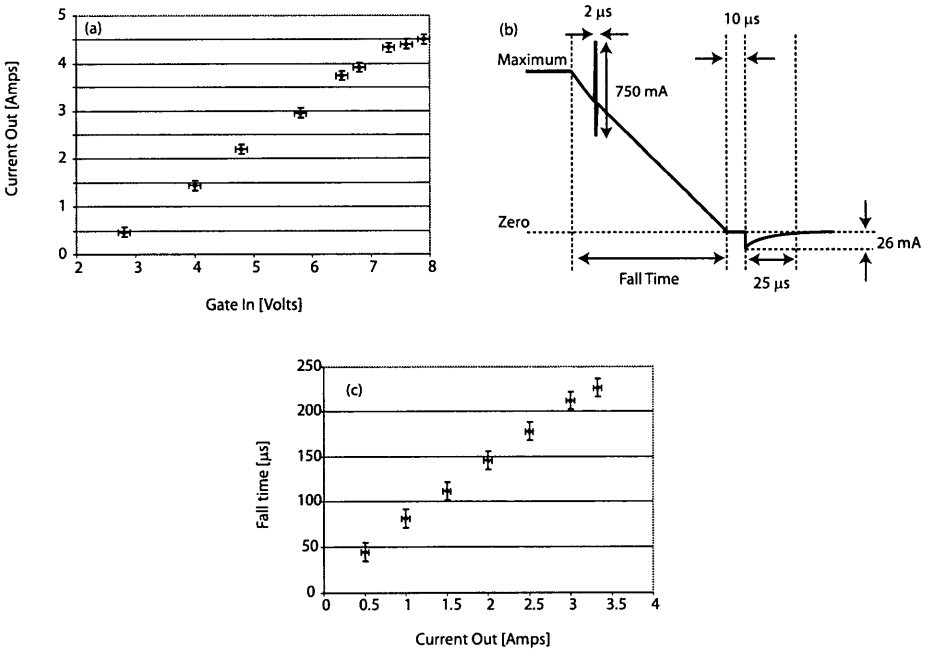

Figure B.5: (a) IGBT current flow as a function of input trigger voltage for the circuit in figure B.4. (b) Typical current flow as measured at the monitor output during current shut-off. Numerous spurious transient effects occur, but they all end within one millisecond. (c) Current shut-off fall time as a function of current flowing through the system.

C C++ Source Code

C.1 Mixing Down

This section provides the source code for electronic, post-processing of the direct heterodyne signal from the atoms and the master oscillator in C++. User inputs are set to defaults, but are prompted to input the number of files and trace point length. The mixing down is done by directly multiplying the two signals. The low pass portion is completed using

```
fftw
```

to Fourier transform into frequency space to apply a hard cut-off. The remaining frequency components are transformed back into time space and exported in plain text.

```
#include <cstdlib>
#include <sstream>  //String stream
#include <fftw3.h>  //Fourier stuff
#include <math.h>
#include <iostream>
#include <string>   //
#include <fstream>  //float streams
#include <windows.h>//Currentpath
#include <direct.h> //Currentpath
//Hard Coded Low Pass Filter
//500 ns/point -> 3.2 MHz Lo Pass
#define FourierCutOff 68
using namespace std;
int main(int argc, char *argv[])
{
    //============================
    //PATH INFORMATION
    //============================
    char CurrentPath[_MAX_PATH];
    getcwd(CurrentPath, _MAX_PATH);
    string CH1FileNameBase="/S2Ch1-";
    string CH2FileNameBase="/S2Ch2-";
    //============================
    //IMPORT VARIABLES
    //============================
    string input;
```

```
    int NumFiles=1600;
    int TraceLength=50000;
    int MasterLoopCounter;
    //Number of Files
    cout << "Enter number of files: (Default 1600)"<<"\t";
    getline(cin, input);      //User Input
    if ( !input.empty() ) {  //If it's not EMPTY,
        istringstream stream( input );  //Convert to stream
        stream >> NumFiles; //Shove stream into Variable name
    }
    //TraceLengths
    cout << "Enter Total Trace Length: (Default 50000)" <<"\t";
    getline(cin, input);      //User Input
    if ( !input.empty() ) {  //If it's not EMPTY,
        istringstream stream( input );  //Convert to stream
        stream >> TraceLength; //Shove stream into Variable name
    }
    //=============================
    //IMPORT VARIABLES
    //=============================
    int ii;
    int jj;
    string ScopePoint;
    double RawCH1[TraceLength];
    double RawCH2[TraceLength];
    char chbuffer[3];
    string CurrentCH1FileName;
    string CurrentCH2FileName;
    //=============================
    //EXPORT VARIABLES
    //=============================
    string OutputFileName;
    string IPOutputFileNameBase;
    string QOutputFileNameBase;
    IPOutputFileNameBase = "/12IP-";
    QOutputFileNameBase = "/12Q-";
    //=============================
    //FFT Stuff VARIABLES
    //=============================
    double *FFTinIP;
    double *FFTmidIP;
    double *FFToutIP;
    double *FFTinQ;
    double *FFTmidQ;
    double *FFToutQ;
    fftw_plan ForwardPlanIP;
    fftw_plan BackwardPlanIP;
    fftw_plan ForwardPlanQ;
    fftw_plan BackwardPlanQ;
    FFTinIP = (double*)fftw_malloc(sizeof(double) * TraceLength);
    FFTmidIP = (double*)fftw_malloc(sizeof(double) * TraceLength);
    FFToutIP = (double*)fftw_malloc(sizeof(double) * TraceLength);
    FFTinQ = (double*)fftw_malloc(sizeof(double) * TraceLength-5);
    FFTmidQ = (double*)fftw_malloc(sizeof(double) * TraceLength-5);
    FFToutQ = (double*)fftw_malloc(sizeof(double) * TraceLength-5);
    cout<< "Creating FFT Plans.  Please wait."<<endl;
    cout<< "Estimating, not using doing battery measurements!" <<endl;
    ForwardPlanIP= fftw_plan_r2r_1d(TraceLength, FFTinIP, FFTmidIP, FFTW_REDFT10,
                   FFTW_ESTIMATE);
    BackwardPlanIP = fftw_plan_r2r_1d(TraceLength, FFTmidIP, FFToutIP,
                   FFTW_REDFT01, FFTW_ESTIMATE);
    ForwardPlanQ= fftw_plan_r2r_1d(TraceLength-5, FFTinQ, FFTmidQ, FFTW_REDFT10,
                   FFTW_ESTIMATE);
    BackwardPlanQ = fftw_plan_r2r_1d(TraceLength-5, FFTmidQ, FFToutQ,
                   FFTW_REDFT01, FFTW_ESTIMATE);
    cout<< "Done planning!  Beginning mixing down."  <<endl;

//REAL IMPORTATION
    for(MasterLoopCounter=0; MasterLoopCounter<NumFiles; MasterLoopCounter++){
       //=============================
       //File 1 IMPORT
       //=============================
       CurrentCH1FileName= CurrentPath+CH1FileNameBase+itoa(1000 +
                        MasterLoopCounter, chbuffer,10)+".";
       //CurrentCH1FileName = "C:/data1/S2CH1-1000.";
       cout <<CurrentCH1FileName<<"\t";
       //IMPORT CHANNEL 1
       ii=0;
```

```
ifstream tempfile (CurrentCH1FileName.c_str());
if (tempfile.is_open()){
    getline (tempfile,ScopePoint,'\n');      //LINE0 HEADER
    getline (tempfile,ScopePoint,'\n');      //LINE1 HEADER
    getline (tempfile,ScopePoint,'\n');      //LINE2 HEADER
    getline (tempfile,ScopePoint,'\n');      //LINE3 HEADER - DATE
    getline (tempfile,ScopePoint,'\n');      //LINE4 HEADER
    getline (tempfile,ScopePoint,'\n');      //LINE5 HEADER - starttime
    getline (tempfile,ScopePoint,'\n');      //LINE6 HEADER - Timestep
    getline (tempfile,ScopePoint,'\n');      //LINE7 HEADER
    while ( tempfile.good()){
    //LINE8 IS DATA!!!!
         getline (tempfile,ScopePoint,'\t');
         RawCH1[ii] = strtod (ScopePoint.c_str(),NULL);
         ii++;
         }
    tempfile.close();
}
//=============================
//File 2 IMPORT
//=============================
CurrentCH2FileName = CurrentPath+CH2FileNameBase+itoa(1000 +
                MasterLoopCounter, chbuffer,10)+".";
//CurrentCH3FileName = "C:/data1/S2CH3-1000.";
cout <<CurrentCH2FileName<<"\n";
//IMPORT CHANNEL 2
ii=0;
//Open File and Start Counting Lines
ifstream tempfile2 (CurrentCH2FileName.c_str());
if (tempfile2.is_open()){
   getline (tempfile,ScopePoint,'\n');      //LINE0 HEADER
   getline (tempfile,ScopePoint,'\n');      //LINE1 HEADER
   getline (tempfile,ScopePoint,'\n');      //LINE2 HEADER
   getline (tempfile,ScopePoint,'\n');      //LINE3 HEADER - DATE
   getline (tempfile,ScopePoint,'\n');      //LINE4 HEADER
   getline (tempfile,ScopePoint,'\n');      //LINE5 HEADER - starttime
   getline (tempfile,ScopePoint,'\n');      //LINE6 HEADER - Timestep
   getline (tempfile,ScopePoint,'\n');      //LINE7 HEADER
   while ( tempfile2.good()){
   //LINE8 IS DATA!!!!
        getline (tempfile2,ScopePoint,'\t');
        RawCH2[ii] = strtod (ScopePoint.c_str(),NULL);
        ii++;
        }
   tempfile2.close();
}
//===============
//IN PHASE
//===============
//Mixing
for(jj=0; jj<= TraceLength; jj++){
     FFTinIP[jj] = RawCH1[jj] * RawCH2[jj];
     }
//FFT
fftw_execute(ForwardPlanIP);
//LowPass
for(jj=FourierCutOff; jj<=TraceLength; jj++){
    FFTmidIP[jj] = 0;
}
//FFT back
fftw_execute(BackwardPlanIP);
cout<< "Exporting: IP "<< "\t";
OutputFileName = CurrentPath+IPOutputFileNameBase+itoa(1000 +
                MasterLoopCounter ,chbuffer,10)+".txt";
cout<<OutputFileName<<endl;
//OutputFileName="C:/Data1/MIP-testROD.txt";
ofstream out(OutputFileName.c_str());
if(out){
    for(jj=0; jj<TraceLength; jj++){
    out << FFToutIP[jj]   << endl;
    }
    out.close();
}
//===============
//QUADRATURE
//===============
//mixing
```

```
        for(jj=0; jj<= TraceLength-5; jj++){
             FFTinQ[jj] = RawCH1[jj] * RawCH2[jj+5];
        }
        //FFT
        fftw_execute(ForwardPlanQ);
        //LowPass
        for(jj=FourierCutOff; jj<=TraceLength-5; jj++){
            FFTmidQ[jj] = 0;
        }
        //FFT back
        fftw_execute(BackwardPlanQ);
        cout<< "Exporting: Quad "<< "\t";
        OutputFileName = CurrentPath+QOutputFileNameBase+itoa(1000 +
                         MasterLoopCounter, chbuffer,10)+".txt";
        cout<<OutputFileName<<endl;
        ofstream outfile(OutputFileName.c_str());
        if(outfile){
                    for(jj=0; jj<TraceLength-5; jj++){
                    outfile << FFToutQ[jj]   << endl;
                    }
                    outfile.close();
        }
      }//End of Loop
      fftw_destroy_plan(ForwardPlanIP);
      fftw_destroy_plan(BackwardPlanIP);
      fftw_destroy_plan(ForwardPlanQ);
      fftw_destroy_plan(BackwardPlanQ);
      fftw_free(FFTinIP);
      fftw_free(FFTmidIP);
      fftw_free(FFToutIP);
      fftw_free(FFTinQ);
      fftw_free(FFTmidQ);
      fftw_free(FFToutQ);
      system("PAUSE");
      return EXIT_SUCCESS;
}
```

C.2 Find Mean

This section provides the source code for electronic, to find the mean of a series of numbers in a file. User inputs are set to defaults, but are prompted to input the number of files and trace point length. The mean is exported in plain text.

```
#include <cstdlib>
#include <iostream>
#include <math.h>
#include <sstream>  //String stream
#include <string>   //Strings
#include <windows.h>//Currentpath
#include <direct.h> //Currentpath
#include <fstream>  //float streams
using namespace std;
int main()
{
    int ii=0;
    string ScopePoint;
    string CurrentFileName1;
    string CurrentFileName2;
    string OutputFileName1;
    string OutputFileName2;
    //============================
    //PATH INFORMATION
    //============================
    char CurrentPath[_MAX_PATH];
    getcwd(CurrentPath, _MAX_PATH);
    string IPFileNameBase="/23IP-";
    string QFileNameBase="/23Q-";
    //============================
    //IMPORT VARIABLES
```

```
//============================
char chbuffer[3];
string UserInput;
int NumFiles=1600;
int TraceLength=42000;
int MasterLoopCounter;
//Number of Files
cout << "Enter number of files: (Default 1600)"<<"\t";
getline(cin, UserInput);      //User Input
if ( !UserInput.empty() ) {  //If it's not EMPTY,
    istringstream stream( UserInput );  //Convert to stream
    stream >> NumFiles; //Shove stream into Variable name
}
//TraceLengths
cout << "Enter Total Trace Length: (Default 42000)" <<"\t";
getline(cin, UserInput);      //User Input
if ( !UserInput.empty() ) {  //If it's not EMPTY,
    istringstream stream( UserInput );  //Convert to stream
    stream >> TraceLength; //Shove stream into Variable name
}
double MeanCollector=0;
double IPVals[TraceLength];
double QVals[TraceLength];

for(MasterLoopCounter=0; MasterLoopCounter<NumFiles; MasterLoopCounter++){
   //============================
   //File 1 IMPORT
   //============================
   CurrentFileName1= CurrentPath+IPFileNameBase+itoa(1000 +
                  MasterLoopCounter, chbuffer,10)+".txt";
   cout <<CurrentFileName1<<"\t";
   //IMPORT CHANNEL 1
   ifstream tempfile;
   tempfile.open(CurrentFileName1.c_str());
   for(ii=0; ii<TraceLength; ii++){
            getline (tempfile,ScopePoint,'\t');
            //cout<< ScopePoint <<"\t";
            MeanCollector = MeanCollector+strtod(ScopePoint.c_str(),NULL);
            //cout<< MeanCollector<<"\t";
            }
   tempfile.close();
   IPVals[MasterLoopCounter]=MeanCollector/TraceLength;
   MeanCollector=0;
   //============================
   //File 2 IMPORT
   //============================
   CurrentFileName2 = CurrentPath+QFileNameBase+itoa(1000 +
                  MasterLoopCounter,chbuffer,10)+".txt";
   cout <<CurrentFileName2<<"\n";
   ifstream tempfile2;
   tempfile2.open(CurrentFileName2.c_str());
   for(ii=0; ii<TraceLength; ii++){
            getline (tempfile2,ScopePoint,'\t');
            //cout<< ScopePoint <<"\t";
            MeanCollector = MeanCollector+strtod(ScopePoint.c_str(),NULL);
            //cout<< MeanCollector<<"\t";
            }
   tempfile2.close();
   QVals[MasterLoopCounter]=MeanCollector/TraceLength;
   MeanCollector=0;
}
OutputFileName1 = CurrentPath+IPFileNameBase+"mean.txt";
cout<<OutputFileName1<<"\t";
ofstream outfile;
outfile.open(OutputFileName1.c_str());
int jj=0;
for(jj=0; jj<NumFiles; jj++){
    outfile<< IPVals[jj]   << endl;
    cout<<IPVals[jj];
}
outfile.close();
cout<<endl;
OutputFileName2 = CurrentPath+QFileNameBase+"mean.txt";
cout<<OutputFileName2<<endl;
ofstream outA;
outA.open(OutputFileName2.c_str());
for(ii=0; ii<NumFiles; ii++){
```

```
        outA<< QVals[ii] << endl;
        cout<<QVals[ii];
    }
    outA.close();
    cout<<endl;
    system("PAUSE");
    return EXIT_SUCCESS;
}
```

C.3 Slicing

This section provides the source code for "slicing" of the echo envelope in C++. electronic, post-processing of the direct heterodyne signal from the atoms and the master oscillator. User inputs are set to defaults, but are prompted to input the number of files, trace point length, and number of slices. The output is the individual time slices exported in plain text.

```
#include <cstdlib>
#include <iostream>
#include <sstream>
#include <string>
#include <math.h>
#include <fstream>
#include <windows.h>
#include <direct.h>
#include <stdlib.h>
using namespace std;
//double *OutputArray;
double**MassiveData;
int main()
{
    //IMPORT VARIABLES
    char CurrentPath[_MAX_PATH];
    getcwd(CurrentPath, _MAX_PATH);
    cout<<CurrentPath<<endl;
    string FileNameBase;
    string ImportBuffer;
    char chbuffer[3];
    //User Input:: Slice Analysis
    string input;
    int NumFiles=1600;
    int TraceLength=42000;
    int NumSlices=200;
    int BackgroundRange=100;
    int SigStart= 9215;
    int SigEnd= 34850;
    int SigLength;
    int SliceLength;
    //Slicing Variables
    double slope;
    double sum=0;
    double BKGStart;
    double BKGEnd;
    //Export Variables
    string OutputFileNameBase;
    //counters
    int i;
    int j;
    int k;
    /*
    //Tired of entering same numbers over and over.  Set Defaults!
    NumFiles = 1600;
    TraceLength = 42000;
    SigStart = 9215;
    SigEnd = 34850;
    NumSlices = 420;
    BackgroundRange =100;
    */
```

```
//Number of Files
cout << "Enter number of files: (Default 1600)"<<"\t";
getline(cin, input);     //User Input
if ( !input.empty() ) {  //If it's not EMPTY,
    istringstream stream( input );  //Convert to stream
    stream >> NumFiles; //Shove stream into Variable name
}
//TraceLengths
cout << "Enter Total Trace Length: (Default 42000)" <<"\t";
getline(cin, input);     //User Input
if ( !input.empty() ) {  //If it's not EMPTY,
    istringstream stream( input );  //Convert to stream
    stream >> TraceLength; //Shove stream into Variable name
}
//Signal Cuf Off
cout << "Enter signal start point: (Default 9215)"<<"\t";
getline(cin, input);     //User Input
if ( !input.empty() ) {  //If it's not EMPTY,
    istringstream stream( input );  //Convert to stream
    stream >> SigStart; //Shove stream into Variable name
}
cout << "Enter signal end point: (Default 34850)"<<"\t";
getline(cin, input);     //User Input
if ( !input.empty() ) {  //If it's not EMPTY,
    istringstream stream( input );  //Convert to stream
    stream >> SigEnd; //Shove stream into Variable name
}
//Number of Slices
cout << "Enter number of slices: (Default 200)"<<"\t";
getline(cin, input);     //User Input
if ( !input.empty() ) {  //If it's not EMPTY,
    istringstream stream( input );  //Convert to stream
    stream >> NumSlices; //Shove stream into Variable name
}
//Background Range
cout << "Background Point Length: (Default 100)"<<"\t";
getline(cin, input);     //User Input
if ( !input.empty() ) {  //If it's not EMPTY,
    istringstream stream( input );  //Convert to stream
    stream >> BackgroundRange; //Shove stream into Variable name
}
/*
cout << "=============================================="<<endl;
cout << NumFiles <<endl;
cout << TraceLength <<endl;
cout << SigStart <<endl;
cout << SigEnd <<endl;
cout << NumSlices<<endl;
cout << BackgroundRange<<endl;
system("PAUSE");
*/
//=========================================
//Condition Trace Chopping
//=========================================
double RawData[TraceLength];
//Resize Slicing to make division easier
SliceLength = (SigEnd-SigStart)/NumSlices;
//Since things are integers, remainder drops out!
cout<< "Slice Length: "<< SliceLength<< endl;
SigEnd = SigStart+SliceLength*NumSlices;
cout<< "New Signal end point:"<< SigEnd<<endl;
SigLength = SigEnd-SigStart;
//=========================================
//Data Array Creation
//=========================================
cout<<"Creating Data Arrays"<<endl ;
//cout<<SigEnd-SigStart;
double CurrentData[SigEnd-SigStart];
//cout<<"Creating Massive Data"<<endl;
MassiveData = new double*[NumFiles+1];
for(i=1; i<=NumFiles; i++)
         {MassiveData[i]=new double[NumSlices+1];
         }
//=========================================
// In-Phase
//=========================================
```

```
FileNameBase="/Ch1-";
OutputFileNameBase="/SliceIP-";
for(i=1; i<=NumFiles; i++){
        //cout<<"Importing Files"<<endl;
        //=========================================
        // Import Trace
        //=========================================
        string CurrentFileName = CurrentPath+FileNameBase+itoa(1000+i,
                        chbuffer,10)+".";
        //cout<<CurrentFileName<<endl;
        ifstream ReadFile (CurrentFileName.c_str());
        if (ReadFile.is_open()){
           getline (ReadFile,ImportBuffer,'\n');
           getline (ReadFile,ImportBuffer,'\n');
           getline (ReadFile,ImportBuffer,'\n');
           getline (ReadFile,ImportBuffer,'\n');
           getline (ReadFile,ImportBuffer,'\n');
           getline (ReadFile,ImportBuffer,'\n');
           for(j=1; j<=TraceLength; j++){
           //         cout<<j<<endl;
                 getline(ReadFile, ImportBuffer, '\t');
                 RawData[j]=strtod(ImportBuffer.c_str(),NULL);
                 //cout<<j<< "\t"<<ImportBuffer<< endl;
                 }
           ReadFile.close();
        }
        if ( i % 25 == 0 )
        {
           cout << CurrentFileName<< "\t" <<"File Import Complete" <<'\n';
        }
        //cout<< "Trace Conditioning" <<endl;
        //=========================================
        // Trace Conditioning
        //=========================================
        //Chop out Data
        for(j=1; j<=SigLength; j++){
                CurrentData[j] = RawData[SigStart+j-1];
                }
        //BACKGROUND Subtraction
        sum=0;
        for(j = 1; j<=BackgroundRange; j++){
               sum = sum + CurrentData[j];
               }
        BKGStart =sum/BackgroundRange;
        //cout<< BKGStart << "\t";
        sum=0;
        for(j = 1; j<BackgroundRange; j++){
               sum = sum+CurrentData[SigLength-j+1];
               }
        BKGEnd = sum/BackgroundRange;
        //cout<< BKGEnd << endl;
        //Linear Slope
        slope = (BKGEnd-BKGStart)/(SigEnd-SigStart);
        //Subtract LinearSlope
        for(j=1; j<=SigLength; j++){
                 CurrentData[j] = CurrentData[j]-(BKGStart + slope*(j-1));
                 }
        //cout<< "Background Subtraction Done" << endl;
        //=========================================
        //Take Slices and Populate MassiveData
        //=========================================
        for(j=1; j<=NumSlices; j++){
                 sum=0;
                 for(k=1; k<=SliceLength; k++){
                          sum = sum + CurrentData[k+j*SliceLength];
                          }
                 //cout<< sum/SliceLength << " ";
                 MassiveData[i][j]=sum/SliceLength;
                 }
        }
cout<<"Finished Importing Files"<<endl;
//=========================================
//Export
//=========================================
//Create OutputFileNames
string OutputFileName[NumSlices+1];
for(i=1; i<=NumSlices; i++){
```

```
        OutputFileName[i] = CurrentPath+OutputFileNameBase+itoa(i + 1000,
                        chbuffer,10)+".txt";
        //cout<<OutputFileName[i]<<endl;
        }
cout<< "Exporting Slice Number: " <<endl;
for(i=1; i<=NumSlices; i++){
         ofstream out(OutputFileName[i].c_str());
         cout << i <<" ";
         if(out){
                 for(j=1; j<=NumFiles; j++){
                         out << MassiveData[j][i]    << endl;
                 }
         out.close();
         }
}
//=========================================
// Quadrature
//=========================================
FileNameBase="/CH2-";
OutputFileNameBase="/SliceQUAD-";
for(i=1; i<=NumFiles; i++){
        //=========================================
        // Import Trace
        //=========================================
        string CurrentFileName = CurrentPath+FileNameBase+itoa( 1000+i,
                        chbuffer,10)+".";
        ifstream ReadFile (CurrentFileName.c_str());
        if (ReadFile.is_open()){
           getline (ReadFile,ImportBuffer,'\n');
           getline (ReadFile,ImportBuffer,'\n');
           getline (ReadFile,ImportBuffer,'\n');
           getline (ReadFile,ImportBuffer,'\n');
           getline (ReadFile,ImportBuffer,'\n');
           getline (ReadFile,ImportBuffer,'\n');
           for(j=1; j<=TraceLength; j++){
           //         cout<<j<<endl;
                 getline(ReadFile, ImportBuffer, '\t');
                 RawData[j]=strtod(ImportBuffer.c_str(),NULL);
                 //cout<<j<< "\t"<<ImportBuffer<< endl;
                 }
           ReadFile.close();
        }
        if ( i % 25 == 0 )
        {
           cout << CurrentFileName<< "\t" <<"File Import Complete" <<'\n';
        }
        //=========================================
        // Trace Conditioning
        //=========================================
        //Chop out Data
        for(j=1; j<=SigLength; j++){
                CurrentData[j] = RawData[SigStart+j-1];
                }
        //BACKGROUND Subtraction
        sum=0;
        for(j = 1; j<=BackgroundRange; j++){
               sum = sum + CurrentData[j];
               }
        BKGStart =sum/BackgroundRange;
        //cout<< BKGStart << "\t";
        sum=0;
        for(j = 1; j<BackgroundRange; j++){
               sum = sum+CurrentData[SigLength-j+1];
               }
        BKGEnd = sum/BackgroundRange;
        //cout<< BKGEnd << endl;
        //Linear Slope
        slope = (BKGEnd-BKGStart)/(SigEnd-SigStart);
        //Subtract LinearSlope
        for(j=1; j<=SigLength; j++){
                 CurrentData[j] = CurrentData[j]-(BKGStart + slope*(j-1));
                 }
        //cout<< "Background Subtraction Done" << endl;
        //=========================================
        //Take Slices and Populate MassiveData
        //=========================================
        for(j=1; j<=NumSlices; j++){
```

```
                    sum=0;
                    for(k=1; k<=SliceLength; k++){
                            sum = sum + CurrentData[k+j*SliceLength];
                            }
                    //cout<< sum/SliceLength << " ";
                    MassiveData[i][j]=sum/SliceLength;
                    }
            }
    //=========================================
    //Export
    //=========================================
    //Create OutputFileNames
    for(i=0; i<=NumSlices; i++){
            OutputFileName[i] = CurrentPath+OutputFileNameBase+itoa(i +1000,
                            chbuffer,10)+".txt";
            //cout<<OutputFileName[i]<<endl;
            }
    cout<< "Exporting Slice Number: " <<endl;
    for(i=1; i<=NumSlices; i++){
             ofstream out(OutputFileName[i].c_str());
             cout <<  i <<" ";
             if(out){
                    for(j=1; j<=NumFiles; j++){
                            out << MassiveData[j][i]   << endl;
                    }
             out.close();
             }
    }
    cout<<endl;
    //CleanUp
    cout<<"Clearing Memory"<<endl ;
    for(i=1; i<=NumFiles+1; i++)
         {delete[] MassiveData[i];
         }
    delete [] MassiveData;
    system("PAUSE");
    return EXIT_SUCCESS;
}
```

D Mathematica Code

D.1 Three Pulse Analysis

This section provides the source code for processing time slides of the echo envelope in Mathematica for the three-pulse AI. The inputs are from the files generated from the C++ section. First, a single slice is used to check the data. Next, the process for a single slice is iterated across all slices. Lastly, all slice data is processed together. The output is the final frequency at the echo time embedded within the notebook.

```
(*Packages*)
Needs["ErrorBarPlots`"]
Needs["NonlinearRegression`"]
Needs["Histograms`"]
(*Hard code variables*)
eqn = A Sin[2 Pi f t + phi]
Navg = 16
timebreak = Table[i Navg, {i, 1, 100}];
(*========Import Low=========*)
SetDirectory[ "F:\\April 30\\2027 t21 7.5ms lo step250ns"]
rawtiming  = Import["Timing Log.txt", "Table"];
p2 = rawtiming[[1, 2]];
p3 = Table[rawtiming[[i, 3]], {i, 1, Length[rawtiming]}];
actualt = p3 - p2;
windowstart = Min[p3]
windowend = Max[p3]
IPSlice = ToExpression[Import["SliceIP-1082.txt", "List"]];
QUADSlice = ToExpression[Import["SliceQUAD-1082.txt", "List"]];
(*Plotting*)
IPval = Table[0, {i, 1, 100}];
IPerrbar = Table[0, {i, 1, 100}];
QUADval = Table[0, {i, 1, 100}];
QUADerrbar = Table[0, {i, 1, 100}];
Do[
 chunk = Take[IPSlice, {i Navg + 1, (i + 1) Navg}];
 IPval[[i + 1]] = Mean[chunk];
 IPerrbar[[i + 1]] = StandardDeviation[chunk];
 chunk = Take[QUADSlice, {i Navg + 1, (i + 1) Navg}];
 QUADval[[i + 1]] = Mean[chunk];
 QUADerrbar[[i + 1]] = StandardDeviation[chunk];
 , {i, 0, 99}]
times1 = Table[actualt[[timebreak[[i]]]], {i, 1, 100}]/10^9;
datum = Transpose[{times1, IPval}];
SigAmp = Sqrt[IPval^2 + QUADval^2];
IPn1 = IPval/SigAmp;
QUADn1 = QUADval/SigAmp;
IPErr1 = IPerrbar/SigAmp;
QUADErr1 = QUADerrbar/SigAmp;
SliceDataWE =
```

```
  Table[{{times1[[i]], IPn1[[i]]}, ErrorBar[IPErr1[[i]]]}, {i, 1,
    100}];
PlotA = ErrorListPlot[SliceDataWE]

(*========Import High=========*)
SetDirectory[ "F:\\April 30\\2105 t21 7.5ms hi step250ns"]
rawtiming  = Import["Timing Log.txt", "Table"];
p2 = rawtiming[[1, 2]];
p3 = Table[rawtiming[[i, 3]], {i, 1, Length[rawtiming]}];
actualt = p3 - p2;
windowstart = Min[p3]
windowend = Max[p3]
IPSlice = ToExpression[Import["SliceIP-1081.txt", "List"]];
QUADSlice = ToExpression[Import["SliceQUAD-1081.txt", "List"]];
IPval2 = Table[0, {i, 1, 100}];
IPerrbar2 = Table[0, {i, 1, 100}];
QUADval2 = Table[0, {i, 1, 100}];
QUADerrbar2 = Table[0, {i, 1, 100}];
Do[
 chunk = Take[IPSlice, {i Navg + 1, (i + 1) Navg}];
 IPval2[[i + 1]] = Mean[chunk];
 IPerrbar2[[i + 1]] = StandardDeviation[chunk];
 chunk = Take[QUADSlice, {i Navg + 1, (i + 1) Navg}];
 QUADval2[[i + 1]] = Mean[chunk];
 QUADerrbar2[[i + 1]] = StandardDeviation[chunk];
 , {i, 0, 99}]
times2 = Table[actualt[[timebreak[[i]]]], {i, 1, 100}]/10^9;
datum = Transpose[{times2, IPval2}];
SigAmp = Sqrt[IPval2^2 + QUADval2^2];
IPn2 = IPval2/SigAmp;
QUADn2 = QUADval2/SigAmp;
IPErr2 = IPerrbar2/SigAmp;
QUADErr2 = QUADerrbar2/SigAmp;
SliceDataWE2 =
  Table[{{times2[[i]], IPn2[[i]]}, ErrorBar[IPErr2[[i]]]}, {i, 1,
    100}];
PlotB = ErrorListPlot[SliceDataWE2]

(*======JOINING========*)
Allamps = Join[ IPn1, IPn2];
Alltimes = Join[times1, times2];
Alldata = Transpose[{Alltimes, Allamps}];
Allerr = Join[IPErr1, IPErr2];
(*======Initial Fit========*)
reg = NonlinearRegress[Alldata,
  Sin[ 2 Pi f t + k ], {{f, 187000}, {k, Pi}}, t,
  RegressionReport -> {BestFit, ParameterCITable, FitResiduals}]
plotme = reg[[1, 2]];
PlotA1 = Plot[plotme, {t, Min[times1], Max[times1]},
   PlotStyle -> Red];
PlotB1 = Plot[plotme, {t, Min[times2], Max[times2]},
   PlotStyle -> Red];
Show[PlotA, PlotA1, PlotRange -> All]
Show[PlotB, PlotB1, PlotRange -> All]
(*=====Conditioning=======*)
(*Drop HUGE error bar points*)
droppoints = {}
Do[
 If[cuterr[[i]] > .5,
   AppendTo[droppoints, i];
   ];
 , {i, 1, Length[cutdata]}]
droppoints
Do[
 cutdata = Drop[cutdata, {droppoints[[-i]]}];
 cuterr = Drop[cuterr,  {droppoints[[-i]]}];
 cuttimes = Drop[cuttimes,  {droppoints[[-i]]}];
 , {i, 1, Length[droppoints]}]
Do[
 If[cuttimes[[i]] - cuttimes[[i - 1]] > 0.0001,
   Print[i];
   cutbreak = i;
   ];
 , {i, 2, Length[cuttimes]}]

(*==New Fit==*)
```

```
reg = NonlinearRegress[cutdata,
   Sin[ 2 Pi f t + k ], {{f, 187000}, {k, Pi}}, t,
   RegressionReport -> {BestFit, ParameterCITable, FitResiduals}];
reg[[2]]
plotme = reg[[1, 2]];
PlotA1 = Plot[plotme, {t, Min[times1], Max[times1]},
   PlotStyle -> Red];
PlotB1 = Plot[plotme, {t, Min[times2], Max[times2]},
   PlotStyle -> Red];
Show[PlotA, PlotA1, PlotRange -> All]
Show[PlotB, PlotB1, PlotRange -> All]
(*Coarse Search*)
startfreq = Table[186500 + 50 i, {i, 0, 40}]
gerr = Table[0, {i, 0, 40}];
Do[
 reg = NonlinearRegress[cutdata,
   A Sin[ 2 Pi f t + k ], {{A, 1}, {f, startfreq[[i]]}, {k, 1}}, t,
   RegressionReport -> {BestFit, ParameterCITable}];
 gerr[[i]] = reg[[2, 2, 1, 2, 2]]/reg[[2, 2, 1, 2, 1]]*10^6;
 , {i, 1, Length[startfreq]}]
ListPlot[Transpose[{startfreq, gerr}]]
gerr
Min[gerr]
beststart = startfreq[[Flatten[Position[gerr, Min[gerr]]]]]
(*Fine Search*)
startfreq = Table[187150 + 10 i, {i, 0, 40}]
gerr = Table[0, {i, 0, 40}];
Do[
 reg = NonlinearRegress[cutdata,
   A Sin[ 2 Pi f t + k ], {{A, 1}, {f, startfreq[[i]]}, {k, 1}}, t,
   RegressionReport -> {BestFit, ParameterCITable}];
 gerr[[i]] = reg[[2, 2, 1, 2, 2]]/reg[[2, 2, 1, 2, 1]]*10^6;
 , {i, 1, Length[startfreq]}]
ListPlot[Transpose[{startfreq, gerr}]]
gerr
Min[gerr]
beststart = startfreq[[Flatten[Position[gerr, Min[gerr]]]]][[1]]
(*===========Single Slice BEST FIT=============*)
reg = NonlinearRegress[cutdata,
  Sin[ 2 Pi f t + k ], {{f, beststart}, {k, 1}}, t,
  RegressionReport -> {BestFit, ParameterCITable, FitResiduals}]
plotme = reg[[1, 2]];
PlotA1 = Plot[plotme, {t, Min[times1], Max[times1]},
   PlotStyle -> Red];
PlotB1 = Plot[plotme, {t, Min[times2], Max[times2]},
   PlotStyle -> Red];
Show[PlotA, PlotA1, PlotRange -> {All, {-1, 1}}]
Show[PlotB, PlotB1, PlotRange -> {All, {-1, 1}}]
Histogram[reg[[3, 2]]]
StandardDeviation[reg[[3, 2]]]


(*========All slices conditioning==========*)
(*USE PREVIOUS BEST FIT FREQUENCY*)
IPFiles = FileNames["SliceIP-**"];
QUADFiles = FileNames["SliceQuad-**"];
StartFreq = 187325;
fs = Table[0, {i, 1, Length[IPFiles]}];
ferr =  Table[0, {i, 1, Length[IPFiles]}];
Do[
 (*IMPORT*)
 SetDirectory[ "F:\\April 30\\2027 t21 7.5ms lo step250ns"];
 rawtiming  = Import["Timing Log.txt", "Table"];
 p2 = rawtiming[[1, 2]];
 p3 = Table[rawtiming[[i, 3]], {i, 1, Length[rawtiming]}];
 actualt = p3 - p2;
 windowstart = Min[p3];
 windowend = Max[p3];
 IPSlice = ToExpression[Import[IPFiles[[i]], "List"]];
 QUADSlice = ToExpression[Import[QUADFiles[[i]], "List"]];
 IPval = Table[0, {j, 1, 100}];
 IPerrbar = Table[0, {j, 1, 100}];
```

```
QUADval = Table[0, {j, 1, 100}];
QUADerrbar = Table[0, {j, 1, 100}];
Do[
 chunk = Take[IPSlice, {j Navg + 1, (j + 1) Navg}];
 IPval[[j + 1]] = Mean[chunk];
 IPerrbar[[j + 1]] = StandardDeviation[chunk];
 chunk = Take[QUADSlice, {j Navg + 1, (j + 1) Navg}];
 QUADval[[j + 1]] = Mean[chunk];
 QUADerrbar[[j + 1]] = StandardDeviation[chunk];
 , {j, 0, 99}];
times1 = Table[actualt[[timebreak[[j]]]], {j, 1, 100}]/10^9;
datum = Transpose[{times1, IPval}];
SigAmp = Sqrt[IPval^2 + QUADval^2];
IPn1 = IPval/SigAmp;
QUADn1 = QUADval/SigAmp;
IPErr1 = IPerrbar/SigAmp;
QUADErr1 = QUADerrbar/SigAmp;
SliceDataWE =
 Table[{{times1[[j]], IPn1[[j]]}, ErrorBar[IPErr1[[j]]]}, {j, 1,
   100}];
PlotA = ErrorListPlot[SliceDataWE];

(*IMPORT*)
SetDirectory[ "F:\\April 30\\2105 t21 7.5ms hi step250ns"];
rawtiming  = Import["Timing Log.txt", "Table"];
p2 = rawtiming[[1, 2]];
p3 = Table[rawtiming[[j, 3]], {j, 1, Length[rawtiming]}];
actualt = p3 - p2;
windowstart = Min[p3];
windowend = Max[p3];
IPSlice = ToExpression[Import[IPFiles[[i]], "List"]];
QUADSlice = ToExpression[Import[QUADFiles[[i]], "List"]];
IPval2 = Table[0, {j, 1, 100}];
IPerrbar2 = Table[0, {j, 1, 100}];
QUADval2 = Table[0, {j, 1, 100}];
QUADerrbar2 = Table[0, {j, 1, 100}];
Do[
 chunk = Take[IPSlice, {j Navg + 1, (j + 1) Navg}];
 IPval2[[j + 1]] = Mean[chunk];
 IPerrbar2[[j + 1]] = StandardDeviation[chunk];
 chunk = Take[QUADSlice, {j Navg + 1, (j + 1) Navg}];
 QUADval2[[j + 1]] = Mean[chunk];
 QUADerrbar2[[j + 1]] = StandardDeviation[chunk];
 , {j, 0, 99}];
times2 = Table[actualt[[timebreak[[j]]]], {j, 1, 100}]/10^9;
datum = Transpose[{times2, IPval2}];
SigAmp = Sqrt[IPval2^2 + QUADval2^2];
IPn2 = IPval2/SigAmp;
QUADn2 = QUADval2/SigAmp;
IPErr2 = IPerrbar2/SigAmp;
QUADErr2 = QUADerrbar2/SigAmp;
SliceDataWE2 =
 Table[{{times2[[j]], IPn2[[j]]}, ErrorBar[IPErr2[[j]]]}, {j, 1,
   100}];
(*ALL DATA*)
Allamps = Join[ IPn1, IPn2];
Alltimes = Join[times1, times2];
Alldata = Transpose[{Alltimes, Allamps}];
Allerr = Join[IPErr1, IPErr2];
(*INITIAL FIT*)
reg = NonlinearRegress[Alldata,
  Sin[ 2 Pi f t + konst ], {{f, StartFreq}, {konst, Pi}}, t,
  RegressionReport -> {BestFit, ParameterCITable, FitResiduals}];
(*DROP OUTLIERS*)
droppoints = {};
Do[
 If[Abs[reg[[3, 2, j]]] > .2,
  AppendTo[droppoints, j];
  ]
 , {j, 1, Length[Alldata]}];
cutdata = Alldata;
cuterr = Allerr ;
cuttimes = Alltimes;
Do[
```

```
  cutdata = Drop[cutdata, {droppoints[[-j]]}];
  cuterr = Drop[cuterr,  {droppoints[[-j]]}];
  cuttimes = Drop[cuttimes,  {droppoints[[-j]]}];
  , {j, 1, Length[droppoints]}];
 (*DROP WONKY POINTS-LARGE STDDEVS*)
 droppoints = {};
 Do[
  If[cuterr[[j]] > .5,
    AppendTo[droppoints, j];
    ];
  , {j, 1, Length[cutdata]}];
 Do[
   cutdata = Drop[cutdata, {droppoints[[-j]]}];
   cuterr = Drop[cuterr,  {droppoints[[-j]]}];
   cuttimes = Drop[cuttimes,  {droppoints[[-j]]}];
   , {j, 1, Length[droppoints]}]
  (*SPLIT IN HALF AGAIN*)
  Do[
   If[cuttimes[[j]] - cuttimes[[j - 1]] > 0.0001,
     cutbreak = j;
     ];
   , {j, 2, Length[cuttimes]}];
 (*FIT*)
 If[Length[cutdata] > 50,
  reg = NonlinearRegress[cutdata,
    Sin[ 2 Pi f t + k ], {{f, StartFreq}, {k, 1}}, t,
    RegressionReport -> {BestFit, ParameterCITable}];
  beststart = reg[[2, 2, 1, 1, 1]];
  fs[[i]] = reg[[2, 2, 1, 1, 1]];
  StartFreq = fs[[i]];
  ferr[[i]] = reg[[2, 2, 1, 1, 2]];
  ,
  fs[[i]] = 0;
  ferr[[i]] = 0;
  ];
 If[Mod[i, 10] == 0,
  Print[(i/Length[IPFiles])*100., "%"];
  ];
 , {i, 1, Length[IPFiles]}]

(*==========CHOP the not important data ==========*)
ChoppedFs = Take[fs, {45, 300}];
ChoppedFerrs = Take[ferr, {45, 300}];
ChoppedDataWE =
  Table[{ChoppedFs[[i]], ChoppedFerrs[[i]]}, {i, 1,
    Length[ChoppedFs]}];
aa = ErrorListPlot[ChoppedDataWE]
(*Initial Linear Fit*)
Needs["LinearRegression`"]
ChoppedFs = Take[fs, {45, 175}];
ChoppedFerrs = Take[ferr, {45, 175}];
ChoppedDataWE =
  Table[{ChoppedFs[[i]], ChoppedFerrs[[i]]}, {i, 1,
    Length[ChoppedFs]}];
aa = ErrorListPlot[ChoppedDataWE];
reg = Regress[ChoppedFs, t, t,
   RegressionReport -> {BestFit, ParameterCITable, FitResiduals}];
reg[[2, 2]]
plotme = reg[[1, 2]];
BBB = Plot[plotme, {t, 0, Length[ChoppedFs]}, PlotStyle -> Red];
Show[aa, BBB]
(*========USE ALL DATA FORCED START FREQS========*)
raw = Import["S2Ch1-1000", "Table"][[8]]
base = ToExpression[StringTake[raw, {9, -5}]][[1]];
mentissa = ToExpression[StringTake[raw, {-3, -1}]][[1]];
timestep = base*10^mentissa;
NumPoints = Length[Import["S2Ch1-1000", "Table"][[10]]];
NumSlices = Length[IPFiles];
SliceTimeStep = NumPoints/NumSlices*timestep
SliceDuration = NumPoints*timestep/2000
fs;
ts = Table[SliceDuration  i , {i, 1, Length[fs]}];
ChoppedFs = Take[fs, {45, 300}];
```

```
Choppedts = Take[ts, {45, 300}];
aa = ListPlot[Transpose[{Choppedts, ChoppedFs}]]
lambda = 780.241*10^(-9)
k = 2 Pi/lambda
g = 9.81
StartFreqs =
  Table[187732.5 +   2k g (2 i SliceTimeStep k g)/(2Pi),  {i, 1, NumSlices}];
StartFreqs[[1]]
StartFreqs[[-1]]
bb = ListPlot[Transpose[{ts, StartFreqs}]];
Show[aa, bb, PlotRange -> All]
IPFiles = FileNames["SliceIP-**"];
QUADFiles = FileNames["SliceQuad-**"];
fs = Table[0, {i, 1, Length[IPFiles]}];
ferr =  Table[0, {i, 1, Length[IPFiles]}];
Do[
 SetDirectory[ "E:\\April 30\\2027 t21 7.5ms lo step250ns"];
 rawtiming  = Import["Timing Log.txt", "Table"];
 p2 = rawtiming[[1, 2]];
 p3 = Table[rawtiming[[i, 3]], {i, 1, Length[rawtiming]}];
 actualt = p3 - p2;
 windowstart = Min[p3];
 windowend = Max[p3];
 IPSlice = ToExpression[Import[IPFiles[[i]], "List"]];
 QUADSlice = ToExpression[Import[QUADFiles[[i]], "List"]];
 IPval = Table[0, {i, 1, 100}];
 IPerrbar = Table[0, {i, 1, 100}];
 QUADval = Table[0, {i, 1, 100}];
 QUADerrbar = Table[0, {i, 1, 100}];
 Do[
   chunk = Take[IPSlice, {i Navg + 1, (i + 1) Navg}];
   IPval[[i + 1]] = Mean[chunk];
   IPerrbar[[i + 1]] = StandardDeviation[chunk];
   chunk = Take[QUADSlice, {i Navg + 1, (i + 1) Navg}];
   QUADval[[i + 1]] = Mean[chunk];
   QUADerrbar[[i + 1]] = StandardDeviation[chunk];
   , {i, 0, 99}]
 times1 = Table[actualt[[timebreak[[i]]]], {i, 1, 100}]/10^9;
datum = Transpose[{times1, IPval}];
SigAmp = Sqrt[IPval^2 + QUADval^2];
IPn1 = IPval/SigAmp;
QUADn1 = QUADval/SigAmp;
IPErr1 = IPerrbar/SigAmp;
QUADErr1 = QUADerrbar/SigAmp;
SliceDataWE =
 Table[{{times1[[i]], IPn1[[i]]}, ErrorBar[IPErr1[[i]]]}, {i, 1,
   100}];
PlotA = ErrorListPlot[SliceDataWE];

SetDirectory[ "E:\\April 30\\2105 t21 7.5ms hi step250ns"];
rawtiming  = Import["Timing Log.txt", "Table"];
p2 = rawtiming[[1, 2]];
p3 = Table[rawtiming[[i, 3]], {i, 1, Length[rawtiming]}];
actualt = p3 - p2;
windowstart = Min[p3];
windowend = Max[p3];
IPSlice = ToExpression[Import[IPFiles[[i]], "List"]];
QUADSlice = ToExpression[Import[QUADFiles[[i]], "List"]];
IPval2 = Table[0, {i, 1, 100}];
IPerrbar2 = Table[0, {i, 1, 100}];
QUADval2 = Table[0, {i, 1, 100}];
QUADerrbar2 = Table[0, {i, 1, 100}];
Do[
  chunk = Take[IPSlice, {i Navg + 1, (i + 1) Navg}];
  IPval2[[i + 1]] = Mean[chunk];
  IPerrbar2[[i + 1]] = StandardDeviation[chunk];
  chunk = Take[QUADSlice, {i Navg + 1, (i + 1) Navg}];
  QUADval2[[i + 1]] = Mean[chunk];
  QUADerrbar2[[i + 1]] = StandardDeviation[chunk];
  , {i, 0, 99}]
 times2 = Table[actualt[[timebreak[[i]]]], {i, 1, 100}]/10^9;
datum = Transpose[{times2, IPval2}];
SigAmp = Sqrt[IPval2^2 + QUADval2^2];
```

```
IPn2 = IPval2/SigAmp;
QUADn2 = QUADval2/SigAmp;
IPErr2 = IPerrbar2/SigAmp;
QUADErr2 = QUADerrbar2/SigAmp;
SliceDataWE2 =
 Table[{{times2[[i]], IPn2[[i]]}, ErrorBar[IPErr2[[i]]]}, {i, 1,
   100}];
PlotB = ErrorListPlot[SliceDataWE2];
Allamps = Join[ IPn1, IPn2];
Alltimes = Join[times1, times2];
Alldata = Transpose[{Alltimes, Allamps}];
Allerr = Join[IPErr1, IPErr2];
(*INITIAL FIT*)
reg = NonlinearRegress[Alldata,
  Sin[ 2 Pi f t + konst], {{f, StartFreqs[[i]]}, {konst, Pi}}, t,
  RegressionReport -> {BestFit, ParameterCITable, FitResiduals}];
fs[[i]] = reg[[2, 2, 1, 1, 1]];
ferr[[i]] = reg[[2, 2, 1, 1, 2]];
(*DROP OUTLIERS*)
droppoints = {};
Do[
 If[Abs[reg[[3, 2, j]]] > .2,
  AppendTo[droppoints, j];
  ]
 , {j, 1, Length[Alldata]}];
cutdata = Alldata;
cuterr = Allerr ;
cuttimes = Alltimes;
Do[
 cutdata = Drop[cutdata, {droppoints[[-j]]}];
 cuterr = Drop[cuterr,  {droppoints[[-j]]}];
 cuttimes = Drop[cuttimes,  {droppoints[[-j]]}];
 , {j, 1, Length[droppoints]}];
(*DROP WONKY POINTS-LARGE STDDEVS*)
droppoints = {};
Do[
 If[cuterr[[j]] > .5,
   AppendTo[droppoints, j];
   ];
 , {j, 1, Length[cutdata]}];
Do[
 cutdata = Drop[cutdata, {droppoints[[-j]]}];
 cuterr = Drop[cuterr,  {droppoints[[-j]]}];
 cuttimes = Drop[cuttimes,  {droppoints[[-j]]}];
 , {j, 1, Length[droppoints]}];
(*SPLIT IN HALF AGAIN*)
Do[
 If[cuttimes[[j]] - cuttimes[[j - 1]] > 0.0001,
   cutbreak = j;
   ];
 , {j, 2, Length[cuttimes]}];
(*FIT*)
reg = NonlinearRegress[cutdata,
  Sin[ 2 Pi f t + konst ], {{f, StartFreq}, {konst, 1}}, t,
  RegressionReport -> {BestFit, ParameterCITable}];
fs[[i]] = reg[[2, 2, 1, 1, 1]];
ferr[[i]] = reg[[2, 2, 1, 1, 2]];
If[Mod[i, 10] == 0,
 Print[(i/Length[IPFiles])*100., "%"];
 ];
, {i, 1, Length[IPFiles]}]

(*Take a look*)
datum = Transpose[{ts, fs}];
dataWE = Table[{{ts[[i]], fs[[i]]}, ErrorBar[ferr[[i]]]}, {i, 1,
    420}];
pp = ErrorListPlot[dataWE];
reg = Regress[datum, t, t,
   RegressionReport -> {BestFit, ParameterCITable, FitResiduals}];
reg[[2, 2]]
plotme = reg[[1, 2]];
qq = Plot[plotme, {t, ts[[1]], ts[[-1]]}];
Show[pp, qq]
(*DROP OUTLIERS*)
droppoints = {};
```

```
Do[
  If[Abs[reg[[3, 2, j]]] > 7,
   AppendTo[droppoints, j];
   ]
  , {j, 1, Length[Alldata]}];
cutdata = datum;
cuterr = ferr ;
cuttimes = ts;
Do[
  cutdata = Drop[cutdata, {droppoints[[-j]]}];
  cuterr = Drop[cuterr,  {droppoints[[-j]]}];
  cuttimes = Drop[cuttimes,  {droppoints[[-j]]}];
  , {j, 1, Length[droppoints]}];
Length[cutdata]
rr = ListPlot[cutdata];
reg = Regress[cutdata, t, t,
   RegressionReport -> {BestFit, ParameterCITable, FitResiduals}];
reg[[2]]
plotme = reg[[1, 2]];
ss = Plot[plotme, {t, ts[[1]], ts[[-1]]}];
Show[rr, ss]
StandardDeviation[reg[[3, 2]]]
Histogram[reg[[3, 2]]]
```

D.2 Two Pulse Analysis

This section provides the source code for the echo envelope amplitude in Mathematica for the two-pulse AI. First, an initial fit to a chirped sinusoid is done with nominal values. A grid search iteratively changes the initial parameters to find the lowest fit error. The output is the final value for g at embedded within the notebook.

```
Needs["NonlinearRegression`"]
Needs["Histograms`"]
Needs["ErrorBarPlots`"]
k = 2 Pi/lambda
lambda = 780.23*10^(-9)
Omegar =    hbar (2 k)^2 / (2 M)
hbar = 6.62606876*10^(-34) /(2 Pi);
M = 84.9117*amu
amu = 1.66053886*10^(-27)
RootDir = "H:\\May 2009\\May12\\";
SetDirectory[ RootDir]
FolderNames = FileNames[]
(*Ordering Folders*)
FolderNames = { FolderNames[[11]], FolderNames[[12]],
  FolderNames[[1]], FolderNames[[3]], FolderNames[[4]],
  FolderNames[[2]]}
FolderNames = Flatten[FolderNames]
TStepNames = {-15, 349.5, 0, 299.5, 50, 100}
Tstep =  {324, 81, 324, 86, 324, 216}

(*Choose Which Data sets*)
(*FolderNames = Drop[FolderNames,{-2}]
TStepNames=Drop[TStepNames,{-2}]
Tstep=Drop[ Tstep,{-2}]*)
(*FolderNames = Flatten[{Take[FolderNames,{1,2}], \
Take[FolderNames,{4}]}]
TStepNames=Flatten[{Take[TStepNames,{1,2}], Take[TStepNames,{4}]}]
Tstep=Flatten[{Take[Tstep,{1,2}], Take[Tstep,{4}]}]*)
FolderNames =
 Flatten[{Take[FolderNames, 1], Take[FolderNames, {5}],
   Take[FolderNames, {4}], Take[FolderNames, {2}]}]
TStepNames =
 Flatten[{Take[TStepNames, 1], Take[TStepNames, {5}],
   Take[TStepNames, {4}], Take[TStepNames, {2}]}]
Tstep = Flatten[{Take[Tstep, 1], Take[Tstep, {5}], Take[Tstep, {4}],
```

```
   Take[Tstep, {2}]}]
(*Timing Info for each window*)
Pulse1 = 0.021594500 + .000032388*ToExpression[TStepNames[[2]]];
Pulse2 = 0.023097000 + 2*.000032388*ToExpression[TStepNames[[2]]];
TList2 = Table[(Pulse2 - Pulse1) + j Tstep[[2]]/10^9, {j, 1,
    Length[Ch1Amp]}];
Pulse1 = 0.021594500 + .000032388*ToExpression[TStepNames[[3]]];
Pulse2 = 0.023097000 + 2*.000032388*ToExpression[TStepNames[[3]]];
TList3 = Table[(Pulse2 - Pulse1) + j Tstep[[3]]/10^9, {j, 1,
    Length[Ch1Amp]}];
Pulse1 = 0.021594500 + .000032388*ToExpression[TStepNames[[4]]];
Pulse2 = 0.023097000 + 2*.000032388*ToExpression[TStepNames[[4]]];
TList4 = Table[(Pulse2 - Pulse1) + j Tstep[[4]]/10^9, {j, 1,
    Length[Ch1Amp]}];
(*Window 1 Check*)
CurrentDir = RootDir <> FolderNames[[1]];
SetDirectory[CurrentDir]
Ch1Amp = Import["Ch1Accumulator.txt", "List"];
Ch1Err = Ch1Amp/4;
Ch2Amp = Import["Ch2Accumulator.txt", "List"];
Ch2Err = Ch2Amp/4;
phase = ArcTan[Ch1Amp, Ch2Amp];
SigAmp = Sqrt[Ch1Amp^2 + Ch2Amp^2];
SigAmpErr = (Abs[Ch1Amp*Ch1Err] + Abs[Ch2Amp*Ch2Err])/SigAmp;
IPWE = Table[{{TList1[[i]], Ch1Amp[[i]]},
    ErrorBar[Abs[Ch1Err[[i]]]]}, {i, 1, Length[Ch1Amp]}];
QWE = Table[{{TList1[[i]], Ch2Amp[[i]]},
    ErrorBar[Abs[Ch2Err[[i]]]]}, {i, 1, Length[Ch2Amp]}];
Pulse1 = 0.021594500 + .000032388*ToExpression[TStepNames[[1]]];
Pulse2 = 0.023097000 + 2*.000032388*ToExpression[TStepNames[[1]]];
TList1 = Table[(Pulse2 - Pulse1) + j Tstep[[1]]/10^9, {j, 1,
    Length[Ch1Amp]}];
p1 = ErrorListPlot[{IPWE, QWE}, Frame -> True, Axes -> False];
pzero = Plot[0, {t, TList1[[1]], TList1[[-1]]}, PlotStyle -> Black];
Show[p1, pzero]
AMPWE =  Table[{{TList1[[i]], SigAmp[[i]]},
    ErrorBar[Abs[SigAmpErr[[i]]]]}, {i, 1, Length[SigAmp]}];
p2 = ErrorListPlot[AMPWE, PlotRange -> All];
Show[p2, Frame -> True, Axes -> False]
(*Variables*)
Taccumulator = {}
Ch1accumulator = {}
Ch2accumulator = {}
TStart = {}
TEnd = {}
SigAmpT = {}
(*IMPORT ALL WINDOWS*)
Do[
 CurrentDir = RootDir <> FolderNames[[i]];
 SetDirectory[CurrentDir];
 Ch1Amp = Import["Ch1Accumulator.txt", "List"];
 Ch2Amp = Import["Ch2Accumulator.txt", "List"];
 phase = ArcTan[Ch1Amp, Ch2Amp];
 SigAmp = Sqrt[Ch1Amp^2 + Ch2Amp^2];
 Print[ListPlot[SigAmp, Joined -> True, PlotRange -> All,
   AxesLabel -> {"Time Step #", "Amplitude"}]];
 Pulse1 = 0.021594500 + .000032388*ToExpression[TStepNames[[i]]];
 Pulse2 = 0.023097000 + 2*.000032388*ToExpression[TStepNames[[i]]];
 TList = Table[(Pulse2 - Pulse1) + j Tstep[[i]]/10^9, {j, 1,
    Length[Ch1Amp]}];
 AppendTo[SigAmpT, TList];
 AppendTo[TStart, TList[[1]]];
 AppendTo[TEnd, TList[[-1]]];
 Print[Pulse2 - Pulse1];
   (*MAKE SURE THIS IS ODD!!*)
 SmoothRange = 3;
 Smoothed = Table[0, {i, 1, Length[Ch1Amp]}];
 SmoothCenter = IntegerPart[SmoothRange/2] + 1;
 SmoothOrder = IntegerPart[SmoothRange/2];
 Do[
  Smoothed[[i]] = Ch1Amp[[i]];
```

```
  , {i, 1, SmoothOrder}];
Do[
  Smoothed[[i]] =
    Total[Take[Ch1Amp, {i - SmoothOrder, i + SmoothOrder }]]/
     SmoothRange;
  , {i, SmoothCenter, Length[Ch1Amp] - SmoothCenter}]
 Do[
  Smoothed[[i]] = Ch1Amp[[i]];
  , {i, Length[Ch1Amp] - SmoothOrder, Length[Ch1Amp]}];
Smoothed = Drop[Smoothed, SmoothOrder + 1];
Smoothed = Drop[Smoothed, -SmoothOrder + 1];
b = ListPlot[Smoothed, PlotRange -> All, Joined -> True,
  PlotStyle -> Red];
SmoothedTList =
 Table[(Pulse2 - Pulse1) + j Tstep[[i]]*10^(-9) +
   SmoothOrder*Tstep[[i]]*10^(-9), {j, 1, Length[Smoothed]}];
LoTimeCh1 = Transpose[{SmoothedTList, Smoothed}];
Show[ListPlot[Ch1Amp, Joined -> True], b];
AppendTo[Ch1accumulator, Smoothed];

Smoothed = Table[0, {i, 1, Length[Ch2Amp]}];
SmoothCenter = IntegerPart[SmoothRange/2] + 1;
SmoothOrder = IntegerPart[SmoothRange/2];
Do[
 Smoothed[[i]] = Ch2Amp[[i]];
 , {i, 1, SmoothOrder}];
Do[
  Smoothed[[i]] =
    Total[Take[Ch2Amp, {i - SmoothOrder, i + SmoothOrder }]]/
     SmoothRange;
  , {i, SmoothCenter, Length[Ch2Amp] - SmoothCenter}]
 Do[
  Smoothed[[i]] = Ch1Amp[[i]];
  , {i, Length[Ch2Amp] - SmoothOrder, Length[Ch2Amp]}];
Smoothed = Drop[Smoothed, SmoothOrder + 1];
Smoothed = Drop[Smoothed, -SmoothOrder + 1];
b = ListPlot[Smoothed, PlotRange -> All, Joined -> True,
  PlotStyle -> Red];
Show[b, ListPlot[Ch2Amp, Joined -> True]];
LoTimeCh2 = Transpose[{SmoothedTList, Smoothed}];
AppendTo[Taccumulator, SmoothedTList];
AppendTo[Ch2accumulator, Smoothed];
, {i, 1, Length[FolderNames]}]

(*Generate Graphs with Error Bars*)
(*set jj = to the folder*)
jj = 1
Ch1Amp = Ch1accumulator[[jj]];
Ch1Err = Ch1Amp/4;
Ch2Amp = Ch2accumulator[[jj]];
Ch2Err = Ch2Amp/4;
times = Taccumulator[[jj]];
phase = ArcTan[Ch1Amp, Ch2Amp];
SigAmp = Sqrt[Ch1Amp^2 + Ch2Amp^2];
SigAmpErr = (Abs[Ch1Amp*Ch1Err] + Abs[Ch2Amp*Ch2Err])/SigAmp;
IP = Transpose[{times, Ch1Amp}];
Q = Transpose[{times, Ch2Amp}];
p2 = ListPlot[{IP, Q}];
IPWE = Table[{{times[[i]], Ch1Amp[[i]]},
    ErrorBar[Abs[Ch1Err[[i]]]]}, {i, 1, Length[Ch1Amp]}];
QWE = Table[{{times[[i]], Ch2Amp[[i]]},
    ErrorBar[Abs[Ch2Err[[i]]]]}, {i, 1, Length[Ch2Amp]}];
p1 = ErrorListPlot[{IPWE, QWE}, Frame -> True, Axes -> False,
   Joined -> True];
pzero = Plot[0, {t, times[[1]], times[[-1]]}, PlotStyle -> Black];
Show[p1, pzero, p2]
AMPWE =  Table[{{times[[i]], SigAmp[[i]]},
    ErrorBar[Abs[SigAmpErr[[i]]]]}, {i, 1, Length[SigAmp]}];
p2 = ErrorListPlot[AMPWE, PlotRange -> All];
Show[p2, Frame -> True, Axes -> False]
ampn = Ch1Amp/SigAmp;
ampnerr = Abs[Ch1Err/SigAmp] + Abs[Ch1Amp/SigAmp^2*SigAmpErr];
NormAmpWE =
  Table[{{times[[i]], ampn[[i]]}, ErrorBar[Abs[ampnerr[[i]]]]}, {i, 1,
```

```
    Length[SigAmp]}];
pA = ErrorListPlot[NormAmpWE];
ampn2 = Ch2Amp/SigAmp;
ampnerr2 = Abs[Ch2Err/SigAmp] + Abs[Ch2Amp/SigAmp^2*SigAmpErr];
NormAmpWE2 =
  Table[{{times[[i]], ampn2[[i]]}, ErrorBar[Abs[ampnerr2[[i]]]]}, {i,
    1, Length[SigAmp]}];
pB = ErrorListPlot[NormAmpWE2];
ErrorListPlot[{NormAmpWE, NormAmpWE2}, Frame -> True, Axes -> False]

(*Put it all together*)
datum1 = Transpose[{Flatten[Taccumulator], Flatten[Ch1accumulator]}];
datum2 = Transpose[{Flatten[Taccumulator], Flatten[Ch2accumulator]}];
ListPlot[{datum1, datum2}, PlotRange -> All, AxesOrigin -> {0, 0},
 PlotRange -> All]
datum3 = Transpose[{Flatten[SigAmpT],Flatten[TotSigAmp]}];
(*DROP LOW SIGNAL POINTS*)
NormFactor =
  Table[  Sqrt[
    Flatten[Ch1accumulator][[i]] ^2 +
     Flatten[Ch2accumulator][[i]] ^2], {i, 1,
    Length[Flatten[Ch1accumulator]]}];
Histogram[NormFactor]
NormData1 =
  Transpose[{Flatten[Taccumulator], (Flatten[Ch1accumulator])/
     NormFactor}];
NormData2 =
  Transpose[{Flatten[Taccumulator], (Flatten[Ch2accumulator])/
     NormFactor}];
SigToNoiseNormData1 = {}
SigToNoiseNormData2 = {}
WeightingFactor = {}
Do[
 If[NormFactor[[i]] > .3,
   SigToNoiseNormData1 = Append[SigToNoiseNormData1, NormData1[[i]]];
   SigToNoiseNormData2 = Append[SigToNoiseNormData2, NormData2[[i]]];
   WeightingFactor = Append[WeightingFactor, NormFactor[[i]]];
   ];
 , {i, 1, Length[NormFactor]}]
Length[SigToNoiseNormData1]
(*
Do[
Print[ListPlot[{NormData1,NormData2},PlotRange->{ \
{Min[SigAmpT[[i]]],Max[SigAmpT[[i]]]},{-1,1}},Joined->True]]
,{i,1,4}]
*)
(*Generate Graphs with Error Bars AFTER S2N consideration*)
(*set jj = to the folder*)
jj = 1
Ch1Amp = Ch1accumulator[[jj]];
Ch1Err = Ch1Amp/4;
Ch2Amp = Ch2accumulator[[jj]];
Ch2Err = Ch2Amp/4;
times = Taccumulator[[jj]];
phase = ArcTan[Ch1Amp, Ch2Amp];
SigAmp = Sqrt[Ch1Amp^2 + Ch2Amp^2];
SigAmpErr = (Abs[Ch1Amp*Ch1Err] + Abs[Ch2Amp*Ch2Err])/SigAmp;
IPN = Transpose[{times, Ch1Amp/SigAmp}];
IPNerr = Ch1Err/SigAmp + Ch1Amp/SigAmp^2 SigAmpErr;
QN = Transpose[{times, Ch2Amp/SigAmp}];
IPNWE = Table[{{times[[i]], Ch1Amp[[i]]/SigAmp[[i]]},
    ErrorBar[Abs[IPNerr[[i]]]]}, {i, 1, Length[IPN]}];
p1nw = ListPlot[IPN]
p1w = ErrorListPlot[IPNWE, Frame -> True, Axes -> False,
   PlotStyle -> Gray];
pzero = Plot[0, {t, times[[1]], times[[-1]]}, PlotStyle -> Black];
Show[p1w, pzero]

(*GRID SEARCH of initial velocity and gravity*)
Clear[giterator, Vnotiterator, ii]
gstart = Table[9.79 + 0.001 i, {i, 1, 20}];
VnotStart = Table[-0.0001 + 0.0001 i, {i, 1, 40}];
```

```
glisting = Table[ 0, {ii, 1, Length[gstart]*Length[VnotStart]}];
Length[glisting]
gstart[[1]]
gstart[[-1]]
VnotStart[[1]]
VnotStart[[-1]]
ii = 0;
normeqn = Sin[2 k g t^2 + 2 Vnot k t + h]
Do[
 Print[gstart[[giterator]],  Regress[[2, 2, 1, 1]]];
 Do[
  ii = ii + 1;
  Regress =
   NonlinearRegress[SigToNoiseNormData1,
    normeqn, {{g, gstart[[giterator]]}, {Vnot,
      VnotStart[[Vnotiterator]]}, {h, 0}}, t,
    RegressionReport -> {BestFit, ParameterCITable, FitResiduals},
    MaxIterations -> 250, Weights -> WeightingFactor];
  glisting[[ii]] = {gstart[[giterator]], VnotStart[[Vnotiterator]],
    Regress[[2, 2, 1, 1]]};
  , {Vnotiterator, 1, Length[VnotStart]}];
,{giterator, 1, Length[gstart]}]
(*Export grid search of gravity*)
SetDirectory["C:\\" ]
Export["glisting.txt", glisting]
Do[
 If[
   Length[glisting[[i]]] > 1,
   gerrors[[i]] =
    ToExpression[StringDrop[ToString[glisting[[i, 4]]], -1]]
   ,
   gerrors[[i]] = .1;
   ];
 , {i, 1, Length[glisting]}]
(*Visualize Grid Search*)
i = 0
row1 = Take[glisting, {40 i + 1, 40 (i + 1)}];
MyGrid = Table[0, {i, 1, 20}]
Do[
 MyGrid[[i]] = Take[glisting, {40 (i - 1) + 1, 40 i}];
 , {i, 1, 20}]
xyzGrid =
  Table[{MyGrid[[i, j, 1]], MyGrid[[i, j, 2]],
    MyGrid[[i, j, 3, 2]]}, {i, 1, 20}, {j, 1, 40}];
ListPointPlot3D[xyzGrid]
(*Find LOWEST g error*)
Do[
 gerrors[[i]] = ToExpression[StringDrop[ToString[gerrors[[i]]], -1]]
 , {i, 1, Length[glisting]}]
posit = Position[ gerrors, Min[gerrors] ]
Do[
 Print[glisting[[posit[[i]]]]];
 , {i, 1, Length[posit]}]
(*Put the initial lowest number to do FINAL FIT*)
normeqn = Sin[2 k g t^2 + 2 Vnot k t + h]
normeqn2 = -Cos[2 k g t^2 + 2 Vnot k t + h]
Regress2 =
  NonlinearRegress[SigToNoiseNormData1,
   normeqn, {{g, 9.8}, {Vnot, .000}, {h, 0}}, t,
   RegressionReport -> {BestFit, ParameterCITable, FitResiduals},
   MaxIterations -> 250, Weights -> WeightingFactor];
Print[Regress2[[1]], Regress2[[2]]];
Do[
 pa = Plot[Regress2[[1, 2]], {t, SigAmpT[[i, 1]], SigAmpT[[i, -1]]}];
 pb = ListPlot[SigToNoiseNormData1,
   PlotRange -> {{SigAmpT[[i, 1]], SigAmpT[[i, -1]]}, All}];
 Print[Show[pa, pb,
   PlotRange -> {{SigAmpT[[i, 1]], SigAmpT[[i, -1]]}, All}]];
 , {i, 1, Length[SigAmpT]}]
Regress3 =
  NonlinearRegress[SigToNoiseNormData2,
   normeqn2, {{g, 9.8}, {Vnot, .000}, {h, 0}}, t,
   RegressionReport -> {BestFit, ParameterCITable, FitResiduals},
```

```
   MaxIterations -> 250, Weights -> WeightingFactor];
Print[Regress3[[1]], Regress3[[2]]];
Do[
 pa = Plot[Regress3[[1, 2]], {t, SigAmpT[[i, 1]], SigAmpT[[i, -1]]},
   PlotStyle -> Red];
 pb = ListPlot[SigToNoiseNormData2,
   PlotRange -> {{SigAmpT[[i, 1]], SigAmpT[[i, -1]]}, All}];
 Print[Show[pa, pb,
   PlotRange -> {{SigAmpT[[i, 1]], SigAmpT[[i, -1]]}, All}]];
 , {i, 1, Length[SigAmpT]}]
```

D.3 Signal-to-Noise Ratio Simulation: Three Pulse AI

This section provides the source code for the signal-to-noise simulation of the three-pulse AI. User inputs are the amplitude noise size, phase noise size and timescale. The number of points is hard-coded to be 100, taking 5 cycles within each time window.

```
Needs["Histograms`"]
Needs["NonlinearRegression`"]
(*Generate Random*)
Ampmean = 0
Ampvar = .1
AmpNoise = RandomReal[NormalDistribution[Ampmean, Ampvar], {200}];
Histogram[AmpNoise]
Phasemean = 0
Phasevar = .2
PhaseNoise =
  RandomReal[NormalDistribution[Phasemean, Phasevar], {200}];
Histogram[PhaseNoise]
(*System Inputs*)
TimeScale = 0.050 (*s*)
T21 = TimeScale/4;
T32 = TimeScale/2;
k = 2 Pi/lambda;
lambda = 780.241*10^(-9);
g = 9.806651
omega = 2 k g T21
period = 2 Pi/omega;
stepsize = period*5/100;
(*ZERO NOISE*)
tees = Table[i*stepsize, {i, 1, 100}];
y1 = Sin[omega tees];
ListPlot[y1]
p1 = ListPlot[Transpose[{tees, y1}]];
tees2 = tees + T32;
y2 = Sin[omega tees2];
ListPlot[y2]
p2 = ListPlot[Transpose[{tees2, y2}]];
allt = Join[tees, tees2];
ally = Join[y1, y2];
Alldatum = Transpose[{allt, ally}];
reg = NonlinearRegress[Alldatum,
  A Sin [ nu t], {{A, 1}, {nu, omega}}, t,
  RegressionReport -> {BestFit, ParameterCITable}]
plotme = reg[[1, 2]];
p3 = Plot[plotme, {t, tees[[1]], tees[[-1]]}, PlotStyle -> Red];
p4 = Plot[plotme, {t, tees2[[1]], tees2[[-1]]}, PlotStyle -> Red];
Show[p1, p3]
Show[p2, p4]
(*Data With Noise*)
y1Noisy =
  Table[ (1 + AmpNoise[[i]])
    Sin[omega tees[[i]] + PhaseNoise[[i]]], {i, 1, 100}];
y2Noisy =
  Table[ (1 + AmpNoise[[i + 100]])
    Sin[omega tees2[[i]] + PhaseNoise[[i + 100]]], {i, 1, 100}];
```

```
p1 = ListPlot[Transpose[{tees, y1Noisy}]];
p2 = ListPlot[Transpose[{tees2, y2Noisy}]];
NoisyData = Join[y1Noisy, y2Noisy];
allt = Join[tees, tees2];
AlldatumNoisy = Transpose[{allt, NoisyData}];
reg = NonlinearRegress[AlldatumNoisy,
  A Sin [ nu t], {{A, 1}, {nu, omega}}, t,
  RegressionReport -> {BestFit, ParameterCITable}]
plotme = reg[[1, 2]];
p3 = Plot[plotme, {t, tees[[1]], tees[[-1]]}, PlotStyle -> Red];
p4 = Plot[plotme, {t, tees2[[1]], tees2[[-1]]}, PlotStyle -> Red];
Show[p1, p3, Frame -> True]
Show[p2, p4, Frame -> True]
reg[[2, 2, 1, 2, 2]]/reg[[2, 2, 1, 2, 1]]*10^6
```

D.4 Signal-to-Noise Ratio Simulation: Two-Pulse AI

This section provides the source code for the signal-to-noise simulation of the thwo-pulse AI. User inputs are the amplitude noise size, phase noise size and timescale. The number of points is hard-coded to be 100, taking a few cycles within three time windows.

```
Needs["Histograms`"]
Needs["NonlinearRegression`"]
(*Generate Noise*)
Ampmean = 0
Ampvar = .1
AmpNoise = RandomReal[NormalDistribution[Ampmean, Ampvar], {300}];
Histogram[AmpNoise]
Phasemean = 0
Phasevar = .7
PhaseNoise =
  RandomReal[NormalDistribution[Phasemean, Phasevar], {300}];
Histogram[PhaseNoise]
TimeScale = 0.050 (*s*)
k = 2 Pi/lambda;
lambda = 780.241*10^(-9);
g = 9.806651
(*Generate Points in different time windows*)
T211 = 0.0015
omega1 = 4 k g T211;
period1 = 2 Pi/omega1 T211;
stepsize1 = 20 period1
T212 = 0.003
omega2 = 4 k g T212;
period2 = 2 Pi/omega1 T212;
stepsize2 = 5 period2
T213 = 0.012
omega3 = 4 k g T213;
period3 = 2 Pi/omega1 T213;
stepsize3 = .5 period3
tees1 = Table[i*stepsize1 + T211, {i, 1, 100}];
y1 = Sin[2 k g tees1^2];
ListPlot[y1]
p1 = ListPlot[Transpose[{tees1, y1}]];
tees2 = Table[i*stepsize2 + T212, {i, 1, 100}];
y2 = Sin[2 k g tees2^2];
ListPlot[y2]
p2 = ListPlot[Transpose[{tees2, y2}]];
tees3 = Table[i*stepsize3 + T213, {i, 1, 100}];
y3 = Sin[2 k g tees3^2];
ListPlot[y3]
p3 = ListPlot[Transpose[{tees3, y3}]];
```

```
(*ZERO NOISE*)
allt = Join[tees1, tees2, tees3];
ally = Join[y1, y2, y3];
Alldatum = Transpose[{allt, ally}];
ListPlot[Alldatum]
reg = NonlinearRegress[Alldatum,
  A Sin [ a t^2], {{A, 1}, {a, 2 k g}}, t,
  RegressionReport -> {BestFit, ParameterCITable}]
plotme = reg[[1, 2]];
p11 = Plot[plotme, {t, tees1[[1]], tees1[[-1]]}, PlotStyle -> Red];
p22 = Plot[plotme, {t, tees2[[1]], tees2[[-1]]}, PlotStyle -> Red];
p33 = Plot[plotme, {t, tees3[[1]], tees3[[-1]]}, PlotStyle -> Red];
Show[p1, p11]
Show[p2, p22]
Show[p3, p33]
tees1 = Table[i*stepsize1 + T211, {i, 1, 100}];
y1 = Sin[2 k g tees1^2];
p1 = ListPlot[Transpose[{tees1, y1}]];
tees2 = Table[i*stepsize2 + T212, {i, 1, 100}];
y2 = Sin[2 k g tees2^2];
p2 = ListPlot[Transpose[{tees2, y2}]];
tees3 = Table[i*stepsize3 + T213, {i, 1, 100}];
y3 = Sin[2 k g tees3^2];
p3 = ListPlot[Transpose[{tees3, y3}]];
(*WITH NOISE, CURRENT VALUES*)
y1Noisy =
  Table[ (1 + AmpNoise[[i]])
    Sin[2 k g tees1[[i]]^2 + PhaseNoise[[i]]], {i, 1, 100}];
y2Noisy =
  Table[ (1 + AmpNoise[[i + 100]])
    Sin[2 k g  tees2[[i]]^2 + PhaseNoise[[i + 100]]], {i, 1, 100}];
y3Noisy =
  Table[ (1 + AmpNoise[[i + 100]])
    Sin[2 k g  tees3[[i]]^2 + PhaseNoise[[i + 100]]], {i, 1, 100}];
p1 = ListPlot[Transpose[{tees1, y1Noisy}]];
p2 = ListPlot[Transpose[{tees2, y2Noisy}]];
p3 = ListPlot[Transpose[{tees3, y3Noisy}]];
NoisyData = Join[y1Noisy, y2Noisy, y3Noisy];
allt = Join[tees1, tees2, tees3];
AlldatumNoisy = Transpose[{allt, NoisyData}];
reg = NonlinearRegress[AlldatumNoisy,
  A Sin [  a t^2], {{A, 1}, {a, 2 k g}}, t,
  RegressionReport -> {BestFit, ParameterCITable}]
plotme = reg[[1, 2]];
p11 = Plot[plotme, {t, tees1[[1]], tees1[[-1]]}, PlotStyle -> Red];
p22 = Plot[plotme, {t, tees2[[1]], tees2[[-1]]}, PlotStyle -> Red];
p33 = Plot[plotme, {t, tees3[[1]], tees3[[-1]]}, PlotStyle -> Red];
Show[p1, p11, Frame -> True]
Show[p2, p22, Frame -> True]
Show[p3, p33, Frame -> True]
(*PROJECTED System Parameters*)
TimeScale = 0.300 (*s*)
k = 2 Pi/lambda;
lambda = 780.241*10^(-9);
g = 9.806651
T211 = 0.0015
omega1 = 4 k g T211;
period1 = 2 Pi/omega1 T211;
stepsize1 = 20 period1
T212 = 0.050
omega2 = 4 k g T212;
period2 = 2 Pi/omega1 T212;
stepsize2 = .03 period2
T213 = 0.150
omega3 = 4 k g T213;
period3 = 2 Pi/omega1 T213;
stepsize3 = .002 period3
tees1 = Table[i*stepsize1 + T211, {i, 1, 100}];
y1 = Sin[2 k g tees1^2];
ListPlot[y1]
p1 = ListPlot[Transpose[{tees1, y1}]];
tees2 = Table[i*stepsize2 + T212, {i, 1, 100}];
```

```
y2 = Sin[2 k g tees2^2];
ListPlot[y2]
p2 = ListPlot[Transpose[{tees2, y2}]];
tees3 = Table[i*stepsize3 + T213, {i, 1, 100}];
y3 = Sin[2 k g tees3^2];
ListPlot[y3]
p3 = ListPlot[Transpose[{tees3, y3}]];
y1Noisy =
  Table[ (170 + AmpNoise[[i]])
    Sin[2 k g tees1[[i]]^2 + PhaseNoise[[i]]/70], {i, 1, 100}];
y2Noisy =
  Table[ (170 + AmpNoise[[i + 100]])
    Sin[2 k g  tees2[[i]]^2 + PhaseNoise[[i + 100]]/70], {i, 1,
    100}];
y3Noisy =
  Table[ (170 + AmpNoise[[i + 100]])
    Sin[2 k g  tees3[[i]]^2 + PhaseNoise[[i + 100]]/70], {i, 1,
    100}];
p1 = ListPlot[Transpose[{tees1, y1Noisy}]];
p2 = ListPlot[Transpose[{tees2, y2Noisy}]];
p3 = ListPlot[Transpose[{tees3, y3Noisy}]];
NoisyData = Join[y1Noisy, y2Noisy, y3Noisy];
allt = Join[tees1, tees2, tees3];
AlldatumNoisy = Transpose[{allt, NoisyData}];
reg = NonlinearRegress[AlldatumNoisy,
  A Sin [  a t^2], {{A, 1}, {a, 2 k g}}, t,
  RegressionReport -> {BestFit, ParameterCITable}]
plotme = reg[[1, 2]];
p11 = Plot[plotme, {t, tees1[[1]], tees1[[-1]]}, PlotStyle -> Red];
p22 = Plot[plotme, {t, tees2[[1]], tees2[[-1]]}, PlotStyle -> Red];
p33 = Plot[plotme, {t, tees3[[1]], tees3[[-1]]}, PlotStyle -> Red];
Show[p1, p11, Frame -> True]
Show[p2, p22, Frame -> True]
Show[p3, p33, Frame -> True]
reg[[2, 2, 1, 2, 2]]/reg[[2, 2, 1, 2, 1]]*10^6
```

E LabVIEW Code

E.1 Main Data Taking Program

This section provides the LabVIEW source code for the data taking program to acquire data. The front panel is shown in figure E.1. The program is taken broken into a number of sub-VIs which follow. The initial setup of the program is as follows:

1. Hardware setup

   Define GPIB addresses of remote machines

   Initialize Oscilloscopes by setting formatting options from the Tektronix oscilloscope

2. Obtain Oscilloscope Settings

   Stores current oscilloscope settings within program for conversion

3. Set File Names

   Chooses file path and file name

4. Generate Timing

   Choose initial pulse parameters and pulse spacing

   Choose step size, number of averages and number of points

   Choose linear pulse delay change or generate a list of randomized order

To begin taking data acquisition, the large green button is pushed. The loop of the data acquisition is as follows:

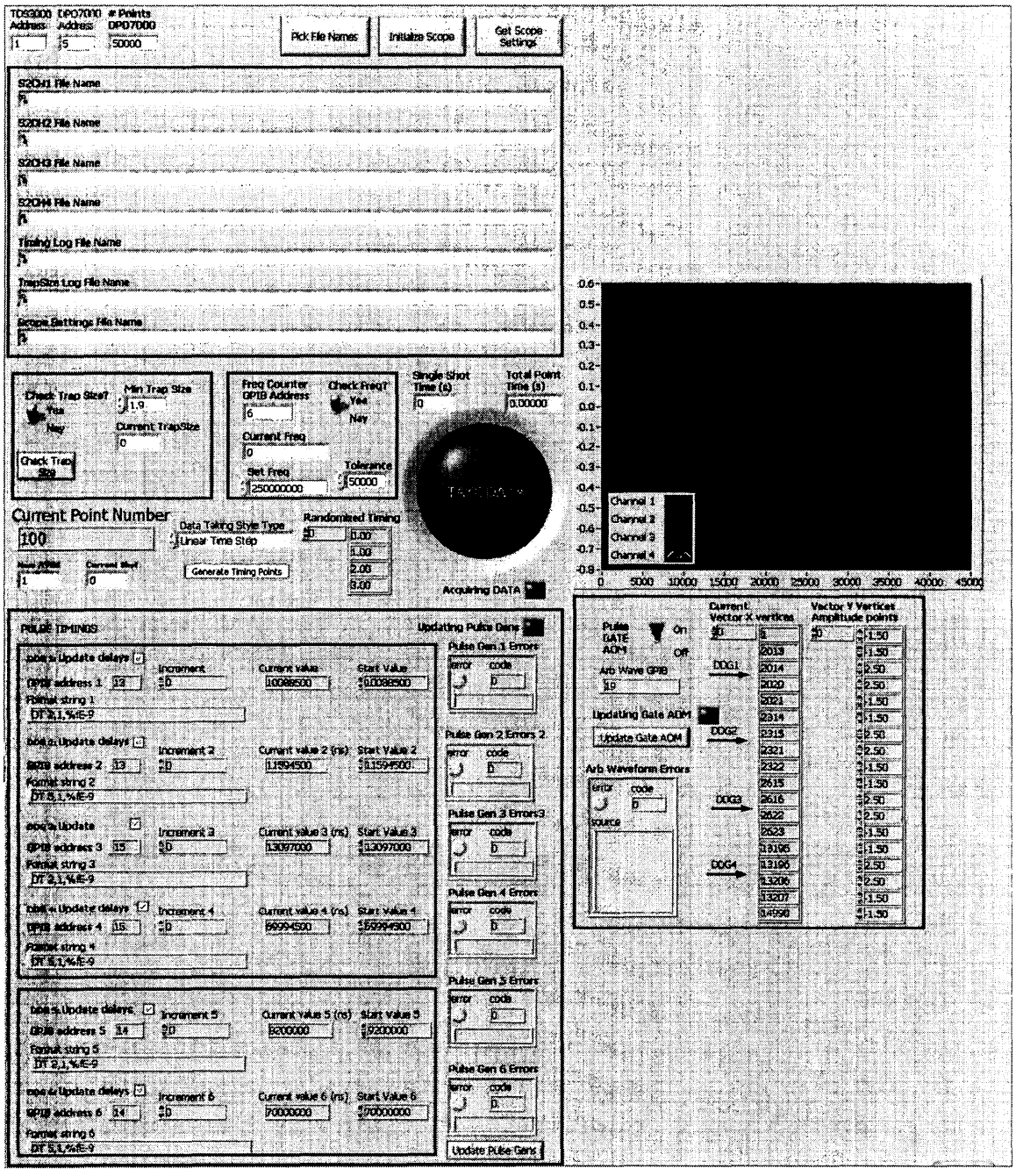

Figure E.1: Front panel of the LabVIEW main data taking program.

1. Send Timing

   Sends the current timing information to pulse generators

2. Generate Gate AOM timing

   Creates Gate AOM pulse timing so that optical pulses overlap

3. Send Timing to Gate AOM

   Sends the arbitrary wave generator data generated from previous step

4. Check Trap size

   Checks trap size to monitor laser frequency locks. If too low, prompt user.

5. Check Frequency

   Polls external frequency counter to monitor PLL frequency. If not at nominal values, prompt user.

6. Synchronize Oscilloscopes

   Sets each oscilloscope for single acquisition

   Begin oscilloscope trigger sequence

   Poll oscilloscopes with *OPC command to see of the operation is completed

   If not, wait, and re-poll

7. Data Transfer

   Poll oscilloscope with CURVe command to transfer current trace from screen to computer

8. Conversion

   Convert binary information from oscilloscope with saved oscilloscope settings to parsed data in ASCII and numeric values

9. Save Data

   Adds pre-amble to file, and bundles voltage trace into file

   Save trap size, frequency and timing information

10. Increment

    If linear timing, increment timing information by step size

    If randomized timing order, look up next item in list

    Increment file name

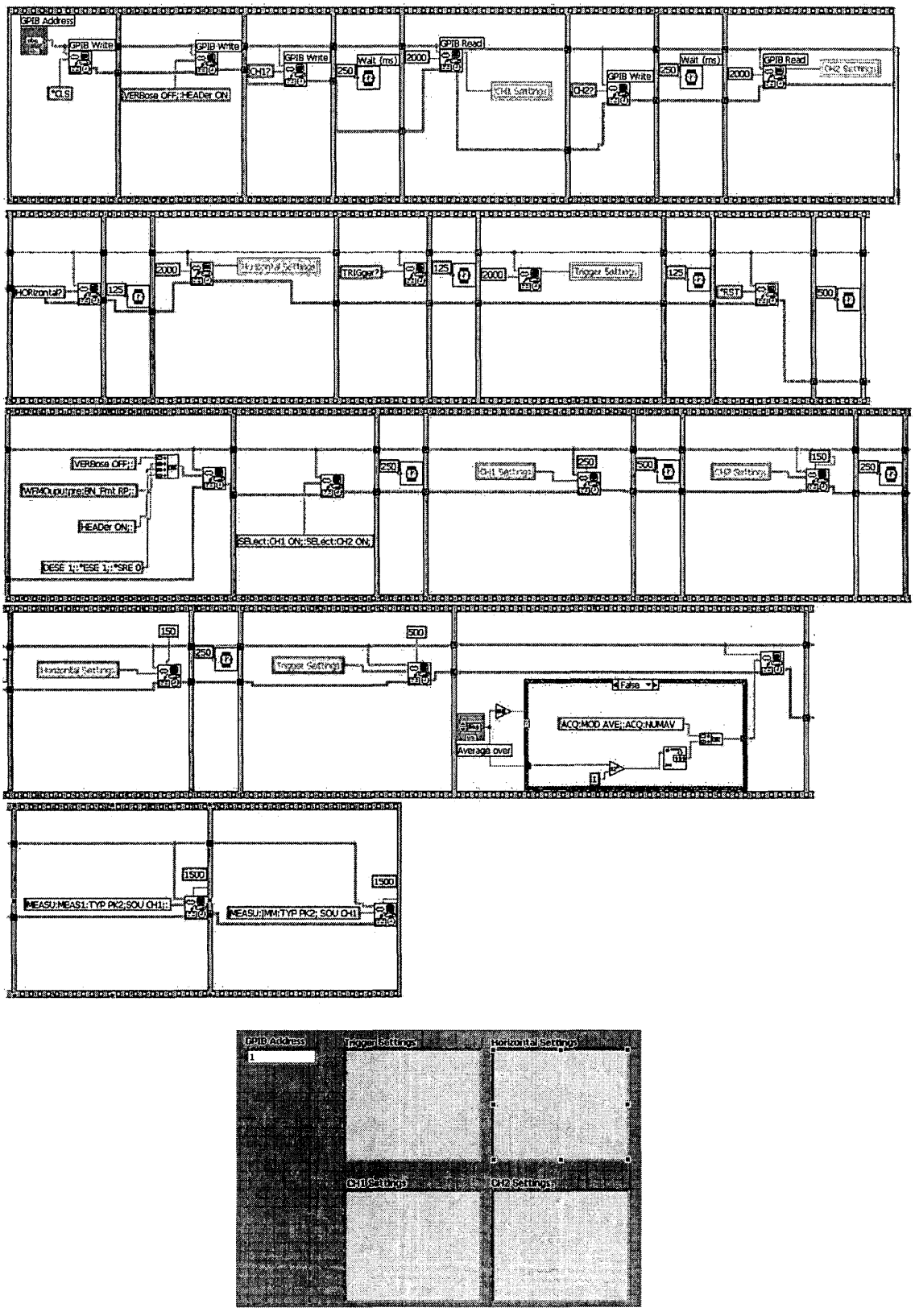

Figure E.2: Front and back panels of the LabVIEW subroutine that initializes the oscilloscopes.

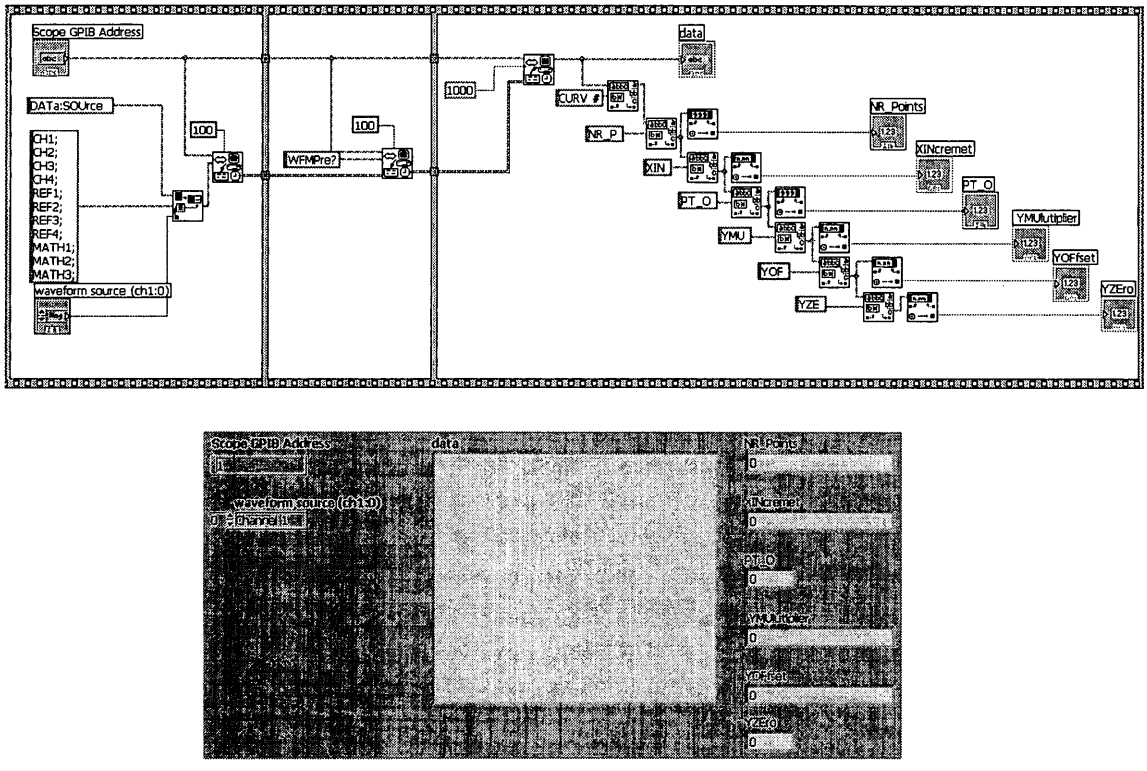

Figure E.3: Front and back panels of the LabVIEW subroutine that acquires and saves oscilloscope settings.

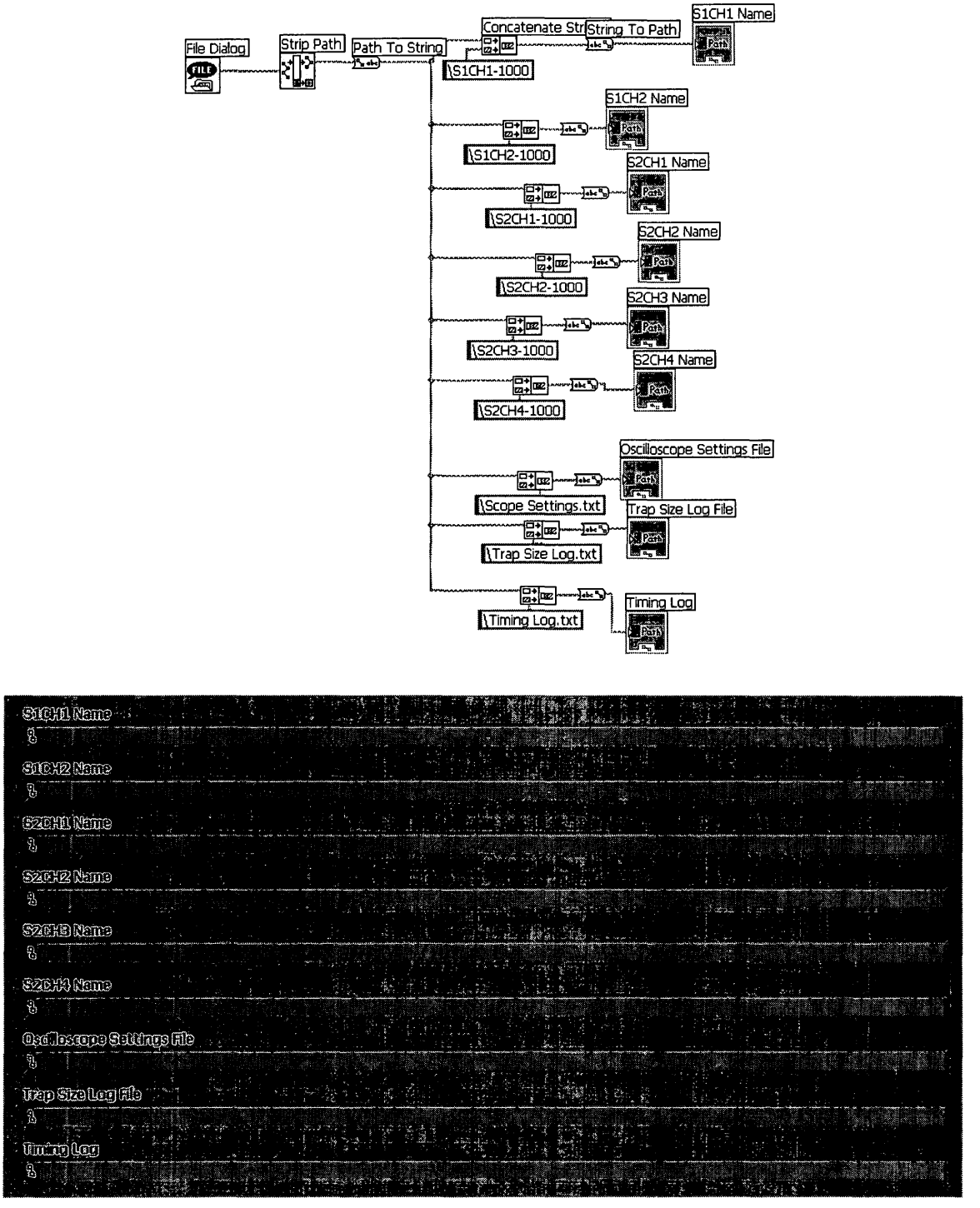

Figure E.4: Front and back panels of the LabVIEW subroutine that acquires and set the file path and file name.

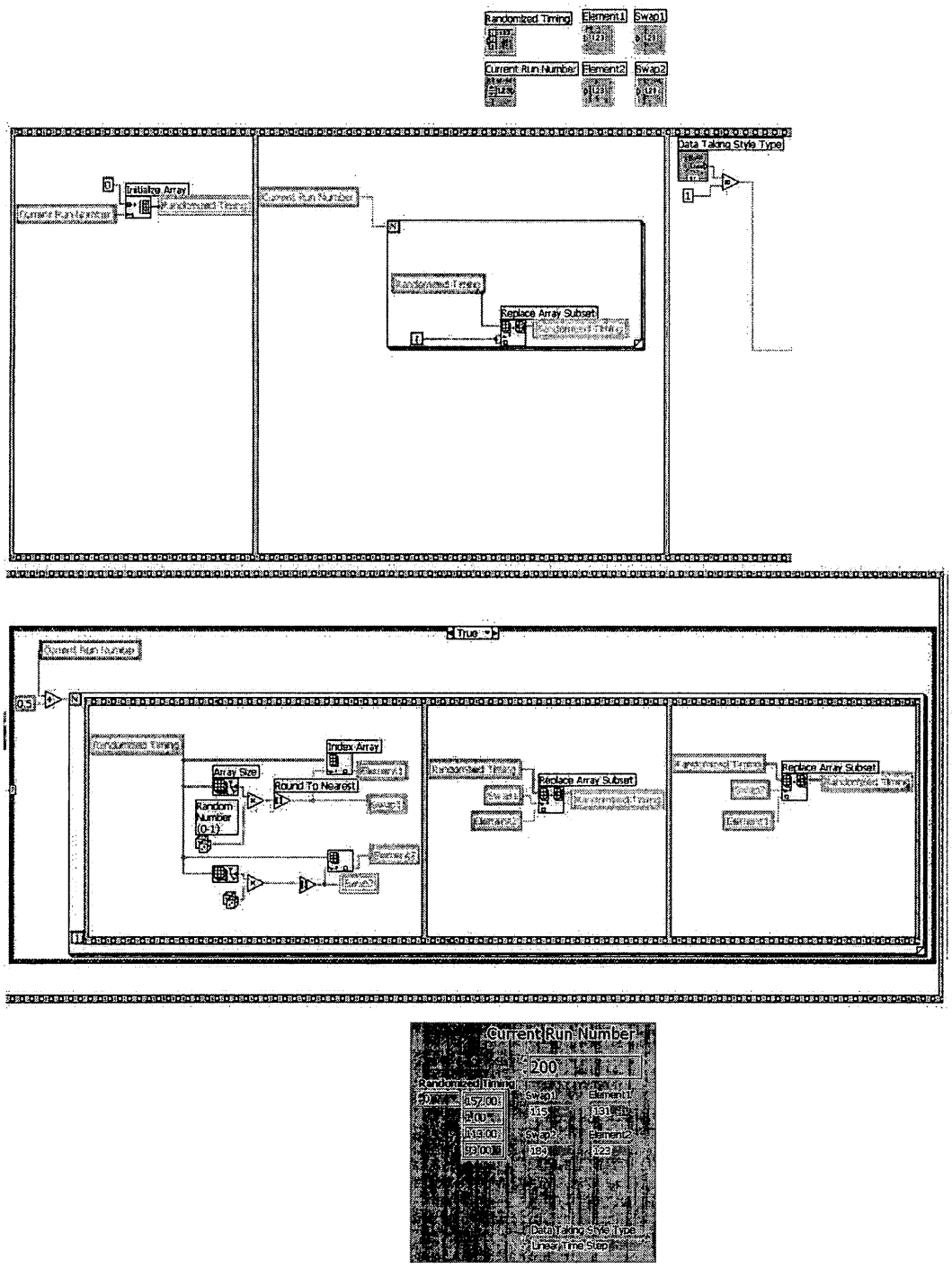

Figure E.5: Front and back panels of the LabVIEW subroutine that generates random timing list.

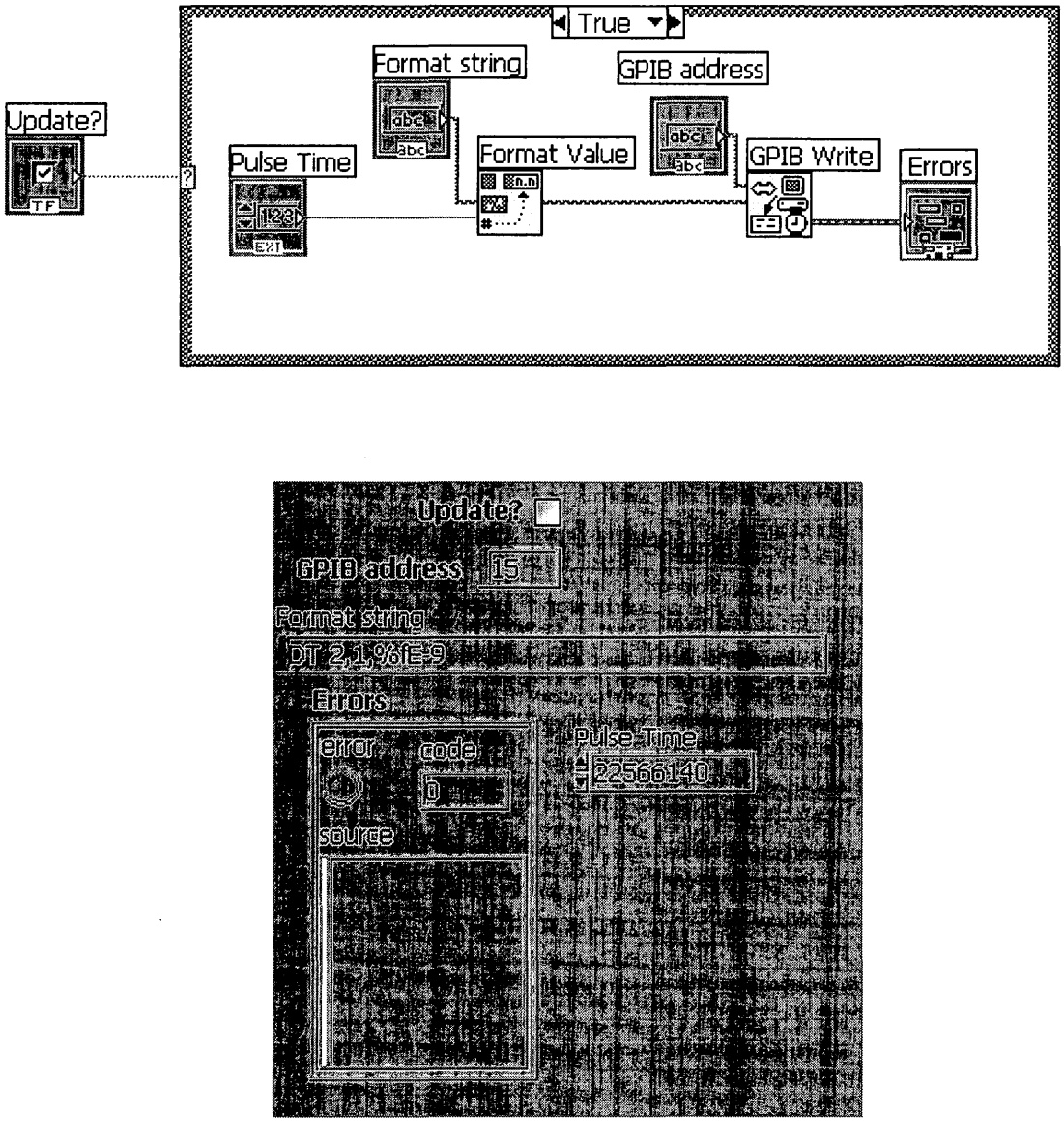

Figure E.6: Front and back panels of the LabVIEW subroutine that sends data to pulse generators.

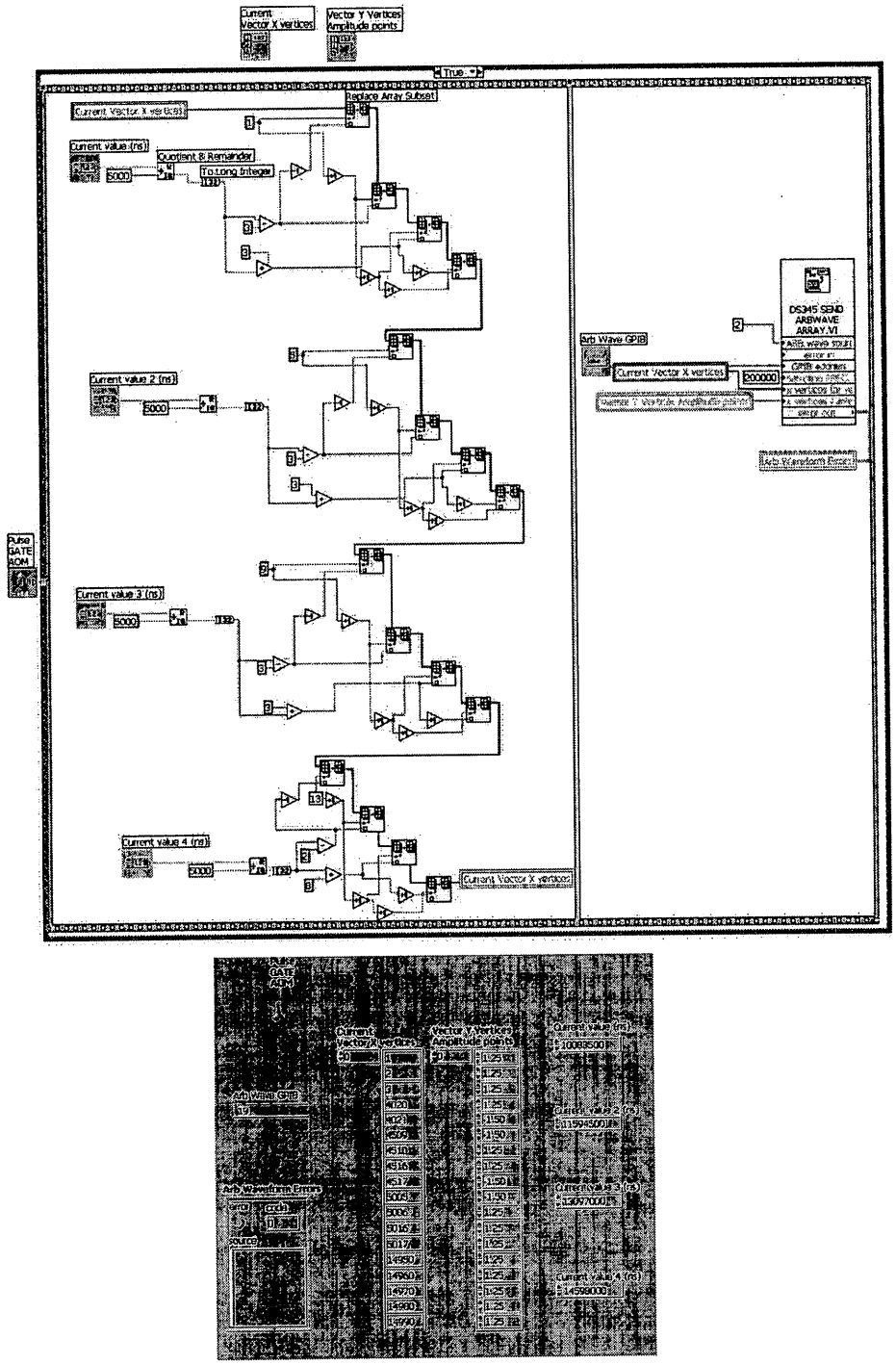

Figure E.7: Front and back panels of the LabVIEW subroutine that generates Gate AOM timing array.

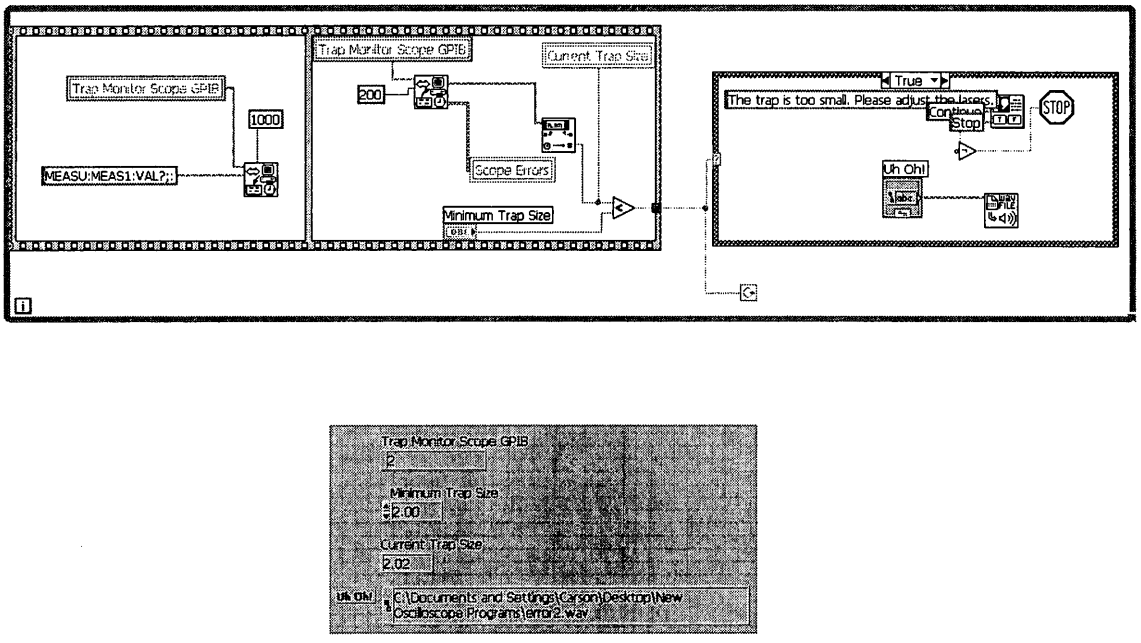

Figure E.8: Front and back panels of the LabVIEW subroutine that checks the trap size monitor.

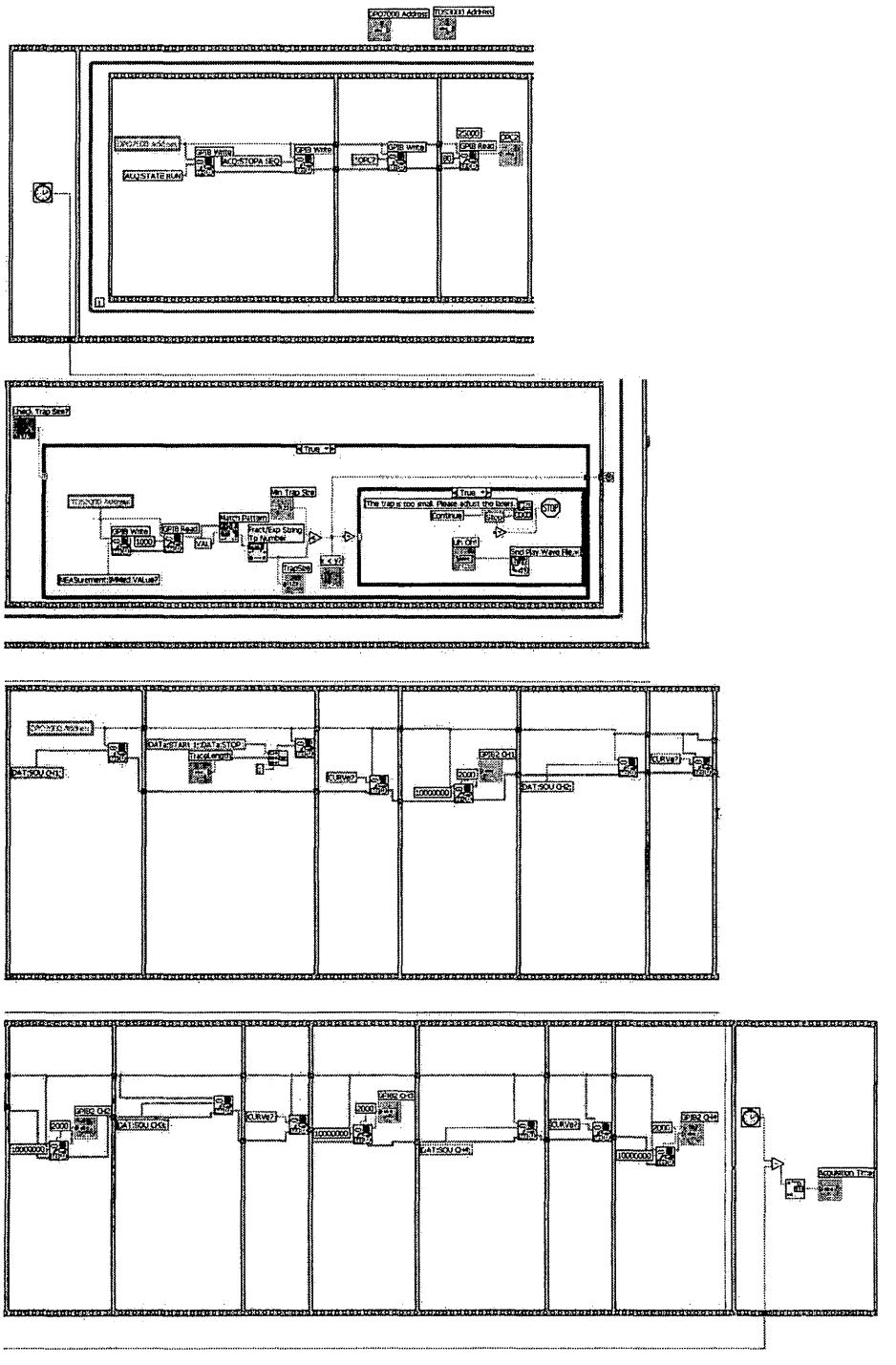

Figure E.9: Back panel of the LabVIEW subroutine that synchronizes different oscilloscopes.

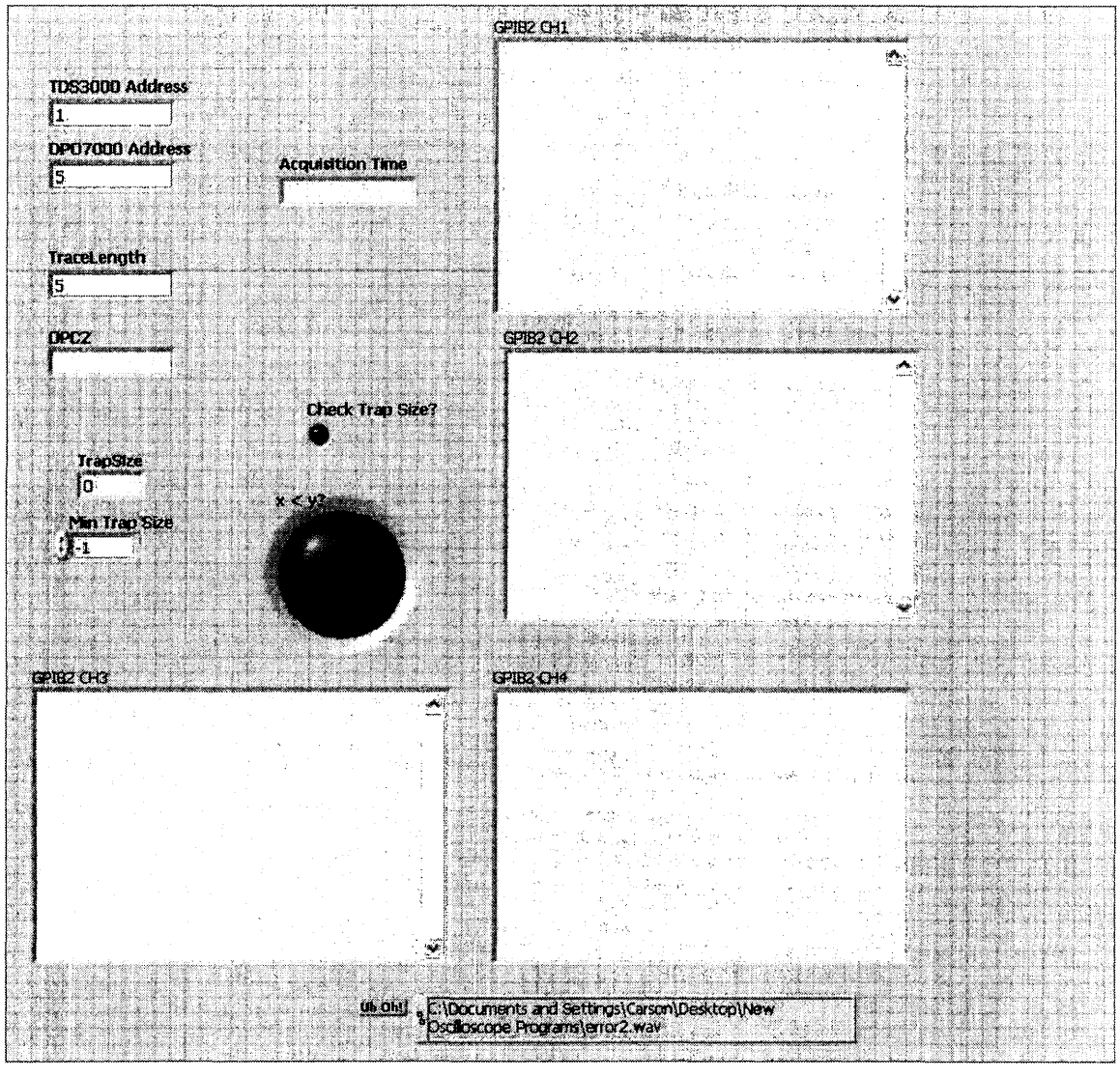

Figure E.10: Front panel of the LabVIEW subroutine that synchronizes different oscilloscopes.

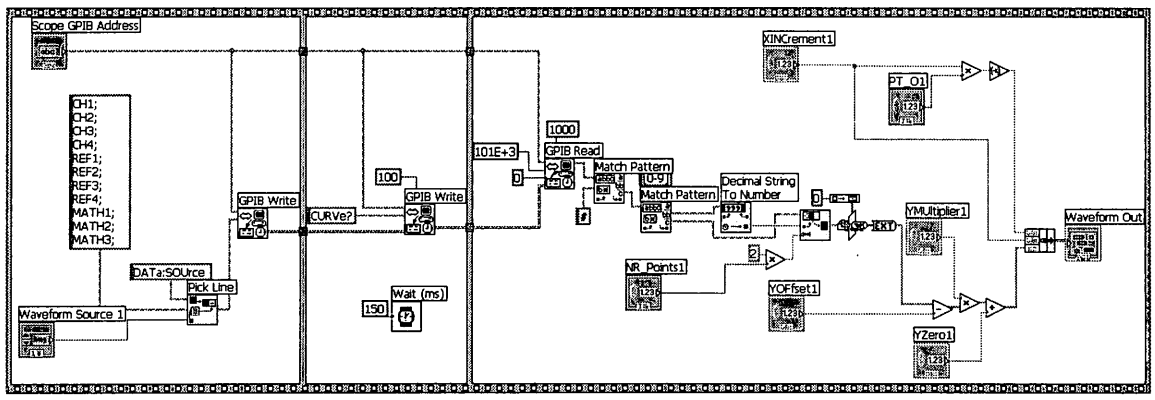

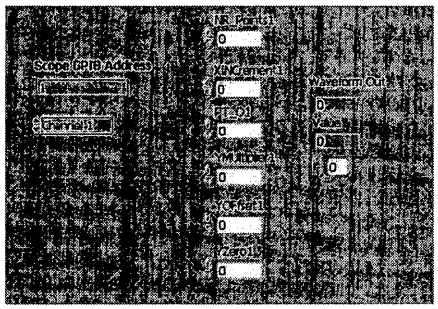

Figure E.11: Front and back panels of the LabVIEW subroutine that acquires only the traces displayed on the oscilloscope screen.

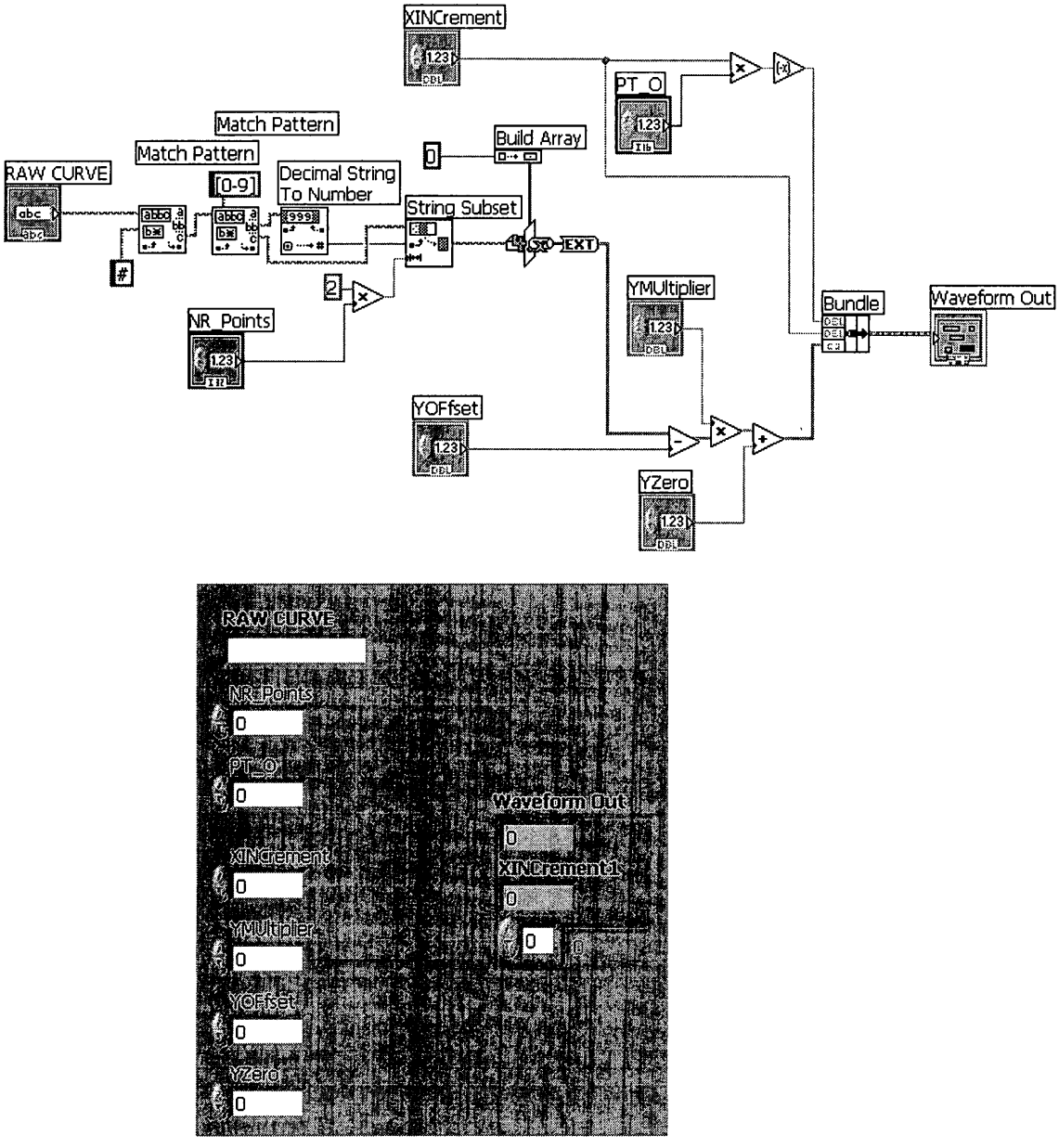

Figure E.12: Front and back panels of the LabVIEW subroutine that converts binary information from the oscilloscope to ASCII and numeric values.

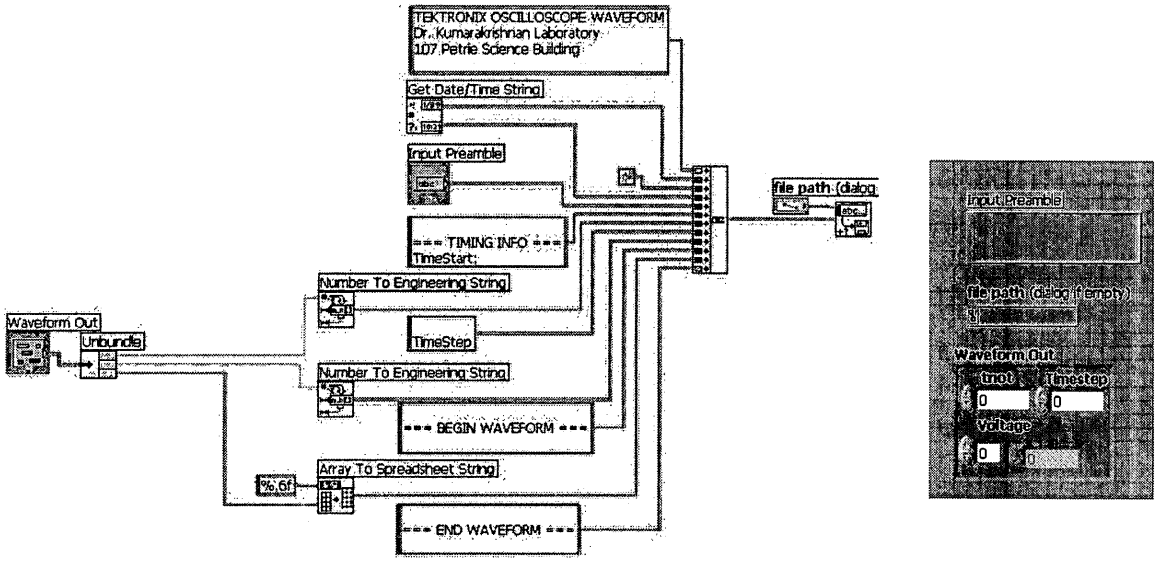

Figure E.13: Front and back panels of the LabVIEW subroutine that converts appends preamble to the raw curve and saves the file.

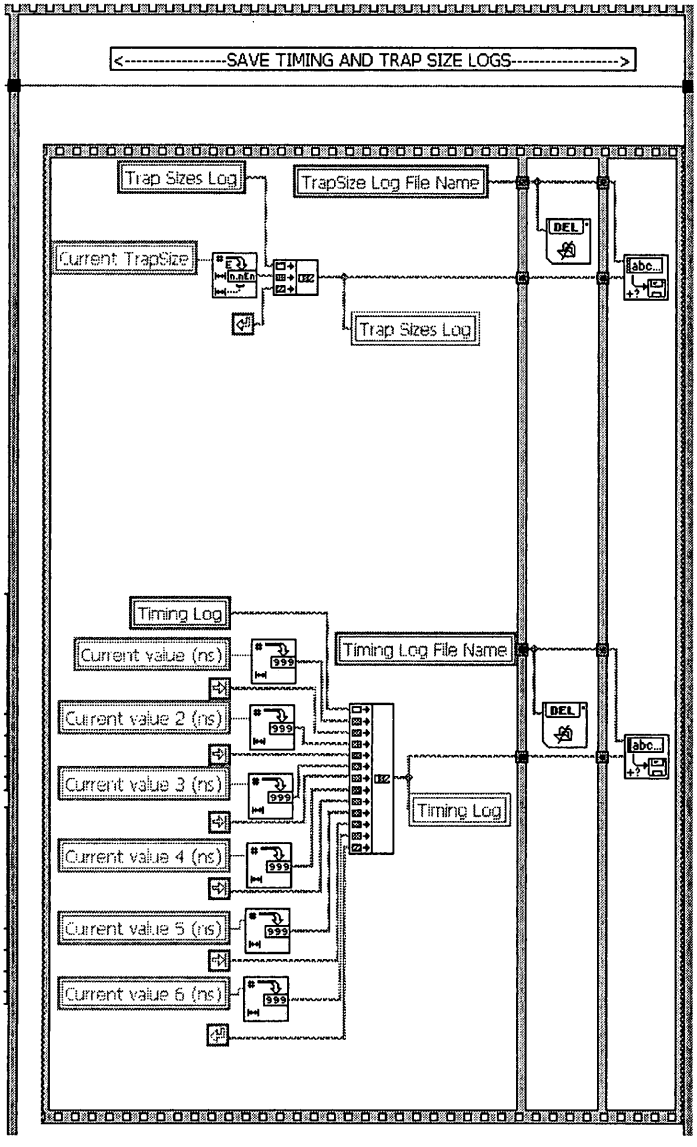

Figure E.14: Front and back panels of the LabVIEW subroutine that converts saves the trap level, PLL frequency, and pulse timing information.

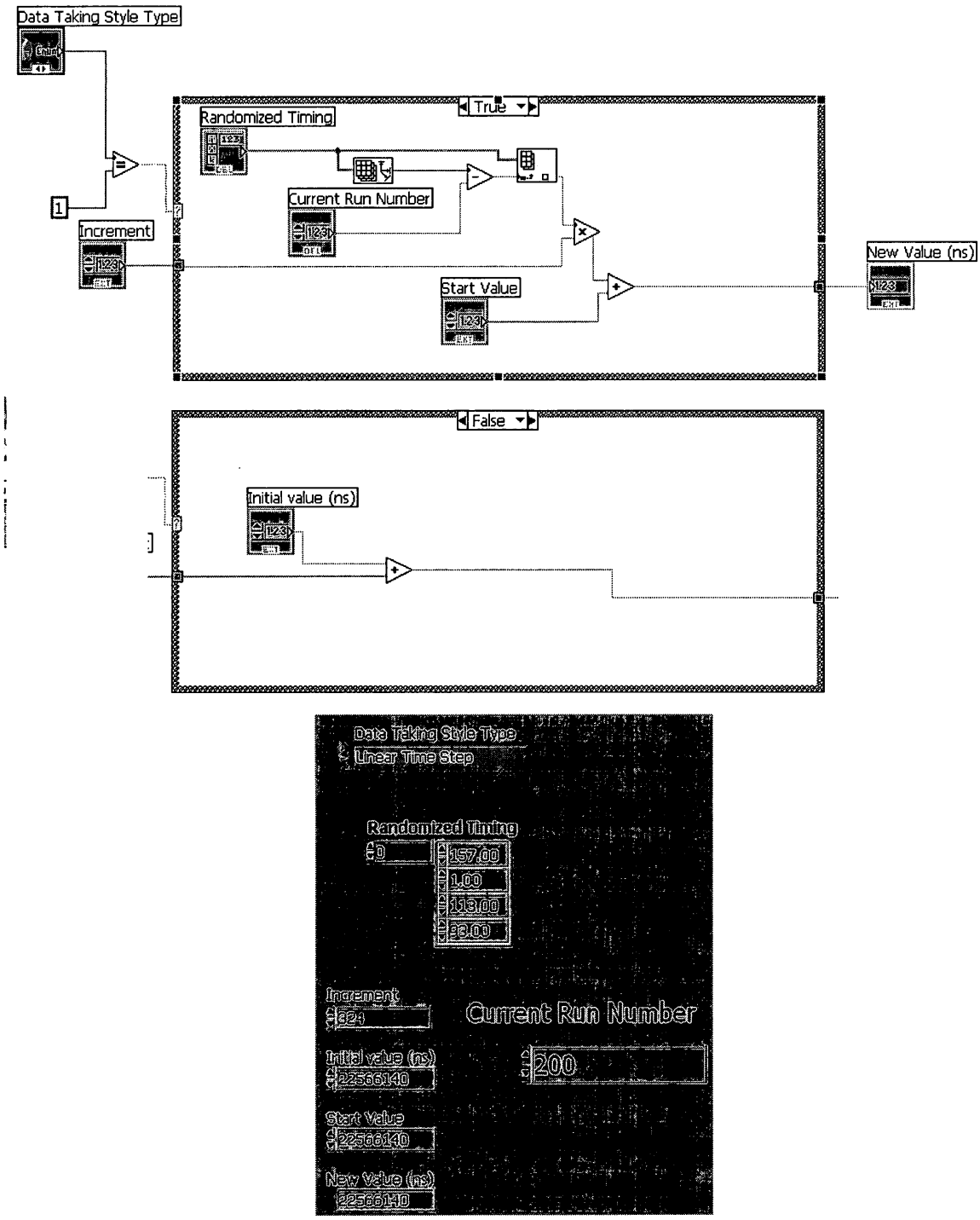

Figure E.15: Front and back panels of the LabVIEW subroutine that increments pulse timing by a single step size. For randomized order, program looks up the next timing from random list.

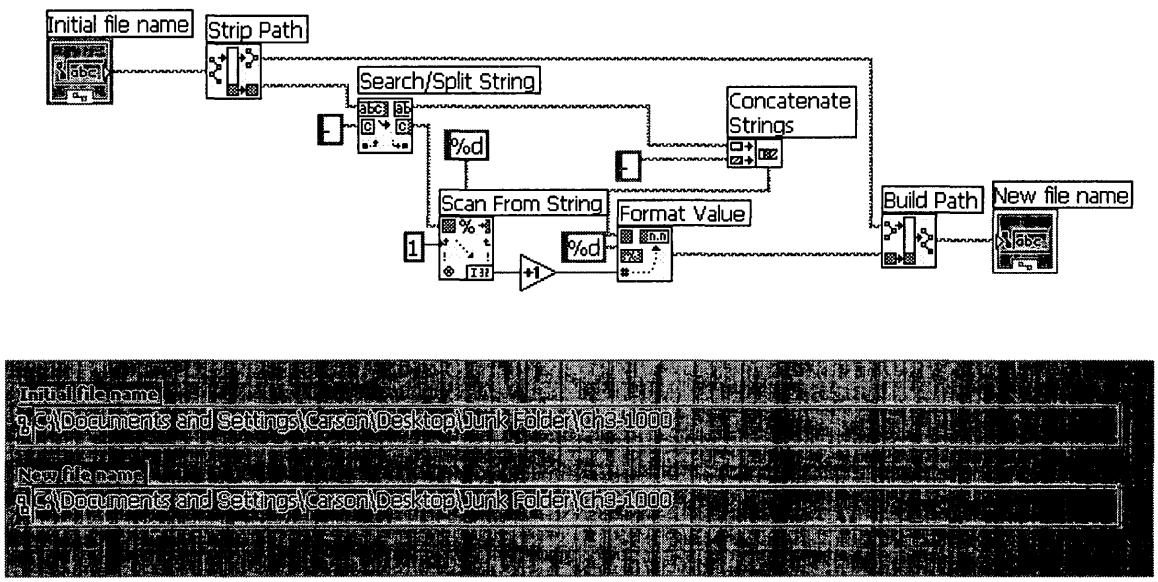

Figure E.16: Front and back panels of the LabVIEW subroutine that increments file names.

F List of Publications

(In preparation) Demonstration of sensitivity to gravitational acceleration using echo interferometers.
C. Mok, B. Barrett, A. Carew, R. Berthiaume, S. Beattie, I. Yavin, and A. Kumarakrishnan.

(In preparation) Atom trapping laboratory for upper-level undergraduates.
S. Winter, H. Beica, C. Mok, B. Barrett, R. Berthiaume, A. Vorozcovs, F. Yachoua, N. Afkhami-Jeddi, R. Marants, M. Aggarwal, and A. Kumarakrishnan.

Design and Construction of an Efficient Electro-optic Modulator for Laser Spectroscopy.
C. Mok, M. Weel, E. Rotberg, and A. Kumarakrishnan. Canadian Journal of Physics. **84**, 775-786 (2006).

Tools for Laser Spectroscopy: The Design and Construction of a Faraday Isolator.
S. Winter, C. Mok, and A. Kumarakrishnan.
Canadian Journal of Physics. **84**, 845-855 (2006).

Advances in Atomic, Molecular and Optical Physics Volume 60 Chapter 3. Time Domain Interferometry With Laser Cooled Atoms.
B. Barrett, I. Chan, C. Mok, A. Carew, I. Yavin, A. Kumarakrishnan, S. B. Cahn and T. Sleator. Edited by E. Arimondo, P.R. Berman and C.C. Lin.
Elsevier (2011).

Atom-Interferometric Studies of Light Scattering.
S. Beattie, B. Barrett, I. Chan, C. Mok, I. Yavin and A. Kumarakrishnan.
Physical Review A 80, 013618 (2009).

Technique for Measuring Atomic Recoil Frequency Using Coherence Functions.
S. Beattie, B. Barrett, I. Chan, C. Mok, I. Yavin, and A. Kumarakrishnan.
Physical Review A 79, 021605 (R) (2009).

Properties of Magnetic Sublevel Coherences for Precision Measurements.
I. Chan, A. Andreyuk, S. Beattie, B. Barrett, C. Mok, M. Weel, and A. Kumarakrishnan.
Physical Review A 78, 033418 (2008).

Influence of Spontaneous Emission on a Single-State Atom Interferometer
S. Beattie, B. Barrett, M. Weel, I. Chan, C. Mok, S.B. Cahn and A. Kumarakrishnan.
Physical Review A. **77**, 013610 (2008).

G List of Presentations

G.1 Presentations

Atom trapping laboratory for upper level undergraduate students.
C. Mok, S. Winter, H. Beica, B. Barrett, R. Berthiaume, A. Vorozcovs, F. Yachoua, N. Afkhami-Jeddi, R. Marants, M. Aggarwal, and A. Kumarakrishnan.
American Physical Society Division of Atomic, Molecular and Optical Physics, Anaheim, June 2012.

Measurements of gravitational acceleration from an echo atom interferometer.
C. Mok, A. Carew, B. Barrett, R. Berthiaume, and A. Kumarakrishnan.
American Physical Society Division of Atomic, Molecular and Optical Physics, Anaheim, June 2012.

Review article: Fragmentation of rods by cascading cracks: Why spaghetti does not break in half.
C. Mok.
York University, Physics Journal Club. September 2010.

Precision Atom Interferometric Measurement of Gravitational Acceleration.
C. Mok, R. Berthiaume, S. Beattie, B. Barrett, I. Chan, and A. Kumarakrishnan.
American Physical Society Divison of Atomic, Molecular, and Optical Physics, Houston, May 2010.

Measuring gravity with a single state atom interferometer.
C. Mok, M. Weel, S. Beattie and A. Kumarakrishnan.
Physics and Astronomy Graduate Executive Woolly Spider Monkey Conference York University. August 2008

Progress on Measurements of Gravitational Acceleration Using a Single State Atom Interferometer.
C. Mok, S. Beattie, B. Barrett, I. Chan, and A. Kumarakrishnan.
Canadian Association of Physicists Congress, Quebec City, June 2008.

Atom Trapping Laboratory For Upper Level Undergraduates.
C. Mok, S. Winter, B. Barrett, V. Popovici, R. Berthiaume, M. Aggarwal, M. F. Yachoua, and A. Kumarakrishnan.
Canadian Association of Physicists Congress, Quebec City, June 2008.

Design and construction of an efficient electro-optic modulator for laser spectroscopy.
C. Mok, M. Weel, E. Rotberg, and A. Kumarakrishnan.
Physics and Astronomy Graduate Executive Red Uakari Monkey Conference, York University. August 2007.

Measurement of Gravitational Acceleration Using a Single State Atom Interferometer.
C. Mok, S. Beattie, I. Chan, and A. Kumarakrishnan.
American Physical Society Divison of Atomic, Molecular, and Optical Physics, Calgary, June 2007.

Design and Construction of an Efficient Electro-Optic Modulator for Laser Spectroscopy.
C. Mok, W. Weel, E. Rotberg, and A. Kumarakrishnan. Canadian Undergraduate Physics Conference, London, October 2005.

A Home-Built Electro-Optic Phase Modulator for Laser Frequency Stabilization.
C. Mok, M. Weel, S. Beattie, and A. Kumarakrishnan.
Canadian Undergraduate Physics Conference, Victoria, November 2004.

G.2 Presentation Contributions

Precise determination of atomic g-factor ratios from a dual isotope magneto-optical trap.
I. Chan, B. Barrett, A. Carew, C. Mok, and A. Kumarakrishnan.
American Physical Society Divison of Atomic, Molecular, and Optical Physics, Anaheim, June 2012.

Active Feedback System for Laser Intensity Stabilization.
E. Davidson, I. Chan, B. Barrett, C. Mok, A. Carew and A. Kumarakrishnan.
Canadian Undergraduate Physics Conference, Halifax, October 2010.

New Experiments in Atomic and Laser Physics for Undergraduate Students.
H. Beica, B. Barrett, C. Mok, A. Vorozcovs, A. Sibilia, H. Morrison, and A. Kumarakrishnan.
Canadian Undergraduate Physics Conference, Halifax, October 2010.

Progress Towards a Precision Measurement of Atomic Recoil Frequency Using an Echo Interferometer.
B. Barrett, A. Carew, S. Beattie, I. Chan, C. Mok, R. Berthiaume, and A. Kumarakrishnan.
American Physical Society Divison of Atomic, Molecular, and Optical Physics, Houston, May 2010.

Simulations of a Multi-Level Atom Interferometer.
B. Barrett, I. Chan, C. Mok, A. Carew, R. Berthiaume, I. Yavin, and A. Kumarakrishnan.
American Physical Society Divison of Atomic, Molecular, and Optical Physics, Houston, May 2010.

Precision Measurements of Atomic g Factor Ratios Using a Dual Species MOT.
I. Chan, R. Berthiaume, B. Barrett, C. Mok. A. Carew, and A. Kumarakrishnan.
American Physical Society Divison of Atomic, Molecular, and Optical Physics, Houston, May 2010.

Realization of an Inexpensive Multi-Channel Frequency Synthesizer.
A. Carew, R. Berthiaume, C. Mok, I. Chan, B. Barrett, M. Weel, and A. Kumarakrishnan.
American Physical Society Divison of Atomic, Molecular, and Optical Physics, Houston, May 2010.

Radio Frequency Power Stabilization by Active Feedback.
K. Reiter, C. Mok, S. Beattie, I. Chan, B. Barrett, E. Davidson, R. Berthiaume and A. Kumarakrishnan.
Canadian Undergraduate Physics Conference, Edmonton, October (2009).

Atom Interferometric Studies of Light Scattering.
S. Beattie, B. Barrett, I. Chan, C. Mok, I. Yavin, and A. Kumarakrishnan.
Canadian Association of Physicists Congress, Moncton, June 2009.

Properties of Magnetic Sublevel Coherences for Precision Measurements.
I. Chan, S. Beattie, B. Barrett, C. Mok, and A. Kumarakrishnan.
Canadian Association of Physicists Congress, Moncton, June 2009.

A New Technique for Measuring Atomic Recoil Frequency Using Coherence Functions.
S. Beattie, B. Barrett, I. Chan, C. Mok, I. Yavin, and A. Kumarakrishnan.
American Physical Society Divison of Atomic, Molecular, and Optical Physics, Charlottesville, May 2009.

An Inexpensive Frequency Synthesizer for Optical Lattice Experiments.
R. Berthiaume, I. Chan, M. Weel, and A. Kumarakrishnan.
Canadian Undergraduate Physics Conference, Toronto, October 2008.

Analysis of Time Domain Measurements of Atomic Recoil Frequency in Laser Cooled Rubidium Gas.
K. Anosov, B. Barrett, M. Weel, S. Beattie, C. Mok, I. Chan, I. Yavin, and A. Kumarakrishnan.

Canadian Undergraduate Physics Conference, Toronto, October 2008.

Improving the Precision Measurement of the Atomic Recoil Frequency Using a Single-State Time-Domain Atom Interferometer.
B. Barrett, S. Beattie, I. Yavin, C. Mok, I. Chan, and A. Kumarakrishnan.
Canadian Association of Physicists Congress, Quebec City, June 2008.

Numerical Simulations of a Single State Atom Interferometer.
B. Barrett, C. Mok, S. Beattie, and A. Kumarakrishnan.
Canadian Association of Physicists Congress, Quebec City, June 2008.

Effect of Spontaneous Emission on Matter Wave Interference.
S. Beattie, B. Barrett, M. Weel, I. Chan, C. Mok, S. B. Cahn, and A. Kumarakrishnan.
Canadian Association of Physicists Congress, Quebec City, June 2008.

Influence of Spontaneous Emission on a Single-State Atom Interferometer.
S.Beattie, B. Barrett, M. Weel, I. Chan, C. Mok , S. B. Cahn, A. Kumarakrishnan.
American Physical Society Divison of Atomic, Molecular, and Optical Physics, State College, May 2008.

Monte Carlo Wavefunction Simulation of a Matter Wave Interferometer. B. Barrett, C. Mok, S. Beattie, and A. Kumarakrishnan. American Physical Society Divison of Atomic, Molecular, and Optical Physics, State College, May 2008.

Atom Trapping Laboratory for Upper Level Undergraduates.
S. Winter, B. Barrett, C. Mok, V. Popovici, R. Berthiaume, M. Aggarwal, F. Yachoua, and A. Kumarakrishnan.

Canadian Undergraduate Physics Conference, Vancouver, October 2007.

An Inexpensive Grating Stabilized Diode Laser for Laser Spectroscopy.
V. Popovici, E. Paradis, C. Mok, B. Barrett, and A. Kumarakrishnan.
Canadian Undergraduate Physics Conference, Fredericton, October 2006.

Tools for Laser Spectroscopy: The Design and Construction of a Faraday Isolator.
S. Winter, C. Mok, and A. Kumarakrishnan.
Canadian Undergraduate Physics Conference, Fredericton, October 2006.

Tools for Laser Spectroscopy: Design and Construction of a Faraday Isolator.
S. Winter, C. Mok, and A. Kumarakrishnan.
Canadian Undergraduate Physics Conference, London, October 2005.

H Scholarships and Awards

February 2013

Faculty of Graduate Studies Three Minute Thesis Finalist

York University, Toronto, ON.

May 2009 May 2011

Natural Sciences and Engineering Research Council (NSERC)

Alexander Graham Bell Canada Graduate Scholarships Doctoral (CGS-D)

York University, Toronto, ON.

September 2008

Faculty of Science & Engineering Excellence in Teaching Award

York University, Toronto, ON.

September 2007

Ontario Graduate Scholarship Program

York University, Toronto, ON.

September 2006

NSERC CGS-Masters

York University, Toronto, ON.

VIII: SCHOLARSHIPS AND AWARDS

September 2006

York Graduate Scholarship

York University, Toronto, ON.

May 2006

Emeritus Professors Prize

York University, Toronto, ON.

May 2006

W.J. Megaw Prize in Experimental Physics

York University, Toronto, ON.

September 2005

York University Continuing Student Scholarship

York University, Toronto, ON.

October 2004

R.M. Hobson Prize

York University, Toronto, ON.

May 2004

NSERC Undergraduate Student Research Awards Program

York University, Toronto, ON.

September 2002

Faculty of Pure & Applied Science Scholarship

York University, Toronto, ON.

September 2002

York University Entrance Scholarship

York University, Toronto, ON.

Bibliography

[1] D. A. Steck, *Rubidium 85 D Line Data. Version 2.1.5 September 2012.* available online at `http://steck.us/alkalidata`.

[2] D. A. Steck, *Rubidium 87 D Line Data. Version 2.1.4 September 2012.* available online at `http://steck.us/alkalidata`.

[3] P. J. Mohr, B. N. Taylor, and D. B. Newell, "Codata recommended values of the fundamental physical constants: 2010," *Review of Modern Physics*, vol. 84, pp. 1527–1605, Nov 2012. `http://link.aps.org/doi/10.1103/RevModPhys.84.1527`.

[4] C. C. Speake and T. J. Quinn, "The gravitational constant: Theory and experiment 200 years after cavendish," *Measurement Science and Technology*, vol. 10, no. 6, 1999. `http://stacks.iop.org/0957-0233/10/i=6/a=001`.

[5] J. H. Gundlach and S. M. Merkowitz, "Measurement of newton's constant using a torsion balance with angular acceleration feedback," *Physical Review Letters*, vol. 85, pp. 2869–2872, Oct 2000. `http://link.aps.org/doi/10.1103/PhysRevLett.85.2869`.

[6] S. Schlamminger, E. Holzschuh, and W. Kündig, "Determination of the gravitational constant with a beam balance," *Physical Review Letters*, vol. 89, p. 161102, Sep 2002. `http://link.aps.org/doi/10.1103/PhysRevLett.89.161102`.

[7] C. D. Hoyle, U. Schmidt, B. R. Heckel, E. G. Adelberger, J. H. Gundlach, D. J. Kapner, and H. E. Swanson, "Submillimeter test of the gravitational inverse-square law: A search for "large" extra dimensions," *Physical Review Letters*, vol. 86, pp. 1418–1421, Feb 2001. http://link.aps.org/doi/10.1103/PhysRevLett.86.1418.

[8] E. Adelberger, B. Heckel, and A. Nelson, "Tests of the gravitational inverse-square law," *Annual Review of Nuclear and Particle Science*, vol. 53, no. 1, pp. 77–121, 2003. http://www.annualreviews.org/doi/abs/10.1146/annurev.nucl.53.041002.110503.

[9] J. Long and C. Price, "Current short-range tests of the gravitational inverse square law," *Comptes Rendus Physique*, vol. 4, no. 3, pp. 337 – 346, 2003. http://www.sciencedirect.com/science/article/pii/S1631070503000422.

[10] J. C. Hafele and R. E. Keating, "Around-the-world atomic clocks: Predicted relativistic time gains," *Science*, vol. 177, no. 4044, pp. 166–168, 1972. http://www.sciencemag.org/content/177/4044/166.abstract.

[11] J. C. Hafele and R. E. Keating, "Around-the-world atomic clocks: Observed relativistic time gains," *Science*, vol. 177, no. 4044, pp. 168–170, 1972. http://www.sciencemag.org/content/177/4044/168.abstract.

[12] C. W. F. Everitt, D. B. DeBra, B. W. Parkinson, J. P. Turneaure, J. W. Conklin, M. I. Heifetz, G. M. Keiser, A. S. Silbergleit, T. Holmes, J. Kolodziejczak, M. Al-Meshari, J. C. Mester, B. Muhlfelder, V. G. Solomonik, K. Stahl, P. W. Worden, W. Bencze, S. Buchman, B. Clarke, A. Al-Jadaan, H. Al-Jibreen, J. Li, J. A. Lipa, J. M. Lockhart, B. Al-Suwaidan, M. Taber, and S. Wang, "Gravity probe b: Final results of a space experiment to test general relativity," *Physical Review Letters*, vol. 106, p. 221101, May 2011. http://link.aps.org/doi/10.1103/PhysRevLett.106.221101.

[13] T. van Zoest, N. Gaaloul, Y. Singh, H. Ahlers, W. Herr, S. T. Seidel, W. Ertmer, E. Rasel, M. Eckart, E. Kajari, S. Arnold, G. Nandi, W. P. Schleich, R. Walser, A. Vogel, K. Sengstock, K. Bongs, W. Lewoczko-Adamczyk, M. Schiemangk, T. Schuldt, A. Peters, T. Könemann, H. Müntinga, C. Lämmerzahl, H. Dittus, T. Steinmetz, T. W. Hänsch, and J. Reichel, "Bose-einstein condensation in microgravity," *Science*, vol. 328, no. 5985, pp. 1540–1543, 2010. `http://www.sciencemag.org/content/328/5985/1540.abstract`.

[14] H. Müntinga, H. Ahlers, M. Krutzik, A. Wenzlawski, S. Arnold, D. Becker, K. Bongs, H. Dittus, H. Duncker, N. Gaaloul, C. Gherasim, E. Giese, C. Grzeschik, T. W. Hänsch, O. Hellmig, W. Herr, S. Herrmann, E. Kajari, S. Kleinert, C. Lämmerzahl, W. Lewoczko-Adamczyk, J. Malcolm, N. Meyer, R. Nolte, A. Peters, M. Popp, J. Reichel, A. Roura, J. Rudolph, M. Schiemangk, M. Schneider, S. T. Seidel, K. Sengstock, V. Tamma, T. Valenzuela, A. Vogel, R. Walser, T. Wendrich, P. Windpassinger, W. Zeller, T. van Zoest, W. Ertmer, W. P. Schleich, and E. M. Rasel, "Interferometry with bose-einstein condensates in microgravity," *Physical Review Letters*, vol. 110, p. 093602, Feb 2013. `http://link.aps.org/doi/10.1103/PhysRevLett.110.093602`.

[15] W. A. Prothero and J. M. Goodkind, "A superconducting gravimeter," *Review of Scientific Instruments*, vol. 39, p. 1257, February 1968. `http://dx.doi.org/10.1063/1.1683645`.

[16] J. M. Goodkind, "The superconducting gravimeter," *Review of Scientific Instruments*, vol. 70, p. 4131, 1999. `http://dx.doi.org/10.1063/1.1150092`.

[17] Geolgical Survey of Canada and Government of Canada, "Observed Gravity Map of Canada," 2000.

[18] T. M. Niebauer, G. S. Sasagawa, J. E. Faller, R. Hilt, and F. Klopping, "A new generation of absolute gravimeters," *Metrologia*, vol. 32, no. 3, p. 159, 1995. http://stacks.iop.org/0026-1394/32/i=3/a=004.

[19] J. P. Schwarz, D. S. Robertson, T. M. Niebauer, and J. E. Faller, "A new determination of the newtonian constant of gravity using the free fall method," *Measurement Science and Technology*, vol. 10, no. 6, p. 478, 1999. http://stacks.iop.org/0957-0233/10/i=6/a=311.

[20] N. Debeglia and F. Dupont, "Some critical factors for engineering and environmental microgravity investigations," *Journal of Applied Geophysics*, vol. 50, no. 4, pp. 435–454, 2002. http://www.sciencedirect.com/science/article/pii/S0926985102001945.

[21] P. D. Lett, W. D. Phillips, S. L. Rolston, C. E. Tanner, R. N. Watts, and C. I. Westbrook, "Optical molasses," *Journal of the Optical Society of America B*, vol. 6, pp. 2084–2107, Nov 1989. http://josab.osa.org/abstract.cfm?URI=josab-6-11-2084.

[22] E. L. Raab, M. Prentiss, A. Cable, S. Chu, and D. E. Pritchard, "Trapping of neutral sodium atoms with radiation pressure," *Physical Review Letters*, vol. 59, pp. 2631–2634, Dec 1987. http://link.aps.org/doi/10.1103/PhysRevLett.59.2631.

[23] C. Monroe, W. Swann, H. Robinson, and C. Wieman, "Very cold trapped atoms in a vapor cell," *Physical Review Letters*, vol. 65, pp. 1571–1574, Sep 1990. http://link.aps.org/doi/10.1103/PhysRevLett.65.1571.

[24] S. Chu, "Nobel lecture: The manipulation of neutral particles," *Review of Modern Physics*, vol. 70, pp. 685–706, Jul 1998. http://link.aps.org/doi/10.1103/RevModPhys.70.685.

[25] P. L. Gould, G. A. Ruff, and D. E. Pritchard, "Diffraction of atoms by light: The near-resonant kapitza-dirac effect," *Physical Review Letters*, vol. 56, pp. 827–830, Feb 1986. http://link.aps.org/doi/10.1103/PhysRevLett.56.827.

[26] A. Peters, K. Y. Chung, and S. Chu, "Measurement of gravitational acceleration by dropping atoms," *Nature*, vol. 400, pp. 849–852, 1999. http://dx.doi.org/10.1038/23655.

[27] A. Peters, K. Y. Chung, and S. Chu, "High-precision gravity measurements using atom interferometry," *Metrologia*, vol. 38, no. 1, p. 25, 2001. http://stacks.iop.org/0026-1394/38/i=1/a=4.

[28] H. Müller, S.-w. Chiow, S. Herrmann, S. Chu, and K.-Y. Chung, "Atom-interferometry tests of the isotropy of post-newtonian gravity," *Physical Review Letters*, vol. 100, p. 031101, Jan 2008. http://link.aps.org/doi/10.1103/PhysRevLett.100.031101.

[29] D. Brown, L. Mauser, B. Young, M. Kasevich, H. Rice, and V. Benischek, "Atom interferometric gravity sensor system," in *Position Location and Navigation Symposium (PLANS), 2012 IEEE/ION*, pp. 30–37, April. http://dx.doi.org/10.1109/PLANS.2012.6236861.

[30] N. Poli, F.-Y. Wang, M. G. Tarallo, A. Alberti, M. Prevedelli, and G. M. Tino, "Precision measurement of gravity with cold atoms in an optical lattice and comparison with a classical gravimeter," *Physical Review Letters*, vol. 106, p. 038501, Jan 2011. http://link.aps.org/doi/10.1103/PhysRevLett.106.038501.

[31] S. B. Cahn, A. Kumarakrishnan, U. Shim, T. Sleator, P. R. Berman, and B. Dubetsky, "Time-domain de broglie wave interferometry," *Physical Review Letters*, vol. 79, pp. 784–787, Aug 1997. http://link.aps.org/doi/10.1103/PhysRevLett.79.784.

[32] M. Weel, I. Chan, S. Beattie, A. Kumarakrishnan, D. Gosset, and I. Yavin, "Effect of a magnetic field gradient and gravitational acceleration on a time-domain grating-echo interferometer," *Physical Review A*, vol. 73, p. 063624, Jun 2006. http://link.aps.org/doi/10.1103/PhysRevA.73.063624.

[33] B. Barrett, I. Chan, C. Mok, A. Carew, I. Yavin, A. Kumarakrishnan, S. B. Cahn, T. S. E. by E. Arimondo, P. Berman, and C. Lin, *Advances in Atomic, Molecular and Optical Physics*, ch. Chapter 3: Time Domain Interferometry With Laser Cooled Atoms. Academic Press, Elsevier, 2011. http://www.sciencedirect.com/science/bookseries/1049250X/60.

[34] E. J. Su, S. Wu, and M. G. Prentiss, "Atom interferometry using wave packets with constant spatial displacements," *Physical Review A*, vol. 81, p. 043631, Apr 2010. http://link.aps.org/doi/10.1103/PhysRevA.81.043631.

[35] B. Barrett, I. Chan, and A. Kumarakrishnan, "Atom-interferometric techniques for measuring uniform magnetic field gradients and gravitational acceleration," *Physical Review A*, vol. 84, p. 063623, Dec 2011. http://link.aps.org/doi/10.1103/PhysRevA.84.063623.

[36] C. Mok, A. Carew, B. Barrett, R. Berthiaume, and A. Kumarakrishnan, "Measurements of gravitational acceleration from an echo atom interferometer," *Bulletin of the American Physical Society*, vol. 57, no. 5, p. 192, 2012. http://meetings.aps.org/link/BAPS.2012.DAMOP.T5.3.

[37] C. Mok, B. Barrett, A. Carew, R. Berthiaume, S. Beattie, I. Yavin, and A. Kumarakrishnan, "Demonstration of improved sensitivity to gravitational acceleration using echo interferometers," *To be submitted to Physical Review A*, 2013.

[38] B. Barrett, A. Carew, S. Beattie, and A. Kumarakrishnan, "Measuring the atomic recoil frequency using a modified grating-echo atom

interferometer," *Physics Review A*, vol. 87, p. 033626, Mar 2013. http://link.aps.org/doi/10.1103/PhysRevA.87.033626.

[39] I. Chan, B. Barrett, and A. Kumarakrishnan, "Precise determination of atomic g-factor ratios from a dual isotope magneto-optical trap," *Physical Review A*, vol. 84, p. 032509, Sep 2011. http://link.aps.org/doi/10.1103/PhysRevA.84.032509.

[40] V. Letokhov, V. Minogin, and B. Pavlik, "Cooling and trapping of atoms and molecules by a resonant laser field," *Optics Communications*, vol. 19, no. 1, pp. 72 – 75, 1976. http://www.sciencedirect.com/science/article/pii/0030401876903886.

[41] V. Letokhov, V. Minogin, and B. Pavlik, "Cooling and capture of atoms and molecules by a resonant light field," *Zhurnal Éksperimentalânoĭ Teoreticheskoĭ Fiziki (Soviet Physics Journal of Experimental and Theoretical Physics)*, vol. 45, no. 4, p. 698, 1977. http://www.jetp.ac.ru/cgi-bin/e/index/e/45/4/p698?a=list.

[42] V. Letkhov and V. Minogin, "Trapping and storage of atoms in a laser field," *Applied Physics B*, vol. 17, pp. 99–103, 1978. http://dx.doi.org/10.1007/BF00885037.

[43] V. Letokhov and V. Minogin, "Cooling, trapping, and storage of atoms by resonant laser fields," *Journal of the Optical Society of America*, vol. 69, pp. 413–419, Mar 1979. http://www.opticsinfobase.org/abstract.cfm?URI=josa-69-3-413.

[44] D. J. Wineland and W. M. Itano, "Laser cooling of atoms," *Physical Review A*, vol. 20, pp. 1521–1540, Oct 1979. http://link.aps.org/doi/10.1103/PhysRevA.20.1521.

[45] A. Ashkin, "Acceleration and trapping of particles by radiation pressure," *Physical Review Letters*, vol. 24, pp. 156–159, Jan 1970. http://link.aps.org/doi/10.1103/PhysRevLett.24.156.

[46] A. Ashkin, "Trapping of atoms by resonance radiation pressure," *Physical Review Letters*, vol. 40, pp. 729–732, Mar 1978. http://link.aps.org/doi/10.1103/PhysRevLett.40.729.

[47] J. E. Bjorkholm, R. R. Freeman, A. Ashkin, and D. B. Pearson, "Observation of focusing of neutral atoms by the dipole forces of resonance-radiation pressure," *Physical Review Letters*, vol. 41, pp. 1361–1364, Nov 1978. http://link.aps.org/doi/10.1103/PhysRevLett.41.1361.

[48] S. Chu, J. E. Bjorkholm, A. Ashkin, and A. Cable, "Experimental observation of optically trapped atoms," *Physical Review Letters*, vol. 57, pp. 314–317, Jul 1986. http://link.aps.org/doi/10.1103/PhysRevLett.57.314.

[49] W. Ertmer, R. Blatt, J. L. Hall, and M. Zhu, "Laser manipulation of atomic beam velocities: Demonstration of stopped atoms and velocity reversal," *Physical Review Letters*, vol. 54, pp. 996–999, Mar 1985. http://link.aps.org/doi/10.1103/PhysRevLett.54.996.

[50] W. D. Phillips and H. Metcalf, "Laser deceleration of an atomic beam," *Physical Review Letters*, vol. 48, pp. 596–599, Mar 1982. http://link.aps.org/doi/10.1103/PhysRevLett.48.596.

[51] J. Prodan, A. Migdall, W. D. Phillips, I. So, H. Metcalf, and J. Dalibard, "Stopping atoms with laser light," *Physical Review Letters*, vol. 54, pp. 992–995, Mar 1985. http://link.aps.org/doi/10.1103/PhysRevLett.54.992.

[52] S. Chu, L. Hollberg, J. E. Bjorkholm, A. Cable, and A. Ashkin, "Three-dimensional viscous confinement and cooling of atoms by resonance radi-

ation pressure," *Physical Review Letters*, vol. 55, pp. 48–51, Jul 1985. http://link.aps.org/doi/10.1103/PhysRevLett.55.48.

[53] T. Hänsch and A. Schawlow, "Cooling of gases by laser radiation," *Optics Communications*, vol. 13, no. 1, pp. 68 – 69, 1975. http://www.sciencedirect.com/science/article/pii/0030401875901595.

[54] J. Dalibard and C. Cohen-Tannoudji, "Laser cooling below the doppler limit by polarization gradients: simple theoretical models," *Journal of the Optical Society of America B*, vol. 6, pp. 2023–2045, Nov 1989. http://josab.osa.org/abstract.cfm?URI=josab-6-11-2023.

[55] J. Dalibard and C. Cohen-Tannoudji, "Dressed-atom approach to atomic motion in laser light: the dipole force revisited," *Journal of the Optical Society of America B*, vol. 2, pp. 1707–1720, Nov 1985. http://josab.osa.org/abstract.cfm?URI=josab-2-11-1707.

[56] D. S. Weiss, B. C. Young, and S. Chu, "Precision measurement of the photon recoil of an atom using atomic interferometry," *Physical Review Letters*, vol. 70, pp. 2706–2709, May 1993. http://link.aps.org/doi/10.1103/PhysRevLett.70.2706.

[57] A. Wicht, J. M. Hensley, E. Sarajlic, and S. Chu, "A preliminary measurement of the fine structure constant based on atom interferometry," *Physica Scripta*, vol. 2002, no. T102, p. 82, 2002. http://stacks.iop.org/1402-4896/2002/i=T102/a=014.

[58] H. Müller, S.-W. Chiow, Q. Long, C. Vo, and S. Chu, "A new photon recoil experiment: towards a determination of the fine structure constant," *Applied Physics B*, vol. 84, pp. 633–642, 2006. http://dx.doi.org/10.1007/s00340-006-2279-x.

[59] R. Bouchendira, P. Cladé, S. Guellati-Khélifa, F. Nez, and F. Biraben, "New determination of the fine structure constant and test of the quantum electrodynamics," *Physical Review Letters*, vol. 106, p. 080801, Feb 2011. http://link.aps.org/doi/10.1103/PhysRevLett.106.080801.

[60] C. W. Oates, K. R. Vogel, and J. L. Hall, "High precision linewidth measurement of laser-cooled atoms: Resolution of the na $3p^2p_{3/2}$ lifetime discrepancy," *Physical Review Letters*, vol. 76, pp. 2866–2869, Apr 1996. http://link.aps.org/doi/10.1103/PhysRevLett.76.2866.

[61] M. H. Anderson, J. R. Ensher, M. R. Matthews, C. E. Wieman, and E. A. Cornell, "Observation of bose-einstein condensation in a dilute atomic vapor," *Science*, vol. 269, no. 5221, pp. 198–201, 1995. http://www.sciencemag.org/content/269/5221/198.abstract.

[62] K. B. Davis, M. O. Mewes, M. R. Andrews, N. J. van Druten, D. S. Durfee, D. M. Kurn, and W. Ketterle, "Bose-einstein condensation in a gas of sodium atoms," *Physical Review Letters*, vol. 75, pp. 3969–3973, Nov 1995. http://link.aps.org/doi/10.1103/PhysRevLett.75.3969.

[63] M. W. Zwierlein, C. A. Stan, C. H. Schunck, S. M. F. Raupach, S. Gupta, Z. Hadzibabic, and W. Ketterle, "Observation of bose-einstein condensation of molecules," *Physical Review Letters*, vol. 91, p. 250401, Dec 2003. http://link.aps.org/doi/10.1103/PhysRevLett.91.250401.

[64] S. R. Granade, M. E. Gehm, K. M. O'Hara, and J. E. Thomas, "All-optical production of a degenerate fermi gas," *Physical Review Letters*, vol. 88, p. 120405, Mar 2002. http://link.aps.org/doi/10.1103/PhysRevLett.88.120405.

[65] J. L. Roberts, N. R. Claussen, S. L. Cornish, and C. E. Wieman, "Magnetic field dependence of ultracold inelastic collisions near a fesh-

bach resonance," *Physical Review Letters*, vol. 85, pp. 728–731, Jul 2000. http://link.aps.org/doi/10.1103/PhysRevLett.85.728.

[66] S. L. Cornish, N. R. Claussen, J. L. Roberts, E. A. Cornell, and C. E. Wieman, "Stable ^{85}Rb bose-einstein condensates with widely tunable interactions," *Physical Review Letters*, vol. 85, pp. 1795–1798, Aug 2000. http://link.aps.org/doi/10.1103/PhysRevLett.85.1795.

[67] G. Santarelli, P. Laurent, P. Lemonde, A. Clairon, A. G. Mann, S. Chang, A. N. Luiten, and C. Salomon, "Quantum projection noise in an atomic fountain: A high stability cesium frequency standard," *Physical Review Letters*, vol. 82, pp. 4619–4622, Jun 1999. http://link.aps.org/doi/10.1103/PhysRevLett.82.4619.

[68] G. K. Campbell, A. D. Ludlow, S. Blatt, J. W. Thomsen, M. J. Martin, M. H. G. de Miranda, T. Zelevinsky, M. M. Boyd, J. Ye, S. A. Diddams, T. P. Heavner, T. E. Parker, and S. R. Jefferts, "The absolute frequency of the 87 sr optical clock transition," *Metrologia*, vol. 45, no. 5, p. 539, 2008. http://stacks.iop.org/0026-1394/45/i=5/a=008.

[69] M. Kasevich and S. Chu, "Atomic interferometry using stimulated raman transitions," *Physical Review Letters*, vol. 67, pp. 181–184, Jul 1991. http://link.aps.org/doi/10.1103/PhysRevLett.67.181.

[70] M. Kasevich and S. Chu, "Measurement of the gravitational acceleration of an atom with a light-pulse atom interferometer," *Applied Physics B*, vol. 54, pp. 321–332, 1992. http://dx.doi.org/10.1007/BF00325375.

[71] P. A. Altin, *The role of interactions in atom interferometry with Bose-condensed atoms.* PhD thesis, Australian National University, 2012. http://atomlaser.anu.edu.au/publications/phd_masters_and_honours_the.html.

[72] S. M. Dickerson, J. M. Hogan, A. Sugarbaker, D. M. S. Johnson, and M. A. Kasevich, "Multi-axis inertial sensing with long-time point source atom interferometry," *arXiv*, 2013. http://arxiv.org/abs/1305.1700.

[73] J. B. Fixler, G. T. Foster, J. M. McGuirk, and M. A. Kasevich, "Atom interferometer measurement of the newtonian constant of gravity," *Science*, vol. 315, no. 5808, pp. 74–77, 2007. http://www.sciencemag.org/content/315/5808/74.abstract.

[74] G. Lamporesi, A. Bertoldi, L. Cacciapuoti, M. Prevedelli, and G. M. Tino, "Determination of the newtonian gravitational constant using atom interferometry," *Physical Review Letters*, vol. 100, p. 050801, Feb 2008. http://link.aps.org/doi/10.1103/PhysRevLett.100.050801.

[75] S. Dimopoulos, P. W. Graham, J. M. Hogan, and M. A. Kasevich, "Testing general relativity with atom interferometry," *Physical Review Letters*, vol. 98, p. 111102, Mar 2007. http://link.aps.org/doi/10.1103/PhysRevLett.98.111102.

[76] H. Muller, A. Peters, and S. Chu, "A precision measurement of the gravitational redshift by the interference of matter waves," *Nature*, vol. 463, pp. 926– 929, 2010. http://dx.doi.org/10.1038/nature08776.

[77] S. Fray, C. A. Diez, T. W. Hänsch, and M. Weitz, "Atomic interferometer with amplitude gratings of light and its applications to atom based tests of the equivalence principle," *Physical Review Letters*, vol. 93, p. 240404, Dec 2004. http://link.aps.org/doi/10.1103/PhysRevLett.93.240404.

[78] M. J. Snadden, J. M. McGuirk, P. Bouyer, K. G. Haritos, and M. A. Kasevich, "Measurement of the earth's gravity gradient with an atom interferometer-based gravity gradiometer," *Physical Review Letters*, vol. 81, pp. 971–974, Aug 1998. http://link.aps.org/doi/10.1103/PhysRevLett.81.971.

[79] J. M. McGuirk, G. T. Foster, J. B. Fixler, M. J. Snadden, and M. A. Kasevich, "Sensitive absolute-gravity gradiometry using atom interferometry," *Physical Review A*, vol. 65, p. 033608, Feb 2002. http://link.aps.org/doi/10.1103/PhysRevA.65.033608.

[80] T. L. Gustavson, P. Bouyer, and M. A. Kasevich, "Precision rotation measurements with an atom interferometer gyroscope," *Physical Review Letters*, vol. 78, pp. 2046–2049, Mar 1997. http://link.aps.org/doi/10.1103/PhysRevLett.78.2046.

[81] J. K. Stockton, K. Takase, and M. A. Kasevich, "Absolute geodetic rotation measurement using atom interferometry," *Physical Review Letters*, vol. 107, p. 133001, Sep 2011. http://link.aps.org/doi/10.1103/PhysRevLett.107.133001.

[82] M. C. Angonin, P. Tourrenc, and P. Delva, "Cold atom interferometer in a satellite: orders of magnitude of the tidal effect," *Applied Physics B*, vol. 84, pp. 579–584, 2006. http://dx.doi.org/10.1007/s00340-006-2389-5.

[83] K. Bongs, R. Launay, and M. Kasevich, "High-order inertial phase shifts for time-domain atom interferometers," *Applied Physics B*, vol. 84, pp. 599–602, 2006. http://dx.doi.org/10.1007/s00340-006-2397-5.

[84] F. Impens, P. Bouyer, and C. Bordé, "Matter-wave cavity gravimeter," *Applied Physics B*, vol. 84, pp. 603–615, 2006. http://dx.doi.org/10.1007/s00340-006-2399-3.

[85] A. Miffre, M. Jacquey, M. Büchner, G. Trénec, and J. Vigué, "Vibration-induced phase noise in mach-zehnder atom interferometers," *Applied Physics B*, vol. 84, pp. 617–625, 2006. http://dx.doi.org/10.1007/s00340-006-2377-9.

[86] Y. Le Coq, J. Retter, S. Richard, A. Aspect, and P. Bouyer, "Coherent matter wave inertial sensors for precision measurements in space," *Applied Physics B*, vol. 84, pp. 627–632, 2006. http://dx.doi.org/10.1007/s00340-006-2363-2.

[87] P. Cheinet, F. Pereira Dos Santos, T. Petelski, J. Le Gouët, J. Kim, K. Therkildsen, A. Clairon, and A. Landragin, "Compact laser system for atom interferometry," *Applied Physics B*, vol. 84, pp. 643–646, 2006. http://dx.doi.org/10.1007/s00340-006-2266-2.

[88] N. Yu, J. Kohel, J. Kellogg, and L. Maleki, "Development of an atom-interferometer gravity gradiometer for gravity measurement from space," *Applied Physics B*, vol. 84, pp. 647–652, 2006. http://dx.doi.org/10.1007/s00340-006-2376-x.

[89] A. Vogel, M. Schmidt, K. Sengstock, K. Bongs, W. Lewoczko, T. Schuldt, A. Peters, T. Van Zoest, W. Ertmer, E. Rasel, T. Steinmetz, J. Reichel, T. Könemann, W. Brinkmann, E. Göklü, C. Lämmerzahl, H. Dittus, G. Nandi, W. Schleich, and R. Walser, "Bose-einstein condensates in microgravity," *Applied Physics B*, vol. 84, pp. 663–671, 2006. http://dx.doi.org/10.1007/s00340-006-2359-y.

[90] F. Yver-Leduc, P. Cheinet, J. Fils, A. Clairon, N. Dimarcq, D. Holleville, P. Bouyer, and A. Landragin, "Reaching the quantum noise limit in a high-sensitivity cold-atom inertial sensor," *Journal of Optics B: Quantum and Semiclassical Optics*, vol. 5, no. 2, p. S136, 2003. http://stacks.iop.org/1464-4266/5/i=2/a=371.

[91] B. Canuel, F. Leduc, D. Holleville, A. Gauguet, J. Fils, A. Virdis, A. Clairon, N. Dimarcq, C. J. Bordé, A. Landragin, and P. Bouyer, "Six-axis inertial sensor

using cold-atom interferometry," *Physical Review Letters*, vol. 97, p. 010402, Jul 2006. http://link.aps.org/doi/10.1103/PhysRevLett.97.010402.

[92] J. L. Gouët, T. Mehlstaübler, S. Merlet, F. P. D. Santos, A. Landragin, and A. Clairon, "Sensitivity and accuracy studies of an atomic gravimeter," in *Bulletin of the American Physical Society*, vol. 52, No. 7, June 2007.

[93] B. Young, D. S. Bonomi, T. Patterson, F. Roller, T. Tran, A. Vitouchkine, T. Gustavson, and M. Kasevich, "Atom optic inertial and gravitational sensors," in *Laser Science*, p. LTuH1, Optical Society of America, 2007. http://www.opticsinfobase.org/abstract.cfm?uri=LS-2007-LTuH1.

[94] J. Le Gouët, T. E. Mehlstäubler, J. Kim, S. Merlet, A. Clairon, A., A. Landragin, and F. Pereira Dos Santos, "Limits to the sensitivity of a low noise compact atomic gravimeter," *Applied Physics B*, vol. 92, pp. 133–144, 2008. http://dx.doi.org/10.1007/s00340-008-3088-1.

[95] O. Carraz, F. Lienhart, R. Charrière, M. Cadoret, N. Zahzam, Y. Bidel, and A. Bresson, "Compact and robust laser system for onboard atom interferometry," *Applied Physics B*, vol. 97, pp. 405–411, 2009. http://dx.doi.org/10.1007/s00340-009-3675-9.

[96] S. Merlet, Q. Bodart, N. Malossi, A. Landragin, F. P. D. Santos, O. Gitlein, and L. Timmen, "Comparison between two mobile absolute gravimeters: optical versus atomic interferometers," *Metrologia*, vol. 47, no. 4, p. L9, 2010. http://stacks.iop.org/0026-1394/47/i=4/a=L01.

[97] M. Schmidt, A. Senger, M. Hauth, C. Freier, V. Schkolnik, and A. Peters, "A mobile high-precision absolute gravimeter based on atom interferometry," *Gyroscopy and Navigation*, vol. 2, pp. 170–177, 2011. http://dx.doi.org/10.1134/S2075108711030102.

[98] Y. Bidel, O. Carraz, R. Charrière, M. Cadoret, N. Zahzam, and A. Bresson, "Compact cold atom gravimeter for field applications," *arXiv*, 2012. http://arxiv.org/abs/1302.1518.

[99] P. A. Altin, M. T. Johnsson, V. Negnevitsky, G. R. Dennis, R. P. Anderson, J. E. Debs, S. S. Szigeti, K. S. Hardman, S. Bennetts, G. D. McDonald, L. D. Turner, J. D. Close, and N. P. Robins, "Precision atomic gravimeter based on bragg diffraction," *New Journal of Physics*, vol. 15, no. 2, p. 023009, 2013. http://stacks.iop.org/1367-2630/15/i=2/a=023009.

[100] P. Cladé, S. Guellati-Khélifa, C. Schwob, F. Nez, L. Julien, and F. Biraben, "A promising method for the measurement of the local acceleration of gravity using bloch oscillations of ultracold atoms in a vertical standing wave," *Europhysics Letters*, vol. 71, no. 5, pp. 730–736, 2005.

[101] P. Cladé, M. Cadoret, E. De Mirandes, S. Guellati-Khélifa, C. Schwob, F. Nez, L. Julien, and F. Biraben, "Bloch oscillations of ultracold atoms: A tool for metrological measurements," *Journal of Physics IV France*, vol. 135, pp. 3–7, 2006. http://dx.doi.org/10.1051/jp4:2006135002.

[102] G. Ferrari, N. Poli, F. Sorrentino, and G. M. Tino, "Long-lived bloch oscillations with bosonic sr atoms and application to gravity measurement at the micrometer scale," *Physical Review Letters*, vol. 97, p. 060402, Aug 2006. http://link.aps.org/doi/10.1103/PhysRevLett.97.060402.

[103] K. J. Hughes, J. H. T. Burke, and C. A. Sackett, "Suspension of atoms using optical pulses, and application to gravimetry," *Physical Review Letters*, vol. 102, p. 150403, Apr 2009. http://link.aps.org/doi/10.1103/PhysRevLett.102.150403.

[104] R. Beach, S. R. Hartmann, and R. Friedberg, "Billiard-ball echo model," *Physical Review A*, vol. 25, pp. 2658–2666, May 1982. http://link.aps.org/doi/10.1103/PhysRevA.25.2658.

[105] R. Beach, B. Brody, and S. R. Hartmann, "Elliptical billiard-ball echo model," *Physical Review A*, vol. 27, pp. 2537–2547, May 1983. http://link.aps.org/doi/10.1103/PhysRevA.27.2537.

[106] R. Friedberg and S. R. Hartmann, "Billiard balls and matter-wave interferometry," *Physical Review A*, vol. 48, pp. 1446–1472, Aug 1993. http://link.aps.org/doi/10.1103/PhysRevA.48.1446.

[107] C. Raman and N. Nagendra Nath, "The diffraction of light by high frequency sound waves. part i," in *Proceedings of the Indian Academy of Sciences, Section A*, vol. 2, pp. 406–412, Indian Academy of Sciences, 1935. http://www.ias.ac.in/j_archive/proca/2/4/406-412/viewpage.html.

[108] C. Raman and N. Nagendra Nath, "Tthe diffraction of light by sound waves of high frequency: Part ii," in *Proceedings of the Indian Academy of Sciences, Section A*, vol. 2, pp. 413–420, Indian Academy of Sciences, 1935. http://www.ias.ac.in/j_archive/proca/2/4/406-412/viewpage.html.

[109] N. A. Kurnit, I. D. Abella, and S. R. Hartmann, "Observation of a photon echo," *Physical Review Letters*, vol. 13, pp. 567–568, Nov 1964. http://link.aps.org/doi/10.1103/PhysRevLett.13.567.

[110] M. Weel and A. Kumarakrishnan, "Observation of ground-state ramsey fringes," *Physical Review A*, vol. 67, p. 061602, Jun 2003. http://link.aps.org/doi/10.1103/PhysRevA.67.061602.

[111] S. Beattie, B. Barrett, M. Weel, I. Chan, C. Mok, S. B. Cahn, and A. Kumarakrishnan, "Influence of spontaneous emission on a single-state

atom interferometer," *Physical Review A*, vol. 77, p. 013610, Jan 2008. http://link.aps.org/doi/10.1103/PhysRevA.77.013610.

[112] S. Beattie, B. Barrett, I. Chan, C. Mok, I. Yavin, and A. Kumarakrishnan, "Technique for measuring atomic recoil frequency using coherence functions," *Physical Review A*, vol. 79, p. 021605, Feb 2009. http://link.aps.org/doi/10.1103/PhysRevA.79.021605.

[113] S. Beattie, B. Barrett, I. Chan, C. Mok, I. Yavin, and A. Kumarakrishnan, "Atom-interferometric studies of light scattering," *Physical Review A*, vol. 80, p. 013618, Jul 2009. http://link.aps.org/doi/10.1103/PhysRevA.80.013618.

[114] D. V. Strekalov, A. Turlapov, A. Kumarakrishnan, and T. Sleator, "Periodic structures generated in a cloud of cold atoms," *Physical Review A*, vol. 66, p. 023601, Aug 2002. http://link.aps.org/doi/10.1103/PhysRevA.66.023601.

[115] T. W. Mossberg, R. Kachru, S. R. Hartmann, and A. M. Flusberg, "Echoes in gaseous media: A generalized theory of rephasing phenomena," *Phys. Rev. A*, vol. 20, pp. 1976–1996, Nov 1979. http://link.aps.org/doi/10.1103/PhysRevA.20.1976.

[116] P. R. Berman and V. S. Malinovsky, *Principles of Laser Spectroscopy and Quantum Optics*. Princeton University Press, 2011.

[117] B. Barrett, I. Yavin, S. Beattie, and A. Kumarakrishnan, "Numerical simulation of a multilevel atom interferometer," *Physical Review A*, vol. 82, p. 023625, Aug 2010. http://link.aps.org/doi/10.1103/PhysRevA.82.023625.

[118] M. Weel, *Measurement of Atomic Recoil Using Atom interferometric techniques*. PhD thesis, York University, 2005.

[119] M. Suzuki, "On the convergence of exponential operatorsthe zassenhaus formula, bch formula and systematic approximants," *Communications in Mathematical Physics*, vol. 57, no. 3, pp. 193–200, 1977.

[120] U. D. Rapol, A. Wasan, and V. Natarajan, "Loading of a rb magneto-optic trap from a getter source," *Physical Review A*, vol. 64, p. 023402, Jun 2001. http://link.aps.org/doi/10.1103/PhysRevA.64.023402.

[121] A. Vorozcovs, M. Weel, S. Beattie, S. Cauchi, and A. Kumarakrishnan, "Measurements of temperature scaling laws in an optically dense magneto-optical trap," *Journal of the Optical Society of America B*, vol. 22, pp. 943–950, May 2005. http://josab.osa.org/abstract.cfm?URI=josab-22-5-943.

[122] R. E. Scholten, "Enhanced laser shutter using a hard disk drive rotary voice-coil actuator," *Review of Scientific Instruments*, vol. 78, p. 026101, Feb 2007. http://dx.doi.org/10.1063/1.2437199.

[123] S. R. Systems, *PRS-10 10 MHz Rubidium Frequency Standard Manual.* Stanford Research Systems, 2005.

[124] S. R. Systems, *DG-535 Digital Delay/Pulse Generator Manual.* Stanford Research Systems, 1997.

[125] G. K. Campbell, A. E. Leanhardt, J. Mun, M. Boyd, E. W. Streed, W. Ketterle, and D. E. Pritchard, "Photon recoil momentum in dispersive media," *Physical Review Letters*, vol. 94, p. 170403, May 2005. http://link.aps.org/doi/10.1103/PhysRevLett.94.170403.

[126] B. Barrett, *Techniques for Measuring the Atomic Recoil Frequency using a Grating-Echo Atom Interferometer.* PhD thesis, York University, 2012.

[127] P. Cladé, E. de Mirandes, M. Cadoret, S. Guellati-Khélifa, C. Schwob, F. Nez, L. Julien, and F. Biraben, "Precise measurement of $\hbar/m_{\mathrm{rb}}$ us-

ing bloch oscillations in a vertical optical lattice: Determination of the fine-structure constant," *Physical Review A*, vol. 74, p. 052109, Nov 2006. http://link.aps.org/doi/10.1103/PhysRevA.74.052109.

[128] M. F. Andersen and T. Sleator, "Lattice interferometer for laser-cooled atoms," *Physical Review Letters*, vol. 103, p. 070402, Aug 2009. http://link.aps.org/doi/10.1103/PhysRevLett.103.070402.

[129] A. Schilke, C. Zimmermann, P. W. Courteille, and W. Guerin, "Photonic band gaps in one-dimensionally ordered cold atomic vapors," *Physical Review Letters*, vol. 106, p. 223903, Jun 2011. http://link.aps.org/doi/10.1103/PhysRevLett.106.223903.

[130] A. Tonyushkin, "Comment on "periodic structures generated in a cloud of cold atoms"," *Physical Review A*, vol. 75, p. 037602, Mar 2007. http://link.aps.org/doi/10.1103/PhysRevA.75.037602.

[131] S. S. Sané, S. Bennetts, J. E. Debs, C. C. N. Kuhn, G. D. McDonald, P. A. Altin, J. D. Close, and N. P. Robins, "11 w narrow linewidth laser source at 780nm for laser cooling and manipulation of rubidium," *Optics Express*, vol. 20, pp. 8915–8919, Apr 2012. http://www.opticsexpress.org/abstract.cfm?URI=oe-20-8-8915.

[132] T. M. Niebauer, A. Schiel, and D. van Westrum, "Complex heterodyne for undersampled chirped sinusoidal signals," *Applied Optics*, vol. 45, pp. 8322–8330, Nov 2006. http://ao.osa.org/abstract.cfm?URI=ao-45-32-8322.